UNIVERSIDAD COMPLUTENSE DE MADRID

FACULTAD DE CIENCIAS FÍSICAS
Departamento de Física de la Tierra, Astronomía y Astrofísica II
(Astrofísica y Ciencias de la Atmósfera)

TESIS DOCTORAL

From Xrays to far infrared: galaxy cluster ZwCL0024+1652 under the multiwavelength limelight

De rayos X a infrarrojo lejano : una mirada multifrecuencia al cúmulo de galaxias ZwCL0024+1652

MEMORIA PARA OPTAR AL GRADO DE DOCTOR

PRESENTADA POR

Ricardo Manuel Pérez Martínez

Directores
Miguel Sánchez Portal
Leo Metcalfe
Ana María Pérez García

Madrid, 2016

Departamento de Astrofísica y Ciencias de la Atmósfera II
Facultad de Ciencias Físicas
Universidad Complutense de Madrid

From Xrays to Far Infrared: Galaxy Cluster ZwCL0024+1652 under the multiwavelength limelight.

De Rayos X a Infrarrojo Lejano: Una mirada multifrecuencia al Cúmulo de Galaxias ZwCL0024+1652

Memoria que presenta

Ricardo Manuel Pérez Martínez

para la obtención del título de Doctor en Ciencias Físicas

Tesis dirigida por

Dr. Miguel Sánchez Portal, **Dr. Leo Metcalfe** y **Dra. Ana María Pérez García**

Diciembre de 2015

A José y Sotera, mis padres,
quienes me enseñaron el valor de las palabras, a no darme nunca por vencido
y el calor de los domingos por la mañana.

Agradecimientos

Ningún trabajo de tesis queda realmente terminado hasta que no se escriben los agradecimientos. Es quizá lo último que uno hace, pero también a lo que más esfuerzo le dedica, porque se le presta toda la energía que queda, todo el entusiasmo y la ilusión que se escurren por los agujerillos de los bolsillos después de haber pasado entre 10 y 1000 horas volcado sobre el teclado de un ordenador sin levantar la vista de gráficos, citas y textos.

Ningún trabajo de tesis queda realmente terminado hasta que no se escriben los agradecimientos. En realidad, ningún trabajo de tesis queda realmente terminado hasta que uno da un paso atrás, mira lo que tiene delante y para un segundo a pensar en cómo se ha desarrollado todo esto.

En mi caso particular, yo he llegado hasta aquí gracias al tiempo, la dedicación y la sabiduría (en la máxima extensión de la palabra) de mis directores de tesis, Miguel, Leo y Ana, a quienes les debo gratitud no sólo por acompañarme en este camino, sino hacerlo dándome de paso su entusiasmo, su aprecio y ese algo inaprensible que da tirarse once noches en un observatorio sin que pare de llover y aún así regresar a casa de buen humor e ilusionado. Y luego, 2 horas de revisión de tesis a las 3 de la mañana (literal). Y más tiempo aún aprendiendo/enseñando IRAF a unas horas a las que Maribel (a quien también estoy muy agradecido) casi que no espera con la cena (y haciendo revisión del mundo, ya de paso). Y luego 14 horas por siete días de una semana en la sala de visitantes del IAC, y eso varias veces seguidas (¿dónde está la piscina?).

También ha sido un placer compartir este camino con Jordi, Ángel, Alessandro, Ignacio y más recientemente Miguel, con su extraordinaria capacidad de trabajo y su no menos extraordinaria capacidad de disfrutar de una buena cena inmediatamente después. Por su forma de hablar de astronomía en cualquier momento y acto seguido pasar a la pintura pre-rafaelista, los misterios de picos de Europa o las dietas neolíticas. Y por supuesto, Irene, Marina e Iván, entusiastas y grandes científicos a partes iguales.

Y, claro, ningún trabajo de tesis queda realmente terminado hasta que uno para, reflexiona un segundo y considera todo lo que ha pasado a su alrededor mientras la escribía. En mi caso todas las cosas que han pasado a mi alrededor se resumen en que mis padres mis hermanas, sus parejas y sus hijas (incluido un pre-bebé de sexo por determinar) siguen siendo el grupo de apoyo más jaleoso y sólido que conozco. Que mis amigos del taller, del coro, de la facultad, de villafranca, del comité de crisis y festejos varios, de munich y, cómo no, del sum-sum corda, siguen siendo (y

lo son aún más) mis amigos del taller, del coro, de la facultad, de villafranca, del comité de crisis y festejos varios, de munich y, cómo no, del sum-sum corda. Y Carl Sagan, quien dijo que si quieres hacer una tarta de de manzana desde cero, primero tienes que crear el Universo.

Y, por último y por ello muchísimo más importante, todo esto se resume en tres palabras: Daniela, Alexa y Mina (o, lo que es lo mismo: la risa, el arte y la banitsa).

Resumen

Los cúmulos de galaxias son las mayores estructuras autogravitantes conocidas. Descubiertas por Charles Messier en el siglo XVII, no fueron estudiadas sistemáticamente hasta doscientos años más tarde, cuando a finales de los 50 Abell y Zwicky comenzaron los primeros estudios sistemáticos de identificación de cúmulos en el Universo local. Estos primeros trabajos concluyeron que los cúmulos de Galaxias están formados por objectos separados entre sí por pequeñas distancias proyectadas en el campo de observación y con índices de color similares. Estas características fueron en ese momento se comenzaron a utilizar para establecer membresías. Desde entonces este ha sido uno de los principales temas de discusión en el campo: la separación precisa de los miembros del cúmulo y los objetos de fuera de él. Otro asunto importante es el establecimiento del estado dinámico del cúmulo como entidad cosmológica y de sus miembros. Del estado de estos últimos se puede deducir el del primero mediante aproximaciones relacionadas con la dispersión de velocidades, el tamaño del cúmulo y aplicando el Teorema de Virial.

Cuando satélites como Uhuru permitieron las primeras observaciones en Rayos X, se descubrió que los cúmulos presentan una emisión extendida de alta energía , que fue rápidamente asociada con la emisión por Bremsstrahlung del gas difuso intracumular. La detección de este gas caliente permitió el cálculo del pozo de potencial necesario para justificar la energía detectada. Las estimaciones basadas en datos de Rayos X presentan una notable diferencia con respecto a los cálculos derivados de la dinámica de las galaxias y el teorema del virial, que en algunos casos llega al 70 %.

A la vez, estudios sobre las características de la población cumular en relación con las propiedades de la galaxias de campo encontraron diferencias notables tanto en las masas típicas, colores y tipos morfológicos. Las galaxias de los cúmulos son más grandes, predominantemente rojas y con tipos morfológicos más tempranos que las observadas fuera de estas estructuras. Además, se encontró que la fracción de galaxias azules crece con el desplazamiento al rojo y la distancia al centro del cúmulo.

De esta forma se estableció que los cúmulos tienen una masa oculta a los métodos de medición basados en la dinámica de sus miembros visibles y que sus galaxias tienen caracterísiticas distintas a las de campo. Para poder estudiar estos asuntos en profundidad es fundamental contar con catálogos de membresías exactos basados en la obtención de desplazamientos al rojo precisos. Sin embargo, esto es difícil de conseguir. Las estimaciones fotométricas de desplazamientos al rojo carecen de la precisión y a menudo la exactitud necesaria, mientras que las espectroscópicas exi-

gen grandes tiempos de exposición. Además, la selección de objetos implica decisiones a priori que pueden sesgar el resultado al favorecer objetos típicos y soslayando otros en los extremos de las distribuciones de luminosidad o índices de color.

Una solución posible viene de la mano de instrumentos con capacidad de hacer espectroscopia de campo integral. Si además cuentan con campos de visión grandes y están instalados en telescopios con gran área colectora, se pueden hacer estudios espectroscópicos de objetos en cúmulos de galaxias con tiempos de exposición aceptablemente bajos. En concreto OSIRIS, instalado en el Gran Telescopio CANARIAS (GTC), puede usar filtros sintonizables para tomar imágenes de banda estrecha (a partir de 12 Å) en un campo de visión de 8 minutos de arco, lo que le permite cubrir áreas de aproximadamente un radio virial en anchura proyectada para cúmulos típicos a z~0.3 y mayores.

GLACE es un programa de observación que pretende usar estas capacidades para realizar un cartografiado de líneas de emisión en cúmulos situados en ventanas de desplazamientos al rojo desde 0.4 hasta 0.8. En este trabajo se presentan los primeros resultados y conclusiones de unos de los cúmulos estudiados, ZwCl0024+1652, junto con el estudio multifrecuencia de sus fuentes desde Rayos–X hasta infrarrojo lejano.

El principal objetivo científico de este trabajo es la determinación de las regiones (entendidas tanto en términos de distribuciones espaciales de masa como del espacio de fases de las densidades locales proyectadas) en las que tienen lugar la mayor parte de las transformaciones por las que una galaxia de campo típica adquiere las características propias de los objetos cumulares.

Con el objeto de identificar estas transformaciones y los mecanismos que las producen, hemos trazado las cías evolutivas de tres distintas poblaciones de objetos en el cúmulo: Los emisores en infrarrojo lejano, los AGNs y las galaxias con tasas significativas de formaciónn estelar.

Primero hemos recolectado y analizado datos de distintas procedencias (observaciones propias en óptico, imágenes de archivo de Rayos X, infrarrojo medio e infrarrojo lejano, catálogos de archivo y publicados en distintos artículos). Luego hemos construido el catálogo multifrecuencia con técnicas precisas de asignación de contrapartidas, estimando el error posible cometido en cada uno de los cruces. Este catálogo presenta entonces las distribuciones espectrales de energía (SEDs) de cada una de las fuentes detectadas en el campo de visión. Hemos seleccionado entonces aquellas fuentes con desplazamientos al rojo correspondientes al cúmulo, obteniendo una muestra de 1262 objetos.

Mediante ajustes a bibliotecas de plantillas espectroscópicas de poblaciones estelares compuestas mediante el algoritmo de acceso público *Le PHARE*, hemos obtenido sus luminosidades ultravioleta, en banda K e infrarroja. Hemos comparado valores obtenidos de esta manera con los derivados por otros métodos descritos en la literatura y establecido la fiabilidad de cada uno de ellos.

Con respecto al grupo formado por las galaxias infrarrojas, estudiadas por primera vez en este estudio, hemos seleccionado 122 objetos en total, encontrando que en general siguen las mismas tendencias que el resto de sus compañeros del cúmulo, con 52 galaxias infrarrojas luminosas (LIRGs, de sus siglas en inglés), y ninguna galaxia infrarroja ultraluminosa (ULIRG, de sus siglas en inglés). En cuanto a los AGNs (143 objetos), hemos determinado por primera vez que están localizados principalmente en la zona intermedia, con un pico de presencia en 0,7 $\sim r_{vir}$. Dominan la zona del "valle verde" en el diagrama de Color-Magnitud, como era de esperar, y tienen morfologías predominantemente espirales o de disco. Las galaxias con formación estelar están también subrepresentadas en la parte interior del cúmulo ($\sim$ 0,3 Mpc) aunque se hayan localizadas a lo largo de toda la estructura. Siguen una distribución bimodal tanto en el diagrama Color-Magnitud como en el de Masa Estelar - Color, marcando claramente la secuencia roja y la nube azul en el primero y la secuencia principal de galaxias rojas en el segundo.

Hemos calculado la tasa de formación estelar (SFR, de sus siglas en inglés) de dos manera independientes: a través de la luminosidad infrarroja y del flujo en Hα . Esta última ha sido corregida de extinción aplicando el decremento de Balmer, derivado del flujo en Hβ. Para los objetos con ambas medidas (27 en total, 24 % de la población de galaxias con líneas de emisión) la extinción es de $A_{H\alpha} \sim$ 1,41 magnitudes.

Hemos estudiado la influencia de la estructura del cúmulo en los colores y las SFRs. El mapa de densidad del cúmulo ha sido derivado de las imágenes de Rayos X y de la distribución de fuentes ópticas y sus velocidades radiales relativas. También hemos hallado la densidad local proyectada (Σ_5). El índice de color B-R de las galaxias situadas en la zona de menor densidad tiene un valor máximo local de 1.1, mientras que en la de máxima es de 2.3. Tanto la SFR como la sSFR (tasa de formación estelar específica) decrecen con el aumento de la densidad local. Es de reseñar el descubrimiento de una cavidad en la zona Este del cúmulo, a aproximadamente 4 minutos de arco del centro.

Con respecto a las masas estelares y su relación con SFR, la población roja está alineada con la llamada "secuencia principal", mientras que la población azul presenta menores masas y mayores SFRs. En general, las galaxias rojas presentan mayores masas estelares, con valores típicos entre $10^{8,5}$ $M\odot$ y $10^{10,5}$ $M\odot$ con un máximo en $10^{9,5}$ $M\odot$. La distribución de masas de las galaxias azules va de $10^{7,0}$ $M\odot$ a $10^{10,0}$ $M\odot$ con un máximo en $10^{8,5}$ $M\odot$. Las galaxias azules son mayoritarias en la estructura secundaria del cúmulo, (un subgrupo en la línea de visión que está siendo acretado por el potencial principal), mientras que las rojas predominan en la zona más interna del cúmulo.

Para finalizar con los estudios presentados en esta tesis, hemos buscado objetos en interacción actual o reciente. Para ellos hemos identificado pares de galaxias a distancias proyectadas por debajo de los 100 kpc, y velocidades peculiares relativas de $\Delta z \leq$ 0,005. Hemos encontrado 88 pares, 96 % de ellos en la estructura principal, principalmente en la zona interna e intermedia del cúmulo $r <$ 1 Mpc. Estos pares representan una fracción significativa (34 %) de las galaxias con elevada SFR. Aunque estas conclusiones están basadas en muestras muy pequeñas, hay una relación apreciable entre fusiones potenciales y mayores SFRs y menores luminosidades infrarrojas.

Abstract

Clusters of Galaxies are the largest gravitationally bound systems known. Discovered by Charles Messier in the XVIII century, they started to be systematically studied two hundred years later, when Abell and Zwicky undertook a series of surveys to identify concentrations of galaxies in the accessible Universe. These initial studies concluded that clusters of galaxies were formed by objects with the same visual colors and used them to establish memberships. This has been since then one of the biggest issues in this field: the accurate separation of cluster population versus projected foreground or background objects. One other issue is to establish the dynamical status of both the cluster itself and the sources within. From the latter, the former can be inferred, even by crude assumptions on the typical mass of the galaxies, since the velocity dispersion of the members and the cluster radius are linked via the Virial Theorem. However, early observations from spaceborne telescopes discovered significant extended X–ray emission from the cluster cores that was soon identified as Bremsstrahlung radiation in the diffuse intracluster plasma. The detection of such hot gas led to the calculation of the potential well needed to keep it bound to the system and the amount of gas required. Both estimates, from optical and X–ray data disagreed by up to (and even beyond) 70% in some cases.

At the same time, the characteristics of the cluster population were studied and compared to field galaxies. It was found that cluster members favoured elliptical morphologies, larger masses and red colours, versus the dominant fraction of blue mid size spirals in the field. Moreover, the fraction of blue galaxies was found to vary along the clustercentric distance and with redshift, increasing this blue fraction directly with both.

It was established that clusters of galaxies harboured much more mass that that directly observable in optical wavelengths and that their members had undergone or were undergoing transformations that made their evolutionary path diverge from their counterparts in the field. To appropriately address those issues a key observable was demanded: accurate redshifts. However, that was found hard to get. On the one hand, photometric redshifts by themselves lack of the precision needed to establish whether a galaxy is within the cluster or not. On the other, spectroscopic redshifts are extremely demanding in terms of observation time and the selection of objects imply some a-priori criteria that may significantly bias the result, focusing in typical cluster members and eventually overlooking objects in the ends of the distribution function of luminosities and colors.

Instruments with large collective area and integral field spectroscopy capabilities are a solution

for this need. In particular, OSIRIS, at the GTC, is able to perform low-resolution tomography by using its Tunable Filter mode and performing extreme narrow band imaging (12 Å) of a field of view of 8 arcminutes. By successively tuning the filter around the wavelength of interest, one can obtain pseudospectra of enough resolution to identify and measure the flux of selected lines. GLACE is a large observational program aiming to benefit from this capability to perform an Hα+ [N II], Hβ, [OIII] and [OII] survey in a series of clusters from redshift 0.4 to 1.2.

This thesis is part of the GLACE program and focus on one of their targets: the cluster of galaxies ZwCl0024+1652. The main scientific aim of the present work is to determine the region (understood as both mass spatial distribution and local surface density space-phase) where the bulk of the transformation from typical field galaxies into cluster objects take place.

To fully identify these transformations and the mechanisms involved we trace the evolutionary paths of three cluster population groups: The far infrared sample, identified and described for the first time in this work. Second, the AGN cluster members, selected from three independent diagnostics. Third, the star forming galaxies, for which the star formation rate has been calculated from three different methods and compared.

First, a detailed description of the data gathering (from both dedicated observation or archival products) is detailed. Then, the specific reduction techniques of the different data sets are presented. Then, we discuss the construction of the multi wavelength catalogue with accurate cross-matching mechanisms.

Our study concluded that the FIR population follows in general the trends of the rest of their cluster companions, finding a significant amount of Luminous Infra Red Galaxies, LIRGs (52 out of 122), but no ULIRGs. About the AGN population (15.4% of the total sample), for the first time it has been established that they are mainly located in the intermediate virial area, peaking at $0.7 \sim r_{vir}$. It dominates the green valley in the color - magnitude diagram, as expected, and is mainly constituted by spirals and disklike galaxies. The star forming galaxies are also underrepresented in the internal core ($\sim$ 0.3 Mpc) although they are scattered along the whole cluster. They follow a bimodal distribution both in the color (B-R) - magnitude and in the stellar mass - color (B-R) diagrams, clearly mapping the red sequence and blue cloud in the former, and the main sequence of red galaxies in the latter. The red objects dominate the internal cluster core, while the blue galaxies represent the most of the sources in the secondary structure (a line-of sight infalling group).

We have calculated the SFRs independently from the infrared luminosities and the Hα data. This last estimate has been corrected from extinction applying the Balmer decrement derived from the Hβ line. For those objects with both Hα and Hβ measurements (27, 24% of the ELG population) the extinction is $A_{H\alpha} \sim 1.41$ magnitude.

The direct influence of the cluster structures in the colours and SFRs of its members has been also studied. The cluster density map has been derived from X–ray images and the distribution of optical sources. The local surface density (Σ_5) has been obtained and related to these galaxy

properties. B-R color peaks at 1.1 in the lowest density area and at 2.3 in the highest one. The SFR and sSFR uniformly decrease with higher local densities. It is worth to remark the discovery of a mass cavity in the cluster, at 4 arcmin east from the centre.

With respect to the stellar mass versus the SFR, the red population is aligned with the so called galaxy main sequence, while the blue cloud subsample is scattered along the low mass / high SFR area in the same diagram. In general, the red galaxy fraction have higher stellar masses, with typical values between $10^{8.5}$ $M\odot$ and $10^{10.5}$ $M\odot$ and peaking at $10^{9.5}$ $M\odot$. The mass distribution of the blue fraction ranges from $10^{7.0}$ $M\odot$ and $10^{10.0}$ $M\odot$ and peaks at $10^{8.5}$ $M\odot$.

To finish with the studies presented in this thesis, we have searched for recent or ongoing mergers. For that we identified galaxy pairs with projected distances below 100 kpc and relative radial velocities of $\Delta z \leq 0.005$. 88 pairs have been found, 96% of them in the main cluster structure, favouring the intermediate and internal area of the cluster with 64% of them in $r < 1$ Mpc. These close encounters are a significant subfraction (34%) of the high SFR side of the cluster distribution. Although these conclusion is affected by small number statistics, there is a noticeable correlation between potential mergers and enhanced star forming activity and lower infrared luminosities.

Acknowledges

This research has made use of data obtained from the 3XMM XMM-Newton serendipitous source catalogue compiled by the 10 institutes of the XMM-Newton Survey Science Centre selected by ESA.

This research has made use of XMM-Newton Science Archive (XSA) data and software provided by the XMM-Newton Science Operations Centre in the application package SAS. In particular, this work has seriously benefited from the support and unique help of Dr. Carlos Gabriel.

This research has made use of data obtained from the Chandra Source Catalog, provided by the Chandra X-ray Center (CXC) as part of the Chandra Data Archive.

Some of the data presented in this work were obtained from the Multimission Archive at the Space Telescope Science Institute (MAST). The GALEX data archive continue to be available via the MAST, which is also the only NASA-sanctioned site that distributes GALEX data to the public. Support for MAST for non-HST data is provided by the NASA Office of Space Science via grant NNX09AF08G and by other grants and contracts.

This research is based in part on observations made with the Gran Telescopio Canarias (GTC), installed in the Spanish Observatorio del Roque de los Muchachos of the Instituto de Astrofísica de Canarias, on the island of La Palma.

This work is based in part on observations made with the Spitzer Space Telescope, which is operated by the Jet Propulsion Laboratory, California Institute of Technology under a contract with NASA.

This work is based in part on observations made with the Herschel Space Observatory, which is an ESA space observatory with science instruments provided by European-led Principal Investigator consortia and with important participation from NASA. The Herschel spacecraft was designed, built, tested, and launched under a contract to ESA managed by the Herschel/Planck Project team by an industrial consortium under the overall responsibility of the prime contractor Thales Alenia Space (Cannes), and including Astrium (Friedrichshafen) responsible for the payload module

and for system testing at spacecraft level, Thales Alenia Space (Turin) responsible for the service module, and Astrium (Toulouse) responsible for the telescope, with in excess of a hundred subcontractors.

This work makes use of data products from the Two Micron All Sky Survey, which is a joint project of the University of Massachusetts and the Infrared Processing and Analysis Center California Institute of Technology, funded by the National Aeronautics and Space Administration and the National Science Foundation.

In this work, we have used HIPE, that is a joint development by the Herschel Science Ground Segment Consortium, consisting of ESA, the NASA Herschel Science Center, and the HIFI, PACS and SPIRE consortia.

IRAF is distributed by the National Optical Astronomy Observatory, which is operated by the Association of Universities for Research in Astronomy (AURA) under cooperative agreement with the National Science Foundation.

This work make use of SExtractor: Software for source extraction, developed by Bertin & Arnouts.

This research use LePhare code (http://www.cfht.hawaii.edu/ arnouts/lephare.html), developed by Arnouts & Ilbert.

This work were carried out in part using SciGrid at the ESA/ESAC Intranet. We want to thank ESAC Computer and GRID Support Group.

We acknowledge support from the Faculty of the European Space Astronomy Centre (ESAC).

This work was partially supported by the Spanish Plan Nacional de Astrononomía y Astrofísica under grant AYA2008-06311-C02-01 and by the Spanish Ministerio de Economía y Competitividad (MINECO) under the grant AYA2011-29517-C03-01.

We acknowledge support from Ingeniería y Sistemas para la Defensa de España (ISDEFE).

Contents

Agradecimientos **iii**

Resumen **v**

Abstract **ix**

Acknowledges **xiii**

Acronyms and Abbreviations **xxii**

List of figures **xxiii**

List of tables **xxvii**

1 Introduction **1**
1.1 Cluster of Galaxies . . . 2
1.2 The GaLAxy Cluster Evolution project . . . 4
1.3 ZwCL0024+1652 . . . 6
1.4 Scientific aims of this work . . . 9

2 Observational material and data reduction **11**
2.1 Optical data: OSIRIS . . . 12
2.1.1 The OSIRIS Instrument . . . 12
2.1.2 Tunable-filters optical data . . . 15
2.1.3 Flux calibration . . . 18
2.2 Derivation of line fluxes . . . 21
2.2.1 Hβ data . . . 24
2.3 Mid Infrared data: Spitzer . . . 24
2.3.1 Spitzer Space Telescope . . . 24
2.3.2 Spitzer data . . . 25
2.4 Far Infrared data: Herschel . . . 26
2.4.1 Herschel . . . 26
2.4.2 Herschel data . . . 28
2.5 X–ray data: XMM–Newton . . . 29
2.5.1 XMM–Newton . . . 29
2.5.2 XMM–Newton Data . . . 31
2.6 Archival catalogs . . . 32
2.6.1 X–ray catalogs . . . 32

2.6.2 GALEX catalogs . . . 34
2.6.3 Broad-band optical-NIR data . . . 35

3 Multiwavelength catalog and spectral energy distribution 37
3.1 Introduction . . . 38
3.2 Likelihood Ratio estimation and match reliability . . . 39
3.3 The photometric catalog . . . 43
3.4 Spectral energy distributions of the cluster members . . . 47
3.4.1 Le Phare and its settings . . . 47
3.4.2 Simulations . . . 48
3.5 Calculation of integrated luminosities . . . 52

4 Extinction correction of the star formation rate derived from Hα measurements: Hβ observations of ZwCl0024+1652. 55
4.1 Observations and data reduction . . . 56
4.2 Estimation of the stellar absorption strength . . . 58
4.3 Estimation of the extinction at Hα and corrected SFR . . . 60
4.4 Comparison with SFRs derived from FIR . . . 61

5 Cluster Population 65
5.1 FIR population . . . 66
5.1.1 Introduction . . . 66
5.1.2 Population characteristics . . . 67
5.1.3 Far-infrared sources in the cluster . . . 70
5.1.4 Far-infrared morphology . . . 71
5.2 AGN population . . . 77
5.2.1 Introduction . . . 77
5.2.2 AGN selection in ZwCl0024+1652 . . . 78
5.2.3 AGN Fraction . . . 84
5.2.4 AGN Luminosity distribution . . . 87
5.2.5 AGN Morphology . . . 91
5.3 Star Forming population . . . 93
5.3.1 Introduction . . . 93
5.3.2 Luminosity distributions . . . 93
5.3.3 SF Morphology . . . 99
5.3.4 ELG fraction . . . 100
5.3.5 Star formation rate . . . 100
5.3.6 Stellar Masses . . . 103

6 Environmental effects 105
6.1 Cluster Substructure Maps . . . 106
6.1.1 X–ray substructure profiles . . . 107
6.1.2 Optical density profile . . . 110
6.2 Local densities . . . 111
6.3 Dependence on local density . . . 117
6.4 Close encounters . . . 119

7 Summary and Conclusions 129

7.1 Summary 130
7.2 Conclusions 133
7.3 Future work 135

A Cl0024+1654 multiwavelength catalogue **137**

B Cl0024+1654 parameters catalogue **141**

Bibliography **154**

Acronyms and Abbreviations

FUV far ultraviolet. 52

$L(IR)$ Bolometric Infrared Luminosity. 9, 37, 47, 48, 52, 61, 68, 69, 72, 74, 87, 89, 95, 100, 101, 120, 134

$L(K)$ K-band Luminosity. 48

$L(R)$ R-band Luminosity. 48

$L(UV)$ Ultraviolet Luminosity. 37, 47, 48, 49, 52, 53, 89, 100, 101, 102

$L(X)$ X–ray Luminosity. 81

Le PHARE Photometric Analysis for Redshift Estimate. 47, 48, 49, 52, 130

R_c reliability parameter. 40, 42, 43

r_{vir} virial radius. 4, 5

AGN Active Galactic Nuclei. 9, 75, 133

BC03 Bruzual and Charlot population synthesis models. 47, 49

C catalog completeness parameter. 42

CMD Color Magnitud Diagram. 67, 84

CSC Chandra Source Catalog. 33

CTA Spitzer Cryogenic Telescope Assembly. 24

DM dark matter. 1, 2

ELG emission line galaxy. 7, 46, 107, 133

EPIC European Photon Imaging Camera. 30, 33

FIR Far-Infrared. 24, 47, 52, 66

FoV field of view. 5, 43, 47

FWHM full width at half maximum. 12

GLACE GAlaxy Cluster Evolution survey. 4, 5, 7, 43

GTC Gran Telescopio CANARIAS. 12

HEPM Herschel Extended Payload Module. 26

HerMES Herschel Multi-tiered Extragalactic Survey. 27

HIFI Heterodyne Instrument for the Far Infrared. 27

ICM intracluster medium. 1, 2, 95, 133

IR infrared. 3

IRAC Infrared Array Camera. 24

IRS Infrared Spectrograph. 25

LIRG luminous infrared galaxy. 2, 133

LR likelihood ratio. 39, 40, 42, 43

M05 Moran+05 Catalogue. 37, 40, 42, 43, 46, 110

MIPS Multiband Imaging Photometer. 24

MIR Mid-Infrared. 24, 40, 78

NIR Near-Infrared. 24, 47

NLAGN Narrow-Line AGN. 78

ODF Observation Data File. 32

OM XMM–newton Optical Monitor. 30

OSIRIS Optical System for Imaging and low-Intermediate-Resolution Integrated Spectroscopy. 12

PACS Photodetector Array Camera and Spectrometer. 27

PEP PACS Evolutionary Probe. 27

POLL Polleta semyempirical models. 47, 49

PSF Point Spread Function. 38

R catalog reliability. 42

RGS Reflection Grating Spectrometer. 30

SAS XMM–Newton Science Analysis System. 31

SED Spectral Energy Distribution. 9, 37, 38, 47

SFH Star Formation History. 38, 47

SFR star formation rate. 2, 3, 7, 9, 37, 48, 53, 133

SP15 Sanchez-Portal+15 Catalogue. 37, 46, 86

SPIRE Spectral and Photometric Imaging Receiver. 27

sSFR Specific Star Formation Rate. 2, 38, 53

TF tunable filters. 5

ULIRG ultra luminous infrared galaxy. 69, 133

UV ultraviolet. 9, 40

XMM–Newton X-ray Multi-Mirror Mission Newton. 28

XSA XMM–Newton Scientific Archive. 31, 32

XUOIR Xray, UV, Optical, IR catalog. 39

List of Figures

1.1 HST image of ZwCL0024+1652 8

2.1 Etalon scheme from the OSIRIS User Manual 13
2.2 Fabry-Pérot vs TF (courtesy of I. Pintos) 14
2.3 Examples of Hα pseudospectra 18
2.4 Spitzer telescope schematics 25
2.5 Herschel telescope schematics 27
2.6 XMM payload schematics 29
2.7 MOS and PN CCD bench 29
2.8 Wolter I optical design 31
2.9 ZwCl0024+1652 integrated X–ray contours 33

3.1 *q(m)* and *n(m)* for each NonOpt catalog 41
3.2 Reliability vs Likelyhood Ratio (normalized) for each of the seven independent NonOpt catalogs 44
3.3 Distribution of the match reliability, R_c 45
3.4 Distribution of the *frequency* the best SED library 49
3.5 Distribution of error estimates in the first (free model) and second (fixed model) runs of *Le PHARE* 50
3.6 Best fit SED library as output by *Le PHARE* second run 51
3.7 Comparison of LUV and L(IR) obtained from different methods 53

4.1 Hβ TF efficiency 57
4.2 Hβ pseudospectra 57
4.3 Distribution of Hβ absorption line equivalent widths 59
4.4 Distributions of extinctions derived from the Balmer decrement and SFR corrected 61
4.5 Relation between extinction corrected and uncorrected Hα SFR 62
4.6 Relation between the IR SFR and Hα SFR (uncorrected and corrected) 63

5.1 Fraction and R distribution of FIR population 68
5.2 Colour Magnitud Diagram of the FIR population 69
5.3 Comparisson between L(IR) estimated from multipoint using Le PHARE SED-fitting and single point (24μm) SED-normalization 70
5.4 LIR luminosity distribution for IR emitters 71
5.5 Cumulative LIR luminosity function for IR emitters 72
5.6 Far infrared fraction detected by PACS and SPIRE 73
5.7 Radial velocity vs. clustercentric distance 74

5.8 Distribution of FIR sources morphology with L(IR) . . . 75
5.9 HST images of selected bright far infrared sources. . . . 76
5.10 Distribution of morphological types and L(IR) for FIR population along the clustercentric distance . . . 77
5.11 EWαn2 diagnostic diagram for ELGs . . . 79
5.12 Simulated pseudo-spectra of BLAGNs . . . 80
5.13 XO diagnostic diagram for AGNs . . . 82
5.14 MIR diagnostic diagram for AGNs . . . 83
5.15 R distribution of AGNs . . . 85
5.16 Colour Magnitud Diagram of the AGN population . . . 86
5.17 Fraction of AGN along clustercentric distance . . . 87
5.18 $L(H_\alpha)$ function of AGN . . . 88
5.19 L_{IR} distribution of AGNs . . . 90
5.20 Ultraviolet luminosity distribution of AGNs . . . 92
5.21 AGN morphological distribution with clustercentric distance . . . 93
5.22 R magnitud distribution of star forming galaxies . . . 94
5.23 Colour magnitude distribution of star forming galaxies . . . 95
5.24 Colour magnitude distribution of galaxies with active star formation . . . 96
5.25 Radial velocity versus clustercentric distance of the SF population . . . 96
5.26 L_{IR} function of star forming galaxies . . . 97
5.27 L_{UV} function of SF galaxies . . . 98
5.28 Morphological separation for all cluster members . . . 99
5.29 Star forming morphological fraction with clustercentric distance . . . 99
5.30 Fraction of ELGs along cluster centric distance. . . . 100
5.31 Distribution of SFR obtained from Hα. . . . 101
5.32 SFR obtained from L_{IR} . . . 102
5.33 SFR obtained from L_{UV} . . . 102
5.34 Stellar masses obtained from LePhare fitting . . . 103
5.35 B-R and B-R vs stellar masses . . . 104

6.1 ZwCl0024+1652 X–ray map . . . 108
6.2 Spatial distribution of FIR and AGN population in X–ray map . . . 109
6.3 Spatial distribution of cluster members in X–ray map . . . 110
6.4 Optical density maps obtained from DEDICA . . . 112
6.5 X–ray map and optical density contours from DEDICA . . . 113
6.6 Σ_{10} versus Σ_5 calculated for all cluster members . . . 114
6.7 B-R colour vs Σ_5 . . . 115
6.8 Σ_5 vs clustercentric distance . . . 116
6.9 B-R colour distribution in each density region . . . 118
6.10 Fraction of different cluster population vs localdensity . . . 121
6.11 Histograms of stellar mass distributions for objects with different colours . . . 122
6.12 SFR vs log(Σ_5) and stellar masses . . . 123
6.13 sSFR vs log(Σ_5) and stellar masses . . . 123
6.14 HST postcards of selected galaxy pairs. . . . 124
6.15 Close encounters distribution with respect to the clustercentric distance . . . 125
6.16 Close encounters distribution with respect to the clustercentric distance versus radial velocity . . . 125

6.17 Fraction of close encounters distribution with respect to Σ_5 126
6.18 Close encounters distribution with respect to L_{IR} 126
6.19 Close encounters number distribution with respect to the star formation rate derived from L(IR) 127

List of Tables

1.1 GLACE sample and status of the observations 6

2.1 Log of the OSIRIS/TF observations of the region centred around the Hα emission line in the Cl0024 cluster. 16
2.2 Spectrophotometric standard stars 19
2.3 Efficiencies for Cl0024 observations 20
2.4 Data summary of broad-band CL0024+16 36

3.1 Crossmatch of NonOpt and Optical sources. 43
3.2 Xmatch multiple matches 46
3.3 Redshift partitioning of the multiwavelenght catalog restricted to the GLACE field of view 47
3.4 Mean error estimate in the first and second *Le PHARE* run. 50

5.1 *Herschel* detections on ZwCl0024+1652 67
5.2 FIR morphology fraction 74
5.3 AGN selection summary 83
5.4 AGN morphology fraction 91

A.1 Fragment of the ZwCl0024+1652 multiwavelength catalogue of cluster members 138
A.2 continued 139
A.3 continued 140

B.1 Fragment of the ZwCl0024+1652 parameters catalogue of cluster members . . . 142
B.2 continued 143
B.3 continued 144
B.4 continued 145
B.5 continued 146
B.6 continued 147

1

Introduction

Abstract: Clusters of galaxies are formed by the hierarchical incorporation of groups and galaxies along the filamentary structure of the cosmic web. This hierarchical growth induces in the involved objects a series of transformations that result in the observed differences between cluster galaxies and field ones. To explore these processes The GaLAxy Cluster Evolution survey will perform an emission line map of 9 clusters at 3 different redshift bins. This thesis has been carried out in this framework. The scientific purpose of this work is the exploration of these transformation processes and their location in different phase spaces of one of the GLACE clusters: ZwCl0024+1652.

Clusters of galaxies are self gravitating systems formed by stars, cold gas and dust, normally bound in galaxies, hot diffuse gas forming the intracluster medium (ICM hereafter) and dark matter (DM hereafter). Their typical masses are $\sim 10^{14-15} h^{-1} M_{\odot}$, 80% of which is DM and roughly 20% is hot intracluster plasma. The amount of mass in galaxies is just a small fraction. In general, the relation between X–ray luminosity, velocity dispersion of members, mass, etc. indicates that most of the clusters are in dynamical equilibrium, although a closer analysis of inhomogeneities in thermal and non-thermal X–ray emission of the ICM, or the morphological distribution of galaxies along the clustercentric distance, shows that there are strong evolutionary processes taking place within.

The commonly accepted hierarchical model proposes that the structures in the Universe form from smaller to larger components. In this sense, cluster of galaxies are formed by the hierarchical accretion of smaller constituents as groups and galaxies that undergo a number of transformations along their infall into the cluster core. These transformations can be categorized as galaxy-galaxy or cluster-galaxy driven. Determining where and how they take place is key to understand the influence of clusters on the evolution of their galaxies.

1.1 Cluster of Galaxies

The first mention of a concentration of galaxies in the firmament dates back to the XVIII century, when Charles Messier described the Virgo Cluster although it was not until 200 years later when Zwicky and Abell started the first systematic survey of these structures.

In a seminal work Dressler (1980) studied the differences between field and cluster galaxies in a sample of 55 local clusters, finding a dramatic deficiency of late morphological types in the cores. The spirals found in the intermediate zones contained less gas and dust but had larger metallicities than their field counterparts. Even within the clusters, an evolutionary trend from the inner area to the outskirts was found in colours, spectroscopic properties and morphologies. The cluster cores are dominated by red, passively evolving ellipticals (Balogh et al. 1999; Pimbblet et al. 2001; Dressler et al. 1997), while the fraction of blue galaxies increases with distance to the cluster centre, the so called Butcher-Oemler effect (Butcher & Oemler 1984). Although this last finding is subject to several biases, the blue fraction shows yet another peculiar characteristic: they have larger velocity dispersions than their red companions, was associated with shorter times of permanence within the cluster potential and therefore less viriliazitation (Biviano & Katgert 2004).

This scenario also evolves with increasing redshift. At $z \sim 1$ not only does the fraction of spirals increase, but also the star formation activity and the fraction of luminous infrared galaxy (LIRG hereafter), (Metcalfe et al. 2005). The fraction of blue galaxies has been also found to increase with redshift. When observed in the infrared, an increase of obscured star formation and number of AGNs is also found at larger distances (Coia et al. 2005; Martini et al. 2009; Altieri et al. 2010; Martini et al. 2013). There is a rapid increase of massive luminous infrared galaxies in the virialized zone with star formation rate (SFR hereafter) > 3 $M_\odot$/yr that Haines et al. (2013) modelled as $f_{SF} \propto (1+z)^n$ with $n = 7.6 \pm 1.1$. In that same work, the authors suggest as origin of this relation a decrease of the mean Specific Star Formation Rate (sSFR hereafter) by a factor of 3 and a decline of 1.5× in the number density. Two thirds of this reduction comes from the steady cosmic decline in sSFR of field galaxies accreted by the cluster, while the remaining one third is due to the action of the cluster on the infalling objects.

However, the nature and timescale of the mechanisms driving this action remain unclear, given the variety of processes taking place simultaneously: baryonic and DM producing the gravitational

well, hot ICM removing the gas content of the cluster members, or compressing it and therefore triggering star formation. Or galaxy-galaxy interaction, happening even before the infalling into the cluster potential (hierarchical accretion for groups) with eventual preprocessing of objects and material.

In general, the effects of the cluster environment on its members can be classified in three main categories:

- Galaxy-galaxy interaction: Depending on the impact parameter and the relative velocities the result may vary. For slow encounters with similar trajectories the event will end up in an accretion (different masses) or a merger (similar masses), with enhancement of nuclear or star forming activity and morphology disturbance. At high relative velocities the interaction results in the removal of the dust and gas contents of the galaxies (*harassment*), that is incorporated into the ICM.

- Galaxy-ICM interaction: Resulting in the depletion of the gas contents of the galaxy by several processes: Thermal evaporation of the interstellar medium by the hot intracluster plasma together with viscous stripping. Ram pressure stripping of the dust and gas reservoirs of the galaxies by the ICM. These two mechanisms stop star formation by the removal of the matter supply. The intergalactic medium can also be compressed by the ICM, triggering star formation.

- Galaxy-gravitational well interaction: Driving the morphological transformation of the galaxies by truncation of the outer regions (halos, arms, etc). This truncation can also quench star formation by gas removal. The potential well can also compress the intergalactic medium increasing the star formation.

The proportion of gas removed in these processes may lead to a complete quench of the star formation or a slow decrease of the SFR (*starvation*). On the other hand, the amount of gas compressed by the mechanisms described above can enhance the star formation or trigger starburst events in the cluster members.

The galaxy-galaxy interactions are dominant in the outer parts of the cluster, where the potential well and the effect of the ICM are still weak. These interactions keep on taking place across the full cluster structure, although they are less evident as the individual objects undergo more and more encounters (Mihos 2003). In the intermediate areas the ICM effect (ram pressure gas stripping and pressure enhanced star formation) are more significant (Treu et al. 2003), while the inner part of the cluster is presided by the gravitational well (tidal halo stripping and triggering of star formation).

The differences found between the population of local clusters with respect to those at intermediate redshifts ($z \sim 0.5$), i.e.: larger fractions of star forming spirals at higher distances, together with

their typical luminosities, imply that this transformation has occurred with a significant addition of new stars (Poggianti et al. 1999; Kodama & Smail 2001). However, surveys searching for star forming galaxies in clusters using optical indicators such as Hα (Sánchez-Portal et al. 2015) fails to detect such enhanced activity. On the other hand, there are stacking evidences of heavily obscured star formation derived from infrared (IR hereafter) that could account for the missing SFRs (Pérez-Martínez et al, in prep). Nevertheless, whether the large scale structure is responsible for the observed SFRs or they are due to a direct effect of the dense environment on the star formation capabilities of galaxies is still unknown (e.g.: Popesso et al. 2007)

Since cold gas is the main fuel of AGNs, any process disturbing its contents and distribution will also affect this population in the cluster. While Kauffmann et al. (2004) and others report a significant decrease of the AGN fraction with increasing density, Ruderman & Ebeling (2005) find an excess of AGNs in the cluster outskirts, attributed to low energy galaxy-galaxy interactions. On the other hand, there is an increasing number os studies indicating the opposite conclusion: environment does not influence the AGN frequency (Miller et al. 2003). Pimbblet et al. (2013) report not only a steep increase of the AGN fraction with clustercentric distance within the virial radius (r_{vir} hereafter), but also that the quickly vanishing traces of merging could mask the influence of local density on AGN enhancement.

In summary, although observations confirm the commonly accepted idea of clusters of galaxies being dominated by red passive ellipticals, this view is drawn mainly from optical data obtained from the inner areas ($r_c \leq 0.5$ Mpc) of local clusters. When other wavelengths are considered (X–rays or IR) and the studies extended to larger areas at further distances, the fraction of AGNs and star forming galaxies are subject to significant changes or at least consistent to less conclusive scenarios. A comprehensive study of such populations over a large range of redshifts and clustercentric distances is mandatory to shed new light on the evolutionary processes driving the transformation of galaxies from typical field objects to cluster ones.

1.2 The GaLAxy Cluster Evolution project

The GAlaxy Cluster Evolution survey (GLACE hereafter) (PIs. Miguel Sánchez-Portal & Jordi Cepa) is a large observational program intended to map the strongest emission lines Hα (only at z ~ 0.4), Hβ, [OII]3727, and [OIII]5007 of galaxies in nine clusters in three different redshift bins z ~0.40, 0.63, and 0.86, chosen to benefit from atmospheric windows relatively free of strong OH emission lines.

By targeting such a wide redshift range, the survey will provide a comprehensive view of the processes driving the galaxy evolution in high density environments. The relatively small redshift steps chosen will also help to bring light upon the timescales of the phenomena studied and the connection of the mechanisms observed in the different distance windows. Since clusters grow by hierarchical accretion of smaller units, it is not straightforward that properties found at a certain

redshift will passively evolve to what is observed at nearer distances.

Covering large areas is also key in this project, provided the known difference in the characteristics of the population in inner regios with respect to the cluster outskirts. Being able to extend the observations to beyond 2 r_{vir} will allow us to trace the morphology, star formation and nuclear activity evolution of cluster members as they fall into the gravitational well.

Another characteristic of the program is the depth of the line survey, designed to trace SFR $2M_{\odot}/yr$ with 1 magnitude of extinction, i.e.: below that of the Milky Way. ($f_{H\alpha} = 1.89 \times 10^{-16}$ erg s^{-1} at z = 0.4 using standard SFR−luminosity conversion factors (Kennicutt 1998)).

By observing the mentioned emission lines, GLACE intends to achieve the following goals:

- Memberships: By detecting emission lines, GLACE will be able to accurately establish objects redshifts and therefore obtain bona fide memberships.

- Star formation rates: Hα and [O II] are common SFR indicators. Obtaining Hα fluxes and correcting them from extinction via the Balmer decrement, using the Hβ measurements, will allow us to account for dust obscuration. Extending the findings from all clusters at the full set of redshift windows will permit to estimate a global star formation history of cluster members, like in Madau et al. (1998), with the already mentioned caveat of cluster own evolutionary process.

- The role of AGNs: The emission lines planned in the survey allow different and powerfull AGNs selection tools (BPT diagrams, Baldwin et al. 1981, $EW\alpha n2$, Cid Fernandes et al. 2010). Mapping the AGN presence in the cluster will help up to establish the physics behind the AGN activity in cluster galaxies.

- Metallicities: Not much is known yet about the metallicities of cluster members. The progressive interaction with the intracluster medium and succession of galaxy-galaxy encounters along the galaxy history within the cluster likely strips the gas from the objects, possibly generating a metallicity gradient across the cluster structure. Diagnostic methods based on targeted emission lines such as N2 (Denicoló et al. 2002), R23 (Pagel et al. 1979) and O3N2 (Alloin et al. 1979) will allow us to asses possible evolutionary trends.

An emission line observation program with these objectives and requirements would be extremely demanding in terms of complexity and exposure times if performed as a standard spectroscopic survey. Moreover, the selection of targets for the slits would imply a bias towards bright red core sources that would compromise the quality of the results. On the other hand, usual narrow–broad band observations lack the needed accuracy to establish memberships or deblend Hα from [N II] (crucial for AGN diagnostics).

Table 1.1: GLACE sample and status of the observations

Name	RA(J2000)	Dec(J2000)	z	Status
ZwCl 0024.0+1652	00 26 35.7	+17 09 45	0.395	Completed; programmes GTC63-09B, GTC8-10AGOS, GTC47-10B & GTC75-13B
Abell 851	09 42 56.6	+46 59 22	0.407	Planned
RX J1416.4+4446	14 16 28.7	+44 46 41	0.40	Planned
XMMLSS-XLSSC 001	02 24 57.1	-03 48 58	0.613	Planned
MACS J0744.8+3927	07 44 51.8	+39 27 33	0.68	Planned
Cl J1227.9-1138	12 27 58.9	-11 35 13	0.636	Planned
XLSSC03	02 27 38.2	-03 17 57.0	0.839	Planned
RX J1257.2+4738	12 57 12.2	+47 38 07	0.866	Completed; ESO/GTC programme 186.A-2012
Cl 1604+4304	16 04 23.7	+43 04 51.9	0.89	Planned; Cl 1604 supercluster

For such an ambitious study an instrument with integral field low resolution spectroscopic capabilities together with a large fied of view is required. GLACE benefits from OSIRIS tunable filters (TF hereafter) capability and field of view (FoV hereafter) of 8 arcmin in diameter to perform such observations(González et al. 2014; Cepa et al. 2005, 2003), as described in more detail in Section 2.1.

The program is currently on going. We have already completed the observations of two clusters: ZwCl 0024.0+1652 and RX J1257.2+4738. Table 1.1 outlines the sample and the current status of the observations.

1.3 ZwCL0024+1652

ZwCl0024+1652 is a rich cluster of galaxies at z $\sim$ 0.395. It was first described by Humason & Sandage 1957. It is one of the four cluster used by Oemler (1974) in their seminal work on cluster galaxy colours. In a previous work we have found that its mass distribution, based on caustic profile analysis, is $M_{200} = 5.9 \pm 0.3 \times 10^{14} h_{70}^{-1} M_{\odot}$, with virial radius $r_{200} = 1.7 \pm 0.1 h_{70}^{-1}$ (Sánchez-Portal et al. 2015). This totally agrees with the values reported by Kneib et al. (2003) from weak lensing analysis, for which the mass distribution corresponds to a NFW-like profile up to 5 Mpc from the centre of the cluster, and its mass is estimated to be $M_{200} = 5.7^{+1.1}_{-1.0} \times 10^{14} h_{70}^{-1} M_{\odot}$ out to $r_{200} = 1.7 h_{70}^{-1}$. X–rays studies, however, provide a total cluster mass of $M_{200} = 2.3 \pm 0.1 \times 10^{14} h_{70}^{-1} M_{\odot}$ (Zhang et al. 2005), 4 times lower than that determined from weak lensing. This discrepancy may be due to the complex structure found in the projected cluster centre, with a bimodality in the radial velocity distribution consistent with an infalling group along the line of sight, as reported by Czoske et al. (2001).

This cluster presents prominent gravitational arcs (up to 8 of the same source, Tyson et al. 1998) and a ring like dark matter structure of r ∼ 75 arcsec also related to the line of sight infalling group (Jee et al. 2007).

In a series of papers, Treu, Moran, Geach, Smith, Kneib and others use optical, near infrared and mid infrared data to explore the characteristics of the cluster population. Treu et al. (2003) use HST data to establish morphological types, finding a steep decrease of early type galaxies from the centre up to 1 Mpc. They also find a significant scatter of the surface local densities beyond $r_c \sim 0.5$ Mpc, with no major difference in the morphology - density relation in the inner and outer zones of the cluster. Moran et al. (2005) look for spectroscopic signatures of evolution of the early type galaxies in the clusters, finding a clear radial trend in their mass to light ratio, with the oldest objects sitting in the cluster core. They also find an increase of the star forming activity around $r_c \sim 1 r_{vir}$ and a downsize in the early type galaxies forming stars. Geach et al. (2006) report an excess of mid-infrared sources from 24μm data, associated to dusty star forming galaxies, and estimate the obscured star formation to be a factor of 5 larger than that derived from optical data.

In Sánchez-Portal et al. (2015), where part of the first findings of GLACE on ZwCl0024+1652 are reported, a total of 174 emission line galaxy (ELG hereafter) are found. 62 of them (36%) are selected as AGNs as per different criteria, a fraction larger than the 20% reported by Pérez-Martínez et al. (2013) in the same cluster, but much smaller than that found by Lemaux et al. (2010) in two clusters at higher redshift (68%). The SFR estimated from Hα fluxes with one magnitude of extinction, is in median 1.4 $M_\odot/yr$. Some of the work done in Sánchez-Portal et al. (2015) was performed by the author of this thesis and is included in Chapter 2 for reference.

To complete the present picture of the cluster, a more extensive selection and analysis of the infrared population is required, since current view is limited to a small 15μm (Coia et al. 2005), or 24μm population observed out of the cluster centre (Geach et al. 2006). The influence of the mass substructures on the AGNs is yet to be fully addressed, since only after the studies published in Sánchez-Portal et al. (2015) a significant number of AGNs has been reliably identified. The SFR estimations must also be expanded to other tracers, like *L(IR)*, and include thorough calculations of dust and gas extinction.

This cluster is particularly convenient for our studies for several reasons: Its redshift and complex structure assures the presence of gas-rich galaxies in the process of being transformed into typical cluster galaxies. The wealth of ancillary data provides a perfect frame to insert the output of GLACE and at the same time, the new Hα/[N II] and Hβ survey opens the possibility of further exploitation of archival data (both images and catalogues) that are largely unexplored.

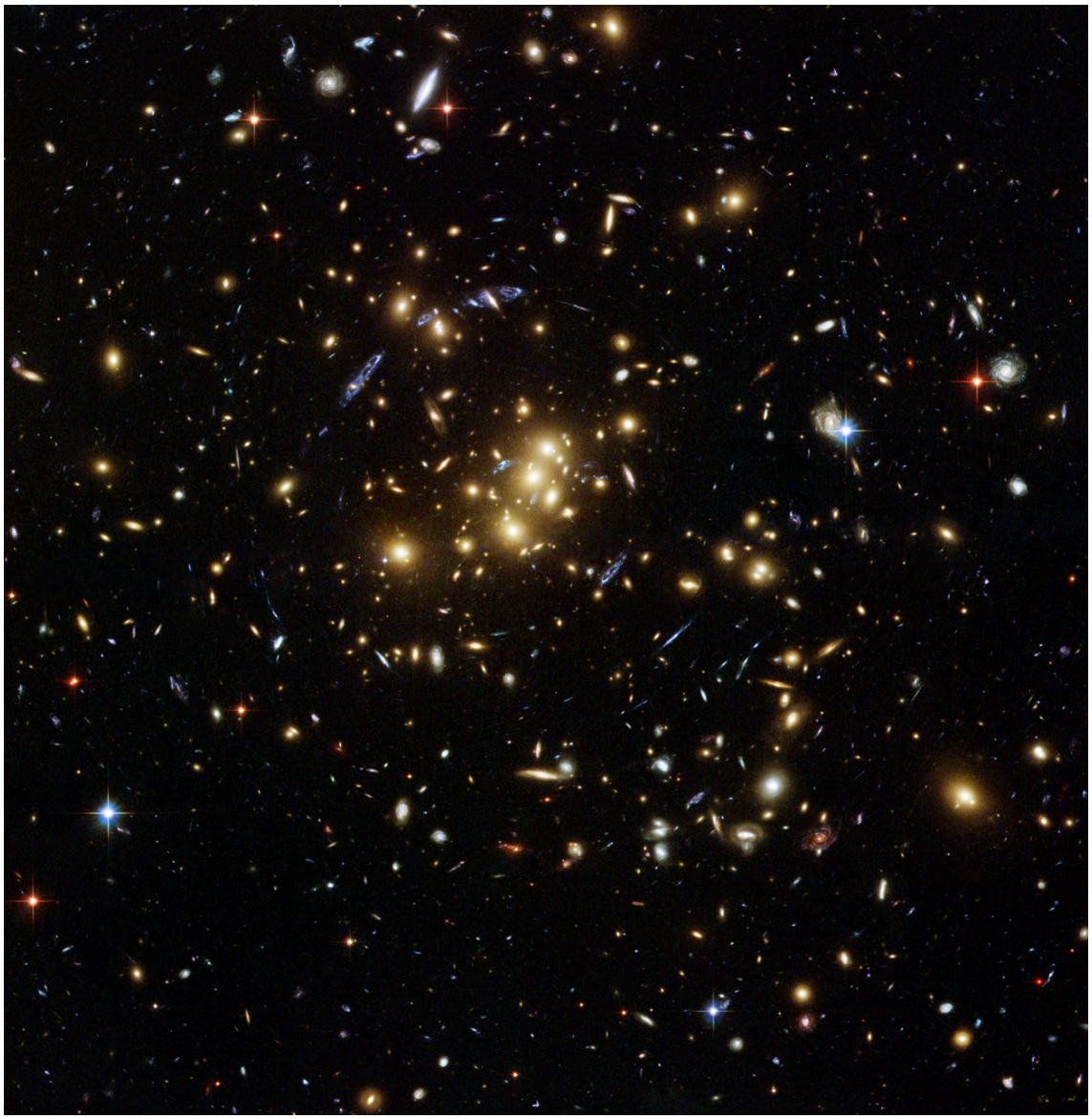

Figure 1.1: HST image of ZwCL0024+1652. Credit: NASA, ESA, H. Lee & H. Ford (John Hopkins U.)

1.4 Scientific aims of this work

The present work performs a multiwavelength study of the members of ZwCl0024+1652 to find the evolutionary trends driving the transformation from typical field galaxies to cluster objects. Our main target is the identification of the areas where the bulk of these transformations take place. By cluster areas we mean spatial zones defined by their distance to the cluster centre, local overdensities and zones in the space phase of projected surface densities, Σ_5, and morphology, SFR and stellar mass.

We first focus on revealing the far-infrared population, in particular those objects detected between 100 μm and 500 μm by *Herschel*. The far-infrared properties of cluster members have not been studied before. They offer a unique view of obscured activity in these galaxies.

We also aim to analyse the influence of the environment on the Active Galactic Nuclei (AGN hereafter) population. For that we need a thorough selection of these sources and an extensive study of their properties in relation with the cluster areas as defined above.

Another objective is to achieve an accurate estimate of the SFR of cluster galaxies and analyse its relation with the environment. Different indicators reveal diverse activity scenarios in terms of dust and gas obscuration. All available means to obtain such estimates (Hα and Hβ as well as Bolometric Infrared Luminosity ($L(IR)$ hereafter)) need to be contemplated, together with precise extinction correction of the optical tracers via the Balmer decrement.

In order to address these issues, we need to obtain key galaxy parameters, such as $L(IR)$s, ultraviolet (UV hereafter) luminosity, stellar masses, SFRs, morphologies etc from different methods and analyse them in the three main cluster populations: far infrared galaxies, AGNs and star forming galaxies.

A key tool in this research is an extensive photometric catalogue comprising information from the widest possible spectral range. We benefit from the wealth of data available, both proprietary and archival, to obtain a catalogue of cluster members with up to 25 photometric points. Provided the variety of data sources, the construction of this catalogue has been carried out paying special attention to advanced cross-matching techniques. The photometric catalogue is an outstanding product of this work and provided its completeness, depth, spectral span of the Spectral Energy Distribution (SED hereafter), redshifts and derived quantities like *L(IR)*, *L(UV)*, SFR or stellar mass will be an important resource for cluster studies in the future.

Throughout this thesis we assume a Universe with $H_0 = 70\,\mathrm{km\,s^{-1}\,Mpc^{-1}}$, $\Omega_\Lambda = 0.7$, and $\Omega_m = 0.3$.

2

Observational material and data reduction

Abstract: ZwCl0024+1652 is a well studied cluster with plenty of data available from various sources. In particular, we have obtained deep Hα, [N II] and Hβ fluxes using OSIRIS at GTC within the GLACE program, partially reported in Sánchez-Portal et al. (2015). We have also reduced archival images performed by the infrared observatories *Spitzer* and *Herschel* and extracted the sources in them by standard means and tools. Similarly, we have processed X-ray data from *XMM–Newton* to obtain 0.5-7 KeV maps of the cluster. We have also used catalogues from *Chandra XMM–Newton* and *GALEX* as well as an extensive catalogue published by Moran et al. (2005). This chapter describes the tools and methods used in the processing of these data.

Data acquisition and processing are the first steps of every astrophysical research. This work makes extensive use of proprietary observations as well as archival data from very different wavelengths and telescopes. In particular, the exposures performed with OSIRIS at GTC in tunable filter mode are infrequent and the subtleties of the data reduction seldom addressed in the scientific literature. This chapter includes an extensive explanation of the processing of these images to produce valid pseudospectra, calibrated in both wavelength and flux, as reported in Sánchez-Portal et al. (2015). The reduction of the Hβ data from the same instrument and telescope is explained in detail in Chapter 4. Unless stated otherwise, all magnitudes used in this work are in the AB system and calculated over an adaptative ellipse around the object (Kron photometry).

2.1 Optical data: OSIRIS

A more detailed discussion on OSIRIS and the importance of its tunable filter mode in the GLACE program has been included in Sánchez-Portal, Pintos-Castro, Pérez-Martínez, et al. (2015). It is described here for full reference, provided the key role of these data in the present thesis.

2.1.1 The OSIRIS Instrument

The Optical System for Imaging and low-Intermediate-Resolution Integrated Spectroscopy (OSIRIS hereafter), Cepa et al. 2003, is the first-light instrument at Gran Telescopio CANARIAS (GTC hereafter) at the Observatorio del Roque de los Muchachos, in the island of La Palma. It is an imaging and spectrograph system covering the 365 - 1000 nm spectral range capable to perform standard images with broad and narrow band filters as well as low resolution spectroscopy in both long slit and multi-object mode. OSIRIS includes also as a key feature the use of two tunable filter devices, consisting each of them in a low-resolution Fabry-Pérot interferometer. The interferometers are constituted by two plane-parallel transparent plates coated for optimal performance over the 370-960 nm. The plates finesse and coating determine the order separation and minimum distance, i.e.: widest full width at half maximum (FWHM hereafter) between them. Figure 2.1 shows the standard optical scheme of an etalon, obtained from the OSIRIS user manual, v3.1. The plate spacing sets the resonance wavelength subject to constructive interference from the internal reflections in the etalon. This interfence builds up a broad image in which there is an area (Jacquinot spot) where change in wavelength does not exceed by $\sqrt{2}$ times the FWHM.

The plates are controlled by a stack of piezoelectric transducers allowing for high accuracy variation over the whole range. This makes possible moderate spectral resolution (between 4.5 and 20 Å of FWHM depending on the wavelength range) over a wide spectral region with an accuracy of 1 Å in the filter central wavelength. Figure 2.2 displays the main differences between a standard Fabry-Pérot interferometer and tunable filters, i.e.: the minimum space between plates, much smaller in the case of the TFs, and the precision of the spacing, higher in the case of the TFs. In summary, this makes the TFs able to produce a interference region in a wider wavelength range.

In the case of the OSIRIS TFs, the spectral range is 3650–6710 Å for the blue TF, and 6510–9345 Å for the red range (Red TF). All these features make possible to get low resolution spectral observations for all the targets within a wide field of view in combination with a telescope that provides a large collecting area. Regarding the technical implementation, the GLACE survey exploits the outstanding characteristics of the tunable filters (TF; González et al. 2014; Cepa et al. 2003, 2005).

The TF transmission profile (Airy function) is periodic with the incident light wavelength. For a beam entering the TF at incidence angle θ, the condition for a maximum transmission (constructive

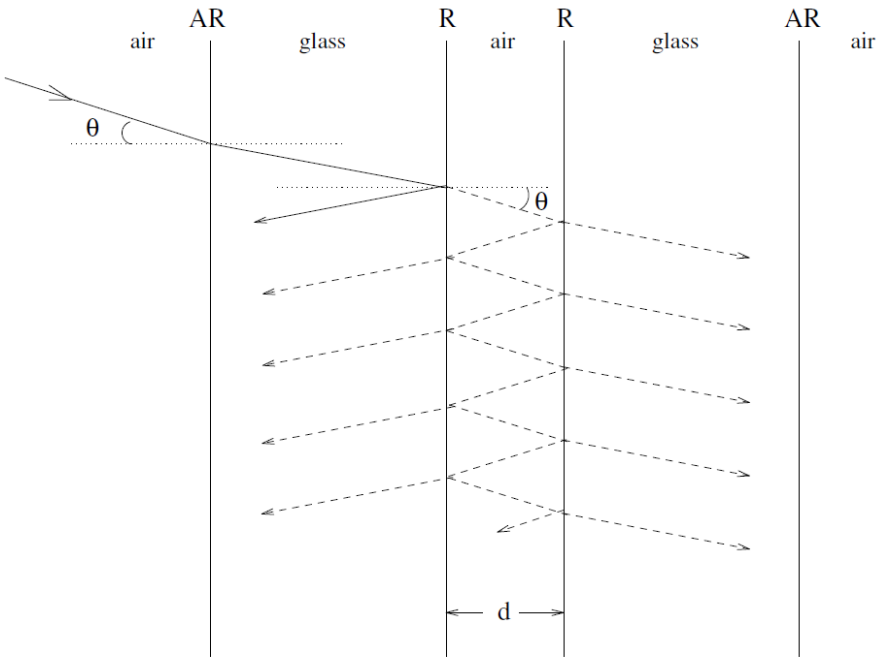

Figure 2.1: Etalon scheme from the OSIRIS User Manual

interference) is

$$m\lambda = 2\mu d \cos\theta \tag{2.1}$$

where m is the integer order of interference; μ, the refractive index of the medium in the cavity between the plates (usually air, $\mu = 1$); and d, the plate separation (gap). To select just one wavelength and order, additional intermediate-band filters, known as order sorters, are required. Since light coming from targets at increasing distance from the OSIRIS optical centre reaches the TF at increasing incidence angle, there is a progressive shift towards the blue as the distance r of the source to the optical centre increases. For the OSIRIS red TF, the dependency of the transmitted wavelength on the radial distance is given by González et al. (2014):

$$\lambda = \lambda_0 - 5.04r^2 + a_3(\lambda)r^3 \tag{2.2}$$

where λ_0 is the central wavelength tune in Å, r the distance to the optical centre in arcmin, and $a_3(\lambda)$ is an additional term expressing the wavelength dependency of the coatings, given by

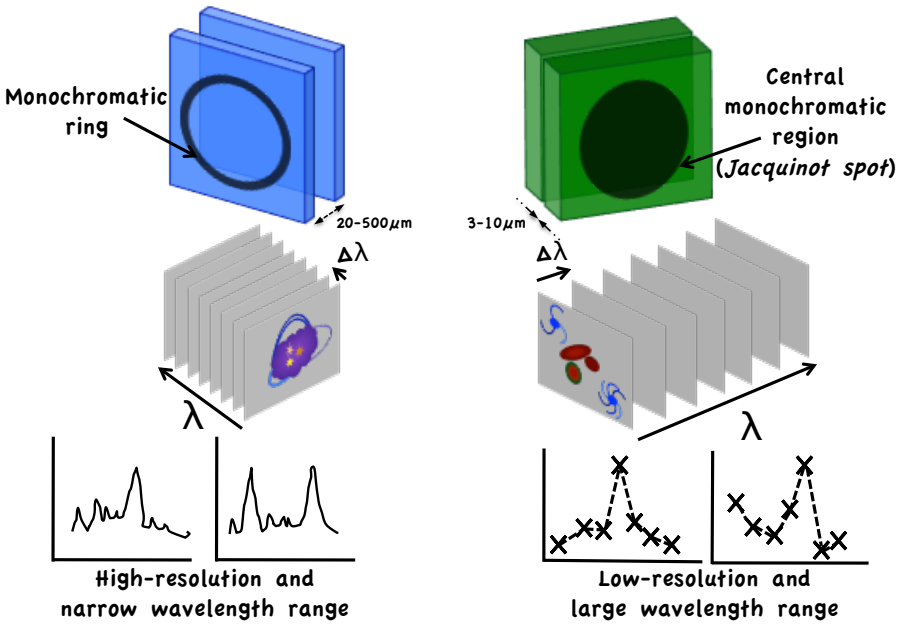

Figure 2.2: Fabry-Pérot vs TF (courtesy of I. Pintos)

$$a_3(\lambda) = 6.0396 - 1.5698 \times 10^{-3}\lambda + 1.0024 \times 10^{-7}\lambda^2 \tag{2.3}$$

Within a wavelength period, the TF transmission profile $T(\lambda)$ can be approximated by the expression:

$$T(\lambda) \simeq \left(1 + \left(\frac{2(\lambda - \lambda_0)}{\Delta_{FWHM}}\right)^2\right)^{-1} \tag{2.4}$$

where λ_0 is the wavelength at which the TF is tuned, and Δ_{FWHM} is the TF FWHM bandwidth.

Within the GLACE survey (see Section 1.2), we applied the technique of TF tomography (Jones et al. 2001; Cepa et al. 2003): for each line, a set of images are taken through the OSIRIS TF, each image tuned at a different wavelength (equally spaced), so that a rest frame velocity range of several thousand km/s (6500 km/s for our first target) centred on the mean cluster redshift is scanned for the full TF field of view of 8 arcmin in diameter. Additional images are taken to

compensate for the blueshift of the wavelength from the centre to the edge of the field of view (as given in Eq. 2.2). Finally, for each pointing and wavelength tuned, three dithered exposures allow correcting for etalon diametric ghosts, using combining sigma clipping algorithms.

The TF FWHM and sampling (i.e. the wavelength interval between consecutive exposures) at Hα are of 12 and 6 Å , respectively, to allow deblending Hα from [NII]λ6584. with an accuracy better than 20% (Lara-López et al. 2010). For the rest of the lines, the largest available TF FWHM, 20 Å is applied, with sampling intervals of 10 Å. These parameters also allow a photometric accuracy better than 20% according to simulations performed within the OSIRIS team. The same pointing positions are observed at every emission line. To trace the relation between SF and environment in a wide range of local densities, we required $\simeq$2 Virial radii (some 4 Mpc) to be covered within the targeted clusters. This determines the number of OSIRIS pointings (two pointings at 0.40 and 0.63 and just one at 0.86).

2.1.2 Tunable-filters optical data

Two OSIRIS/ GTC pointings using the red TF were planned and executed towards Cl0024+1652. The first one (carried out in GTC semesters 09B, 10A and 13B) targeted the Hα/ [N II], Hβ and [O III] lines. The observations were planned to keep the cluster core well centered within CCD1. The second pointing was carried out in semesters 10B and 13B and targeted the same emission lines. This second pointing was offset by $\sim$ 3.4 arcmin in the NW direction).

The Hα/[N II] spectral range 9047–9341 Å was covered by 50 evenly spaced scan steps[1] ($\Delta\lambda$ = 6 Å). Taking the radial wavelength shift described by Eq. 2.2 into account, the spectral range sampled over the entire field of view (of 8 arcmin diameter) is somewhat smaller, 9047–9267 Å . (The ranges 9267–9341 Å and 8968–9047 Å are partially covered in the central and external regions of the field of view, respectively.) At each TF tune, three individual exposures with an 'L-shaped' dithering pattern of 10 arcsec amplitude were taken (to allow the removal of fringes and to ease the identification of diametric ghosts; the amplitude was chosen similar to the gap between the detectors). While this observing strategy has revealed itself to be useful for removing the fringing patterns that are especially evident beyond $\lambda \simeq 9300$ Å , it introduces an additional complexity since the position of a source within the CCD varies in each dither position and as a consequence also the wavelength at which it is observed owing to the radial wavelength shift experienced in TFs.

The data was reduced using a version of the TFRED package Jones (2002) modified for OSIRIS by A. Bongiovanni (Bongiovanni et al. in prep.) and private IRAF[2] and IDL scripts written by our team. The basic reduction steps were carried out using standard IRAF procedures and included bias

[1] Three scan steps, at 9317.4 and 9323.4 and 9341.4 Å were accidentally omitted in the observations of the offset positions, so only 47 slices are available for that pointing.

[2] IRAF is distributed by the National Optical Astronomy Observatory, which is operated by the Association of Universities for Research in Astronomy (AURA) under cooperative agreement with the National Science Foundation.

Table 2.1: Log of the OSIRIS/TF observations of the region centred around the Hα emission line in the Cl0024 cluster.

Centre position						
$\lambda_{0,i}$ (nm)	OS filter	Date	Seeing ($''$)	N^o steps	N^o exp.	Exp. time (s)
904.74	f893/50	2009 Dec 05	0.7 – 0.9	6	3	53
		2010 Aug 17	0.8	6	3	85
908.34	f902/40	2010 Aug 21	0.8	11	3	60
908.74	f902/40	2009 Dec 05	0.7 – 0.9	2	3	53
909.54	f902/40	2009 Nov 25	0.9 – 1.1	9	3	53
914.94	f910/40	2009 Nov 25	0.9 – 1.1	9	3	53
		2010 Aug 01	0.8	14	3	60
920.34	f910/40	2009 Dec 05	0.6 – 0.8	5	3	53
923.34	f919/41	2009 Dec 05	0.6 – 0.8	4	3	53
		2010 Aug 18	0.8	3	3	60
925.14	f919/41	2010 Aug 18	0.8	5	3	100
928.14	f919/41	2010 Aug 18	0.8	3	3	120
929.94	f919/41	2010 Aug 19	0.9	3	3	190
931.74	f923/34	2010 Aug 19	0.9	2	3	170
932.94	f923/34	2010 Aug 21	0.8	3	3	120

Offset position						
$\lambda_{0,i}$ (nm)	OS filter	Date	Seeing ($''$)	N^o steps	N^o exp.	Exp. time (s)
904.74	f893/50	2010 Oct 01	<1.0	6	3	60
908.34	f902/40	2010 Nov 08	1.0 – 1.2	11	3	60
914.94	f910/40	2010 Sep 20	<0.8	14	3	60
923.34	f919/41	2010 Nov 08	0.9 – 1.2	3	3	60
925.14	f919/41	2010 Nov 08	0.9 – 1.2	5	3	100
928.14	f919/41	2010 Nov 08	0.9 – 1.2	3	3	120
929.94	f919/41	2010 Nov 08	1.0 – 1.2	3	3	120
932.94	f923/34	2010 Oct 01	<1.0	2	3	120

subtraction and flat-field normalisation. The next reduction step was a TF-specific one, namely the removal of the diffuse, optical-axis centred sky rings produced by atmospheric OH emission lines as a consequence of the radial-dependent wavelength shift described by Eqs. 2.2 and 2.3.

The TFRED task `tringSub2` was used to this end. It corrects each individual exposure by means of a background map created by computing the median of several dithered copies of the object-masked image. Fringing was also removed when required using the dithered images taken with the same TF tune. Then, the frames were aligned and a deep image obtained by combining all individual exposures of each scan step. This combination was achieved by applying a median filter. While this could potentially lead to the loss of line emitters with a very low continuum level, it is the best method of removing spurious features as ghosts.

When we compared the deep image resulting from the procedure described above with that obtained by adding up all the individual scans and applying a simple minimum-maximum rejection filter, we observed that one line emitter per CCD gets lost, but more than one hundred spurious features are removed effectively. The astrometry was performed in the resulting deep image, using IRAF standard tasks (`ccxymatch` and `ccmap`). The sky position of reference objects were gathered from the USNO B1.0 catalogue (Monet et al. 2003) in the centre position, while for the offset one we obtained better results using the 2MASS catalogue (Skrutskie et al. 2006); the achieved precision was in both cases equal to or better than 0.3 arcsec r.m.s. (i.e.close to the binned pixel size). The deep images were used to extract the sources by means of the SExtractor package (Bertin & Arnouts 1996). The number of sources detected above 3σ are 931 in the centre and 925 in the offset position (after removing several clearly spurious sources appearing on the edges of the detectors). Since there is quite a large overlap between both positions, we found 374 common sources after matching both source catalogues using TOPCAT (Taylor 2005). These common sources were used as a test of the relative consistency of our astrometry: 245 sources (65%) were found within a match radius of 0.5 arcsec (i.e. consistent with the quoted accuracy), 88 (24%) within 0.75 arcsec, and 15 (4%) within 1.0 arsec radius. Twenty-six objects (i.e. 7%) were matched at larger radii (around 1.5 arcsec), but these sources were always found on the edges of the images, where the OSIRIS field suffers a larger distortion.

The catalogue of detections contains 1482 unique sources. For each detected source and scan step, the best possible combination of individual images was computed, defining this as the best combination of TF tune and dither position at the location of the source. In practise, we deemed the "best combination" algorithm as the selection of all the images for which the TF wavelength at the position of the source lies within a range of ± 3 Å (i.e. half scan step) of the given one. For each of these combinations, a synthetic equivalent filter transmission profile was derived by adding up the transmission profiles of all the images entering the combination and fitting the result to the function given in Eq. 2.4. These synthetic profiles allowed us to verify that our combination approach does not introduce a significant error in the wavelength of the central position (less than 1 Å maximum) or in the FWHM (the average equivalent FWHM is 12.7 Å with a deviation of 0.4 Å). The output combined image is used to determine the flux at this specific scan step and source position by means of SExtractor. The resulting "pseudo-spectra" consist of 50 (47) tuples (λ at source position, flux). The FWHM of the equivalents (synthetic) TF Airy transmission profiles derived at each source position and TF tune were also included in each pseudo-spectrum file. A pseudo-spectrum

should not be confused with a standard spectrum produced by a dispersive system: the flux at each point of the pseudo-spectrum is what is integrated within a filter passband centred on the wavelength of the point. Mathematically, a pseudo-spectrum is therefore the convolution of the source spectrum with the TF transmission profile.

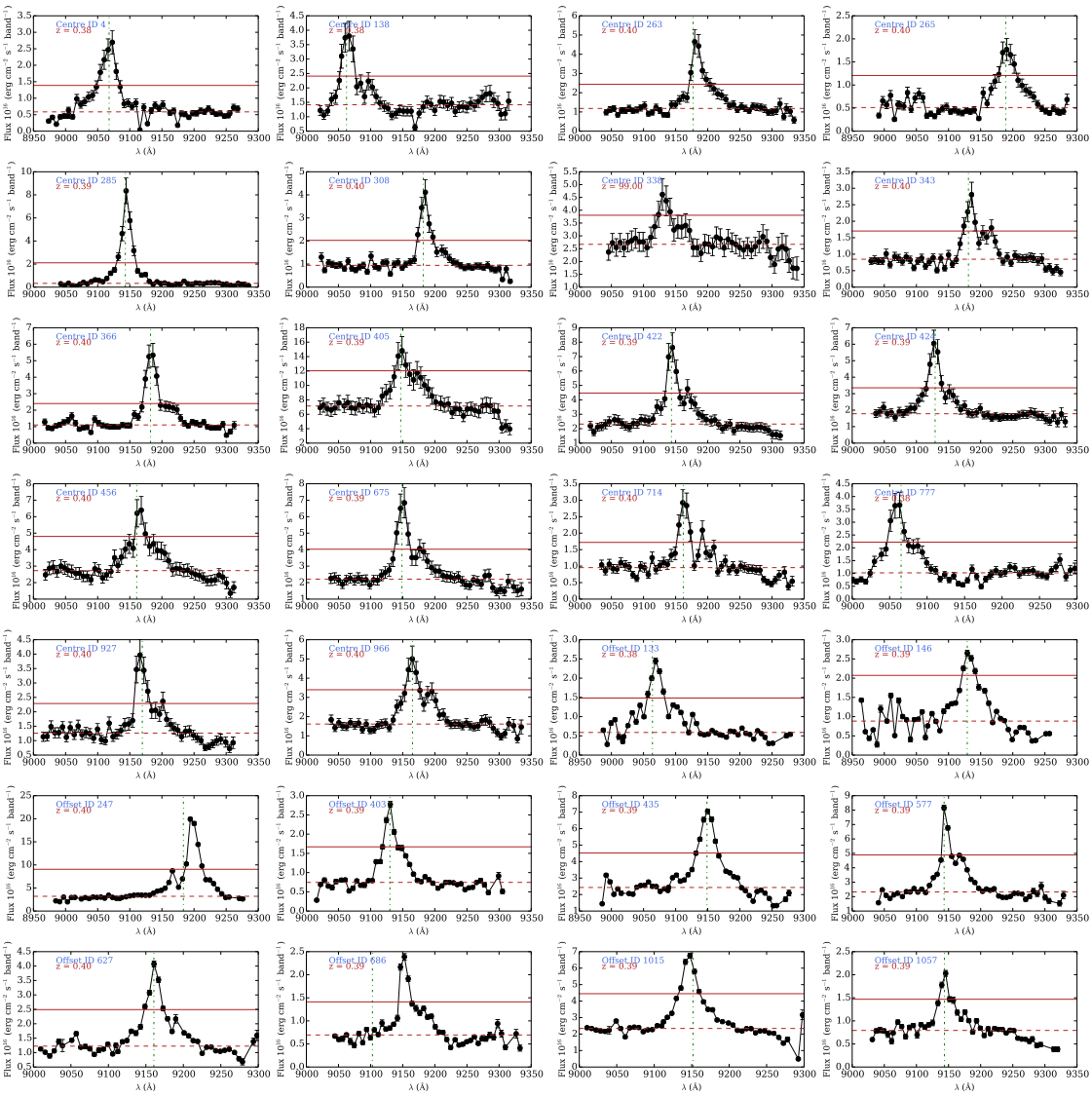

Figure 2.3: Examples of Hα pseudospectra. The green dashed-dotted lines correspond to spectroscopic or secure photometric redshifts from M05 (when available). The dashed red line corresponds to the approximate pseudo-spectrum continuum level, and the solid red line to the $3\sigma_{cont}$ level, where σ_{cont} is the pseudo-continuum noise.

2.1.3 Flux calibration

The flux calibration of each TF tune has been carried out in two steps: First, the total efficiency $\epsilon(\lambda)$ of the system (telescope, optics and detector) should be derived and is computed as the ra-

Table 2.2: Spectrophotometric standard stars

Name	mag(λ, Å)	Reference	Position
G157–34	15.35(5400)	Filippenko & Greenstein (1984)	offset
G191–B2B	11.9(5556)	Oke (1990)	offset
Ross 640	13.8(5556)	Oke (1974)	centre

tio of the measured-to-published flux $F_m(\lambda)/F_p(\lambda)$ for a set of exposures of spectrophotometric standard stars (Table 2.2) taken in photometric conditions within a range of tunes compatible with the cluster observation (ideally at the same tunes). The fluxes of the standards are measured by aperture photometry, and the exact wavelengths at the positions of the star are derived from Eqs. 2.2 and 2.3. The published fluxes are also derived at these wavelengths by means of a polynomial fit to the tabulated fluxes (see references in Table 2.2). Then, measured fluxes in engineering units (ADU) are converted to physical units (ergs s^{-1} cm^{-2} Å $^{-1}$) using the expression

$$F_m(\lambda) = \frac{g\,K(\lambda)\,E_\gamma(\lambda)}{t\,A_{tel}\,\delta\lambda_e} F_{ADU}(\lambda) \tag{2.5}$$

where g is the CCD gain in $e^- ADU^{-1}$, $E_\gamma(\lambda)$ is the energy of a photon in ergs, t the exposure time in seconds, A_{tel} the area of the telescope primary mirror in cm^2, $\delta\lambda_e$ the effective passband width[3] in Å, and $K(\lambda)$ the correction for atmospheric extinction,

$$K(\lambda) = 10^{0.4\,k(\lambda)\,\langle\chi\rangle}, \tag{2.6}$$

which depends on the extinction coefficient $k(\lambda)$ and the mean airmass $\langle\chi\rangle$ of the observations. In our case, we estimated $k(\lambda)$ by fitting the extinction curve of La Palma[4], in the wavelength range of interest.

The uncertainty in the efficiency was computed by error propagation, taking the errors in the measured fluxes into account (which in turn include terms for coping with the error of the aperture photometry and the uncertainty of the wavelength tune) and those of the published ones.

The efficiency $\epsilon(\lambda)$ (sampled with nine tunes at position A and 19 tunes at position B must then be fitted to an analytical function of λ in order to perform the calibration at the wavelength of each

[3] $\delta\lambda_e = \frac{\pi}{2} FWHM_{TF}$

[4] `http://www.ing.iac.es/Astronomy/observing/manuals/ps/tech_notes/tn031.pdf`

Table 2.3: Efficiencies for Cl0024 observations

Position	$\lambda \leq 9270$ Å	$\lambda > 9270$ Å	
	$\langle\epsilon\rangle$	Zero point	Slope
Centre	0.1779 ± 0.0236	10.2497 ± 1.2181	-0.0011 ± 0.0001
Offset	0.1993 ± 0.0035	12.8566 ± 0.9074	-0.0014 ± 0.0001

tune and source. In both cases, the best solution has been a constant efficiency for $\lambda \leq 9270$ Å and a linear decreasing dependency at longer wavelengths (Table 2.3).

The second step is to convert the measured flux in ADU of each source at each tune i to physical units (ergs s^{-1} cm^{-2} Å $^{-1}$) by means of the expression

$$f(\lambda)_i = \frac{g\,K(\lambda)\,E_\gamma(\lambda)}{t\,A_{tel}\,\delta\lambda_e\,\epsilon(\lambda)} f_{ADU,i}, \tag{2.7}$$

where $\epsilon(\lambda)$ is the total efficiency computed above and the remaining terms are as in Eq. 2.5. The flux errors are computed again by propagation, taking the efficiency errors derived above into account, along with the source flux measurement uncertainty computed by the TFRED `tspect` task as

$$\Delta f = \sqrt{A_{pix}\sigma^2 + f/g} \tag{2.8}$$

where A_{pix} is the measurement aperture area in pixels, σ the standard deviation of the background noise, and g the gain in in e$^-$ADU^{-1}.

Estimating the wavelength of the Hα line is possible with TF tomography, but it is generally a complex issue, since on the one hand, we have a blend of three lines (the Hα line plus the two components of the [N II] doublet), convolved with the transmission profile of the TF. As described in sect. 2.2, in many cases the pseudo-spectrum line "profile" (hereafter referred to as line pseudo-profile) is affected by absorption-like features. We attempted to derive the Hα line position by considering a model comprising three Gaussian lines plus a linear continuum. The rest-frame wavelength's relative positions are fixed, as is the ratio of the two [N II] doublet components (set to $f_{6548}/f_{6583} = 0.3$). Free parameters of the model are the observed wavelength of the Hα line,

the line width (constrained to be the same for the three lines), the [N II] λ 6583 and Hα fluxes, and the continuum level. This model spectrum was convolved with the TF transmission profile and fitted by means of non-linear least squares to the pseudo-spectra profiles.

For some 30% of the sources, the result of the fit reproduces the pseudo-spectrum profile accurately, but in a vast majority of the cases, the fit either fails or provides inaccurate results owing to noise in the pseudo-continuum, absorption-like features in the line pseudo-profile, etc. Eventually, we decided to derive the position of the line by manually fitting the pseudo-spectrum using the IRAF `splot` task after inspection and either a Gaussian or a Lorentzian profile, choosing the appropriate range to avoid continuum noise and contaminant lines. There is very good agreement between the line positions computed by `splot` and those resulting from the trustful, accurate model fits ($\sim$ 1 Å). In a minority of the cases, where the line profile showed very asymmetric (e.g. when absorption-like features are present, most likely from random noise as shown in sect. 2.2 below), the position of the line was chosen to be the peak value of the pseudo-spectrum. Given the difficulty of providing a trustful uncertainty figure, we have assumed a constant error value of 3 Å for the fit to the peak of the line, i.e. half of a scan step. This error is square-added to the tuning uncertainty of 1 Å and to the wavelength error introduced by the combination of images used to produce the pseudo-spectrum, also considered to be 1 Å at most; hence, $\sigma_{pos} \simeq 3.3$ Å.

Applying an automatic algorithm and a careful visual classification Sánchez-Portal et al. (2015) have obtained 210 robust candidates to be emitter galaxies. Final catalogue of cluster ELGs has 174 objects, after removing putative interlopers (galaxies at different redshift, mostly oxygen emitters at z $\sim$ 0.9) and 8 sources without ancillary data to perform the assessment. For further details, refer to Sánchez-Portal et al. (2015).

2.2 Derivation of line fluxes

From the pseudo-spectra described, it is possible to derive the Hα and [N II] fluxes following several approaches. We applied a straightforward procedure derived from the standard narrow-band on-band/off-band technique, using for each source the flux in the scan slice closest to the computed position of the Hα line and that of the slice closest to the [N II] line. As is shown below, this method, though simple, produces acceptable results when compared to the more sophisticated procedure based on least-squares fitting of the pseudo-spectrum to a model spectrum convolved with the transmission profile of the TF with the advantage that the former method is always applicable, while the latter can only be used in a minority of cases.

We start by subtracting a linear continuum. This can be done easily by applying a linear fit to the regions of the pseudo-spectrum excluding the emission line. Then, assuming infinitely thin lines, the Hα and [N II] line fluxes, denoted by $f\,(H\alpha)$ and $f([N\,\textsc{ii}])$ respectively, are given by the expressions (Cepa, priv. comm.):

$$\begin{aligned} f_{on,H\alpha} &= T_{H\alpha}(H\alpha)f(H\alpha) + T_{H\alpha}([NII])f([NII]) \\ f_{on,[NII]} &= T_{[NII]}(H\alpha)f(H\alpha) + T_{[NII]}([NII])f([NII]) \end{aligned} \tag{2.9}$$

where $f_{on,H\alpha}$ and $f_{on,[NII]}$ are the continuum-subtracted fluxes in the chosen Hα and [N II] slices, and $T_{<slice>}$ ($< line >$) denotes the TF transmission of a given slice at a given line wavelength. The different transmission values can be easily derived from the approximate expression given in Eq. 2.4. From Eq. 2.9 we can easily derive the flux in the Hα line:

$$f\,(H\alpha) = \frac{f_{on,H\alpha} T_{[NII]}\,([NII]) - f_{on,[NII]} T_{H\alpha}\,([NII])}{T_{H\alpha}\,(H\alpha)\,T_{[NII]}\,([NII]) - T_{H\alpha}\,([NII])\,T_{[NII]}\,(H\alpha)} \tag{2.10}$$

and a similar expression for the [N II] line. The errors in the lines have been derived by propagation, taking not only the errors in the Hα and [N II] "on" bands, but also the continuum noise into account (i.e. the noise around the zero-level continuum after removing the linear fit explained above). As a result, the line error has been computed as

$$\begin{aligned} \Delta f\,(H\alpha) = &((T_{[NII]}\,([NII])\,\Delta f_{on,H\alpha})^2 \\ &+ (T_{H\alpha}\,([NII])\,\Delta f_{on,[NII]})^2) \\ &+ ((T_{[NII]}\,([NII]) - T_{H\alpha}\,([NII]))\,\sigma_{cont})^2)^{1/2} \\ &/\,(T_{H\alpha}\,(H\alpha)\,T_{[NII]}\,([NII]) - T_{H\alpha}\,([NII])\,T_{[NII]}\,(H\alpha)) \end{aligned} \tag{2.11}$$

where $\Delta f_{on,H\alpha}$ and $5\Delta f_{on,[NII]}$ are the flux errors in the "on" Hα and [N II] bands computed as indicated in sect. 2.1.3 and σ_{cont} is the continuum error measured as the standard deviation of the points within the region of the pseudo-spectrum excluding the emission lines. The contribution of the continuum noise to the total error is important, on average $\sim 30\%$ at the central position and much greater at the offset position where the exposure times are shorter, on average 60–70%.

The median fractional error in the Hα fluxes is $\approx 24\%$. Seventy percent of the sample objects have relative errors below 30%. These errors are compatible with those quoted by Lara-López et al. (2010), though somewhat larger than those derived from their simulations due to our larger continuum errors. However, since the [N II] line is usually fainter than the Hα line, its flux errors

are in general much greater: the average fractional error is $\approx 54\%$, and only 15% of the sample objects have a relative error below 30%. This was, of course, expected since the detection/selection algorithm is driven by the strongest line present in the pseudo-spectrum. In many cases, therefore, the Hα line acts as a "prior", and the nitrogen flux is extracted at the expected wavelength of the (otherwise barely detected) [N II] line.

As mentioned above, the line flux estimation is based on an infinitely thin line approximation that assumes that the line can be represented well by $\delta(\lambda - \lambda_z)$, where $\lambda_z = \lambda_0(1 + z)$. According to Pascual et al. (2007), for star-forming galaxies, emission line widths are mass-related and typically FWHM $\lesssim 10$ Å $\times (1 + z)$, and for narrow-band filters of some 50 Å width, it is possible to recover $\sim 80\%$ of the line flux up to $z \sim 4$. We investigated the impact of applying such an approximation to our very narrow TF scans (~ 12 Å).

To this end, we performed several simulations using Gaussian line profiles of several widths peaking at different offsets with respect to the maximum of the filter transmission profile (Eq. 2.4). The emission line broadening is given by the relation (Fernández Lorenzo et al. 2009):

$$2V_{max} = \frac{\Delta\lambda c}{\lambda_0 \sin(i)(1 + z)} \tag{2.12}$$

where V_{max} is the maximum rotation velocity, λ_0 the line wavelength at $z = 0$, and $\Delta\lambda$ the line width at 20% of peak intensity. For a Gaussian line, $\Delta\lambda = 1.524 \times$ FWHM. Assuming as a safe upper limit $V_{max} = 200\,\mathrm{km\,s^{-1}}$ (see, for instance, Fernández Lorenzo et al. 2009), the Hα line FWHM $\simeq 8$ Å. Here we assume that the line is unresolved. The possibility that the line appears resolved in our pseudo-spectra due to kinematical split is investigated below. For narrow lines, FWHM = 2 Å, we are able to recover 96% to 98% of the flux (from 0 to 2 Å offset), while for the widest simulated lines, FWHM = 8 Å, the fraction of recovered flux is in the range 73% to 76%.

To compare the simulations with real results, we used the small set of pseudo-spectra for which a reliable fit to the model spectrum was achieved, finding that the average ratio between the flux derived from the infinitely thin line approximation and the one derived from the best fit is 0.81 and 0.88 for the Hα and [N II] lines, respectively, hence well aligned with the results of our simulations. The completeness limit of the ELG sample, is $\sim 0.9 \times 10^{-16}\,\mathrm{erg\,s^{-1}cm^{-2}}$, which is better than the GLACE requirements.

2.2.1 Hβ data

As for the Hα line, two OSIRIS/GTC pointings using red TF were performed towards ZwCl0024-+1652. Details of observations and specific procedures to reduce Hβ data are described in Chapter 4.

2.3 Mid Infrared data: Spitzer

2.3.1 Spitzer Space Telescope

The Spitzer Space Telescope (Werner et al. 2004), is an orbital telescope designed to observe the Universe in the infra-red, between 3.6 μm to 160 μm. It is part of NASA's Great Observatories Program, together with Hubble Space Telescope, the Compton Gamma–Ray Observatory, and the Chandra X–Ray Observatory. It was launched on the 25^{th} of August, 2003 and is expected to run until 2018, subject to biannual reviews.

Spitzer is formed by two main units, the Spitzer Cryogenic Telescope Assembly (CTA hereafter), which contains the telescope and its instruments; and the Spacecraft, which controls the telescope and provides the services managing the overall telescope operation. In order to be able to observe at the required wavelengths, the CTA must be at a temperature of 5 K, what is achieved by the evaporation of liquid helium stored in a cryostat. The helium was exhausted in July 2009, after what the so called "warm phase" started. In this warm phase only the bands at 3.6 μm and 4.5 μm are still in operation.

The satellite payload is formed by three instruments:

- Infrared Array Camera (IRAC hereafter), described in Fazio et al. 2004, is an imaging camera capable of observing simultaneously at Near-Infrared (NIR hereafter) and Mid-Infrared (MIR hereafter) in four channels (3.6, 4.5, 5.6 and 8 μm). IRAC uses one detector for each of its bands, with different types of material in the detector arrays: indium and antimony for the shorter–wavelength channels (3.6 and 4.5 μm), and arsenic–doped silicon technology for the two longer–wavelengths (5.6 and 8 μm).

- Multiband Imaging Photometer (MIPS hereafter), described in Rieke et al. 2004, is an imaging camera designed to observe the Far-Infrared (FIR hereafter) at wavelengths of 24, 70 and 160 μm. The detectors are made of arsenic-doped silicon (24 μm) and gallium-doped germanium (70 and 160 μm). The 160 μm detector is treated with mechanical pressure to lower the band-gap and extend its sensitivity to this long wavelength. MIPS has a moving mirror

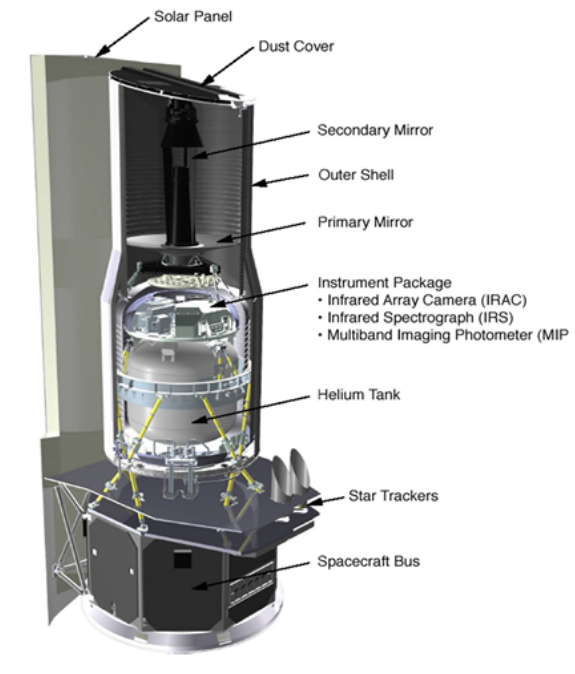

Figure 2.4: Spitzer telescope schematics. Credit: Spitzer Space Telescope Handbook.

for efficiently scan large sky areas.

- Infrared Spectrograph (IRS hereafter), described in Houck et al. 2004, is an infrared spectrometer capable of high– and low–resolution spectroscopy at MIR wavelengths, from 5.3 to 40 μm. Its detectors are made of arsenic-doped and antimony–doped silicon for the shortest and longest wavelengths respectively. IRS comprises four different modules: two low–resolution units, one operating at short wavelengths from 5.3 to 14 μm and other at long wavelengths between 14 and 40 μm; and two high–resolution modules, one covering the 10 - 19.5 μm range and other between 19 and 37 μm.

The data collected by Spitzer are available via the Spitzer Heritage Archive (SHA), at the Infrared Science Achive (IRSA).

2.3.2 Spitzer data

We retrieved archival IRAC images on ZwCl0024+1652, observed in December, 2003. The FoV of the different IRAC channels do not fully overlap: there are two adjacent fields in the focal plane viewed by the channels pairs (3.6 - 5.8 μm and 4.5 - 8 μm). We have downloaded and reprocessed the BCD (Basic Calibrated Data) images in order to construct the final map (avaliable post-BCD products are known to present instrument artefacts). Due to the first frame effect (frames with a shorter exposure and a depression in the response curve of up to 15%), we discarded the

initial frame of each exposure. Then we have corrected the BCD data from low-level jailbars and gradients. The process includes the removal image background variations due to foreground light sources. Finally, the new BCD images are mosaiced, reassembling all data onto a common pixel grid and combining them into a final image with its corresponding noise map.

The exposure times of these images are 2.7 ksec in the 3.6 and 5.6μm bands and 4 ksec in the 4.5 and 8 μm band, reaching a 2σ limiting flux of 5 μJy and 8 μJy respectively. The final image, centred in the cluster, covers an area of 5.6×5.6 arcmin^2. The number of objects detected at least in one of the IRAC bands is 2338.

MIPS 24 μm data were obtained from the Spitzer Heritage Archive. Two different programs cover the cluster area. The observations of Cl0024+1652 are centred on RA=00 26 35.70, DEC=+17 09 45 (J2000). The first program (P 3143) avoided the central 5×5 arcmin^2 of the cluster (see details in Geach et al. 2006). The total exposure time per pixel is 938 s. On the other hand, the centre of the cluster was covered as part of the Guaranteed Time Observations (Program 83). The total exposure time per pixel is 1979 s in the inner 2×2 arcmin^2 of the map, and 989 s in the external zone of this central scan. The reduction process is similar to that used for IRAC images. We retrieved the BCD images and reprocessed them using MOPEX (Makovoz & Marleau 2005). The final map covers a total area of 0.22 deg^2.

Source extraction was performed using Sextractor 2.5 (Bertin & Arnouts 1996) with a minimum area of 4 pixels and 2σ detection threshold. We used Kron photometry in our analysis. We visually inspected the extracted objects over the images to asses the detection quality and found it within requirements. The final catalogue contains 2099 sources with a limiting flux of 120μJy at 2σ. This output agrees with that described in Geach et al. (2006).

2.4 Far Infrared data: Herschel

2.4.1 Herschel

Herschel (Pilbratt et al. 2010) was an orbital telescope launched by the ESA in May 2009 and placed at the second Lagrange point of the Earth-Sun pair, at 1.5 million kilometres from Earth. It was designed to observe the Universe in the far-infrared, from 55 μm to 625 μm. *Herschel* had the largest primary mirror ever put in space (3.5 metres) and operated at a temperature of 1.7 K, achieved by a superfluid helium dewar. Further cooling to 0.3 K, required by two of its instruments, was provided by a dedicated ^{3}He. The coolant was exhausted on April, 2013, finishing the operational phase of the mission.

The observatory was formed by two main components: the Herschel Extended Payload Module

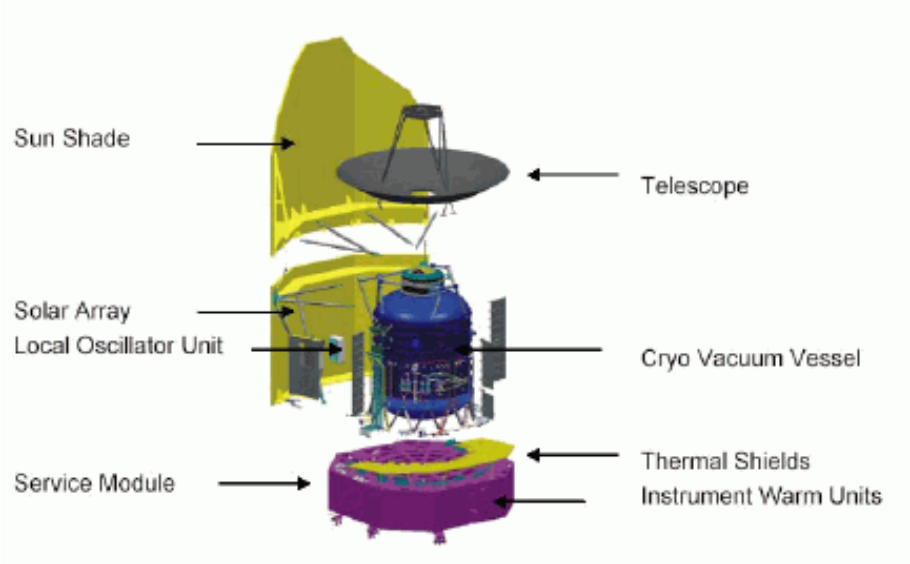

Figure 2.5: Herschel telescope schematics. Credit: Herschel Observers' Manual.

(HEPM hereafter), and the Service Module, this last one managing the overall spacecraft operation. The HEPM harbours the telescope, the cryostat and the three instruments:

- Heterodyne Instrument for the Far Infrared (HIFI hereafter), described in de Graauw et al. 2010, produced high resolution spectra from 157 to 625 μm (from 480 to 1910 GHz) in six bands, reaching the sub-millimetre range, using heterodynes and a bolometer.

- Photodetector Array Camera and Spectrometer (PACS hereafter), described in Poglitsch et al. 2010, was an imaging camera with medium resolution spectroscopy capabilities from 57 to 210 μm. It could perform simultaneous images in the 130-210 micron band and one of the two other bands (60-90 μmor 90-120 μm). The detector arrays were made with silicon and germanium-gallium subtracts.

- Spectral and Photometric Imaging Receiver (SPIRE hereafter), described in Griffin et al. 2010, was another imaging camera with medium resolution spectroscopy capabilities working at higher wavelengths, from 194 to 672 μm. It used five array bolometers with thermistors made of neutron transmutation doped germanium, able to perform simultaneous observations in three bands. The Fourier Transform Spectrometer produced low to medium spectra by splitting and recombining the incoming light after introducing a difference in the optical path with a scan mirror.

2.4.2 Herschel data

ZwCl0024+1652 was observed with Herschel within the PACS Evolutionary Probe (PEP hereafter) and Herschel Multi-tiered Extragalactic Survey (HerMES hereafter) guaranteed time programs Lutz et al. (2011) and Oliver et al. (2010). Both data sets are public and accessible from Herschel Science Archive (HSA).

ZwCl0024+1652 was observed in June, 2011 by PACS, using the photometer scan mapping mode at constant speed (default mode for PACS photometric mapping of large areas) as described in Lutz et al. (2011) using 100 and 160μm filters. The area of the final map is 4×4 arcmin^2, centered at RA = 00:26:36.0, DEC = +17:09:45. Total exposure time was 6.4 hours, reaching a depth (at 5σ level) is 4.85 and 11.35 mJy for 100 and 160 μm filters respectively.

We downloaded the level 2.5 reduced maps from the Herschel archive, with a combination of different observations. Standard pipeline reduction procedure includes a sliding high-pass filtering on the detector timeline to remove instrument drifts and 1/f noise with an iterative masking of the sources. We used the Herschel Interactive Processing Environment (HIPE) (Ott et al. 2006) in order to extract objects from the maps. We obtained the catalogues at 100 and 160μm using the MIPS 24μm positions as priors. We also performed a blind extraction of sources in the 100μm map and in the 160μm data to get objects not detected by MIPS, using a 3σ threshold. We extracted flux densities via standard aperture photometry techniques (Sussextractor, Savage & Oliver (2007); Hobson et al. (2010)). The uncertainties calculated include contributions from instrumental noise and absolute flux calibration. The projected maps have a pixel size of 2 arcseconds at 100 μm and 3 arcseconds at 160 μm. The total number of objects obtained is 471 in 100μm and 745 in 160μm.

Images at 250, 350 and 500 μm were acquired on June 2011 by SPIRE, with an area covered of 0.15 deg ^{2} and a total exposure time in each band of 12728 sec. We obtained the level 2.5 reduced images from the HSA archive. Pixel sizes are 6.0, 8.3 and 12.0 arcsec for 250, 350 and 500 μm maps (approximately 1/3 the full width at half-maximum (FWHM) of the beam in the relevant band). For SPIRE 250μm band we made a blind catalogue with a detection limit of 2σ using Sussextractor. For SPIRE 350 and 500μm bands we used the 250μm prior positions. Total sources detected in 250μm are 3479. Limiting flux for 250μm is 9.2 mJy Oliver et al. (2010). For 350 and 500μm we considered 7.7 and 11 mJy as upper limits.

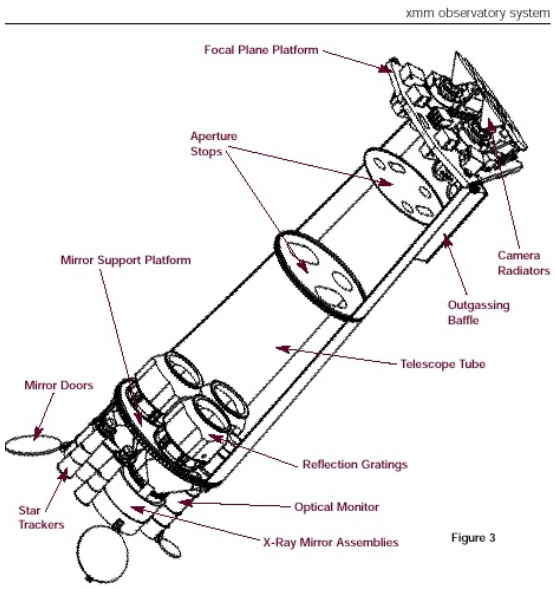

Figure 2.6: XMM payload schematics. Credit: XMM User Manual.

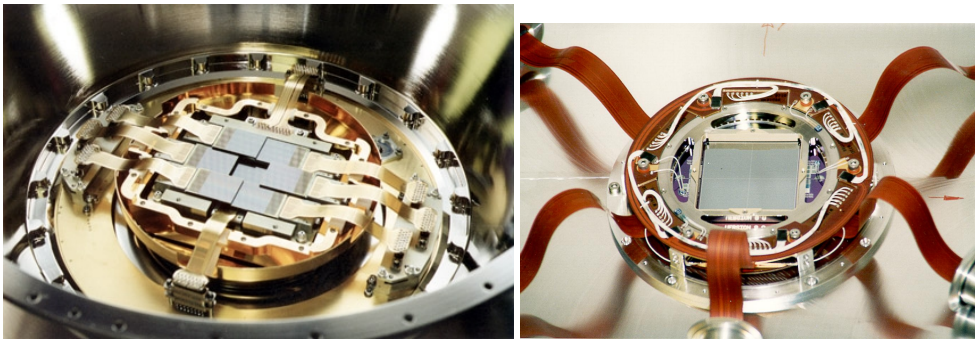

Figure 2.7: *Left:* MOS CCD bench. *Right:*PN CCD bench.

2.5 X–ray data: XMM–Newton

2.5.1 XMM–Newton

The X-ray Multi-Mirror Mission Newton (XMM–Newton hereafter) is a spaceborne X–ray telescope launched on December, 1999. It is one of ESA's cornerstone mission of the Horizon 2000 Science Programme, together with SOHO, Cluster–II and Rosetta. It is expected to be operational beyond 2020, subject to biannual reviews.

It is placed at a highly elliptical orbit with an inclination of approximately 66.5 degrees and a semimajor axis of 120 000 km, with a period of 47.86 hours. This orbit allows for observations of up to 144 kiloseconds in a low radiation background environment.

Its payload is formed by three instrumental systems:

- European Photon Imaging Camera (EPIC hereafter), described in Turner et al. (2001); Strüder et al. (2001), are in fact three X–ray imaging cameras using either metal oxide semiconductor CCDs arrays (MOS1 & MOS2) or pn-CCDs (PN). MOS are sensitive to the 0.2-10 keV energy range, while PN can detect photons up to 15 keV, with different response curves and efficiencies. The cameras are able to register the energy of the photons collected, producing low resolution spectra. Since the detectors are sensitive to infra-red, optical and ultra violet light as well, four filters are available in each camera in oder to decrease the impact of these photons in the exposures. A fourth instrument is also part of EPIC: the Radiation Monitor. It serves information of the space radiation environment for the correct operation of the rest of the instruments.

- Reflection Grating Spectrometer (RGS hereafter), described in den Herder et al. (2001), are two twin spectrometers with R 150 - 800 over an energy range of 0.33 to 2.5 keV. They seat on the *XMM–Newton* focal plane assembly with the EPICs, and share two telescope tubes with MOSs. In these tubes, two reflection grating arrays disperse the X–ray light into the CCD bench, aligned along the Rowland circle. The instrument field of view is 30 arcmin and its spatial resolution of about 6 arcsec (FWHM).

- XMM–newton Optical Monitor (OM hereafter), described Mason et al. (2001), is a modified 30 cm Ritchey-Chretien telescope with a focal ratio of f/12.7 mounted off-axis with respect to the mirror assembly. It seats on the upper part of the spacecraft, 8 metres apart of the X–Ray focal plane. OM is able to perform optical and ultraviolet (from 170 to 650 nm) imaging observations over a field of view of 17 arcmin^2.

Another important subsystem of the satellite is the Mirror Assembly. The optical design is based in the Wolter I grazing-incidence system, with 58 of such units coaxially nested in three parallel tubes. Each mirror shell consists in a paraboloid and a hyperboloid whose optical path is shown in Figure 2.8. The two pieces individual pieces are constructed in once block to ease alignment and integration.

Two of the mirrors are devoted to one MOS and one RGS each via a beam splitter and a reflection grating. The third one dedicated to PN. The focal length of the system is 7.5 metres.

One of the key parameters of the *XMM–Newton* observations is the mirror effective area convolved with the response curve of the different instruments. In general, the telescope mirror efficiency best energy range is from 0.1 to 10 keV, peaking at 1.5 keV.

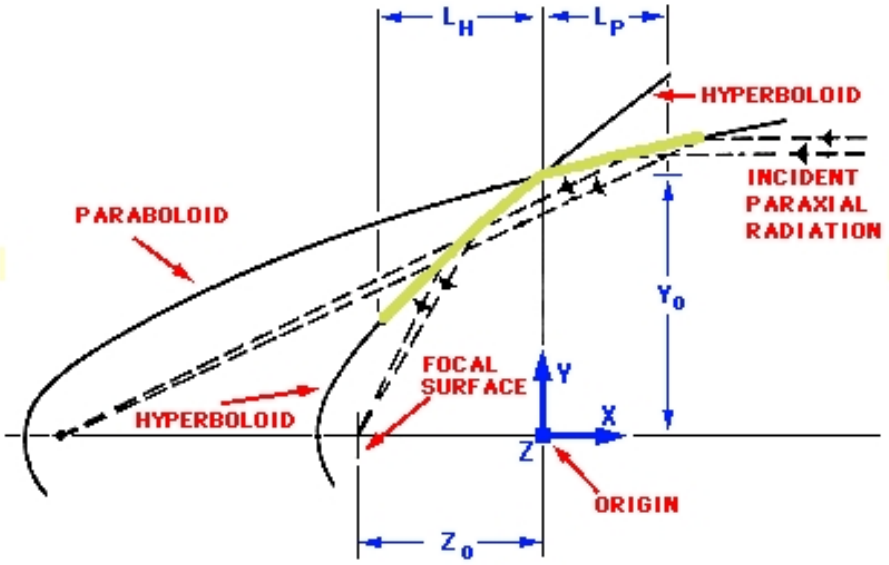

Figure 2.8: Wolter I optical design. Credit: XMM User Manual.

2.5.2 XMM–Newton Data

ZwCl0024+1652 was observed by *XMM–Newton* in January, 2001 in two different observations. The first one, of roughly 12 ks, was executed with the EPIC filters in "CLOSED" mode and although available, the data are useful for internal calibration purposes only. In the second observation, of 55 ks, the EPIC were configured in Full Frame (MOS) and ExtFullFrame (PN) with Filter Wheel "THIN", what extends the cameras FoV to their maximum.

The Observation Data Files (ODFs) and the Current Calibration Files (CCFs) are available from the XMM–Newton Scientific Archive (XSA hereafter) and were processed with XMM–Newton Science Analysis System (SAS hereafter) v 14.0.0. SAS is the software bundle provided by*XMM–Newton* in form of a collection of tasks, scripts and libraries, specifically designed to reduce and analyze data collected by the XMM-Newton observatory.

The X–ray data are often contaminated by flares of high background radiation depending on local space wheather. To reduce the data, we first identified the good time intervals (gti) by unselecting events with energies above 10 KeV and $PATTERN = 0$. We also remove bad events by setting $PATTERN = 4$ for events above 500 keVs. The good time interval filtered images had total exposure times of 34 ks.

Then the images where background subtracted by estimating the ratio of the events in the non-illuminated CCD areas vs the counts from the correspondent scaling factor from the CCFs. Then the bad pixel were treated by applying the standard masks provided. Finally the resulting data corrected of exposure maps.

The reduced image files were combined in an integrated energy image from 0.5 to 7.5 KeV. We produced also two more images following the same method, one for 0.5-2.5 KeV and other for 2.5 - 7.5 KeV.

The Observation Data File (ODF hereafter) of the referred observation are available from the *XMM–Newton* Science Archive (XSA). We have performed a standard reduction procedure using *XMM–Newton* Science Analysis Software (SAS) v14.0.0 consisting in good time interval selection, bad pixel and bright source masking (bright sources were selected from the 3XMM catalogue) of the images. Then we subtracted the background, performed the exposure correction and merged the bands in 0.5-7.5 KeV, 0.5-2.0 KeV and 2.0-7.5 KeV energy ranges.

The good time intervals (gti) were selected by removing flaring events in the 10 - 12 KeV. This band is known to be dominated by background particles due to the low instrument effciency in that range. Bad pixel masking was performed using the correspondent Current Calibration Files (CCFs) and bright sources in the field were masked using a SAS dedicated task.The background was substracted by scaling the information in the CCFs with the event counts in the not illuminated CCDs area. Once the images were exposure corrected, the multiple energy bands were merged in the three ranges stated in previous paragraph and the result smoothed with an adaptative kernel provided by SAS. The net exposure time in each resulting image was 40.2 ks.

Zhang et al. (2005) report a $L_X^{bol} = 2.9 \pm 0.01 \times 10^{44} h_{70}^{-2}\ erg\ s^{-1}$ in the 3 arcmin radius region around the observation central position and considers neglible the contribution beyond 5.5 arcmin. They also provide the $L_X^{bol} = 0.24 \times 10^{44} h_{70}^{-2}\ erg\ s^{-1}$ for a 100 arcsec radius area around RA=00 26 50.1, Dec=+17 19 37.8, named as *northern group* in their article. We use these values to flux calibrate our three maps.

2.6 Archival catalogs

2.6.1 X–ray catalogs

XMM–Newton serendipitous source catalog

For this thesis, we used the 3XMM-DR5 catalog (Rosen et al. 2015) containing source detections drawn from 7781 XMM-Newton EPIC observations, covering an energy interval from 0.2 keV to 12 keV. These observations were made between 2000 February 3 and 2013 December 20 and all datasets were publicly available by 2013 December 31, although not all public observations are included in this catalogue. This release corrects minor issues that exist in earlier versions. 3XMM-DR5 uses revised source lists with respect to those generated by the pipeline (PPS) and

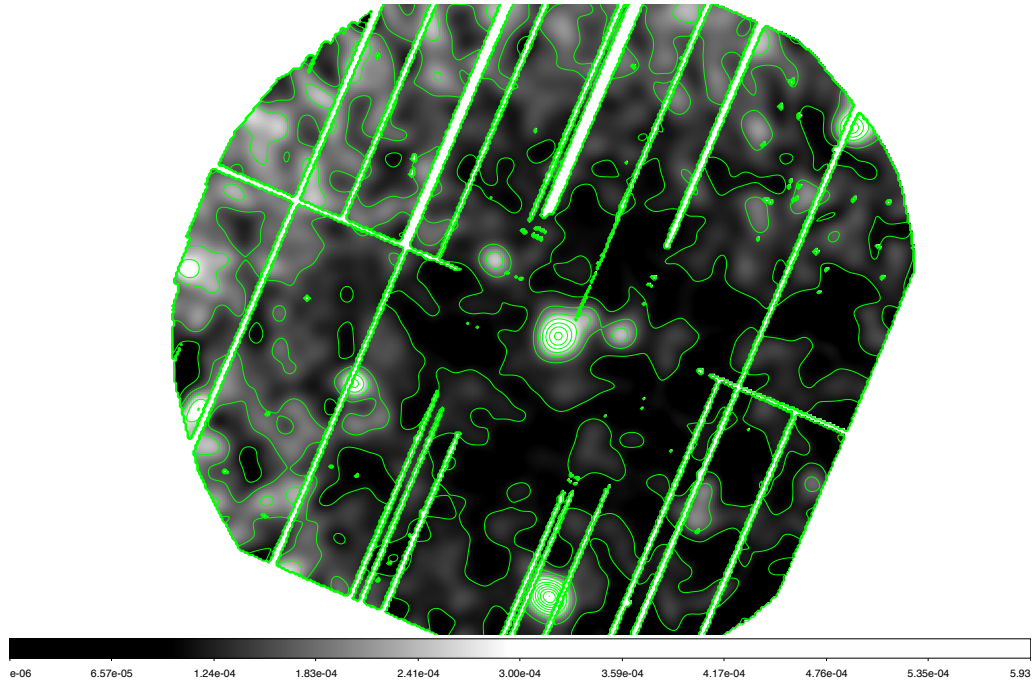

Figure 2.9: Integrated X–ray contours. North is up, East is left. Total area covered is ~ 0.125 deg^2.

distributed by the XSA.

ZwCl0024+1652 was observed by *XMM–Newton* EPIC on Jan, 2001 with MOS1, MOS2 and PN for a total exposure time of 52.1 ks, 52.1 ks and 48.3 ks respectively in Full Frame (MOS) and Extended Full Frame (PN) modes and Thin filter. The central position of the observation is RA = $00^h26^m35.7^m$, Dec = 17deg09'35.8". Total area covered in the cluster is ~ 0.45 deg ^{2}.

The observations described in Section 2.5 are included in the last release of *XMM–Newton* catalog (3XMM-DR5). This catalogue is the sixth publicly released XMM-Newton X-ray source catalogue produced by the XMM-Newton Survey Science Centre (SSC) consortium.

The median flux (in the total photon-energy band 0.2-12 keV) of the ZwCl0024+1652 detections is $\sim 1.2\ 10^{-14}$ erg cm^{-2}s^{-1}; in the soft energy band (0.2-2 keV) the median flux is $\sim 7.2\ 10^{-15}$ erg/cm^{-2} s^{-1}, and in the hard band (2-12 keV) it is $\sim 1.5\ 10^{-14}$ erg cm^{-2} s^{-1}. The average of positional accuracy of the ZwCl0024+1652 detections is 1.33 arcsec. From 173 sources in the original catalogue, we have selected good sources imposing over 'summary flag' keyword that they are clean detections. Final number of objects in the cluster is 148.

We used the central cluster position and a search radius of 15 arcminutes. The source list was then cropped to the assumed field of study (see section 3.3). 148 sources were obtained.

Chandra source catalog

We used as well the Chandra Source Catalog (CSC hereafter), v1.1 (Evans et al. 2010). The first official release of the CSC includes sources detected in ACIS and HRC observations in image mode from public observations made during roughly the first eight years of the mission. Only point sources, and compact sources, with observed spatial extents < 30 arcseconds, are included. Highly extended sources, and sources located in selected fields containing bright, highly extended sources, are excluded from the first release.

Each source is recorded in a single entry in the database and in one or more "source observation" table entries. The individual source entries contain the properties of a single detection from a single observation. The master source entry is the best estimate of all the properties of a source, based on the data extracted from the individual source entries.

ZwCl0024+1652 was observed with ACIS camera on September 2000. The area covered for in the CSC catalogue is ~ 0.1 deg^2 and the total exposure time is ~ 40 ksec. Data are included in the public Chandra Source Catalog (CSC, Release 1.1). The CSC contains positions and multi-band count rates for the sources, as well as derived spatial, spectral, and temporal calibrated source properties. The CSC also include images, photon event lists, light curves, and spectra for each source. All sources have a significance (S/R) ≥ 3. Measured fluxes cover three bands: soft (0.5-1.2 keV), medium (1.2-2.0 keV) and hard (2.0-7.0 keV), plus a total flux (broad band, 0.5-7 keV). The depth of sources detected in broad band (0.5-7 keV) is 1. 10^{-13} erg cm^{-2} s^{-1}. The number of sources detected by Chandra-ACIS in ZwCl0024+1652 is 31. Astrometry accuracy is 0.7 arcsec.

We used the central cluster position and a search radius of 15 arcminutes. The source list was then cropped to the assumed field of study (see section 3.3). A total number of 32 sources were obtained.

2.6.2 GALEX catalogs

The ultraviolet data has been extracted from GALEX public archive. ZwCl0024+1652 was observed for 13 ksec with GALEX in 2004 (GO-22; Cycle 1; PI Treu) in both near and far ultraviolet filters (Martin et al. 2005; Morrissey et al. 2007). Astrometric precision is of the order of 0.5 arcsec in both bands and limiting magnitude (at 5 σ) is 24.6 in FUV and 24.4 in NUV band (Morrissey et al. 2007).

2.6.3 Broad-band optical-NIR data

We have used the optical/NIR catalogue of ZwCl0024+1652 published by Moran et al. (2005). Public 'master catalogue' include photometry for all objects detected and extracted from HST and ground based telescopes. Ground-based optical broad-band data in this catalogue are BVRI-band imaging with the 3.6 m Canada-France-Hawaii Telescope (CFHT) using the CFH12k camera (Cuillandre et al. 1996). The CFH12k data reach 3σ depths of 27.8, 26.9, 26.6 and 25.9 for B, V, R and I bands (Treu et al. 2003; Czoske et al. 2002). Total area mosaiced is 26 x 40 arcmin^2. In addition, F814W HST photometry is included (Treu et al. 2003), although covered area is smaller ($\sim$ 14 arcmin of radius). HST observations are complete to F814W $\geq$ 25 (Smith et al. 2003). Optical broad-band catalogue have 73318 detected sources.

The optical data are complemented with wide-field NIR data from WIRC camera (Wilson et al. 2003) on the Hale 200-inch Telescope. Filters used are J and K_s. The details of the observations and data reduction are described by Kneib et al. (2003). The 3σ point source detection thresholds are J = 22.0 and K_s = 20.4. These NIR observations provides an observed area of 26 x 26 arcmin^2 around the cluster center. All images (HST and ground based) were registered to the astrometry of Czoske et al. (2002) and Treu et al. (2003). NIR sources measured are 60444.

Moreover, this catalogue also contains spectroscopic or photometric redshifts where available. Most of spectroscopy redshifts has been obtained by Moran et al. (2005) with DEIMOS on Keck2, while photometric redshifts has been calculated by Smith et al. (2005). For more details, see Moran et al. (2005).

Table 2.4: Data summary of broad-band CL0024+16

Instrument	Band	FoV	Exposure Time	Number of objects
(1)	(2)	(3)	(4)	(5)
*XMM–Newton*EPIC	0.2-12 keV	0.23	50000	148
*Chandra*ACIS	0.5-7 keV	0.1	40000	31
GALEX	FUV (1528Å)	1.28	13000	1131
	NUV (2271Å)	1.28	13000	3547
CFHT 12K	B,V,R,I	0.29	12000	60457
HST WFPC2	F814W	0.06	4400-19800	22000
Hale-200inch WIRC	J,K_S	0.19	11000	60444
*Spitzer*IRAC	3.5, 4.5μm	0.01	2700	1961
	5.8, 8.0μm	0.01	4000	1408
*Spitzer*MIPS	24μm	0.22	938 (1979)	2099
*Herschel*PACS	100, 160μm	0.004	23400	471, 745
*Herschel*SPIRE	250, 350, 500μm	0.15	12728	3479

Note: (1) Telescope/Instrument, (2) Energy/spectral band, (3) Field of View (sqr deg), (4) Exposure time (sec), (5) Objects detected

3

Multiwavelength catalog and spectral energy distribution

Abstract: This chapter presents a detailed discussion of the techniques employed to build a reliable multiwavelength catalog, as well as a description of the tools used to obtain the best fit SED of the cluster members. It also discusses the validity of the physical parameters derived from these SEDs.

The construction of a consistent catalog with all photometric information available in the OSIRIS observations of ZwCl0024+1652 is one of the main targets of this work and the entry point to a comprehensive study of the cluster members. The wide variety of characteristics of the different data sets in terms of depth, astrometric uncertainties, area covered, etc, on top of the intrinsic differences of X–ray, optical and infrared measurements, requires the utilization of cross matching algorithms beyond the mere association of closest sources. This is even more important in a field with significant surface density structures as ZwCl0024+1652. SEDs analysis with off–the–shelf tools, carefully assessing the scope where these tools are reliable, allows to infer important galaxy characteristics (SFR, age of an eventual burst in the start forming galaxies, stellar mass...). In this chapter though, we will focus on those parameters we cannot obtain otherwise due to the lack of the needed photometric information, like Ultraviolet Luminosity ($L(UV)$ hereafter) or $L(IR)$ where $L(FUV)$ or $L(24\mu m)$ are not available. In this chapter, the catalogues published in Moran et al. (2005) and Sánchez-Portal et al. (2015) are referred as Moran+05 Catalogue (M05

hereafter) and Sanchez-Portal+15 Catalogue (SP15 hereafter) respectively.

3.1 Introduction

When facing the study of an object based in a collection of photometric data of diverse provenances, obtained in different epochs with different techniques, one should make sure the data sets are coherent in terms of, at least, completeness, spatial resolution and photometric accuracy. However this is seldom possible since the observations are frequently conceived and executed independently, with their own scientific aims and methodology requirements. Moreover, the radical differences in the characteristics of the astronomical instruments (and the facilities they are in) used to observe from the high energy ranges to the lower ones make it extremely difficult to assemble a coherent set of data from the start. A number of techniques have been traditionally used to overcome such difficulties, although once the observations are made little can be done apart from the adoption statistical approaches to deal with the different completeness of the catalogues. The spatial resolution is determined by the instruments themselves and the data reduction methods should in principle provide the best possible photometric accuracy.

Once the data have been treated to improve the coherence of the set, the next step is to assign each datapoint to its corresponding physical source. One factor to consider is the different astrometry errors derived from the characteristics of the instruments and the telescopes, both ground based or satellite-borne (pointing accuracy, focal plane distortions, etc). Another one is the intrinsic uncertainties due to the various Point Spread Function (PSF hereafter), especially important when dealing with X–ray and FIR data. The construction of a multiwavelength catalog must take into account all these in order to be a reliable tool to analyze the characteristics of the objects.

The availability of a series of photopoints of the same galaxy makes it possible to produce its SEDs by fitting them to a family of low resolution templates. From the best fit templates one can infer some galaxy physical properties such as SFR, stellar masses, sSFRs , Star Formation History (SFH hereafter) or redshifts, although these results are bound to large uncertainties and careful statistical analysis is required to properly incorporate them.

In this chapter a detailed discussion of the techniques employed to obtain reliable matches and the building of the multiwavelength catalog is given, as well as a description of the tools used to obtain the best SED fits of the cluster members.

3.2 Likelihood Ratio estimation and match reliability

As explained in Chapter 2 , this work makes use of seven different catalogs, each of them containing coordinates, fluxes or magnitudes in different systems and wavelenght ranges and, in the case of the optical ones (Moran et al. 2005; Sánchez-Portal et al. 2015), some other information like morphology, redshift, AGN classification etc.

In order to get a single catalog containing all photometry available for each source, every non optical catalog (NonOpt hereafter) was independently crossmatched with M05. Each of the NonOpt sources with a reliable match was then linked to its optical counterpart. The set of photometric values from all matches of a specific optical source found this way is then its multiwavelength fingerprint (X–ray - UV - Optical - IR), and the collection of all sources in M05 is the multiwavelength catalog of ZwCl0024+1652, Xray, UV, Optical, IR catalog (XUOIR hereafter) hereafter.

Provided the variety of astrometric uncertainties, the spatial resolution and the wide spectral range covered by the catalogs, we applied a maximum likelihood ratio algorithm following a bayesian approach similar (but not identical) to that described in de Ruiter et al. (1977) and Sutherland & Saunders (1992). Since ZwCl0024+1652 is an overdense region and, more important, given the intrinsic errors of the NonOpt sources centroiding positions, a criterion merely based in the proximity of the sources does not guarantee a true match. It is needed to consider the expected magnitude distribution of the candidates and the background population (ie: non related sources) and establish a parameter that allow to estimate the reliability of the true matches.

In order to achieve that, we define the likelihood ratio (LR hereafter) of an optical source of magnitude m being the true counterpart of an NonOpt object as the ratio of the probability of that optical source be the true counterpart over the probability of being a spurious match.

$$LR(m, r) = \frac{q(m)f(r)}{n(m, r)} \tag{3.1}$$

where $q(m)$ is the magnitude distribution of the true counterparts, $f(r)$ is the probability distribution function of a true counterpart being at a distance r of the object and $n(m, r)$ is the surface density of the non-matches sources with the same magnitude m of the candidate.

As in Ciliegi et al. (2003), we consider a two dimensional gaussian as the probability distribution of the angular distances between an object and its true match:

$$f(r) = \frac{1}{2\pi\sigma^2} \exp(\frac{-r^2}{2\sigma}) \tag{3.2}$$

with a standard deviation $\sigma = \sqrt{\sigma_{NO}^2 + \sigma_{Opt}^2}$, where σ_{NO} is the positional error of the NonOpt object and σ_{Opt} is the positional error of the optical source, each of them considered again as the square root of the quadratic sum of the error in RA and DEC.

For the calculation of $n(m, r)$ it is needed to take into account the nature of the field studied. The surface density of sources in the field of view of a galaxy cluster varies significantly with the clustercentric distance, and in the particular case of ZwCl0024+1652 there are as well two clear substructures apart from the main one. This means that not only does $n(m, r)$ depend on the distance to the cluster core but on the specific coordinates of the object considered. For this reason estimations of the surface density of background (ie: non cluster) objects based in the cumulative distances of the sources brighter than a certain magnitude to a specific position, smoothed with various kernels, like in Sutherland & Saunders (1992) or Pineau et al. (2011), can not be applied. First, we estimate a $n(m, r)$ for each object to be matched by distributing all the sources in the optical catalogue (M05) in magnitude bins of size one magnitude. Then, the area of the annular region between the 5^{th} and 10^{th} closest sources with luminosities in the same magnitude bin as the candidate is calculated. The surface density is then the ratio between the number of elements (6 in this case) and this area expressed in Mpc^{-2}. Starting counting from the 5^{th} object gives confidence that no true candidate is included. The number of objects defining the annular area have been chosen to make sure that there are enough sources in the vicinity with the required magnitude. In the cases where this condition could not be fulfilled (galaxies in the bright or faint end of the magnitude distribution), $n(m, r)$ has been set to 0 (10^{-6} in fact, for practical purposes).

The estimation of $q(m)$ is done with a recursive algorithm, similar but not equal to what Luo et al. (2010) describes. We first select the XUOIR sources that lie within 0.5 arcsec of the NonOpt object, since it is realistic to assume they are good counterparts with a small (but not null) contamination of false matches. The magnitude distribution of the true sources is then:

$$real(m) = total(m) - \pi r_0^2 n(m, r) \tag{3.3}$$

where $total(m)$ is the magnitude distribution of the sources lying closer than this initial distance. Here we deviate from Luo et al. (2010) by making $total(m)$ depend on the position within the cluster via $n(m, r)$. Due to the M05 limit in magnitude we can only detect a fraction of the true counterparts, Q, so we need to derive $q(m)$ by normalizing $real(m)$ and multiplying by this detected fraction, Q, defined as $Q = \int_{-\infty}^{m_{lim}} q_m dm$.

$$q(m) = \frac{real(m)}{\Sigma_m real(m)} Q \tag{3.4}$$

Q is initially set to $Q = N_1/N_{NO}$, with N_1 being the number of matches found with $r_0 = 0.5$ arcsec and N_{NO} the number of NoOpt objects in the catalog. Once both $q(m)$ and $n(m, r)$ are obtained, they are used to calculate the LR of all optical sources within a radius of 5 arcsec of each object in the non optical catalogs.

Figure 3.1 shows $q(m)$ and $n(m)$ corresponding to to the different catalogs. $n(m, r)$ has been transformed into $n(m)$ by integrating it along the full r range for visualization purposes, ie: $n(m) = \int_{r_{min}}^{r_{max}} N(m, r) dr$. The magnitude distribution of background objects calculated in this way typically peaks at B magnitude $\approx 25 - 26$, benefitting from the depth of M05. $q(m)$ behaves differently depending on the NonOpt data source, with similar peak positions in the wavelength ends but with a dominance of matches at brighter magnitudes in the UV to MIR ranges.

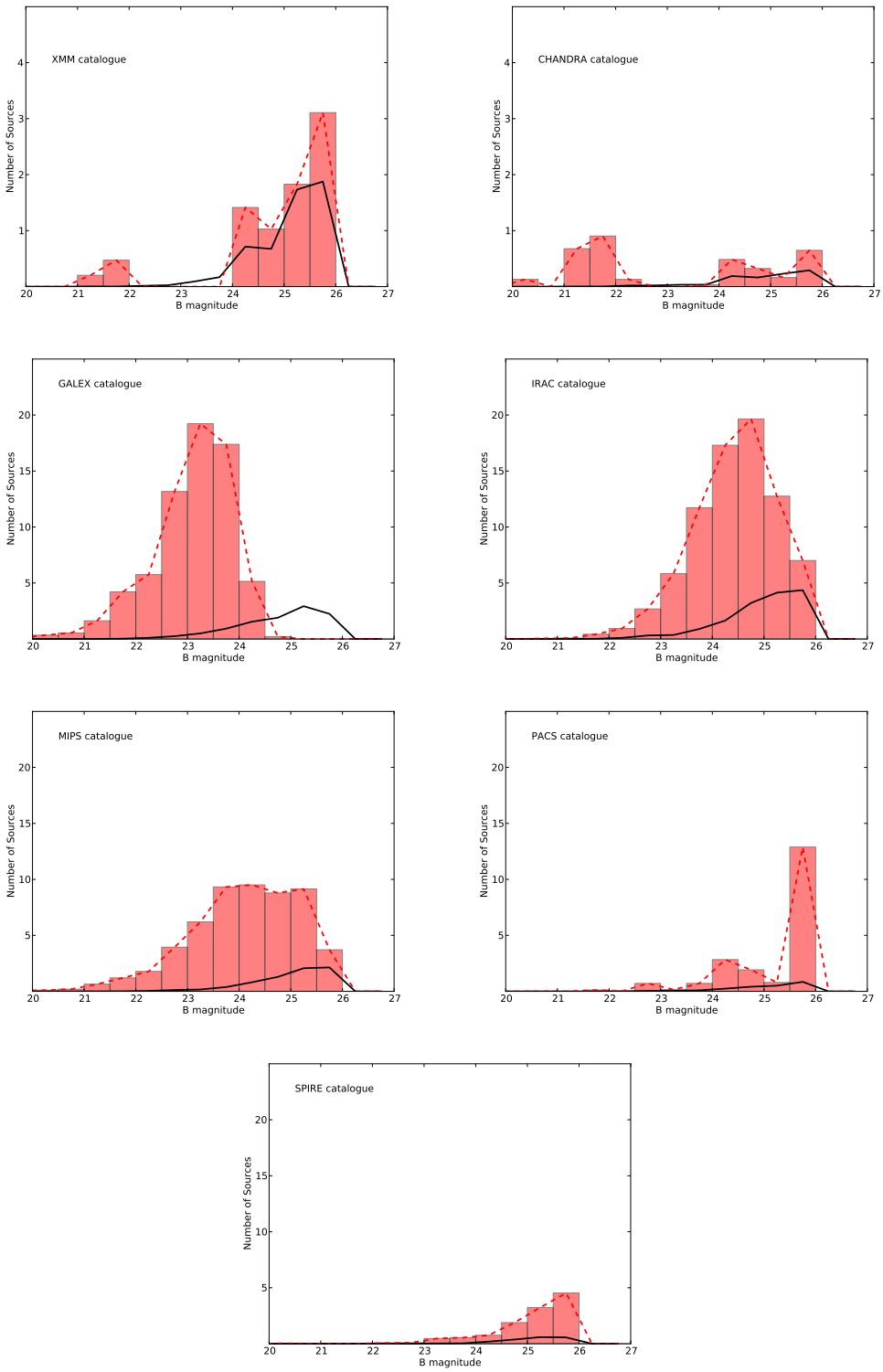

Figure 3.1: *q(m)* and *n(m)* for each NonOpt catalog. The histogram bars show the number of sources within a particular bin of the magnitude distribution of true counterparts, *q(m)*, while the dashed red line is *q(m)* smoothed with a boxcar average. The solid black line is the magnitude distribution of the surface density of non-related sources, *n(m)*. The latter peaks at fainter magnitudes than the magnitude distribution of true matches in the *GALEX* and *Spitzer* catalogs.

When the LR of a match is less than a certain threshold LR_{thr}, it is discarded. For all the matches of one object, those whose LRs are below 20% of the maximum LR are discarded as well. The rest are kept as candidates in this run. Then, we calculate a reliability parameter (R_c hereafter) for each remaining counterparts, indicating their probability of being the correct one. R_c is defined as the ratio of the LR of a candidate over the sum of the LRs of all other possible counterparts of one non optical object plus the fraction of good matches not found yet

$$R_c = \frac{LR}{\Sigma LR + (1 - Q)} \tag{3.5}$$

The average of the reliabilities R_c of all possible counterparts of all objects in the non optical catalog is the catalog reliability (R hereafter). We define as well the catalog completeness parameter (C hereafter) as the ratio of the sum of R_c of all the sources over the total number of objects in the non optical catalog.

$$C = \frac{\Sigma R_c}{N_{NO}} \tag{3.6}$$

These two parameters, R and C, actually describe the success of a run, meaning its ability to obtain true matches over the larger possible set of non optical objects. As seen in the discussion, both heavily depend on the election of LR_{thr}. We apply different values of LR_{thr} in a range defined by the minimum LR and the third quartile of the LR distribution and choose that maximizing $R + C$.

For the subsequent runs of this recursive method, $real(m)$ is re-defined as the magnitude distribution of the sources identified as true matches in the previous iteration, and Q is recalculated as the ratio of the number of these true matches over the total number of sources in the non optical catalog. The process is repeated until the R and C converge, typically in 2 or 3 rounds.

The typical numbers that LR actually takes depends on the catalog tried, increasing with its depth and decreasing with its positional uncertainty, what makes it an invalid proxy of the overall trustworthiness of the matches. R_c however, depends only on the amount of possible matches of a source and gives a correct idea of the validity of the result in a wider context. As shown in Figure 3.2, R_c rapidly increases with LR for all the catalogs, although its asymptotic approximation to 1 is slower in the case of the *Herschel* data. The distribution of R_c per data source can be seen in Figure 3.3. Again, the reliability of the matches globally decreases in the longer wavelengths, due to the lower positional accuracy (wider centroiding errors) of the *Herschel* catalogs.

Table 3.1: Crossmatch of NonOpt and Optical sources.

Catalog	Depth	σ_{NO}	R	C	N_X	N_{ID}	N_{mult}
(1)	(2)	(3)	(4)	(5)	(6)	(7)	(8)
XMM–Newton	1.2×10^{-13}	1.33	0.89	0.64	148	107	0
Chandra	1.0×10^{-13}	0.7	0.61	0.55	31	20	6
GALEX	25.3	0.5	0.88	0.44	3748	872	23
IRAC	23.6	0.18	0.94	0.64	2337	1529	0
MIPS	19.6	1.0	0.86	0.73	1549	956	0
PACS	20.6	2.0	0.47	0.39	408	330	0
SPIRE	19.6	3.0	0.41	0.31	3211	126	0

Note: Col.1: Catalog name. *Col.2*: Depth of the NonOptical catalog in AB magnitude, except for *Chandra* and *XMM–Newton* expresed in *erg* cm^{-2} s^{-1}. When a data source comprises several bands, either the integrated value (X–ray data) or the closest to optical is provided. *Col.3*: Positional accuracy in *arcsec*. *Col.4*: Reliability. *Col.5*: Completeness. *Col.6*: Number of sources in the NonOptical catalog. *Col.7*: Number of reliable matches found. *Col.8*: Number of sources with multiple matches with similar reliability (discarded).

The LR and the R_c of each match depends on the positional errors of both the optical and non optical catalogs. The magnitude distribution of both real and impossible counterparts, $q(m)$ and $n(m, r)$, depends only on M05. Therefore the probability of two non optical objects being a true match of a source in M05 without being the same galaxy is already minimised.

Table 3.1 shows a summary of the results of the one to one crossmatch, listing the Reliability of the process and Completeness parameters. In the cases where an optical source has been assigned to two or more different NonOpt object with similar LRs and R_c (*Col.8* the pair has been removed from the final list. Table 3.2 shows a few examples of this kind of cases).

3.3 The photometric catalog

One of the main scientific targets of this thesis is the construction of a consistent catalog of cluster members that includes all the available photometric information. This is achieved by following a series of steps: First, each NonOpt catalog is independently cross matched with M05, following the LR method described in section 3.2. Second, all reliable matches are joined using their Opt counterpart from M05 as reference key. Then, two filters are applied to keep only cluster members: FoV and redshift.

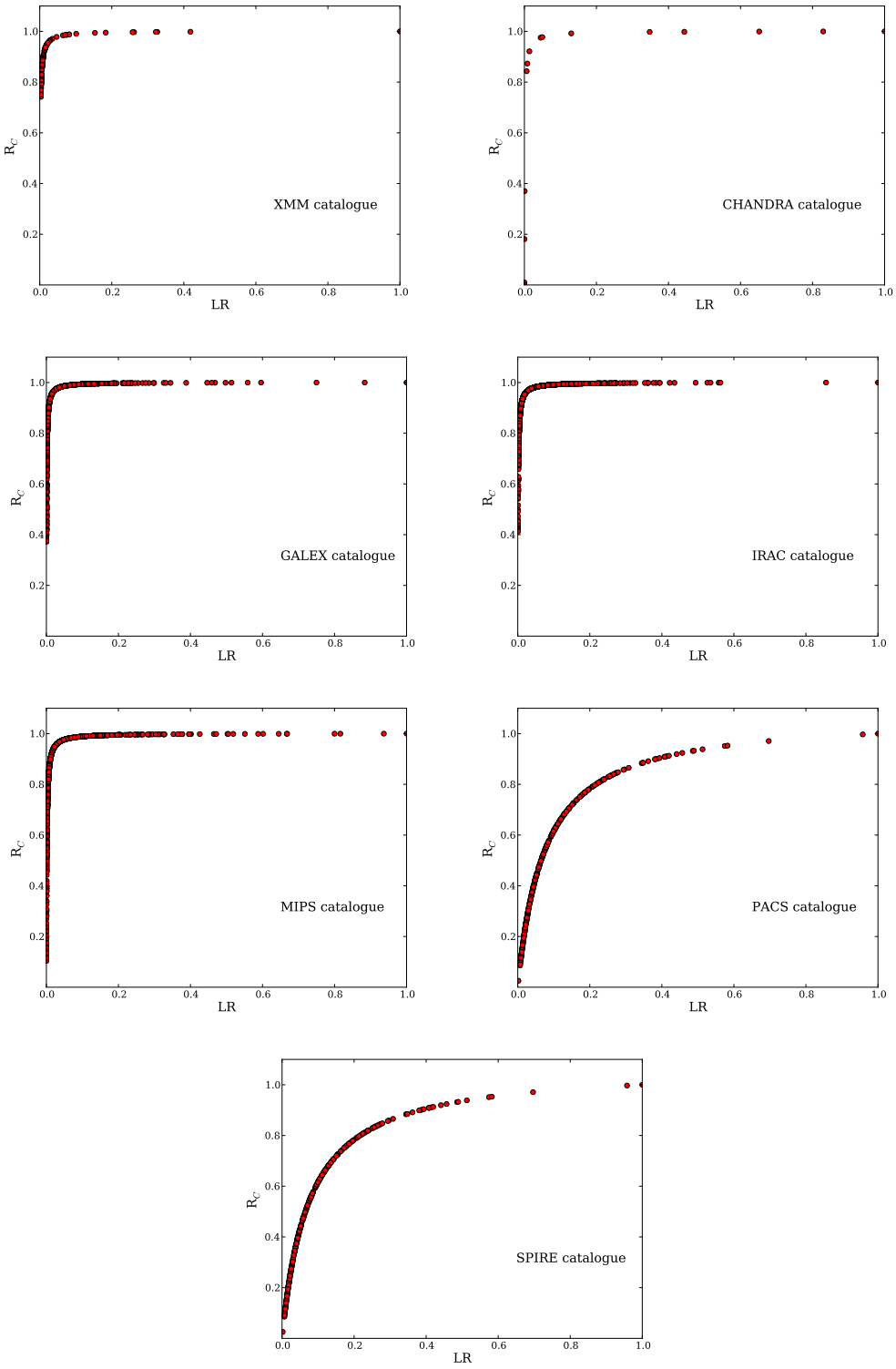

Figure 3.2: Reliability vs Likelyhood Ratio (normalized) for each of the seven independent NonOpt catalogs. R_c rapidly increases with *LR*, getting an overall constant high value. This trend in less pronounced in the *FIR*.

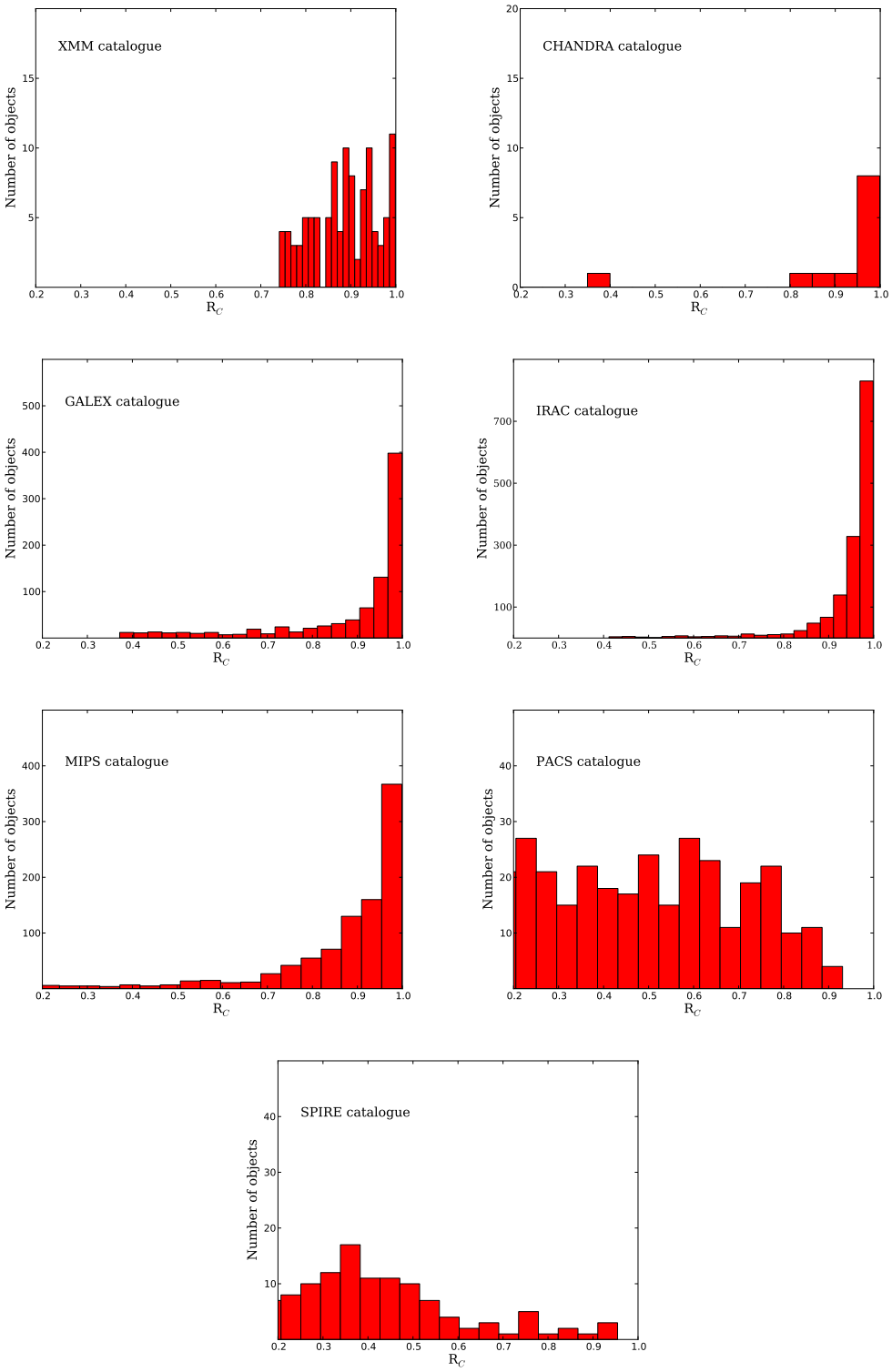

Figure 3.3: Distribution of the match reliability, R_c, across the seven independent *NonOpt* catalogs.

Table 3.2: Xmatch multiple matches

OptId	ID	LR	R_c	C
(1)	(2)	(3)	(4)	(5)
34352	27031707239	64.2262	0.9985	0.6106
34352	27031707233	64.2262	0.9985	0.6106
34392	26431707208	7.5537	0.9874	0.6106
34392	26431707205	7.5537	0.9874	0.6106
19594	3050065184164942046	88.1502	0.9944	0.8821
19594	6380943405686459646	96.7394	0.9949	0.8821
32426	3050065184164943005	2.0114	0.8023	0.8821
32426	6380943405686460156	1.9181	0.7947	0.8821
34818	6375982408150286337	749.1526	0.9993	0.8821
34818	6380943405686459969	730.9607	0.9993	0.8821

Note: Col.1: Object identification ID in the Opt catalog. *Col.2*: Object identification ID in the NonOpt catalog. *Col.3*: likelyhood ration of the match. *Col.4*: Reliability of the match. *Col.5*: Completeness of the cross match catalog.

As described in Section 2.1, GLACE covered ZwCl0024+1652 beyond its virial radius with two pointings. We define the GLACE FoV as the squared area marked by the upper-right and lower-left corners of the two overlapping pointings. A margin of 5 *arcmin* is added to each of its limits to guarantee that the matches found are not affected by border effects and benefit from the M05 catalogue to extend the study to 2.9 virial radius. We have considered these 5 *arcmin* as an acceptable limit to minimise off-cluster sample contamination. At this stage, the preliminary catalogue kept 19670 objects with at least 4 photometric points.

Then we applied a filter in redshift: M05 includes redshifts for 88% of its sources, although only 46 %, both spectroscopic and photometric, are considered reliable by the authors (see Moran et al. (2005)). SP15 provides redshifts for 174 objects, 112 of which have also redshifts in M05. The scatter between both measurements, defined as $|z_{SP15} - z_{M05}|/(1 + z_{spec})$, is on average (median) 0.002 (0.0005). We therefore consider the values from the TF observations of spectroscopic quality (Sánchez-Portal et al. 2015).

Using redshifts from SP15 when possible, we ended up with 7% and 39% of sources with spectroscopic and photometric redshift respectively in the GLACE FoV. Then we selected those within the cluster applying two different boundaries. For objects with z_{spec}, those whose redshift laid between 0.365 and 0.425 were consider members. Moran et al. (2005) used a more restrictive range: from $z_{spec}\approx$ 0.374 to 0.402. However, our ELGs list spanned from $z_{spec}\approx$ 0.371 to 0.421, so we considered the referred z_{spec}interval more appropriate. For the z_{phot}population we used a wider range due to the intrinsic uncertainties of the photometric redshifts. As in Moran et al. (2005), we select galaxies with z_{phot}between 0.3 and 0.48 (mean photometric error is Δ z « 0.01 in the cluster redshift range). For an extensive discussion on the reliability of memberships determined by z_{phot}in M05, see Smith et al. (2005). In Section 6.1 we show that those objects photometric redshift follow the same trends as their fellows with spectroscopic ones, which makes us believe

Table 3.3: Redshift partitioning of the multiwavelenght catalog restricted to the GLACE field of view

Sample	N_{obj}	%	Z range
(1)	(2)	(3)	(4)
Objects with redshift	19670	100	full
Objects with reliable redshift	9117	46	full
Objects with photometric redshift	7753	39	full
Objects with spectroscopic redshift	1364	7	full
Total cluster members	1262	6	ZwCl0024+1652
z_{phot}cluster members	735	4	0.395 ± 0.09
z_{spec}cluster members	527	3	0.395 ± 0.03

Note: Col.1: Sample name. *Col.2*: Number of objects in the sample. *Col.3*: Percentage over the total number of objects in the full catalog restricted only to the GLACE FoV. *Col.4*: redshift range considered.

the number of contaminants is similar to that in the spectroscopic sample. More details about the redshift partitioning of the multiwavelength catalogue can be found in Table 3.3.

The photometric catalog built this way contains 19670 sources in the GLACE FoV, 1262 of them being cluster members. Each object has from 4 to 32 datapoints from X–ray to FIR.

3.4 Spectral energy distributions of the cluster members

3.4.1 Le Phare and its settings

We used the Photometric Analysis for Redshift Estimate (*Le PHARE* hereafter), (see Arnouts et al. (1999) and Ilbert et al. (2006)), to obtain the best model of the SED ZwCl0024+1652 cluster members. There is a number of publicly available codes to analyse multiwavelength data via SED fitting (see Walcher et al. (2011) and references therein for a more extensive analysis), mostly focused in getting photometric redshifts. In our case, we did not aim for that but for the reverse estimate of the library input parameters such as stellar mass, integrated $L(IR)$ and $L(UV)$, extinction etc. *Le PHARE* uses various template SEDs to build model libraries with different physical parameters as input. By finding the best fit of the observed photometric points of a source, those physical parameters can be derived by inverting the process. *Le PHARE* provides those magnitudes together with the SED best fit.

We use three different template families when running *Le PHARE*: The Bruzual and Charlot population synthesis models (BC03 hereafter) (Bruzual & Charlot 2003), and semiempyrical templates from Polletta et al. (2007), Polleta semyempirical models (POLL hereafter) hereafter, that includes

six AGNs and three composite (AGNs+starburst) models. We also used the *Chary-Elbaz* SEDs to fit the infrared datapoints, since *Le PHARE* allows us to use a separated photometric library to fit points in the 8 μm to 1000 μm range (rest frame). We derived the BC03 library by taking the original family, that uses models with SFHs exponentially declining with time as $e^{-t/\tau}$, and making τ and t vary with a tool provided within the *Le PHARE* bundle. τ ran through nine different values: 0.1, 0.3, 1.0, 2.0, 3.0, 5.0, 10.0, 15.0 and 30.0 Gyr, while t (ie: age) went from 0.001 to 13.5 with 221 steps and three metallicity values (42, 52, 62). The IMF used is that of Chabrier (2003). For POLL, we selected only the nine templates with an AGN component (ie: pure AGNs or composite), disregarding the rest, derived from spirals, elliptical and starburst models. For the infrared spectral range, we used the SED family from Chary & Elbaz (2001), formed by 105 different templates. The code subtracts from these templates the stellar component calculated from the optical part to get only the dust contribution at the NIR. It also applies a dust extinction correction based in an extragalactic extinction curve from Calzetti et al. (2000). We set the extinction factor $E(B-V)$ to go from 0 to 1 in steps of 0.1.

Since the redshifts of our sample are already known, we set *Le PHARE* to run in *fixed redshift* mode, so it searches for the best model calculated at that z and outputs the physical parameters used to build the SED library: Extinction $E(B-V)$, $L(IR)$, Burst Age, stellar mass, SFR, $L(UV)$, R-band Luminosity ($L(R)$ hereafter) and K-band Luminosity ($L(K)$ hereafter)

3.4.2 Simulations

In order to get the best estimate of the *Le PHARE* output parameters and their associated errors, we build 499 simulated catalogs by modifiying each photometric point along its corresponding error bar. For that purpose we use a function that assigns to each band a random value within a gaussian law centered in the original measurement and with σ equals to one third of its photometric error. This new value is allowed to be within a $\pm 3\ \sigma$ range.

Then we run *Le PHARE* over the 500 instances of the multiwavelength catalog, getting 500 independent results. For each source we calculate how many different SEDs libraries have been found as best fit for any of the simulations, its frequency and its average reduced χ^2 and define a *quality parameter*, Q_{sim} as:

$$Q_{sim} = \chi^2 \times (1 - freq) \tag{3.7}$$

where *freq* is the number of times that model has been selected as best fit, normalised to the total number of simulations. The SED with a lower Q_{sim} is then selected as best fit for the object.

Figure 3.4 shows an histogram of the best fit *frequency* of the cluster members. Q_{sim} depends on the reduced χ^2 of each match and therefore can only be used to compare different instances of the same sources amomg themselves. 700 out of 1262 (i.e.: 55%) cluster members are fitted by

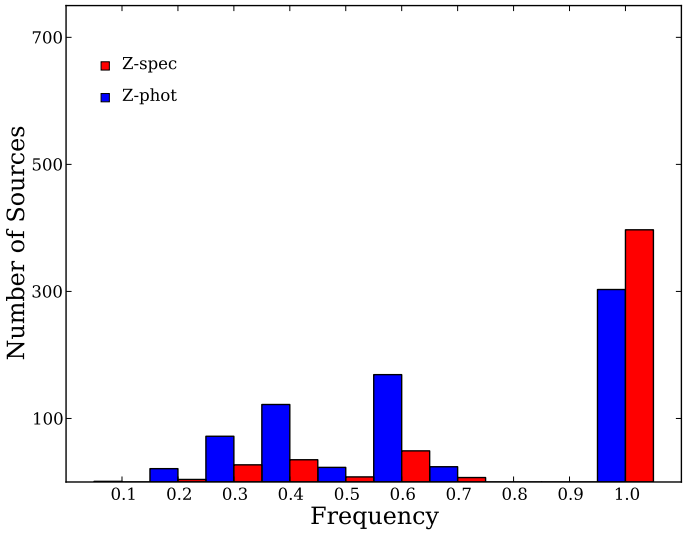

Figure 3.4: Distribution of the *frequency* the best SED library (i.e.: that with the lowest Q_{sim}) has been selected. Blue and red bars represent those objects with photometric and spectroscopic redshift respectively.

an unique SED model across all the simulations. This number increases to 75% (397 out of 527) when considering only objects with spectroscopic redshift.

Then we process the 500 catalogs with *Le PHARE* again, setting it to use the best model fit found in the initial run as a fixed SED template. The median of the output parameters of this second step is taken as the magnitude value and its standard deviation as its error measurement. This double run approach improves the error estimates since it does expand its calculation over the full set of simulations, including the less favourable ones, while in the first run only the good fittings are considered, significantly biasing the result. A summary of the error estimates of various output parameters can be seen in 3.4. On average, the uncertainties are 67% larger in the second run.

Figure 3.5 shows the distribution of the error estimates of the Stellar Mass and the Burst Age, as obtained in the first and second *Le PHARE* run.

Figure 3.6 shows some examples of best fit SEDs over the object photometric points for both POLL and BC03 libraries (flagged as AGN or SF respectively). The infrared range has been fit by a CE01 template when at least one data point was available. Both ELGs and normal galaxies, as well as two examples of best fits with low *frequency* ($freq \sim 0.5$) are displayed.

Table 3.4: Mean error estimate in the first and second *Le PHARE* run.

		Mean error (fixed model) (1)	Mean error (free model) (2)	ratio (3)
Stellar mass	$(M_\odot)$	0.19	0.11	1.72
Burst age	(Gyr)	1.1	0.77	1.42
SFR	$(M_\odot/yr)$	0.27	0.27	1.92
sSFR	$(M_\odot/yrM_\odot)$	0.35	0.15	2.33
L(UV)	$(log(L_\odot))$	0.12	0.10	1.20
L(R)	$(log(L_\odot))$	0.14	0.10	1.40
L(K)	$(log(L_\odot))$	0.22	0.13	1.69

Note: Col.1: Le PHARE output and their units. *Col.2:* Mean error estimate from the second run. *Col.3:* Mean error estimate from the first run. *Col.4:* Ratio of col.2 over col.3.

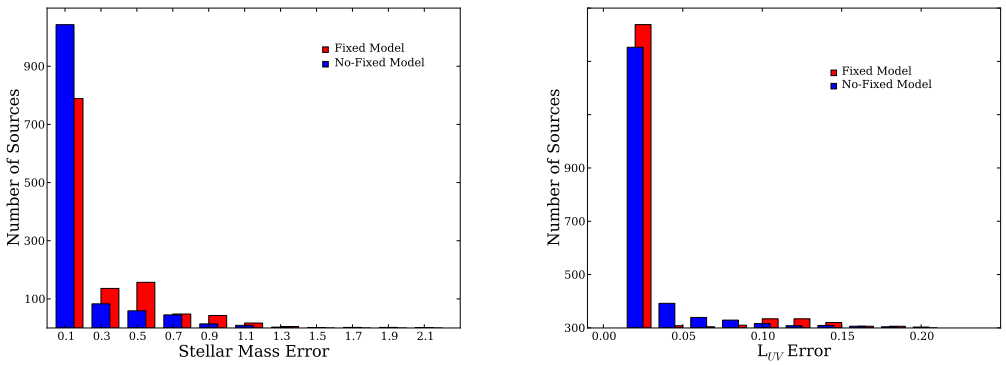

Figure 3.5: Distribution of error estimates in the first (free model) and second (fixed model) runs of *Le PHARE* for the stellar mass and the ultraviolet luminosity. The uncertainties from the first run are significantly lower than those from the second due to the restricted simulation sample they are calculated from, providing a less realistic value.

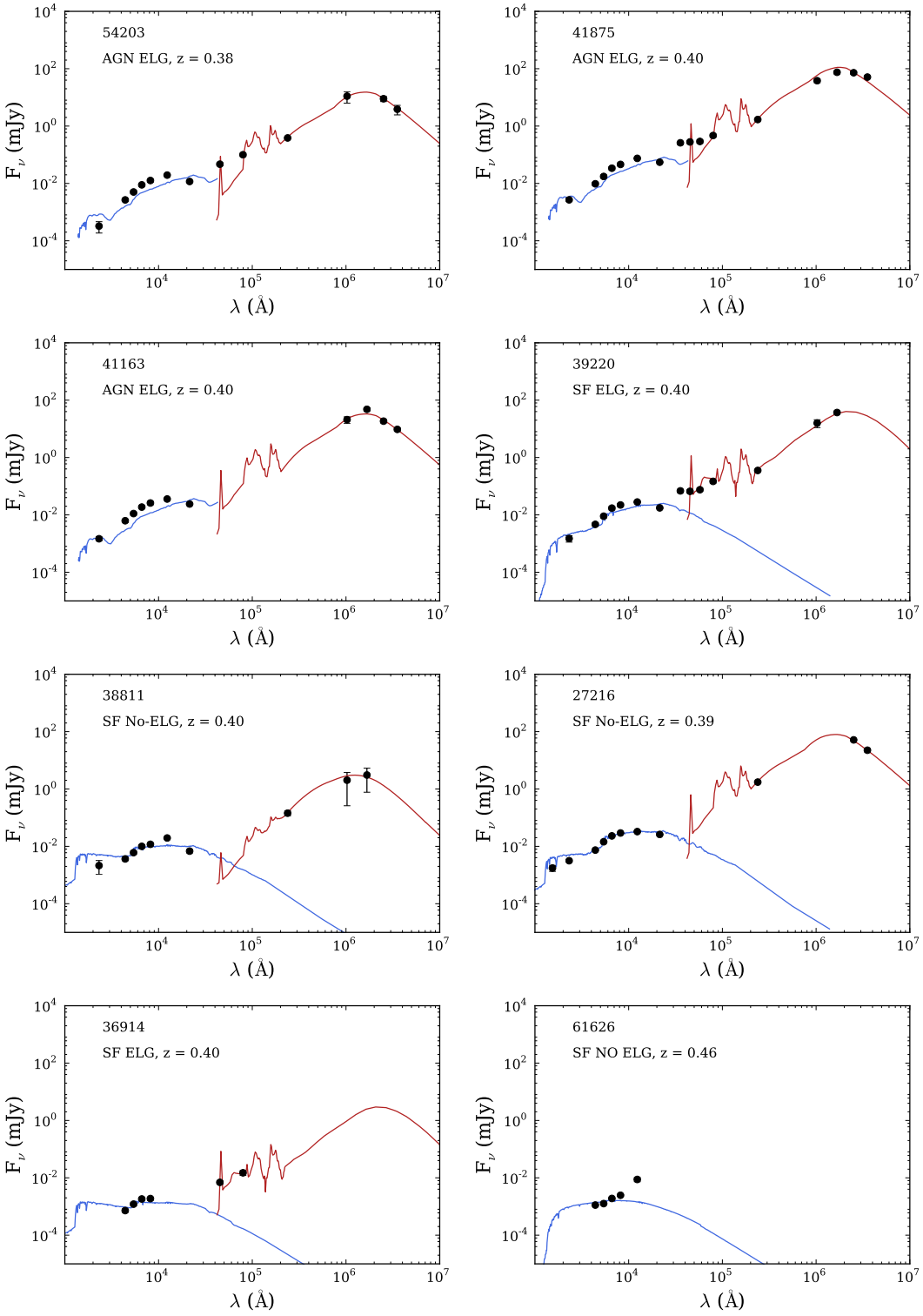

Figure 3.6: Best fit SED library as output by *Le PHARE* second run. Blue lines are the BC03 or POLL libraries for star forming galaxies or AGNs respectively. The red line is the best fit libraries from CE01. The ELG (or NoELG) label flag sources found (or not found) to be emission line galaxies in paper I.The six upper figures show objects fit by a unique model in all the simulations. The two lower figures show fits with $freq \sim 0.5$.

3.5 Calculation of integrated luminosities

As discussed in section 3.4.1, *Le PHARE* provides a series of physical parameters as output of the SED fitting process by reverse extraction of the inputs for library construction from the initial templates. It can also calculate some other, like integrated luminosities, by measuring them in the best fit SED library. This is especially convenient when the direct observable linked to a parameter is not available, e.g.: ultaviolet photometry for the $L(UV)$.

From all those parameters *Le PHARE* can provide, we have selected those with special impact in the characterization of an eventual AGN or the star formation activity in the galaxy. Some of them can also be directly calculated from observed photometric data and specific relations in the literature. We have compared the results from these two different procedures in order to assess the most reliable methodology.

In the case of $L(UV)$, it can be calculated from the measured luminosity at far ultraviolet (FUV hereafter) as per equation 3.8 (Domínguez Sánchez et al. 2014)

$$L_{UV} = 4\pi d_L^2 \times F_{FUV} \times \nu_{RF} \tag{3.8}$$

where d_L^2 is the luminosity distance, F_{FUV} is the observed flux at 1516Å and $\nu_{RF} = \nu/(1+z) = c/\lambda_{RF}$ is the restframe frequency.

For the comparison of SED derived $L(UV)$ vs $L(UV)$ obtained as per equation 3.8, we have taken the 111 objects detected by *GALEX* in 1514Å and calculated its integrated ultraviolet luminosity in both ways. We found a bivaluated correlation among the results in both the spectroscopically established members or the photometric redshift ones (see Figure 3.7). This is due to the way *Le PHARE* calculates $L(UV)$, by taking the monochromatic F_μ corresponding to the best fit library and integrating it along the UV band considered (FUV and NUV) with a top-hat profile. The result heavily depends on the particular cuadratic difference of the best fit and the observed values in those specific points, what is bound to large variations. Therefore we can not assume the values of $L(UV)$ extracted from SED fitting as reliable. We must constrain ourselves to those objects with observed photometry.

A similar approach can be followed with $L(IR)$, defined as the total infrared luminosity integrated from 8μm to 1000μm. It can be obtained from the flux at 24μm and the extrapolation of the CE01 library of template SEDs, as extensively described in the literature (see Oteo et al. (2013), Domínguez Sánchez et al. (2014) and many others). We have applied this method to the 148 sources in our MIPS catalogue and compared with the value provided by *Le PHARE*. In this case there is a clear correlation between them, although the values derived by normalization CE01 to 24μm are typically lower than those fit from *Le PHARE*, with an average ratio of $L_{IR}(LePHARE)\ vs\ L_{IR}(24\mu m) = 1.26$ and a standard deviation of 0.20 (see Figure 3.7). After visually inspecting the best fit SED selected in both methods, it is apparent that the FIR bump is

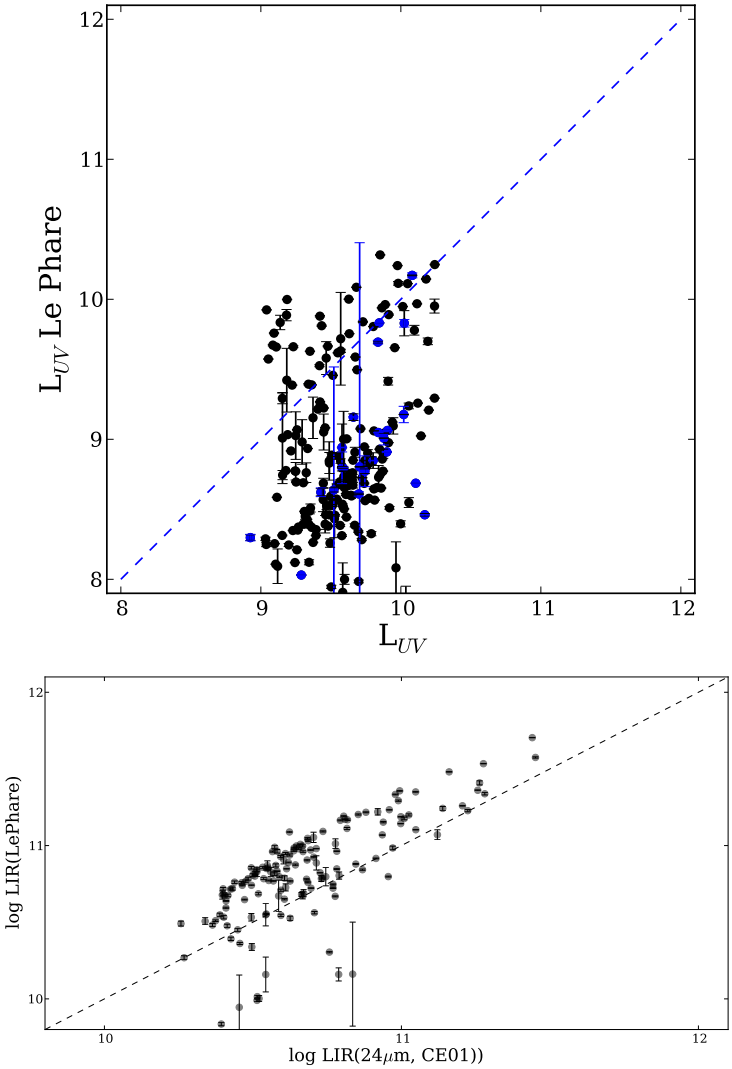

Figure 3.7: *Top:* Calculation of $L(UV)$ by *Le PHARE* and by equation 3.8. *Bottom:* Calculation of $L_{IR}(24\mu m)$ by *Le PHARE* and by extrapolating CE01 libraries.

underestimated when using only the 24μm datapoint. We take therefore the value provided by *Le PHARE* as valid.

Other magnitudes provided by *Le PHARE*, like the stellar mass, burst age, or derived from *Le PHARE* luminosities, like SFR and sSFR will be discussed in the following chapters, especially the SFR.

4

Extinction correction of the star formation rate derived from Hα measurements: Hβ observations of ZwCl0024+1652.

Abstract: In this chapter, we describe our attempt to perform an assessment of the actual extinction correction to be applied to the Hα SFR by means of the Balmer decrement derived from the Hβ line. To this end, we performed OSIRIS TF observations scanning the Hβ line. The observations and reduction process are described, as well as the derivation of the Hβ line flux. A description of the results on the (skinny) output sample and comparison with IR SFR are shown.

In Sánchez-Portal et al. (2015), the Hα SFR was derived using the standard assumption of one magnitude of extinction at the line (an average value derived by Kennicutt 1992, from the relation between Hα + [N II] and Hβ line EWs in a sample of 90 local ELG). In order to test the correctness of this assumption for our cluster ELG, we have performed TF observations of ZwCl0024+1652 mapping a velocity field of some ± 3000 km/s around the wavelength of the Hβ line at the cluster redshift (6871.1 Å). The chapter is structured as follows: first, a description of the observations carried out and the data reduction procedures is presented. Next, the method to estimate the magnitude of the correction for the underlying stellar absorption is outlined, as well

as the derivation of the total line flux (i.e. emission corrected for underlying absorption). These fluxes then used to estimate the extinction at the Hα line for the SF galaxies using the Balmer decrement, i.e. the ratio of the line fluxes $f_{H\alpha}/f_{H\beta}$. The results are presented in a final section.

4.1 Observations and data reduction

As for the Hα line (see Chapter 2 for details), two OSIRIS/GTC pointings using the red TF were performed towards ZwCl0024+1652. The coordinates of the "center" and "offset" positions were the same as for Hα. An identical dithering pattern was applied. The center position was targeted on the 24^{th} and 25^{th} of November 2009 (program GTC63-09B) and 17 August 2010 (program GTC8-10AGOS), covering a spectral range (defined by wavelength at the TF optical center of each scan) 6701.1–6911.1 Å in 22 scan steps at fixed steps of 10 Å. The TF FWHM was either 18 or 20 Å. Individual exposure times were either 124 or 130 sec. The offset position was observed in 9 October 2013. The spectral range was 6702.8–6892.3 Å in 20 scan steps (i.e. the two longer wavelengths were not observed), also at 10 Å steps. The TF FWHM values were slightly smaller, ranging from 17.6 to 18.1 Å. Individual exposure times were 138 sec.

The reduction was carried out using the same procedures applied to the Hα images. However, no fringing correction was required since sky lines are much weaker in the spectral range observed than those present in the Hα range. The raw source catalogues were derived as described in chapter 2, containing 788 and 1277 sources at the center and offset positions, respectively.

The flux calibration of the center position was performed following the same procedures as those described in Chapter 2. For the offset position, a different approach was applied: rather than performing TF imaging of standard stars, long slit OSIRIS spectra of stars within the cluster field were obtained. These spectra were reduced and calibrated using standard `IRAF` procedures. From these spectra, the calibrated flux $F_p(\lambda)$ required for the computation of the efficiency were derived (see definitions in Chapter 2). The measured flux $F_m(\lambda)$ is obtained directly from the pseudo-spectra catalogue, and calibrated using eq. 2.5. The final efficiency was estimated as the mean of the ratio $F_m(\lambda)/F_p(\lambda)$ for both stars. To estimate the efficiency error we used standard error propagation. For the error of $F_p(\lambda)$ we used the sigma of the spectra calculated by the task *apall* and for the error of $F_m(\lambda)$ we propagated errors from eq. 2.5, considering errors in the effective band pass and in the measured flux. The derived efficiencies are depicted in Fig. 4.1. It should be noticed that for the observations towards the offset position, photometric conditions were not enforced. Thus, we cannot assume that sky conditions hold from one scan step to another and therefore, the efficiency computed from a given scan step is not necessarily valid for another step. As a result, we do not have an actual $\epsilon(\lambda)$ curve but an $\epsilon(n_{scan})$ one. We have assumed that the efficiency is constant within the wavelength range covered by the center-to-border wavelength range of each spectral scan step. This is a very reasonable assumption, especially in the wavelength range around 7000 Å, where the efficiency profile is remarkably flat (see for instance Cabrera-Lavers 2015).

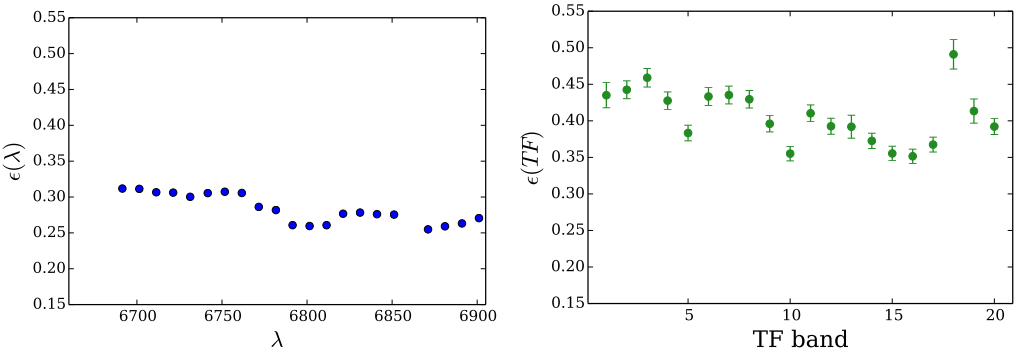

Figure 4.1: *Left:* TF efficiency computed as a function of wavelength for the center position using the same procedures as those used for Hα and described in Section 2.2.3. *Right*: Average efficiency per TF scan (band) for the offset position. The difference in the values obtained in both observing campaigns is outstanding. Nevertheless, there is a remarkable agreement between the calibrated fluxes in common sources of both positions.

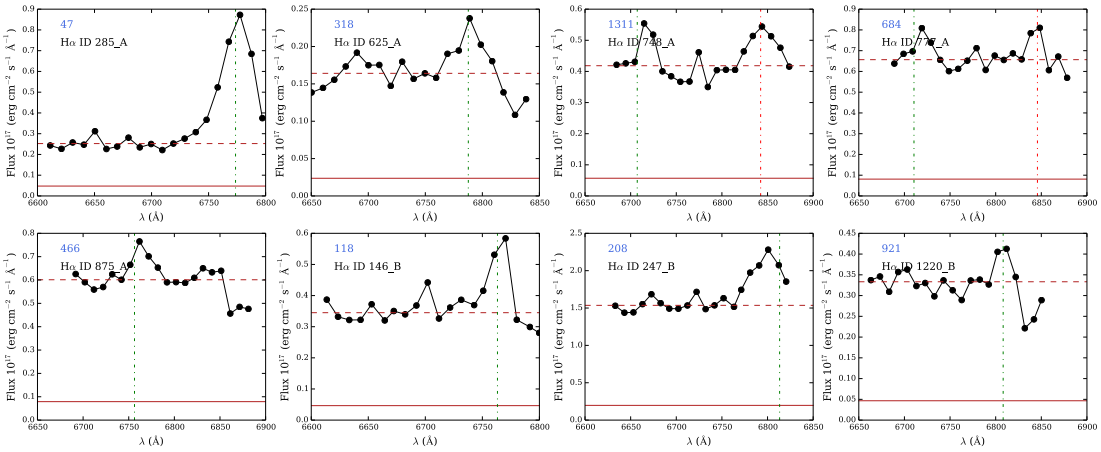

Figure 4.2: Selection of Hβ pseudo-spectra. The green dashed vertical lines mark the predicted position of the Hβ line derived from the Hα line. The red dashed lines mark the position of the [O III] λ 4959 line.

Even though the efficiencies derived for the center position are somewhat lower than those computed for the offset one, the obtained fluxes are compatible. In fact, we have compared the continuum flux values (see computation method below) for a set of 55 common sources of center and offset positions, finding a very tight correlation around the 1–1 line. The median value of the ratio between continuum fluxes at the center and offset positions is 1.08.

We have cross-matched the resulting Hβ catalogue with the catalogue of 167 Hα ELG from Sánchez-Portal et al. (2015), obtaining a sample of 150 unique objects (i.e. after removing duplicate sources). The calibrated pseudo-spectra have been visually inspected, selecting only those objects with clear emission features at the expected position of the Hβ line, as measured from the position of Hα (as in table 5 of Sánchez-Portal et al. 2015). These are depicted in Fig. 4.2. In some cases, not only the Hβ line, but also the [O III] λ 4959 emission is observed.

As explained in Chapter 2, each point of a pseudo-spectrum is the integrated flux of the source in the corresponding TF slice (i.e. the result of the convolution between the spectrum of the source and the response of the TF). We have converted the values to standard flux units (erg s^{-1} cm^{-2} $Å^{-1}$) by simply dividing them by the effective filter passband width $\delta\lambda_e = \frac{\pi}{2} FWHM_{TF}$. The line flux computation is simpler than for Hα since we have only one emission line rather than a blend of several emission lines. Hence, the flux collected by the TF is just the sum of the continuum plus the Hβ line (emission plus absorption). The process to obtain the Hβ emission is as follows:

(i) Definition of the continuum as the subset of pseudo-spectrum points resulting from discarding "high/low" outlier values, defined as those above or below the median value $\widetilde{flux}_{alldata}$ $\pm$ 2 $\times$ $\sigma_{alldata}$. The continuum level, $flux_{pseudoc}$, is defined as its median and the continuum noise, $\sigma_{pseudoc}$, as its standard deviation.

(ii) Subtraction of the continuum level from the pseudo-spectrum, calculating the errors with the propagation error formula.

(iii) Determination of the Hβ flux as the continuum-subtracted flux corresponding to the maximum in a range of ±2 scan steps (±20 Å) within the expected position of the Hβ line. This allows to account for certain line position uncertainties derived from inaccuracies in the Hα line centroid (e.g. when absorption-like features are present, see Sánchez-Portal et al. 2015). Only objects with peak fluxes above 2 $\times$ $\sigma_{pseudoc}$ have been considered as genuine line emitters.

The line flux errors have been computed by error propagation. The average relative line errors are 15.0/18.6% (median/mean). These figures are lower than those obtained for Hα (23.8/26.0%), but it should be taken into account that for Hα the line has to be de-blended from the [N II] one. Hence, there is an additional error contribution to be added in quadrature.

The final list of Hβ emitters has of 41 objects. The list has been further reduced to 27 SF galaxies after removing AGN (both BLAGN and NLAGN). The line flux distribution peaks at 2.08×10^{-17} erg s^{-1} cm^{-2}.

4.2 Estimation of the stellar absorption strength

One outstanding signature of population of young and intermediate age stars in the optical spectra of galaxies is the presence of the Balmer series in absorption. Emission lines appear superimposed on the underlying absorption. This effect grows in importance towards the higher order Balmer lines: the Hα absorption line equivalent width (W_{abs}) is very small and can be safely ignored upon computation of the emission line flux (Rosa-González et al. 2002). However, the Hβ line is moderately affected by absorption and it is fainter than Hα (the intrinsic Balmer decrement

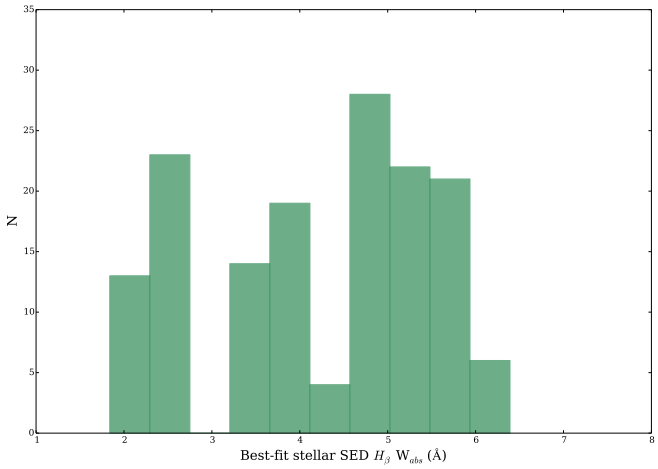

Figure 4.3: Distribution of Hβ absorption line equivalent widths derived from best-fitting templates and ages.

for case B recombination $f_{H\alpha}/f_{H\beta}$ is 2.85 Osterborck 2006). Hence, in this case the underlying absorption must be accounted for.

In several works, a constant Hβ W_{abs}, representative of the population of the galaxies under study has been chosen: Hopkins et al. (2013) assume a $W_{abs} = 2.5$ Å for the GAlaxy and Mass Assembly (GAMA) sample in the range $0 \leq z \leq 0.5$ range. Kennicutt (1992) apply a constant $W_{abs} = 5$ Å to his sample of local ELG. We have applied a different approach, deriving for each object the Hβ absorption equivalent width from the best-fitting host galaxy stellar SED template and age from Bruzual & Charlot (2003) (BC03) as described in Chapter 3. The *Le PHARE* code makes use of the low-resolution Composite Stellar Populations (CSP). In order to measure W_{abs} for the Hβ line, high-resolution templates are required. These have been computed using the GALAXEV[1] code (Bruzual & Charlot 2003). The spectral evolution of the CSPs has been derived by integrating the evolution equation of Single Stellar Population (SSP) BC03 templates with metallicities $Z = 0.0001$, 0.0004, 0.004, 0.008 and 0.02 (models m22, m32, m42, m52 and m62, respectively) with star formation histories exponentially declining with time as $SFR \propto e^{-t/\tau}$ with τ ranging from 0.1 to 30.0 Gyr and the initial mass function (IMF) from Chabrier (2003). The output of this code includes the Hβ absorption equivalent width (as defined in Trager et al. 1998) at different ages. We have chosen the values at the closest ages to those given by the best fit from *Le PHARE* (interpolation was not required since the age steps were almost identical in both codes).

The distribution of Hβ absorption line equivalent widths is depicted in Fig. 4.3. Two maxima are observed, precisely around 2.5 and 5 Å. The average equivalent width is $W_{abs} = 4.18$ Å, the median $W_{abs} = 4.67$ Å, and the standard deviation of the distribution 1.32 Å.

The absorption line flux was then computed by multiplying the value of W_{abs} by the pseudo-

[1] `http://www2.iap.fr/users/charlot/bc2003/`

continuum derived as explained in Sect. 4.1. The estimated absorption component is on average a significant fraction of the total line flux. The ratio $f_{H\beta,absorption}/f_{H\beta,emission}$ peaks at 0.35 with an average value of 0.42 with a maximum of 1.04 and minimum of 0.05.

4.3 Estimation of the extinction at Hα and corrected SFR

The total Hβ flux, measured as the sum of the emission and absorption components computed as explained above, has been used to compute the extinction correction from the Balmer decrement $f_{H\alpha}/f_{H\beta}$ using the equation:

$$A_{H\alpha} = \frac{2.5}{k_{H\alpha}/k_{H\beta} - 1} \log\left(\frac{1}{2.85}\frac{f_{H\alpha}}{f_{H\beta}}\right) \tag{4.1}$$

where $k_{H\alpha}/k_{H\beta} = 1.48$ for the galactic extinction law from Seaton (1979). The distribution of extinctions is depicted in the left panel of Fig. 4.4 . The largest peak corresponds to unabsorbed galaxies ($A_{H\alpha} \simeq 0$). This could be expected since, due to the incompleteness of the Hβ sample (the Hβ line is actually detected for some 24% of Hα emitters), our observations favour the detection of strong Hβ emitters, i.e. intrinsically luminous sources or unabsorbed ones. On the other hand, a second peak is observed close to $A_{H\alpha} \simeq 1$, i.e. the value usually assumed (after Kennicutt 1992).

The relative error in the Balmer decrement, as computed by error propagation, is on average 35.6/39.7% (median/mean). This translates into an uncertainty of approximately 0.8 mag in the extinction at the Hα line. More precisely, the average uncertainty obtained by error propagation from eq. 4.1 is 0.9 mag.

Once the extinction correction is known, the SFR can be computed using a suitable scaling relation, as the one from Kennicutt (1998):

$$SFR(M_\odot yr^{-1}) = \frac{10^{A_{H\alpha}/2.5}}{1.58} 7.94 \times 10^{-42} L(H\alpha)(ergs^{-1}) \tag{4.2}$$

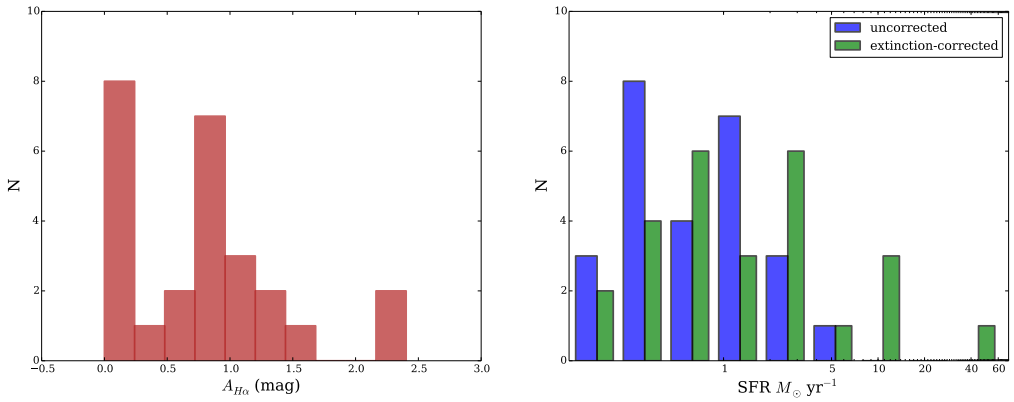

Figure 4.4: *Left:* Distribution of extinctions derived from the Balmer decrement and assuming a Seaton (1979) galactic extinction law. *Right:* Distribution of SFR derived from the Hα line after correcting for extinction.

where the factor 1.58 corresponds to the conversion from Salpeter to Chabrier (2003) IMF. The distribution of Hα SFR corrected using the equation 4.2 above is depicted in the right panel of Fig. 4.4.

The errors in both the uncorrected and corrected SFR have been computed as usual by propagation. The average uncertainty in the uncorrected SFR is 19.5/20.9% (median/mean). However, given the large uncertainty in $A_{H\alpha}$, the fractional errors in the corrected SFR are much larger, 76/86% (median/mean).

The relation between the uncorrected and corrected SFR is depicted in Fig. 4.5. Even though the results should be taken with caution, given the large uncertainties involved, a quite clear correlation is observed. Moreover, if the range is restricted to $SFR_{H\alpha,corrected} < 12\,M_\odot$ yr^{-1}, thus avoiding a luminous and highly absorbed ($A_{H\alpha} = 2.3$ mag) object, a reasonable linear correlation at $A_{H\alpha} = 1.4 \pm, 0.1$ mag is observed.

4.4 Comparison with SFRs derived from FIR

Domínguez Sánchez et al. (2014) performed a study of commonly used SFR estimates in a sample of *Herschel* counterparts of SDSS galaxies up to $z \sim 0.4$. The SFR_{total} is computed as the sum of the uncorrected SFR in the UV and the IR SFR, comparing it with other SFR estimates, and in particular the Hα SFR, finding a very good agreement between the estimates, with smaller dispersions than typical SFR uncertainties. We have attempted to perform a similar study with our small sample of SF galaxies for which the extinction correction is available. For this, we have not taken into account the SFR derived from UV, since the values obtained are negligible in comparison to those derived from $L(IR)$ and only applicable to an even smaller subsample of

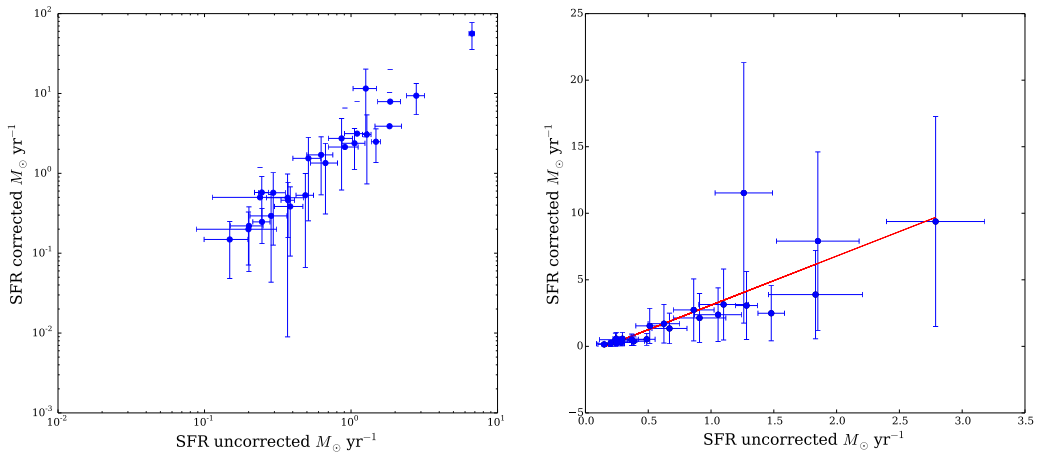

Figure 4.5: *Left:* Relation between extinction corrected and uncorrected Hα SFR (logarithmic scale). *Right:* The same relation as before (linear scale), but limited to $SFR_{H\alpha,corrected} < 12\,M_\odot$ yr^{-1} and showing the best linear fit. The slope corresponds to $A_{H\alpha} = 1.41$ mag.

sources with both SFR sources.

Our initially skinny sample (27 galaxies) is further reduced to 15 galaxies for which a FIR counterpart is found. Fig. 4.6 shows the relations. In the left panel, the uncorrected Hα is plotted against the FIR SFR. The amount of extinction required to reconcile the infrared SFR with Hα is also depicted. It is shown that, for a majority of the objects, a dust extinction ranging from 0 to 3 magnitudes at Hα can account for the observed relation. In particular, the value of 1.4 magnitude derived above seems especially good to account for the observed relation. However, for a fraction of the sample, and even taking into account the relatively large error bars, the required extinction should be extremely large to reconcile the discrepancy between the uncorrected Hα SFR and the infrared one ($A_{H\alpha} \simeq 6$ mag).

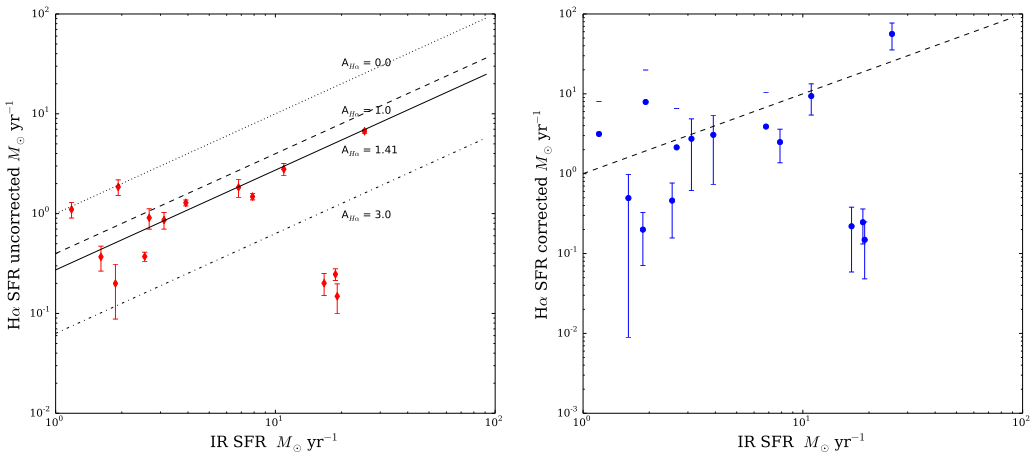

Figure 4.6: *Left:* Relation between the IR SFR and the uncorrected Hα SFR. *Right:* Comparison of the IR SFR and the extinction-corrected Hα SFR. The dashed line corresponds to the one-to-one relation.

5

Cluster Population

Abstract: The high density environment influences the objects accreted into the cluster structure in several ways. In order to study what transformations and where they take place we focus on three different populations: Sources detected in the far-infrared, AGNs and galaxies with significant star formation activity. This is the first time the cluster FIR population is studied, with a general IR sample three times larger than previous works in this cluster. It is also the first time a large sample of AGNs (72 objects) in a cluster at this redshift is obtained and studied. This is also the first time the SFRs of cluster members derived from Hα and from *L(IR)* are compared, identifying a large amount of obscured star formation. The intermediate region located at approximately 0.7 r_{vir} is where the main tracers of galaxy evolution (SFRs, AGN presence, morphology) shows larger concentrations.

Galaxies do alter their evolutionary path when entering a cluster, but what kind of transformations do they suffer along their way into the core? How do they mutate from fresh active spirals from the suburbs into respectable downtown passive red ellipticals? Where does their star formation activity stop and why? Are the processes enhancing their creation of new stars the same that quench it later? Why their shapes invariably adopt the same morphologies? By what means does the cluster remove the AGN fuel from their hosts? Are those processes ubiqui-

tous in the cluster and their effects detected in different areas only because of observational biases or do they favour specific regions? Are these regions determined by the clustercentric distance or are there other ways to define the environment? To address these questions, we accompanied three different populations in their journey from the region beyond the virial radius into the cluster core: Far-infrared galaxies, AGNs and star forming galaxies. In this chapter we will mainly identify the transformations that have taken place, leaving the considerations about mobile, scene and prime suspects to Chapter 6.

5.1 FIR population

5.1.1 Introduction

Local rich clusters are characterised by harbouring mainly passive, early type galaxies within their virialised regions (Dressler 1980; Biviano et al. 2004), while many studies have found larger fractions of non-quiescent, late type galaxies at higher redshifts (Coia et al. 2005; Pintos-Castro et al. 2013). The possible mechanisms able to drive such transformations and at the same time match the evolution between the typical spirals at higher redshifts and local ellipticals require significant formation of new stars (Poggianti et al. 1999; Kodama & Smail 2001). The study of such activity is key to understand the evolutionary processes within clusters. However, finding star formation tracers in high density environments has been traditionally elusive since different star formation indicators are sensitive to different galaxy characteristics.

Mid and far infrared luminosities are efficient probes of dust obscured activity in galaxies. Several studies have uncovered hidden star formation in clusters using infrared observations with *ISO* (Metcalfe et al. 2005), *Spitzer* (Webb et al. 2013) and more recently *Herschel* (Oliver et al. 2012). Others, like Gruppioni et al. 2013, use FIR observations by *Herschel* to establish the IR luminosity function up to $z \sim 4$ as a crucial tool to understand galaxy evolution and growth, both for AGN and star forming galaxy population. On the other hand, Burton et al. 2013 find a decrease of the far infrared fraction in high local density environments with increasing redshift up to 0.5. Summing up, the far infrared population in galaxy clusters is key to understand the evolutionary processes and the role and status of both passive and active populations in the cluster galaxy evolution.

5.1.2 Population characteristics

Far-infrared fraction

In our case, *Herschel* observations on ZwCl0024+1652 described in Chapter 2 comprise 122 objects in the wavelength range 100 μm - 500 μm, with source counts peaking in 14.5 mJy at 100 μm and in 22.9 mJy at 250 μm respectively. The limiting fluxes are 0.1 mJy and 1.7 mJy in those bands. 24 sources have been detected by both PACS and SPIRE simultaneously, and 85 of them have a 24μm counterpart. A summary of these result can be found in Table 5.1.

Table 5.1: *Herschel* detections on ZwCl0024+1652

	Total	All instrument band	Common with MIPS
	(1)	(2)	(3)
100 μm	87	79	74
160 μm	97	79	68
250 μm	41	21	29
350 μm	36	21	26
500 μm	21	21	13
Total (*)	122	24	85

Note: Col.1: Total objects detected in the band *Col.2:* Number of objects detected by all instrument bands simultaneously (PACS: 100 μm and 160 μm, SPIRE: 250 μm, 350 μm and 500 μm) *Col.3:* Number of objects with a 24μmcourterpart. *(*) Last row*: Number of objects detected by either PACS or SPIRE simultaneously, number of objects detected by PACS and SPIRE simultaneously and total far infrared objects with a 24 μmcounterpart

Figure 5.1 shows the far infrared fraction in the cluster, using R as reference optical band. Our sample peaks in R 21-22 (histogram bars), while the general magnitude distribution of cluster members does it at R 23-24 (black dots in the figure, referred to left vertical axis). There is no differences between the FIR population with and without MIR (8 and/or 24μm) detection (grey versus red bars). To further confirm this statement, we have performed a *Kolmogorov-Smirnoff* test on both sets, getting a p-value of 0.04, what accepts the null hypothesis of both samples being extracted from the same population.

A similar effect can be seen in the Color Magnitud Diagram (CMD hereafter), (Figure 5.2), depicting rest-frame B - R vs. R. In this case the optical magnitudes have been K-corrected using `kcorrect v4_2` (Blanton & Roweis 2007). Both the red sequence and the blue cloud can be clearly traced in the total cluster population. We fitted both components by two gaussians and defined the boundary between them as the line B - R = k = 1.58, where k is defined by the intersection of both gaussians. The far infrared population follows a bimodal distribution as well, marking the red sequence but with a significant underrepresentation in the blue cloud, favouring the transformational region instead. This is similar for both the FIR population and the FIR sample whitout MIR emission, although this last set shows a more even distribution. Although the diffe-

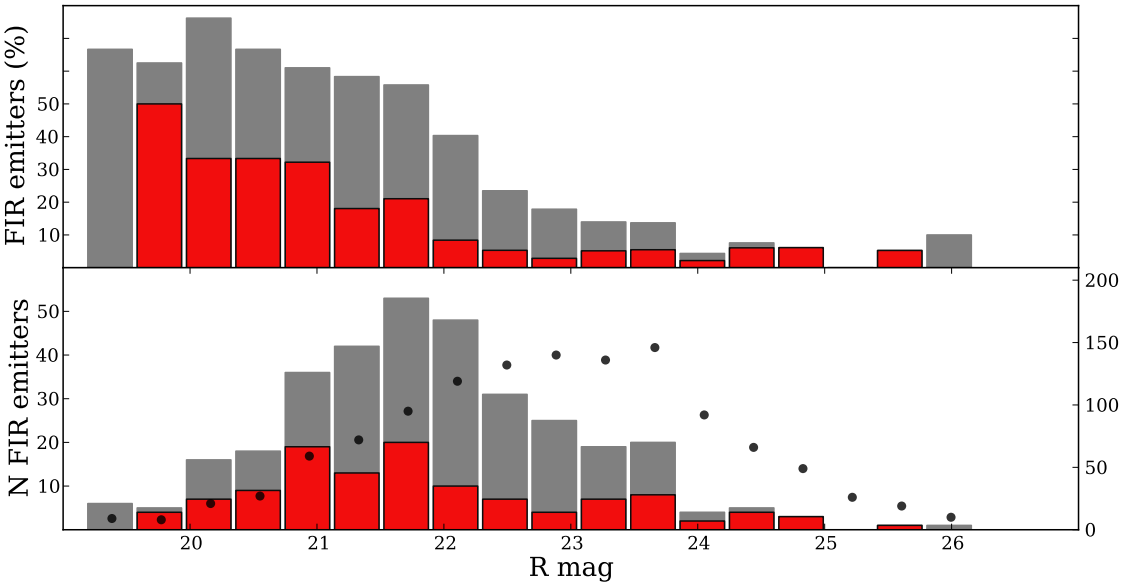

Figure 5.1: *Top:* Ratio between the number of FIR selected objects over the total cluster population (grey bars). The ratio of FIR sources without MIR detection is depicted in red bars. *Bottom:* The histogram shows the R magnitude distribution of FIR sources. Grey bars are the total FIR selected population. Red bars are the FIR population without MIR (8 and/or 24μm) detection. Scale is on the left vertical axis. Black dots are the representative values of the R band fraction of the 1262 cluster members in the correspondent magnitud bin. Scale is on the right vertical axis.

rence in plane numbers is small, the qualitative behaviour might lead to infer a difference in colour distribution of both populations. To investigate such possibility we ran a *Kolmogorov-Smirnoff* test of these subsamples (the MIR and no MIR selected FIR sources) checking for differences in the source sets. The test accepts the null hypothesis that both samples are drawn from the same distribution with a p-value of 0.13.

Far-infrared luminosity distribution

The luminosity distribution of a cluster gives the number of galaxies with a luminosity within a certain flux or magnitude bin. The integrated luminosity distribution N(L) for a particular spectral range is the number of galaxies with luminosities greater than L. Luminosity functions can also be defined in terms of galaxy magnitudes $m \propto -2.5log_{10}(L)$; $N(\leq m)$ is the number of galaxies in a cluster brighter than magnitude m.

The *far infrared luminosity function* is the distribution of the number of sources with $L(IR)$ between L and dL. We took the $L(IR)$ as the total object luminosity integrated from 8μm to 1000μm and calculated it for our FIR population in two different ways. We first took the 148 objects with a 24μm detection and fitted this photopoint to CE01 templates to extrapolate their $L(IR)$ as described in Chary & Elbaz (2001). Then we fitted the whole IR sample (347 sources) with *Le PHARE* using

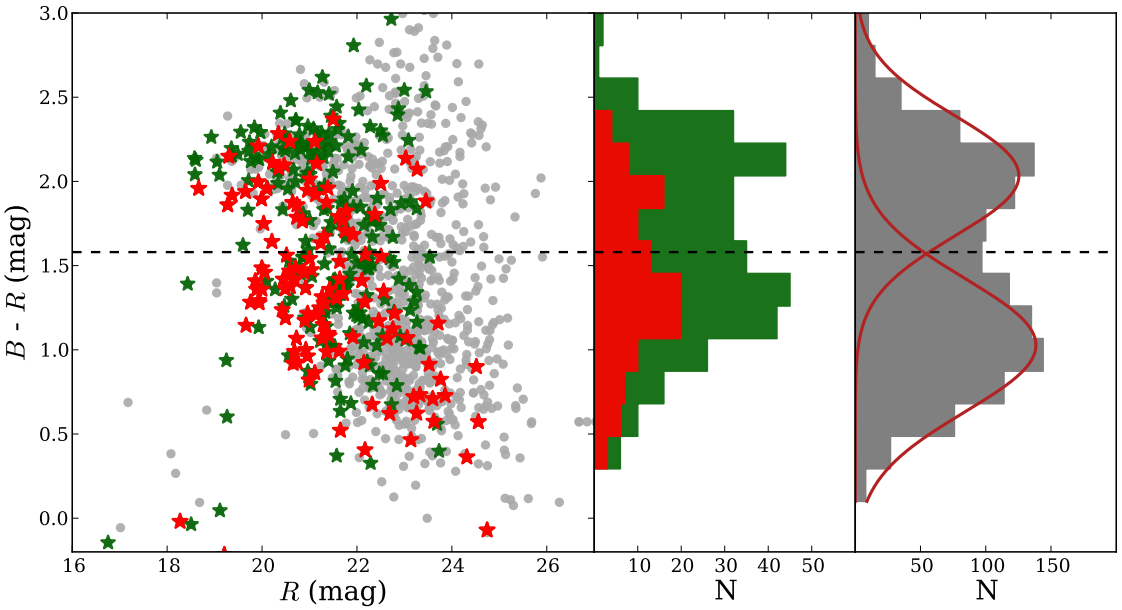

Figure 5.2: *Left:* Colour Magnitud Diagram of the FIR selected sources with and without 24μm(green and red stars respectively). The grey points represent the total cluster population. *Centre:* Histogram depicting the number of FIR selected sources per colour bin. Green bars are the overall FIR selected sources, red bars are FIR sources with no 24μmdetection.*Right:* Histogram showing the number of cluster members per colour bin. The distribution bimodality can be fitted by two gaussians intercepting at (B-R) = 1.58 (horizontal dashed line), separating the red sequence from the blue cloud. FIR selected sources favours the red sequence and the green valley, being underrepresented in the blue cloud.

only the IR range and using the same photometric libraries, but fitting them with all the available points. As already explained in Section 3.5, in both cases each object was represented by 500 instances of random variations of their photometric values as per a Gaussian pattern of mean equal to the original value and standard deviation of one third of their photometric error, allowing the variation to go to $\pm 3\sigma$. The comparison of both results can be seen in Figure 5.3. The output from the single point fit (24μm) to CE01 systematically gives lower values of the $L(IR)$. Visual inspection of best fit SEDs with one and the other method clearly favours those coming from *Le PHARE* since the FIR bump is better approximated. We therefore take *Le PHARE* $L(IR)$ as the correct estimate and its standard deviation, as its error.

We calculated then the FIR luminosity function of our *Herschel* sources within the virial radius of ZwCl0024+1652 (1.7 Mpc). All our FIR detections are above $10^{10} L_{\odot}$, with a mean value of $10^{11.24 \pm 0.02} L_{\odot}$. 57 out of 122 FIR sources qualify as LIRGs, altough no ultra luminous infrared galaxy (ULIRG hereafter) is found. This is consistent with the results in Geach et al. (2006), although we do detect a much larger number of faint FIR sources (i.e.: $L_{IR} < 10^{11} L_{\odot}$). We also find less objects in its faintest $L(IR)$ bin, probably due to an overestimate in the extrapolation of the luminosity function below that threshold. If we include in the analysis the infrared luminosity function calculated over the full cluster population with IR data (ie: those objects that not only have a *Herschel* detection, but also those with 8 μm and/or 24 μm photopoints) the $L(IR)$ fraction obtained diverges even more from the that result but better rersembles the general understanding of the FIR fraction in clusters (see Figure 5.4). In Geach et al. (2006), the $L(IR)$ fraction is calculated

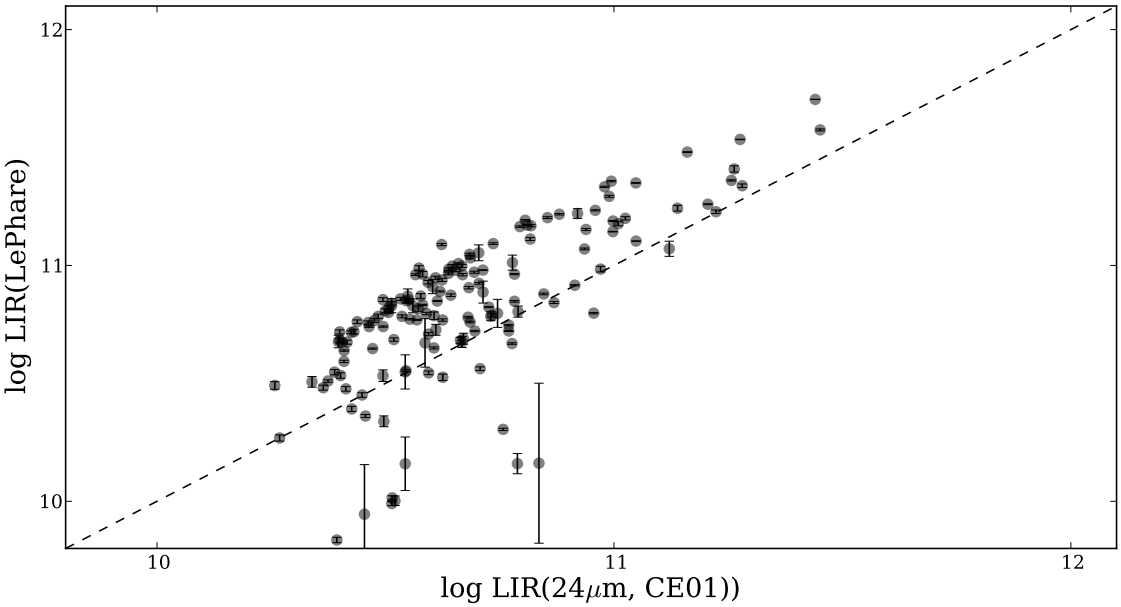

Figure 5.3: Comparisson between $L(IR)$ estimated from multipoint using *Le PHARE* (vertical axis) SED-fitting and single point (24μm) SED-normalization using Chary & Elbaz (2001) (horizontal axis) to CE01 templates for the 85 objects with MIR and FIR data. Black dashed line shows the one to one relationship.

from the 24μm data in an off-centred *Spitzer* observation, limited in flux to 200 mJy, and with cluster members selected by a colour-colour diagram. All these factors bias their findings towards brighter FIR sources and make them suffer from inaccurate count number estimate, due both to the uncertainties in membership from colour selection and extrapolation of core counts from the off-centred maps.

Figure 5.5 displays our cumulative LIR fraction. Open circles shows the results from Geach et al. (2006).

A significant conclussion is that FIR selected objects with no MIR detection follows the same trends than the overall FIR population.

5.1.3 Far-infrared sources in the cluster

The distribution of the far infrared sources along the cluster spatial structure has been addressed in multiple studies. Haines et al. (2010) reports a strong dependance of the FIR fraction with the clustercentric distance, finding variations up to a factor of 2 from the cluster core (0.3 r_{vir}) to the virial radius in the LoCuSS clusters from $z \sim 0.022$ to $z \sim 0.395$. This is suggestive of the morphology-density relation found in clusters from low to high redshift (Dressler et al. 1997; Treu et al. 2003).

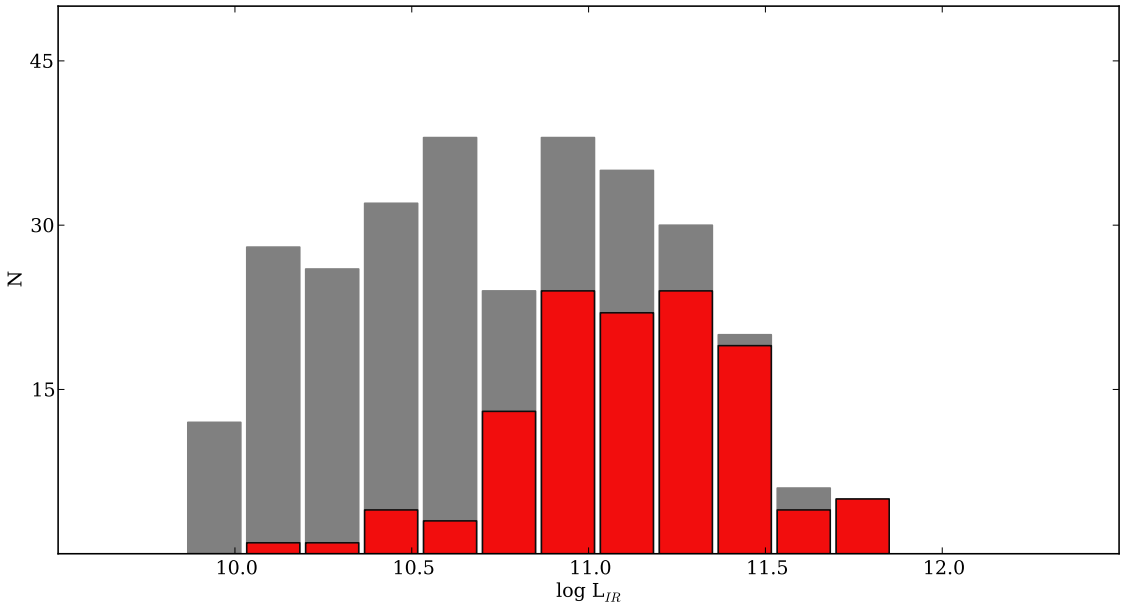

Figure 5.4: LIR luminosity distribution extended to all IR members. In general the proportion of sources with a far infrared detection (red bars) is more significant in the brighter side of the distribution than the general infrared population (i.e.: including detections between 8μm to 24μm)

Our FIR fraction is evenly distributed along the projected distance to the cluster core. As stated in Chapter 2, the PACS observation layout impede the extension of the FIR fraction estimate obtained from 100 μm and 160 μm beyond 1.2 $\sim$ r_{vir}. SPIRE data reached up to 2.2 $\sim$ r_{vir}, but with a shallower depth (the faintest SPIRE detection at 250 μm corresponds to a 5σ detection at 100μm). Having this into account, FIR fractions detected independently by both instruments keep similar trends with increasing projected distances. Figure 5.6 shows both the distribution (both simple and cumulative) along the instrument coverage. In general, the FIR fraction distribution per distance bin stays roughly around 0.15 for 100 μm and 0.04 for 250 μm up to $r \sim 2.2$ Mpc and $r \sim 3.8$ Mpc.

The distribution of the FIR emitters along the radial velocitiy vs. clustercentric projected distance (Figure 5.7) favours the main cluster structure, with a less significant presence in the line of sight infalling estructure reported as Structure B by Moran et al. (2007); Czoske et al. (2002) and Sánchez-Portal et al. (2015). The FIR fraction, f_{FIR}, in the main structure is larger than in Structure B by a factor of ~ 2 ($f_{FIR} \sim 0.09$ and $f_{FIR} \sim 0.05$ respectively).

5.1.4 Far-infrared morphology

We have morphological classification of 51 far infrared sources from Treu et al. (2003), obtained by analysing WFPC2 - HST maps reaching $I_{AB} \sim 25$. In that work, Treu *et al.* limited their study to objects brighter than $I_{AB} \sim 22.5$ to guarantee enough S/N to produce a reliable result.

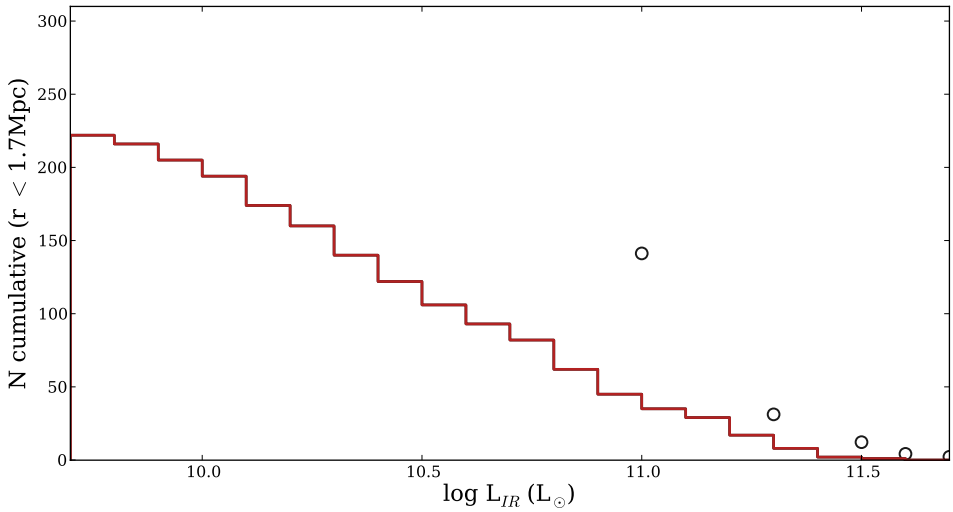

Figure 5.5: LIR luminosity function. Black solid line indicates the cummulative number of sources detected by *Herschel* per LIR in magnitud bins of 0.1 $L_\odot$. Open circles shows the results found by Geach et al. (2006), with no source found below $10^{11} L_\odot$ and a much larger sources found in the $logL_{IR}(L_\odot) \sim 11$ bin.

We rebin their morphologies in four types: Ellipticals, (E), equivalent to type 0 in Abraham et al. (1996), Disk (E/S0), equivalent to types 1 and 2 (E/S0 and S0), Late Type, comprising types 3 to 6 (different kind of spirals) and Irregular, correspondent to types 6 to 8 in the referred work.

The FIR population clearly favours late type galaxies (31 out of 51) versus pure ellipticals (6 out of 51). This is an indication of the enhancement of the $L(IR)$ by the higher activity of spiral galaxies. The bulk of these spirals have $L(IR)$ below $10^{11} L_\odot$, with only 10 qualifying as *LIRGs*. On the other hand, 6 out of the total amount of 23 LIRGs are disk-like galaxies, and 3 are irregular. The *LIRGs* fraction is therefore formed mostly by late type (fraction 0.43), disk galaxies (0.26) and, more marginally, irregular (0.13) and ellipticals (0.17).

The effect is even more evident when calculating the fraction of LIRGs per morphology type. The LIRGs fraction of irregular galaxies is 0.75, and 0.60 of disk galaxies. Even taking into account the small number statistics involved, it appears evident that our LIRG population is mainly formed by galaxies going through the transformation from field galaxies into massive S0 and elliptical cluster objects. Such processes are typically triggered during galaxy-galaxy interaction and merging during the viralization.

Petty et al. (2014) have found a clear shift towards bulge dominated galaxies in a sample of local LIRGs observed within the GOALS collaboration. They have also simulated how merging LIRGs would appear at $z \sim 0.5 - 3$ in deep optical images, such as those used by Treu *et. al.* to classify the galaxies, and found that they often result in misclassified disklike galaxies. This would also contribute to the high E/S0 fraction of LIRGs in our sample.

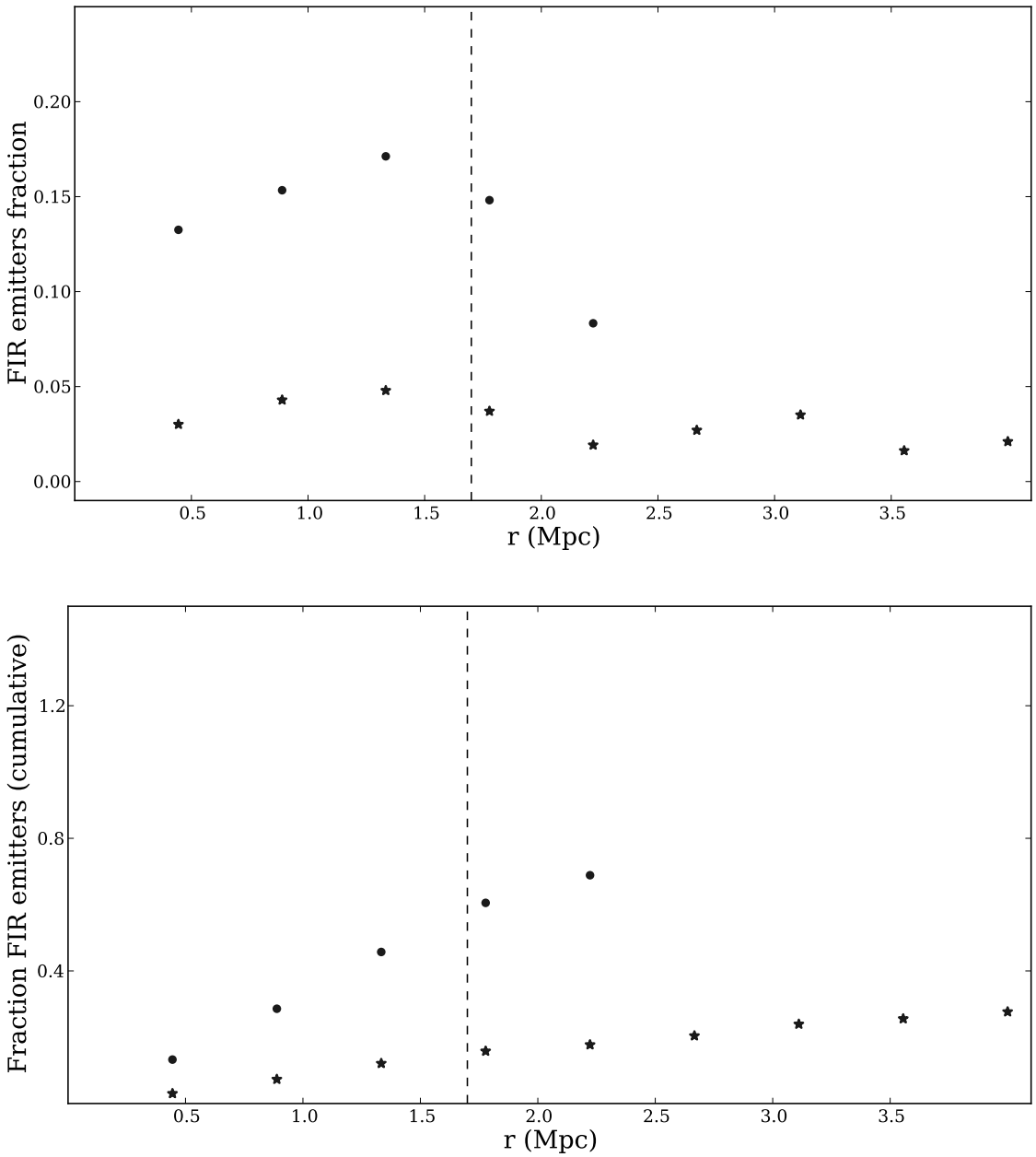

Figure 5.6: *Top:* Far infrared fraction detected by (dots) and SPIRE (stars) up to their correspondent coverage.*Bottom:* Cumulative fraction. Dashed vertical line is the virial radius.

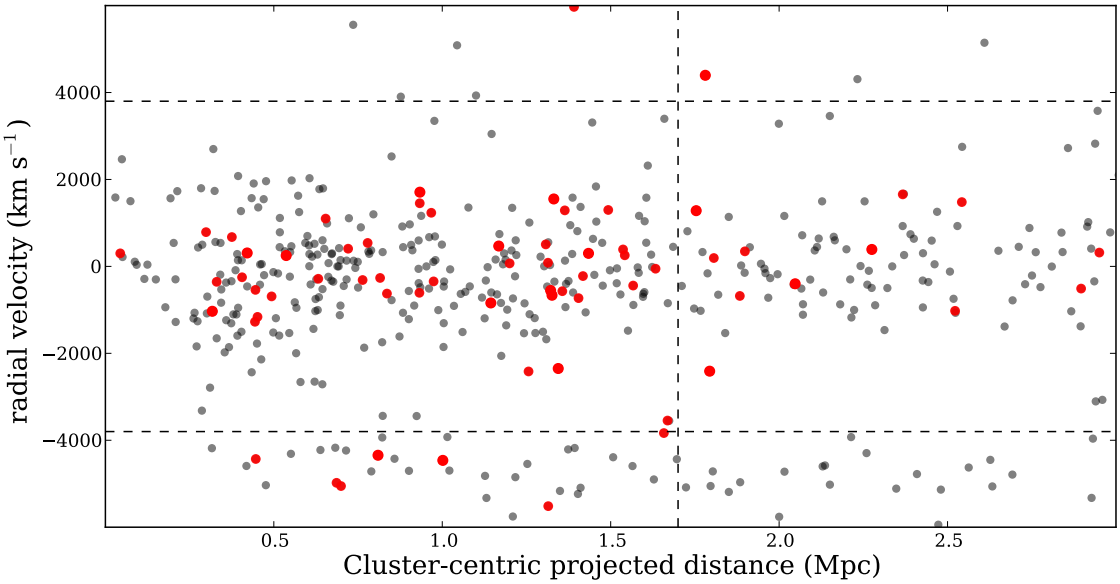

Figure 5.7: Radial velocity vs. clustercentric distance. Grey dots represents the cluster population. Red dots are the FIR emitters. The FIR fraction favours the main structure by a factor of 2.

Table 5.2 summarises the number of sources per morphological type and their infrared luminosity fraction.

Table 5.2: FIR morphology fraction

Morphological Type	N_{Total}	LIRG fraction
(1)	(2)	(3)
Elliptical	6	0.17
Disk like	10	0.26
Late Type	31	0.43
Irregular	4	0.13

Note: Col.1: Morphological classification, adapted from Treu et al. (2003). *Col.2:* Total number of FIR objects with that classification. *Col.3:* Fraction of LIRGs with that morphology.

Figure 5.8 shows the distribution of morphological types with respect to their infrared luminosities. While spirals dominates the $L_{IR} < 10^{11} L_{\odot}$ range, the relative frequency of disk galaxies increases in the LIRG domain, specially in its fainter end. This is more evident when considering the direct proportion of spiral versus ellipticals and spiral versus disk galaxies.

Figure 5.9 shows thumbnails of a variety of bright FIR sources, extracted from HST-WFPC2 observation on ZwCl0024+1652, including ELGs, AGNs and examples of different morphologies. Even in this small selection it is noticeable the high proportion of bright IR FIR sources with a close companion (nearer than 20 arcsecs). See Chapter 6 for a more detailed study.

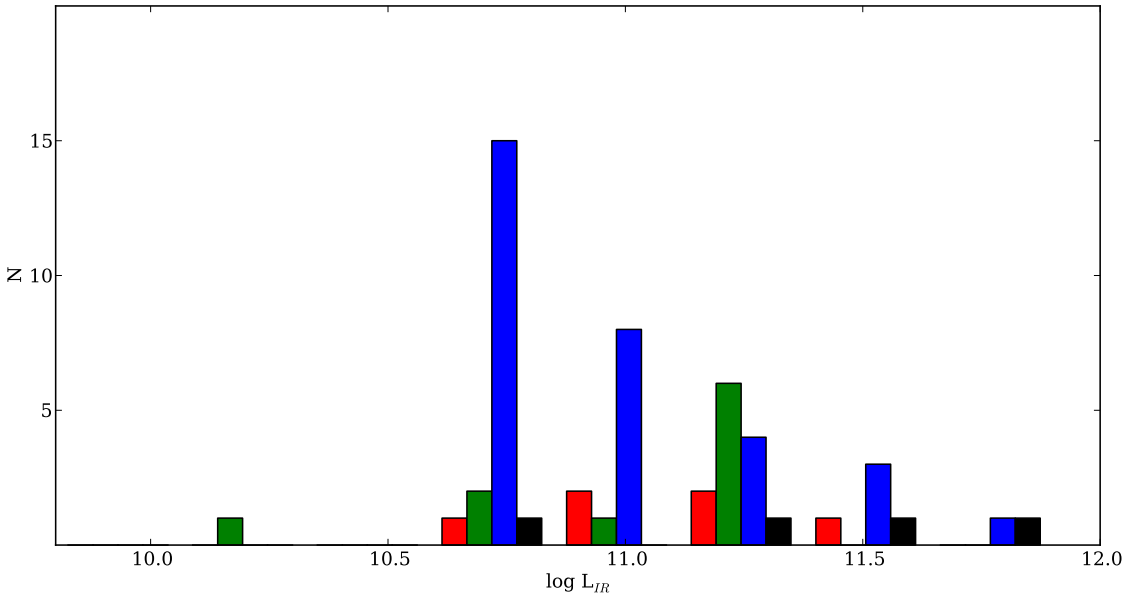

Figure 5.8: Distribution of FIR sources morphology with $L(IR)$. Blue: Late Type. Green: Disk galaxies. Red: Ellipticals. Black: Irregular. Late type galaxies dominates the sample, although fractional presence of E/S0 and S0 increases at $L_{IR} > 10^{11} L\odot$

We studied the distribution of the FIR morphological types along the cluster structure to test the traceability of the transformation region by a double indicator: high $L(IR)$ and intermediate morphologies. These two indicators may have the same physical cause but obey to different phenomenologies and time scales. The so called "dry mergers" are able to alter the morphology of the galaxies involved without interfering in their, normally low, star formation or nuclear activity. We are interested in identifying regions where the two processes are contributing simultaneously to the field-cluster mutation.

By inspecting the distribution of the FIR morphological types along the cluster structure we found a significant increase of the disk-like galaxy fraction of luminous infrared galaxies around $r_c \sim 0.9 r_{vir}$. In this region, the number of spirals is only slightly higher than that of disk morphologies (see Figure 5.10). Moreover, the fraction of disk-like galaxies with intermediate - high $L(IR)$ is remarkably higher than in any other $L(IR)$ bin (see Figure 5.8).

This suggests a significant correlation between transitional morphologies and enhanced $L(IR)$, i.e.: higher SFR or nuclear activity. This is an indicator of transformation mechanisms, approximately located at the internal edge of the virial radius, acting simultaneously on these objects and affecting both their morphological types and their internal physical processes.

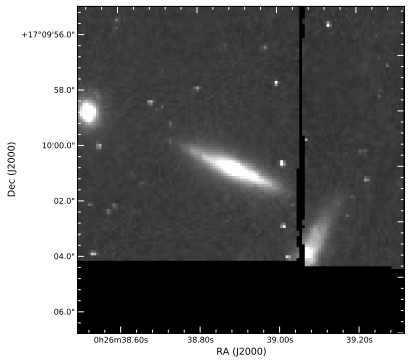

(a) Spiral galaxy. $L_{IR} = 10^{11.7} L\odot$

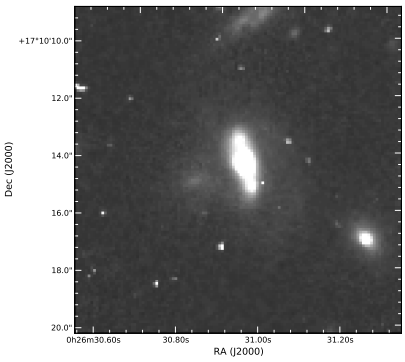

(b) Irregular galaxy (AGN, ELG). $L_{IR} = 10^{11.7} L\odot$

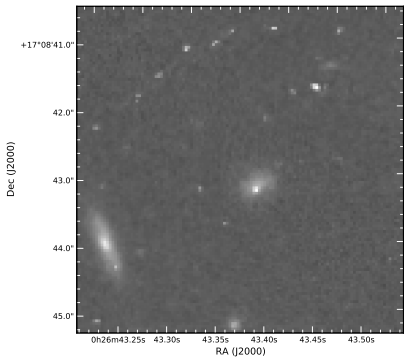

(c) Irregular galaxy. $L_{IR} = 10^{11.5} L\odot$

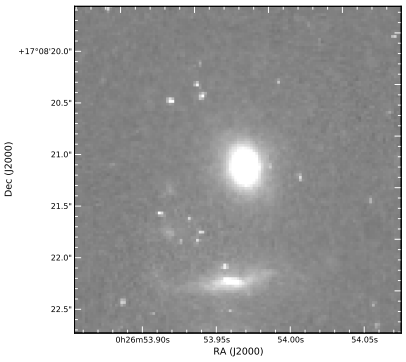

(d) Elliptical galaxy. $L_{IR} = 10^{11.4} L\odot$

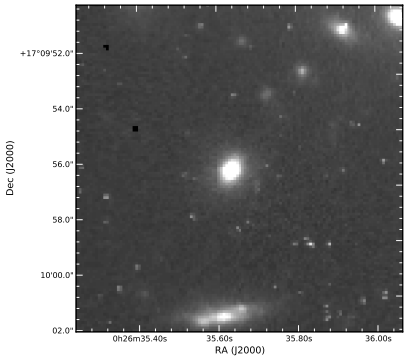

(e) Disk galaxy. $L_{IR} = 10^{11.3} L\odot$

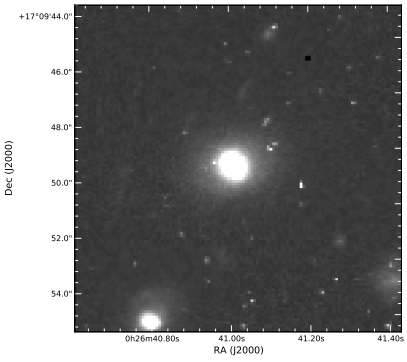

(f) Spiral galaxy (AGN, ELG). $L_{IR} = 10^{11.4} L\odot$

Figure 5.9: HST images of selected bright far infrared sources.

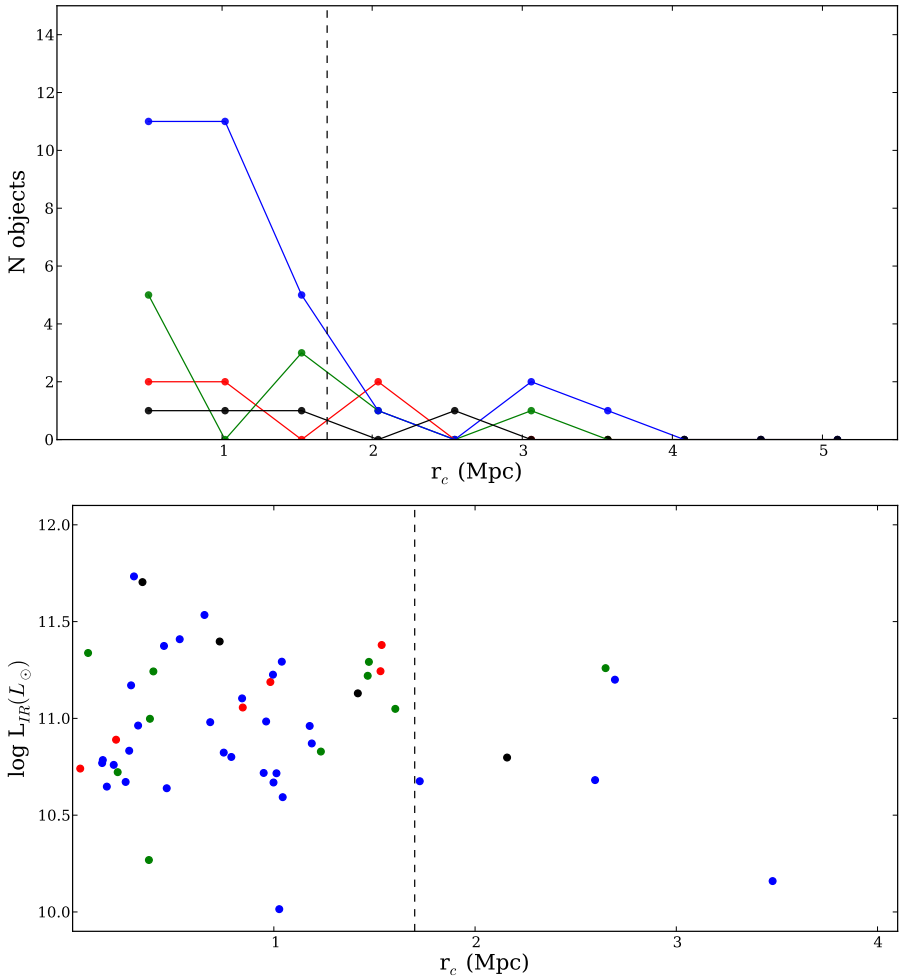

Figure 5.10: Distribution of morphological types (top) and L(IR) (bottom) for FIR population along the clustercentric distance. Blue dots and lines mark the locus of spiral galaxies and green, the disklike galaxies. Black traces the irregular galaxies and red, the elliptical ones.

5.2 AGN population

5.2.1 Introduction

The amount and characteristics of AGN in galaxy clusters are known to have a strong dependence with local and global environments, (Kauffmann et al. (2004), Gilmour et al. (2007) or Constantin et al. (2008) among others). AGNs consume cold gas to fuel their activity and therefore share with star forming galaxies the effects of the cluster on the available material. Kauffmann et al. (2004) suggests the AGNs are less common and have lower luminosities in clusters than in the field.

Eastman et al. (2007) have reported the first evidence of the rapid increase of the cluster AGN fraction in clusters with redshift up to $z \sim 0.6$, comparing fractions of spectroscopically confirmed AGNs with similar X–ray luminosities in low and high redshift clusters. Galametz et al. (2009) have quantified this increment analysing the AGN fraction using measurements of X–ray, MIR and radio AGN surface densities (up to $z \sim 1.5$). Martini et al. (2009) have shown that AGN fraction increases as $(1 + z)^{5.3}$ for AGN with $L_X > 10^{43} erg\ s^{-1}$ in hard X-rays. This study includes 32 clusters from local universe to $z \sim 1.3$, with spectroscopically confirmed AGN. On the other hand, Haines et al. (2009) finds a similar trend in the evolution of the fraction of star forming galaxy in dense environments, although in both cases the power index is still uncertain. Understanding the behaviour of active galaxies in clusters is crucial to better understand the evolution of galaxies with cosmological time and its relation with the environment.

5.2.2 AGN selection in ZwCl0024+1652

There is a number of selection techniques to identify AGNs based in different wavelengths (X–rays, optical spectra, MIR). Each of them selects different AGN populations and misses some others. For example, both X–ray and optical methods can miss AGNs due to absorption, although X-ray can find lower luminosity AGNs, and AGNs behind larger absorbing columns compared to emission–line selection criteria. Methods based in MIR are affected by the poor spatial resolution in those bands and are more sensitive to objects with high extinction in the 3 - 9 μm range. Contamination from the host galaxy (nebular emission lines, dust re-emission of young stars heat fields, high energy photons from supernovae...) also needs to be taken into account. We have applied three different methods for obtaining the AGN fraction to take advantage of the wide variety of data available: diagnostics based in emission line equivalent width and ratios in the optical, X/O selection in X–rays and MIR colour–colour diagnostics.

Optical selected AGN

Diagnostic diagrams based on flux ratios of several emission lines are efficient tools to distinguish between AGNs and SF galaxies (Baldwin et al. 1981; Veilleux & Osterbrock 1987). More recently, Stasińska et al. (2006) have shown that a classification with only Hα/[NII] is feasible and useful. In Sánchez-Portal et al. (2015), we have explored the available mechanisms to separate the population of star forming galaxies and AGNs using TF (Hα + [NII]) pseudospectra data.

We have separated Narrow-Line AGN (NLAGN hereafter) from SF galaxies using the ratio between the [N II] and the Hα lines, as per the diagnostic diagram described in Cid Fernandes et al. (2010) based in EW(Hα) and Hα/[NII] ratio. According the EWαn2 diagram, EWHα > 0.6 separates between LINERS and Seyfert galaxies. Different authors have proposed distinct conditions over Hα/[N II] ratio to discriminate SF galaxies, composite objects and pure AGN (Ho et al. 1997; Kauffmann et al. 2004; Stasińska et al. 2006; Kewley et al. 2001). After analysing results adopting

the different criteria, we have selected NLAGNs according Ho et al. (1997), i.e.: [N II]/H$\alpha \geq$ 0.6. Figure 5.11 shows [N II]/Hα vs EWHα of our ELG sample. See Sánchez-Portal et al. (2015) for a more extense discussions.

The number of NLAGNs ("classical AGNs", under Ho et al. (1997) definition) found is 39 , i.e.: 22% over the ELG population. This value is similar to our previous estimates for this cluster (20%; Pérez-Martínez et al. (2013)).

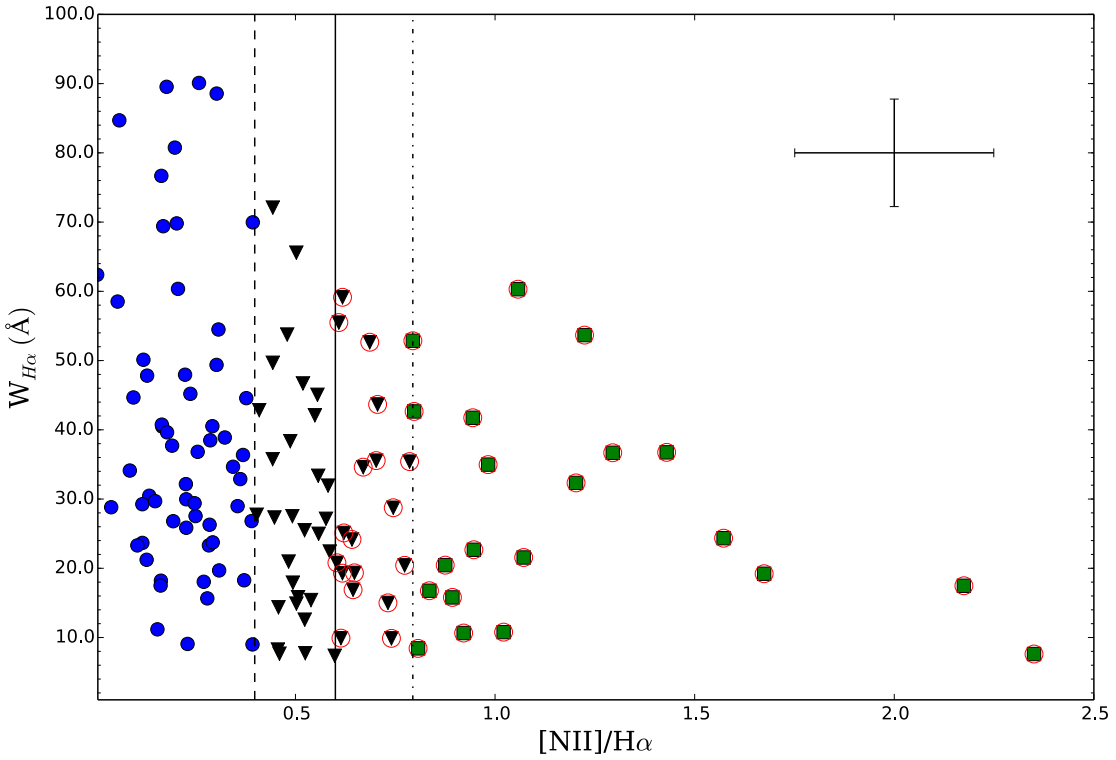

Figure 5.11: EWαn2 diagram showing pure SF galaxies according to Stasińska et al. (2006) criterion (blue dots), pure Kewley et al. (2001) AGN (green squares) and composite SF+AGN objects (black triangles). Classical AGNs as defined by Ho et al. (1997) are denoted by open red circles. The dashed vertical line corresponds to the separation criterion of Stasińska et al. (2006), the solid one to Ho et al. (1997) boundary, and finally the dashed-dotted line marks the Kewley et al. (2001) boundary. The error bars in the top right corner correspond to the median errors within our sample of ELG.

On the other hand, Broad-Line AGNs (BLAGNs), characterized by showing permitted lines with widths of thousands of kilometers per second in their spectra, were identified as well in our data. We first verified that the profiles of broad lines are well reproduced in the TF data. We simulated BLAGNs built from real spectra of local universe Seyfert 1 (3C 120, García-Lorenzo et al. 2005) and Seyfert 1.5 galaxies (NGC 3516, Arribas et al. (1997); NGC 4151, Kaspi et al. (1996)), which were displaced to the redshift of Cl0024 and convolved with the TF transmission profile. A noise component was added by drawing random values from a normal distribution with zero mean and a standard deviation equal to 10% of the difference between the peak of the pseudo-spectrum and its median value. In all generated instances of such pseudo-spectra, the broad component of the

Hα line was clearly traced. Then we performed series of simple Gaussian fit to the pseudo spectra, setting a low line width threshold of FWHM = 36Å (1180 km s^{-1}). The results of the fitting process were carefully inspected, rejecting incorrect or unclear cases (for details, see Sánchez-Portal et al. 2015). Figure 5.12 shows three instances of simulated pseudospectra and three real objects together with their best gaussian fit. 25 robust candidates BLAGNs were selected (14% over the ELG population).

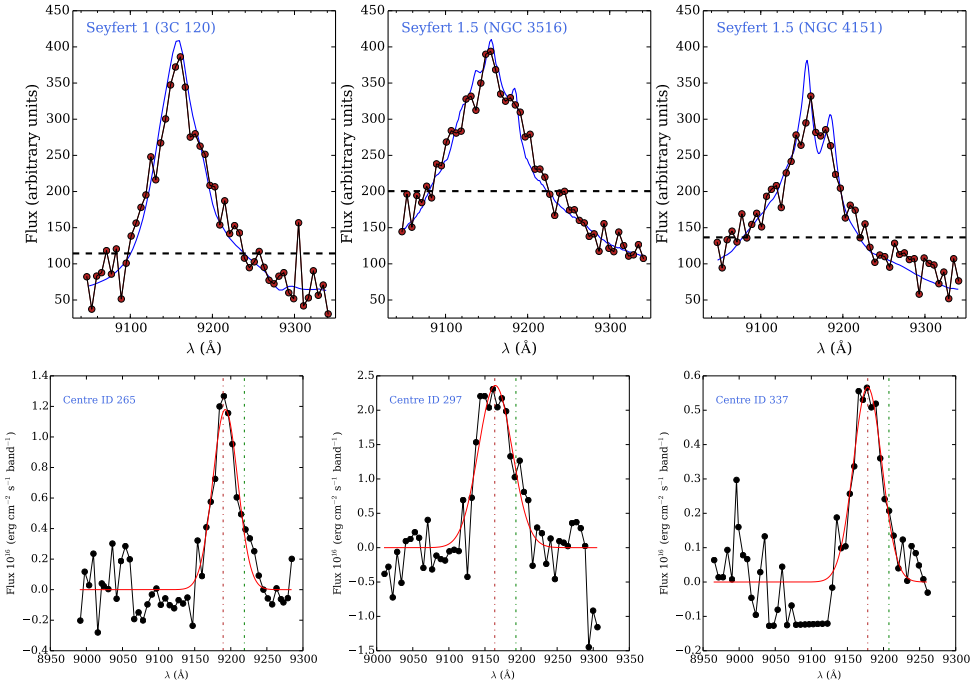

Figure 5.12: Top row: Simulated pseudo-spectra (red dots and black continuum line) over real BLAGNs redshifted to z = 0.395 (blue solid line). The dashed horizontal line denotes the median value of the pseudo-spectra. The bottom row shows actual pseudo-spectra classified as BLAGN. The red and green vertical dash-dotted lines mark the positions of the Hα and [N II] lines, respectively. The red solid line corresponds to the best fit to a Gaussian profile.

The fraction of AGNs (both BLAGNs and NLAGNs) with respect to the total number of ELGs obtained using these methods is 37%. This result is smaller than those obtained by Lemaux et al. (2010) from [O II] and Hα measurements in two clusters at a higher redshift, RXJ1821.6+6827 at z ∼ 0.82 and Cl1604 at z ∼ 0.9. These authors found that a fraction as large as 68% of the objects can be classified as AGNs (Seyfert/LINER, using Ho et al. (1997) boundaries), and that nearly half of the sample have [O II] to Hα equivalent width ratios higher than unity, the typical value observed for star-forming galaxies.

X-ray selected AGN

As already noted, AGNs are preferentially selected in X–rays, where the typical AGN outshines even the most actively star-forming galaxy. In early studies (Maccacaro et al. 1988), AGN were

found to populate a well defined region of the X–ray/optical plane, defined by an X–ray/optical flux ratio X/O = −1, where X/O ratio is defined as (Szokoly et al. 2004):

$$X/O = Log(F_X) + 0.4R + 5.71 \tag{5.1}$$

where F_X is the 0.5–2 keV flux, and R is the optical apparent magnitude in the R filter. Other works (Bauer et al. 2004 and references therein) have confirmed that the value X/O = −1 can be taken as a rough boundary between objects powered by star formation (X/O < −1) and by nuclear activity (X/O > −1). X–ray luminosities above 10^{42} erg s^{-1} are also considered as another AGN selector. This condition misses low luminosity AGNs though, so it must be used together with complementary criteria.

In this work we adopt a selection criterium of X/O ratio > -1 to flag AGNs. X-ray luminosities are extracted from Chandra and XMM-Newton public catalogs (see section 2.6). As explained before (section 3.1), there are 31 and 148 sources detected by *Chandra*–ACIS and *XMM–Newton*–EPIC, respectively in the GLACE FoV, having 8 of them a unique optical counterpart in our redshift restricted catalog. We found 6 AGNs in the cluster as per our established X/O criterion, 5 of them with a integrated X-ray luminosity > 10^{42} erg s^{-1}. Figure 5.13 shows the X–ray Luminosity ($L(X)$ hereafter) vs R band diagnostic diagram and the selection boundary. There are four ELGs with an X–ray counterpart, marked as blue stars in the plot. They are all identified as AGNs (3) or SF (1) consistently with the previous optical selection.

Mid-Infrared selected AGN

The two methods described above are sensitive to gas and dust obscuration and can miss AGNs in heavily absorbed objects. We used a complementary third diagnostic based in the characterization of the galaxy emission in the 1 μm to 8 μm range. It helps to separate those sources depending on the different SED shapes of AGNs and SF galaxies. The former are dominated by a power-law continuum up to $\lambda \sim 5$ μm, while the latter have a composite blackbody spectra that peaks at $\lambda \sim 1.6$ μm.

Stern et al. (2005) have proposed a simple empirical mid-infrared colour criteria providing a robust separation between active and normal galaxies, using [3.6]-[4.5] vs [5.6]-[8.0] colours. This method is more reliable for BLAGN (90% accuracy) that NLAGN (40% accuracy). Figure 5.14 shows this diagnostic diagram applied to our sample of cluster members (see section 3.3). There are 142 objects detected in all chanels of IRAC in our catalog, and following Stern et al. (2005) criterion, we found 8 AGNs, 4 of them included in the ELG list from Sánchez-Portal et al. (2015),

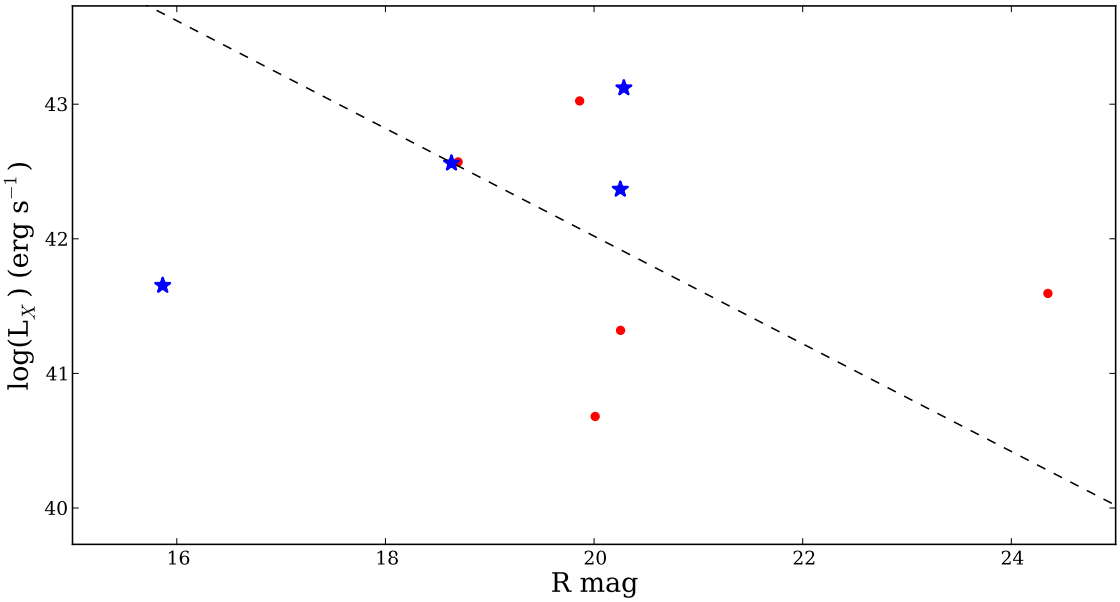

Figure 5.13: XO diagnostic diagram. Blue stars represents ELGs. Dashed line marks the boundary between AGNs and SF galaxies

although only one is identified in that work as AGN (specifically, as BLAGN).

More recently, Donley et al. (2012) have applied a new criterion, following the same arguments, but imposing stronger conditions about MIR colours. They have demostrated that for high redshifts (z > 0.5), SF galaxies can be placed in the AGN region defined by Stern et al. (2005). According with Donley et al. (2012), none of our galaxies could be classified as AGN. Nevertheless, given the intermediate redshift of ZwCl0024+1652 we decided to adopt the diagnostic in Stern et al. (2005) and accept 8 galaxies as AGNs selected according their MIR colours.

AGN selection summary

The three criteria described in previous paragraphs favour different aspects of the AGN characteristics with respect to, among others, obscuration, narrow/broad emission lines, bolometric luminosities etc and must be considered complementary.

In total we select 72 galaxies as AGNs. One of them is selected under the three criteria (Objid: 41875, see Figure 5.9b for a postcard of the object), another one is selected by both MIR and optical diagnostics (objid: 39753) and two more are identified in both X–rays and optical (objid: 44083 and 58199). 25 out of the 64 optically determined AGNs are BLAGNs (emission–line $FWHM \geq 36$Å (1180 km s^{-1}), including the object selected by the three criteria. A summary of this result can be found in Table 5.3.

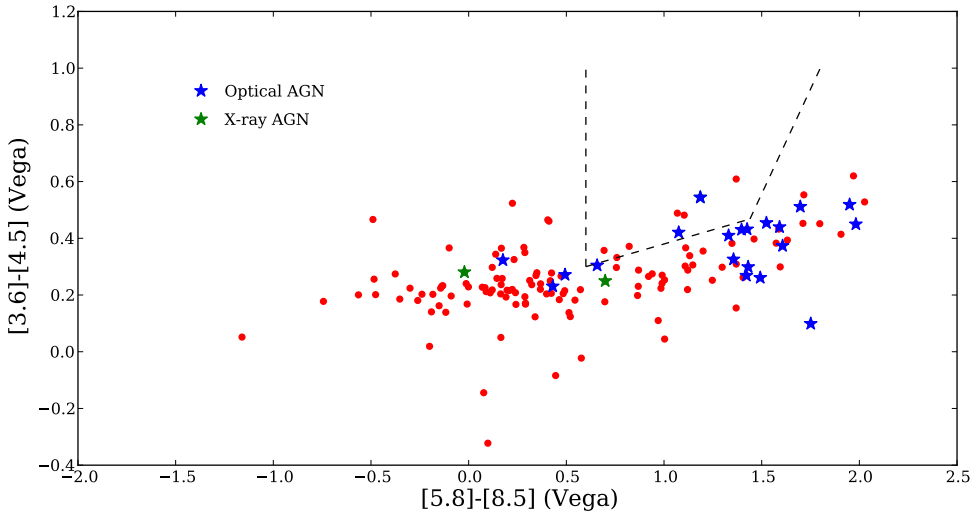

Figure 5.14: IRAC diagnostic diagram based on Stern et al. (2005) criterion. AGNs selected from optical pseudospectra (blue stars) and X–ray data (green stars) are shown. Dashed line separates MIR selected AGNs

It is worth to take into account the depth of the Hα /[N II] GLACE survey, ($f_{H\alpha} \sim 0.9 \times 10^{-16} erg\ s^{-1} cm^{-2}$) and its wide field of view (12 arcmin in diameter) with respect to the deep (5μJy and 8μJy for channels 2 and 4) but small (5.6 arcmin $\times$ 5.6 arcmin) IRAC coverage or the wide (27 arcmin in diameter) but shallow (median flux of detected sources $\sim$ 1.2 10^{-14} erg cm^{-2}/s) *XMM–Newton* maps. This is one of the major contributors to the differences in the ammount of AGNs selected in one or other method.

Table 5.3: AGN selection summary

Criterion	N_{Total}	Common with optical
(1)	(2)	(3)
ELG (BLAGN)	64 (25)	
Mid Infrared	8	2
X / O	6	3
Total	72	64

Note: Col.1: AGN selection criterion *Col.2:* Total number of objects selected by this criterion *Col.3:* Number of sources that are selected by optical criteria as well

5.2.3 AGN Fraction

AGN fraction by optical magnitudes and colour s

The selected AGN population represents a 13.5% of the total cluster members in our multiwavelength catalogue, computed as the number of AGNs over the amount of cluster members limited to the same R magnitude (24.1, the R magnitude of the faintest AGN in the sample) and area. This result is lower than that found in the same cluster in previous studies. For example, we found an AGN fraction of ∼20% over a NLAGN sample (Pérez-Martínez et al. 2013), and Sánchez-Portal et al. (2015) found a 22% fraction using only optical criteria ([N II]/Hα vs EWHα diagnostic, as detailed in Section 5.2.2).

Martini et al. (2002) studied Abell 2104, a massive cluster at $z = 0.154$, and found an AGN fraction above 5% for objects brighter than R = 20 from a deep X–ray *Chandra* observation. In Sánchez-Portal et al. (2015) we adapted this result to ZwCl0024+1652 by cutting at R≤ 22.3 and obtained a fraction of 17%. Assuming these same conditions on the catalogue presented in this thesis (see section 3.3), we obtain an AGN fraction of 15.4%, more inline with the mentioned works.

The distribution of the AGN count numbers with R band can be seen in Figure 5.15. The sample spans from R ∼ 16 to 24, peaking at 22. The overall R band distribution of cluster members peaks at 23 and reaches R ∼ 26.

The CMD, of the AGN population can be seen in Figure 5.16. We have calculated the B-R colours of our subsample and plot them against R, together with the overall cluster set. The blue cloud and the red sequence are clearly distinguishable. We fitted both components by two gaussians and defined the boundary between them as the line $B - R = k = 1.58$, where k is defined by the intersection of both curves. The AGN population fails to trace the red sequence and is clearly underrepresented in the blue cloud, favouring the so called green valley. This is specially noticeable for the NLAGNs (green bars in the figure). NLAGN and BLAGN actually follow the same trend, though. To further study the differences in behaviour between NLAGNs and BLAGNs we performed a *Kolmogorov-Smirnoff* test checking for differences in the population. The test accepts the null hypothesis that both samples are drawn from the same distribution with a p-value of 0.15.

AGN fraction by radius

To estimate the dependence of galaxy properties with the distance to the cluster centre, we decided to take as reference point the position of the BCG, in consonance with other works in this same cluster (Treu et al. 2003; Sánchez-Portal et al. 2015), although other options (caustics analysis reported in Sánchez-Portal et al. (2015), peak X–ray flux location (see section 6.1) could be have

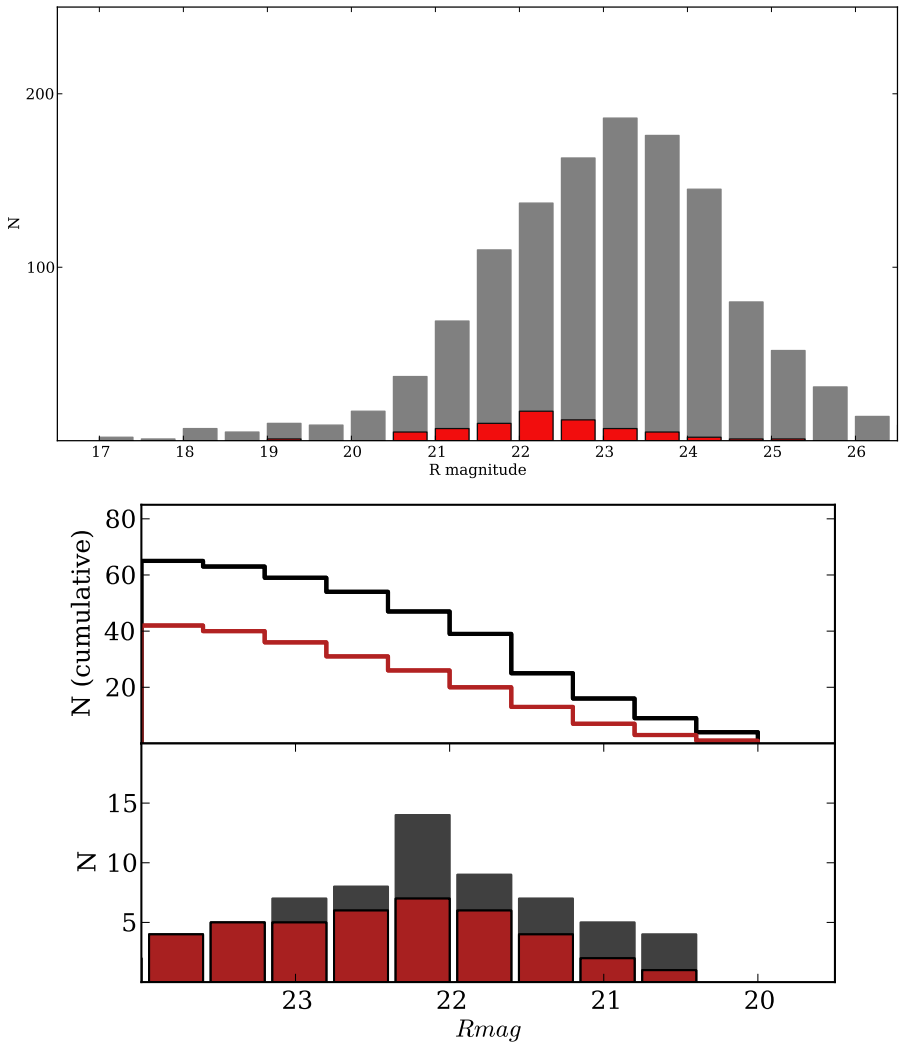

Figure 5.15: *Top:* Magnitud distribution of AGN (red bars) together with the magnitud distribution of the cluster members. *Bottom:* NLAGN(grey) and BLAGN(red) number counts per R mag bin, cummulative.(*top*) and simple (*bottom*).

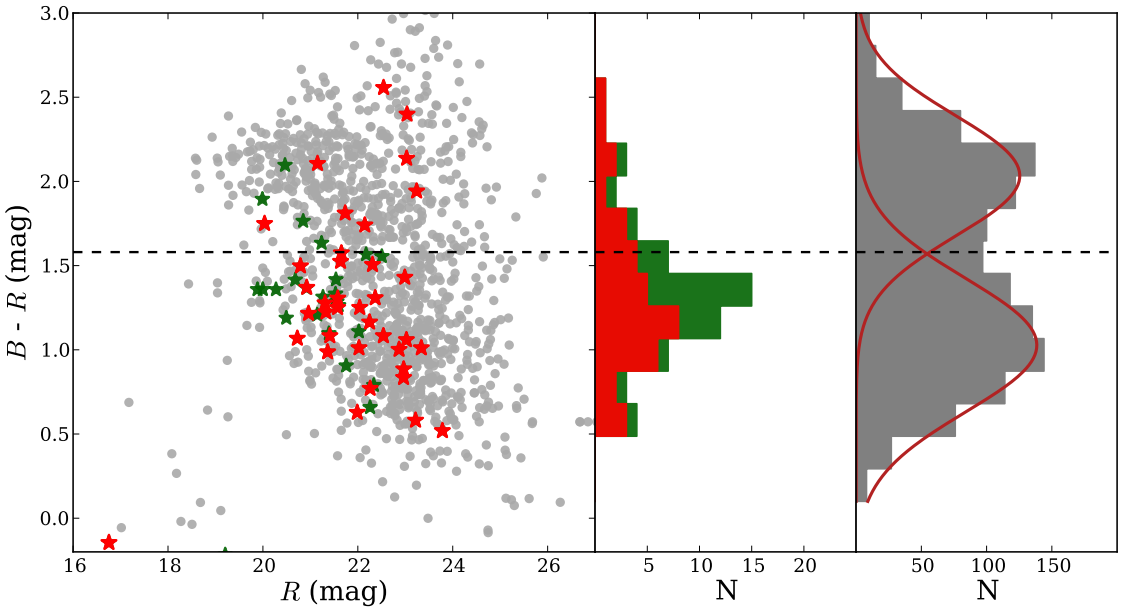

Figure 5.16: *Left:*Colour Magnitud Diagram of the AGN population. *Red stars:* BLAGN. *Green stars:* NLAGN. *Centre:* histogram of sources with ther correspondent colour . AGNs clearly favours the green valley. *Right* Histogram of cluster members.

used. In fact, varying this choice does not alter the results presented here.

We calculated the number of AGNs vs the total number of cluster sources along the clustercentric distance in bins of 20% of the r_{vir} (0.3 Mpc) (see Figure 5.17). For this calculation we considered only the circular area fully covered by OSIRIS in order to avoid incompleteness biases. We found that the fraction of AGN peaked ($\sigma \sim 2.4$) at 1.2 Mpc (~ 0.7 virial radius) and is clearly under represented in the cluster core ($\sigma \sim 3.1$).

This contrasts with what Ruderman & Ebeling (2005) report on a collection of 51 clusters from MAssive Cluster Survey (MACS) with redshifts ranging from 0.3 to 0.7. These authors find an excess of X–ray selected AGNs in the cluster cores ($r < 0.5 Mpc$), and a second overdensity at around the virial radii. Galametz et al. (2009) and Klesman & Sarajedini (2014), however, find that the concentration of AGNs peaks at 0.5-1.0 Mpc in a selection of 12 clusters at redshift 0.5 to 0.9. There is a number of factors that might explain these deviations: the difference in the selection methods, the area and depth of the observations and the effect of the number count correction applied by the referred authors, for example. In our case, all AGNs are selected from spectroscopically confirmed cluster members, and 90% of them are extracted from a deep emission line catalogue (SP15). We count as well with the largest population in a single cluster. We are therefore self confident of our results.

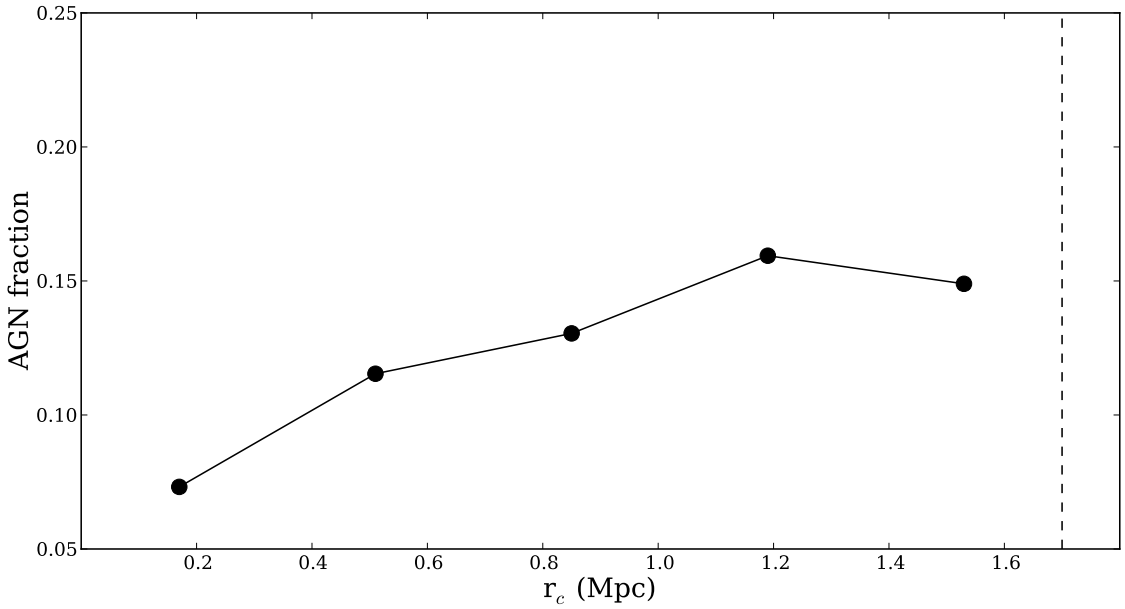

Figure 5.17: Fraction of AGN along clustercentric distance. Dashed vertical line represents the virial radius. It follows an even distribution with a peak at 1.2 Mpc ($\sigma \sim 2.4$) and an under representation at 0.2 Mpc ($\sigma \sim 3.1$).

5.2.4 AGN Luminosity distribution

Optical and Hα luminosity distribution

We built the luminosity distribution of our AGN sample in three different spectral ranges. This allowed us to trace possible differences between its characteristics and the overall cluster trends. The luminosity function also permits to trace the luminous mass of the selected sample along the cluster structure.

We started by getting the number distribution of AGNs with respect R band (see Figure 5.15). As already commented, our subset peaks at R 22, one magnitud brighter than the overall cluster population. In $L(H_\alpha + [NII])$ however, the distribution follows quite closely the general trend of the ELGs, peaking at $log_{10}(L(H_\alpha)) \sim 40.65$ In this case, the maximum emission falls in $log_{10}(L(H_\alpha)) = 40.75$. This is consistent with previus works done on the same cluster (Sánchez-Portal et al. 2015) over the whole Hα emitters (Figure 5.18)

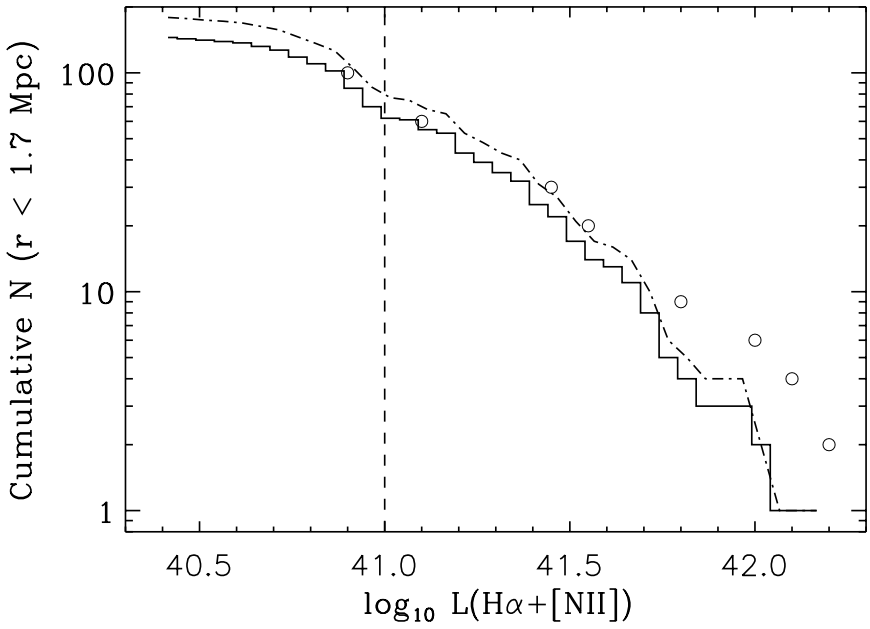

(a) *Top:* $L(H_\alpha)$ function of Hα emitters (Sánchez-Portal et al. 2015)

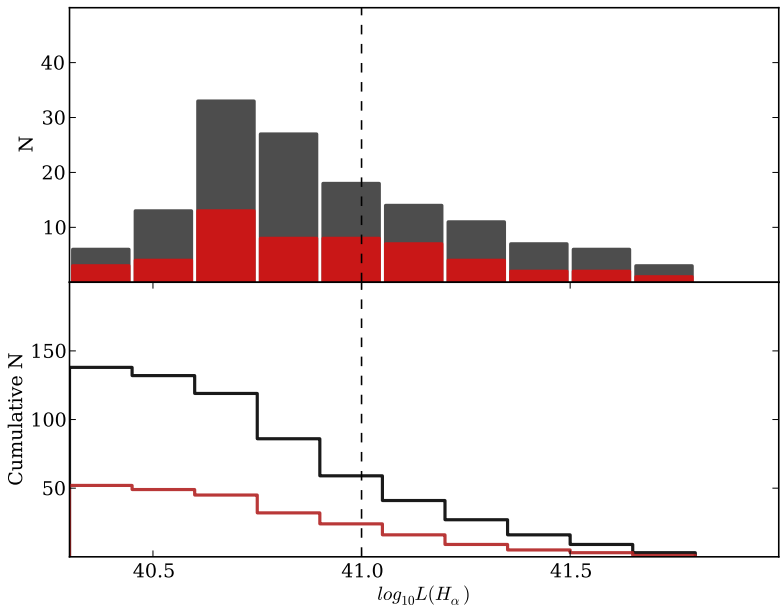

(b) *Top:* $L(H_\alpha)$ function of AGN (grey bars). Red lines marks the luminosity distribution of the BLAGNs *Bottom:* Cummulative number counts per magnitude bin.

Figure 5.18: $L(H_\alpha)$ function of AGN

Infrared luminosity function

We use the infrared luminosity function, $L(IR)$, to unveil the obscured activity in cluster galaxies. As dicussed in Section 5.1, $L(IR)$ is a particularly good tracer of enhanced activity driven by the transformation mechanisms taking place along the infall in the cluster estructure. We have calculated the $L(IR)$ of the selected AGNs by fitting their photometric points with a combination of optical SED libraries from Polletta et al. (2007) and infrared models from Chary & Elbaz (2001) using *Le PHARE* (see Chapter 3). The $L(IR)$ obtained is preferred over the calculated over direct fit of the 24μm to the same libraries (see Section 5.1.2 and Figure 5.3 therein).

We obtained $L(IR)$ values for those objects with at least one photometric point between 8μm and 500μm (50 out of 72) in our AGN sample. Figure 5.19 shows the number count distribution per $L(IR)$ bin for both the AGN population and the overall cluster objects. The AGN sample fulfilling previous condition perfectly follows the general distribution, peaking both at $log_{10}(L_{IR}) \sim 10.8 L_{\odot}$. All these AGNs are noticeable IR emitters (i.e.: $log_{10}(L_{IR}) \geq 10.0 L_{\odot}$), with 13 of them qualifying as LIRGs.

Ultraviolet luminosity distribution

We also calculated the integrated ultraviolet luminosity $L(UV)$ of the AGN subsample to achieve a complete view on the galaxy activity. The typical SEDs of AGNs show a flux increment between the optical and soft X–ray spectral ranges, the so called *big blue bump*, that concentrates more than half of the bolometric luminosity of an un-obscured AGN (Wilkes 1999). Together with this, a bump in the infrared due to thermal dust reemission is also observed. On the other hand, UV luminosity provides a direct observation of the recent and ongoing star formation activity, helping to distinguish pure AGNs from composite objects. Our sample contains 22 objects with UV detections from which we have estimated the $L(UV)$ as per equation 5.2:

$$L_{UV} = 4\pi D_L^2 \times F_{UV} \times \nu_{RF} \tag{5.2}$$

where F_{UV} is the observed flux at the selected UV band, D_L is the luminosity distance set to the cluster redshift, and ν_{RF} is the restframe effective frequency of the photometric band ($\mu_{RF} = \mu/(1+z) = c/\lambda_{RF}$).

The ultraviolet luminosity distribution ranges from $10^9 L_{\odot}$ to $10^{10.2} L_{\odot}$ with a flat number count distribution. This small ultraviolet luminosities are consistent with what Domínguez Sánchez

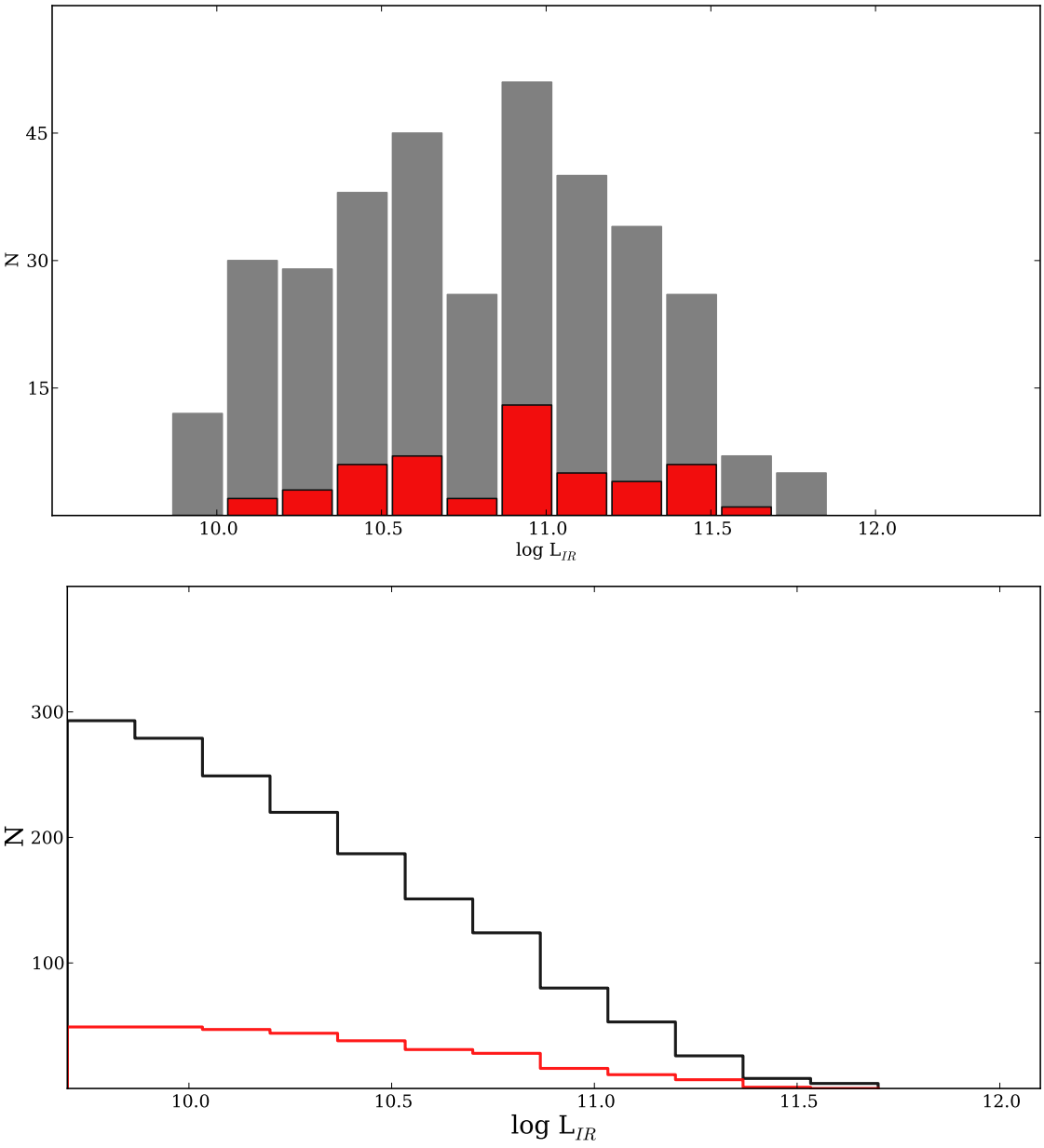

Figure 5.19: L_{IR} distribution of AGNs. *Left*: L_{IR} distribution. *Right:* L_{IR} distribution of AGN (grey bars). Red bars and line mark the luminosity distribution of the AGNs versus the overall population.

et al. (2014) found for the distribution of L_{UV} for AGNs in an SDSS survey up to $z \sim 0.4$.

5.2.5 AGN Morphology

We have morphological classification of 38 objects in our AGN sample from Treu et al. (2003), obtained by analysing WFPC2 - HST maps reaching $I_{AB} \sim 25$. In that work, Treu *et al.* limitted their study to objects brighter than $I_{AB} \sim 22.5$ to guarantee enough S/N to produce a reliable result.

We rebin their morphologies in four types: Ellipticals, (E), equivalent to type 0 in Abraham et al. (1996), Disk (E/S0), equivalent to types 1 and 2 (E/S0 and S0), Late Type, comprising types 3 to 6 (different kind of spirals) and Irregular, correspondent to types 6 to 8 in the referred work. The AGN population clearly favours late type galaxies (23 out of 38) versus pure ellipticals (2 out of 38). There are 8 disk galaxies (E/S0 and S0) in the sample. This proportion holds in the AGN-LIRGs subsample for which we have morphological information (11 out of 13).

A summary of these result can be found in Table 5.4.

Table 5.4: AGN morphology fraction

Morphological Type	N_{Total}	LIRG fraction
(1)	(2)	(3)
Elliptical	2	0.0
Disk like	8	0.27
Late Type	23	0.45
Irregular	5	0.09

Note: Col.1: Morphological classification, adapted from Treu et al. (2003).*Col.2:* Total number of AGN objects with that classification. *Col.3:* Fraction of LIRGs with that morphology

The fraction of the different morphological types along the clustercentric distance is depicted in Figure 5.21. The numbers are only significative within the virial radius due to the lack of uniform coverage beyond that limit. Any way, and taking into account the small number statistics, there is a noticeable increase in the number of transitional morphological types around r_{vir}, where the effect of the cluster environment on infalling galaxies enhances the mutation of late type galaxies into E/S0s.

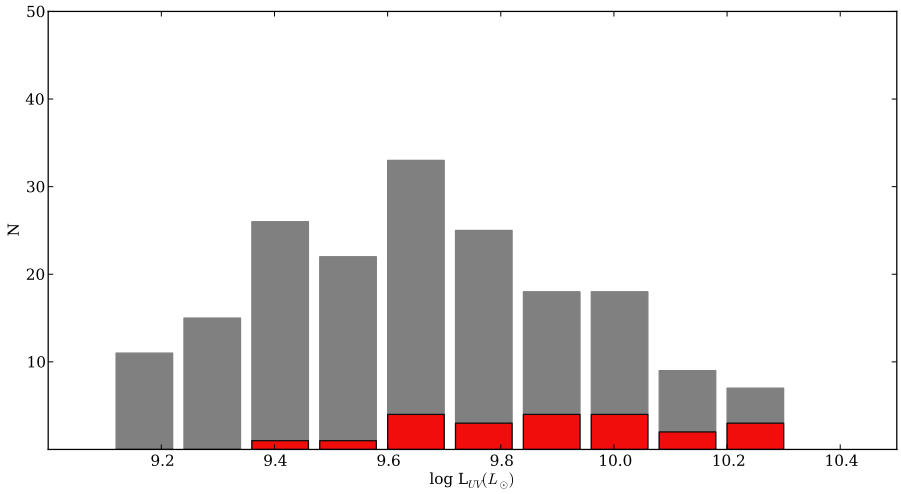

(a) L_{UV} distribution of AGNs in the NUV band. Cluster members (grey bars) and AGNs (red bars)

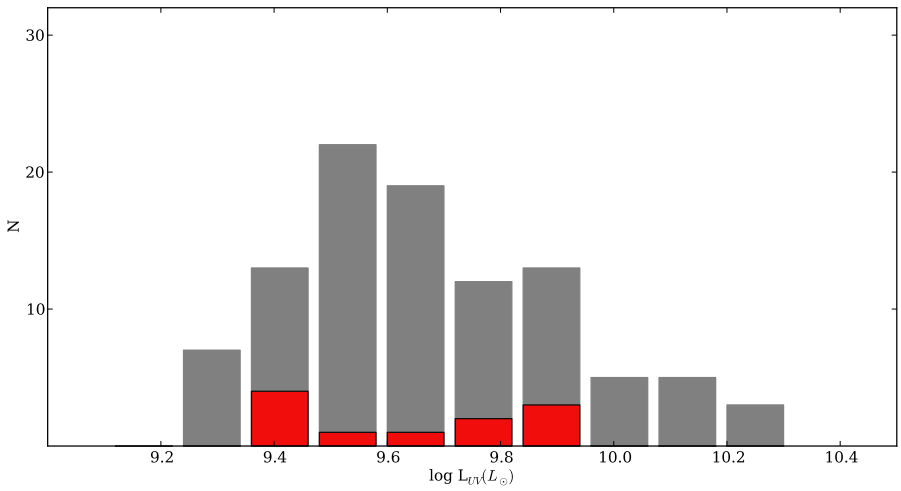

(b) L_{UV}distribution of AGNs in the FUV band: Cluster members (grey bars) and AGNs (red bars)

Figure 5.20: Ultraviolet luminosity distribution of AGNs

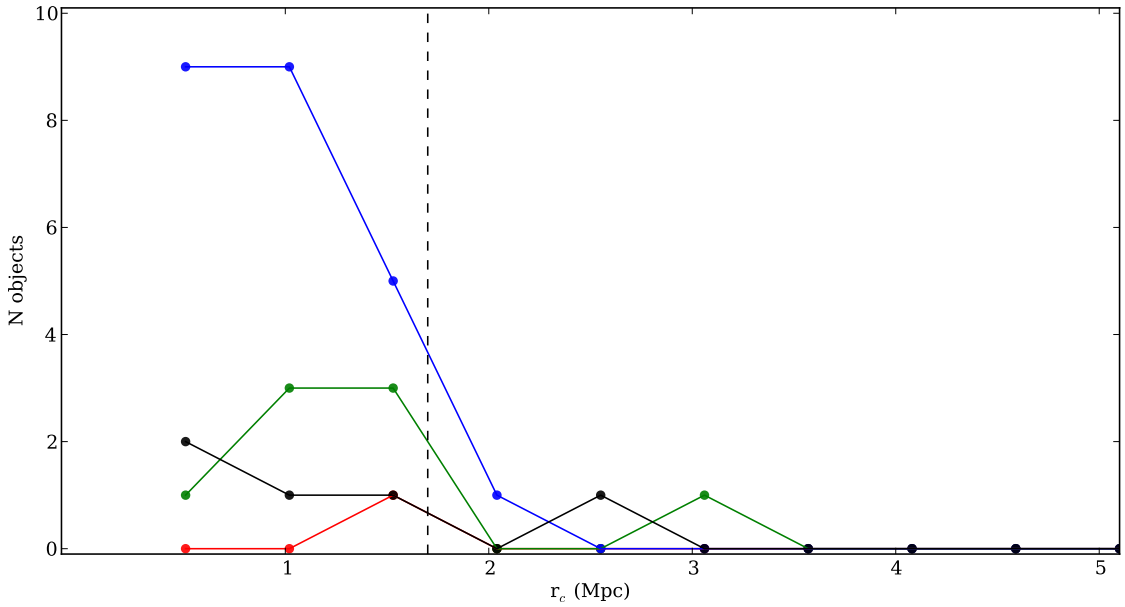

Figure 5.21: AGN morphological distribution with clustercentric distance. Blue line marks the spiral galaxies, while green one marks the disk-like objects. Black and red traces the irregular and elliptical galaxies respectively.

5.3 Star Forming population

5.3.1 Introduction

We call *star forming galaxies* to objects with both significant and passive star formation rates or even quiescent, that do not show evidences of harbouring an AGN. They form the bulk of the cluster population and their characteristics mark those of the members. We do, however, make a distinction among them depending on whether or not they are emission line galaxies, since this subsample represents the population with higher chances of actually having high SFR.

5.3.2 Luminosity distributions

Optical luminosity distribution

Number counts of the star forming population with respect R-band follows a smooth distribution peaking in 22.5, and reaching up to $R \sim 26.5$. The ELG subsample follows the same trend with only a narrower magnitude range, due to the differences in depths of M05 and SP15 catalogs. See

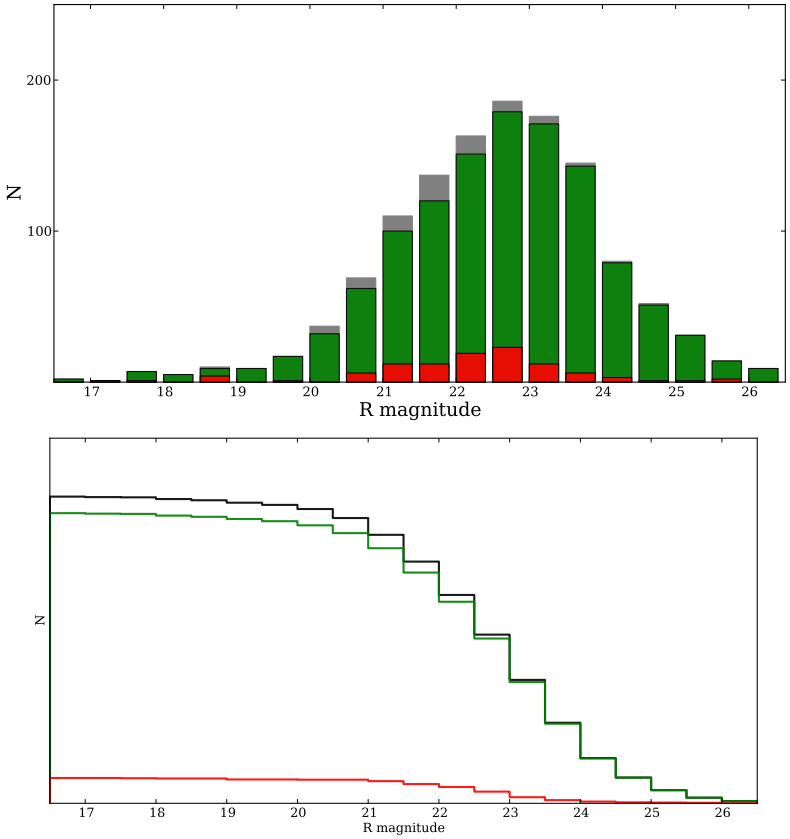

Figure 5.22: *Top:* Magnitud distribution of star forming galaxies (green bars) together with the magnitud distribution of the cluster members. Magnitud distribution of ELGs selected in Sánchez-Portal et al. (2015) are also shown (red bars) *Bottom:* Cummulative counts per mag bin.

Figure 5.22.

We plotted the colour–magnitude diagram for SF in the cluster. The K-correction was applied to the magnitudes from M05 by means of `kcorrect v4_2` (Blanton & Roweis 2007). Fig. 5.23 shows the rest-frame $B - R$ vs. R. The bi-modality in the distribution of optical colours is clearly noticed, with a well developed red sequence. We defined a boundary between the red sequence and the blue cloud as the intersection of the Gaussian functions resulting from the fit to each colour peak: $B - R = 1.58$.

When focusing on objects with active star formation (see Figure 5.24), ELG population dominates the blue cloud in the CMD. ELGs with infrared luminosity are shifted towards the green valley. Non infrared emitters ELGs seat predominantly in the bluer area. Infrared galaxies without emission lines preferentially populate the red sequence.

This smooth transition is an indication of the galaxy reddening being due to dust and gas re-emission, rather than to intrinsic red colours of the infrared population. The Hα flux tracing star formation activity is clearly visible in the blue cloud, and gradually absorbed with increasing dust

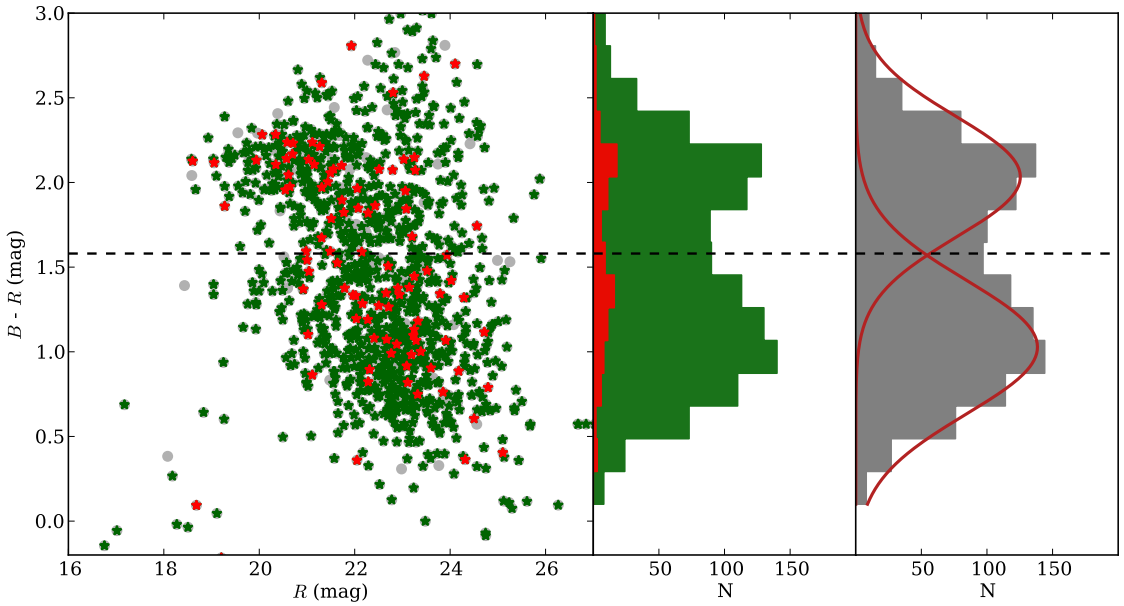

Figure 5.23: Colour magnitud distribution of star forming galaxies. Red stars/bars are emission line galaxies. Grey dots/bars are AGNs.

and gas contents (green valley) until it is completely obscured and its photons re-emitted in the infrared.

The radial velocity - clustercentric distance diagram (Figure 5.25) shows the concentration of red sequence objects in the internal part of the cluster main structure. The blue cloud galaxies are spread across both components, the main one and the line-of-sight infalling group, increasing its fractional presence in the second structure and with larger distances. This fully agrees with the general picture of typical cluster core galaxies being red objects, with the blue population having spent less time within the environment influence. The overpopulation of blue sources in the infalling group indicates an enhanced nuclear and star forming activity due to the collision with the ICM.

L_{IR} luminosity function

We have inspected the $L(IR)$ distribution of the star forming sample (see Figure 5.26). The full L_{IR} span is traced by the SF population, where the ELGs show smaller values of the infrared luminosity, specially noticeable in the bright end, with a relative subrepresentation of ELGs in the LIRG region. This is consistent with what Koyama et al. (2010) reports on.

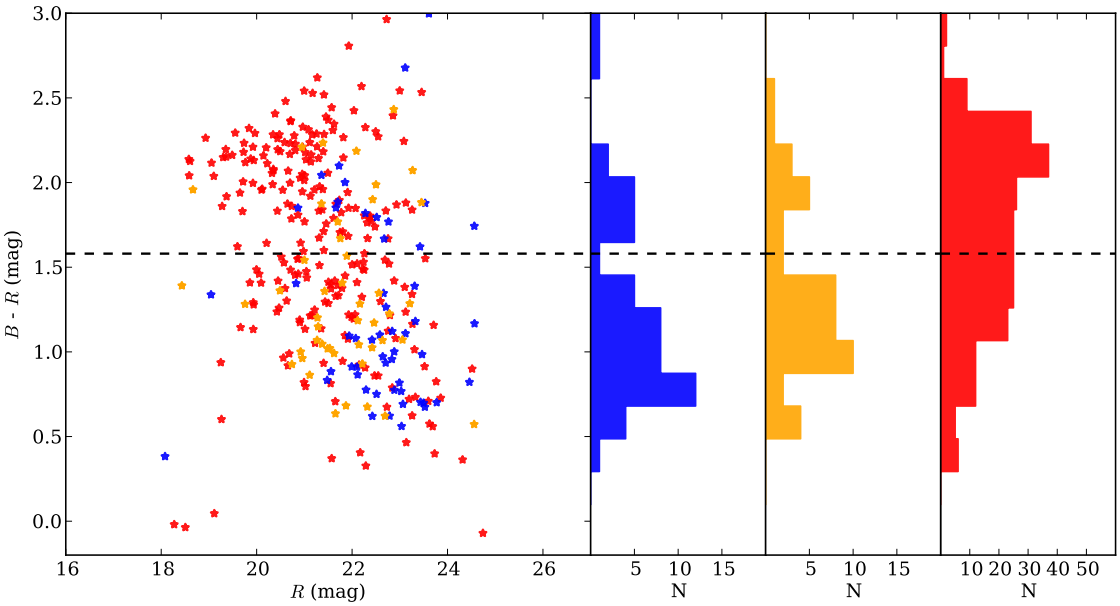

Figure 5.24: Colour magnitud distribution of galaxies with active star formation. Red stars/bars are infrared objects without emission lines. Orange stars/bars are ELG - infrared objects. Blue stars/bars are ELGs with no infrared emision.

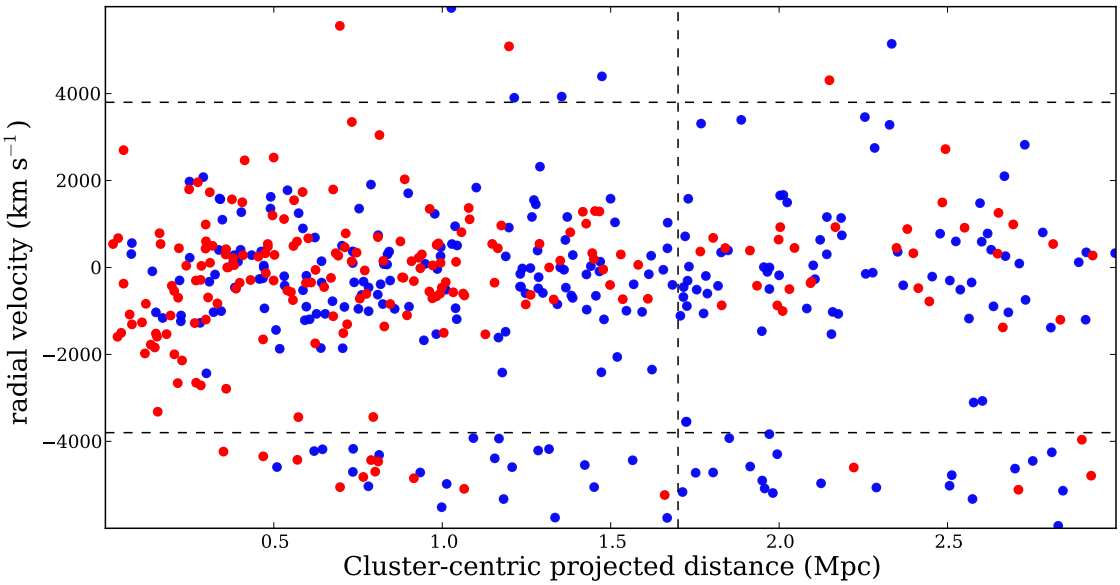

Figure 5.25: Radial velocity versus clustercentric distance of the SF population. Red dots are the red sequence objects. Blue dots are the blue cloud galaxies. Red galaxies dominates the internal region of the main cluster structure. The fraction of blue galaxies in the line-of-sight infalling group is consistent with enhanced star forming activity due to the collision with the cluster (see text).

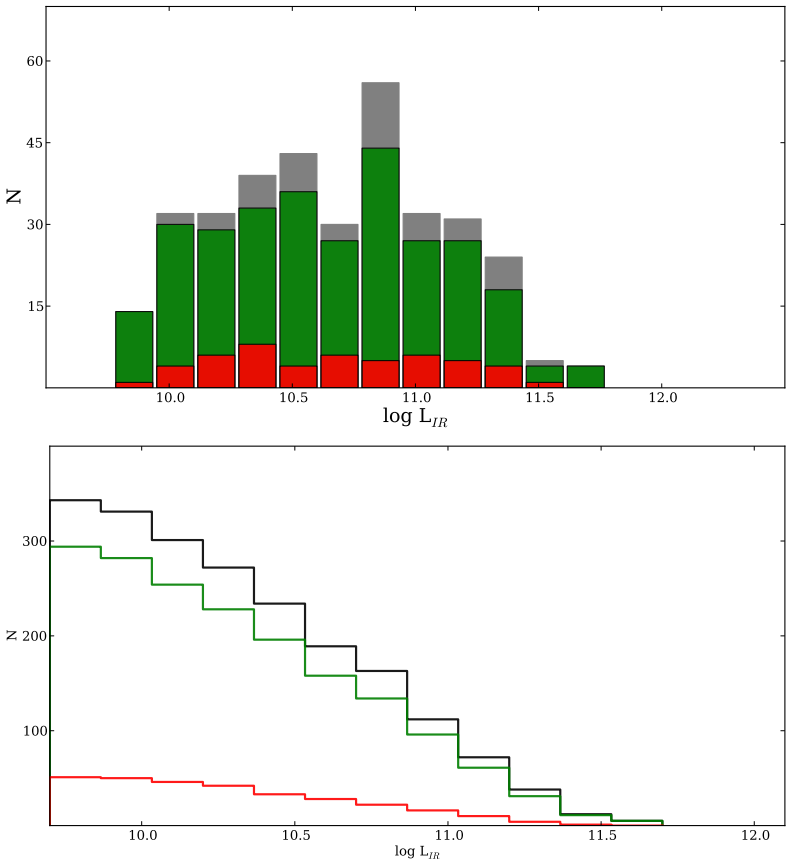

Figure 5.26: L_{IR} function of star forming galaxies. *Top*:L_{IR} distribution *Bottom:* L_{IR} function of ELGs (red bars). Green bars mark the luminosity distribution of L_{IR} SF vs the overall population (grey bars).

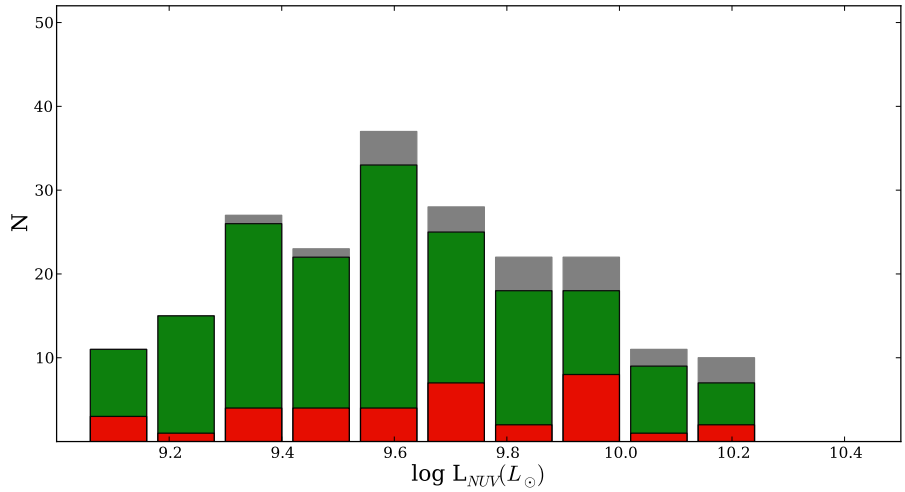

(a) L_{UV} function SF (NUV)

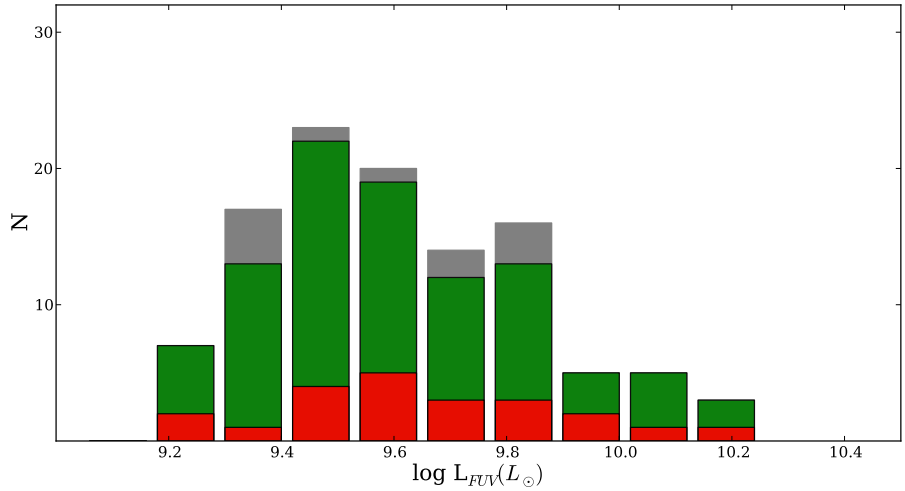

(b) L_{UV} function SF (FUV).

Figure 5.27: L_{UV} function of SF galaxies, both L_{FUV} and L_{NUV}. Colors bars are the same than in Fig 5.26

Ultraviolet luminosity function

The ultraviolet luminosity function traces the current star formation in the galaxies. Our sample shows a smooth distribution peaking at 9.4 and 9.5 in the NUV and FUV bands respectively (see Figure 5.27). The ELG population shows slightly higher luminosities (peaks in both bands and fraction in 9.5 and 9.8 respectively), indicating significant ongoing star formation traced by both the Hα spectral line and the UV luminosity.

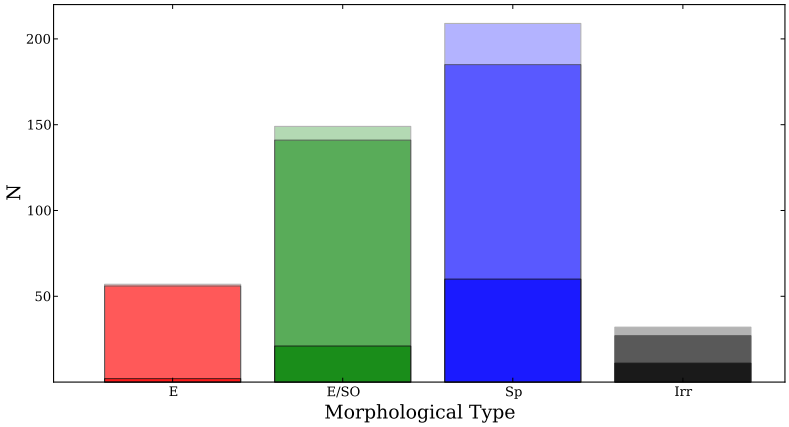

Figure 5.28: Morphological separation for all cluster members (lightest colors), SF galaxies (medium color) and ELGs (darkest colors)

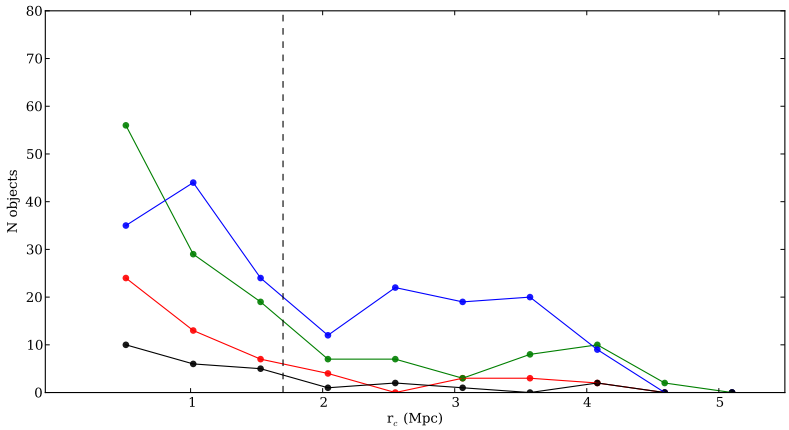

Figure 5.29: Star forming morphological fraction with clustercentric distance. Blue line marks spiral galaxies, while green depicts disklike objects. Red traces elliptical galaxies and black are the irregular ones.

5.3.3 SF Morphology

We have morphological classification for 409 out of 1193 objects. As depicted in Figure 5.28, the sample favours spirals and disk like galaxies. It is significant the underrepresentation of ELGs in the elliptical group, as expected, and the higher fraction of ELGs in the late type and irregular morphological types.

The fraction of the different morphological types of star forming galaxies along the clustercentric distance is depicted in Figure 5.29. The presence of transitional morphological types in the inner core dominates the morphological fraction landscape, with increasing weight of late type galaxies at r_{vir} and beyond. This scenario suggests that the effect of the cluster environment on the galaxy morphologies, transforming the field spirals into cluster elliptical / lenticulars has already taken place at $0.5r_{vir}$, as suggested by Treu et al. (2003) and many others.

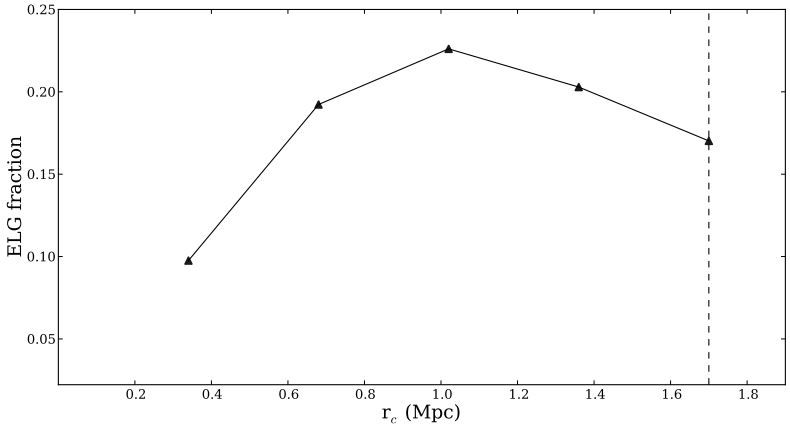

Figure 5.30: Fraction of ELGs along cluster centric distance.

5.3.4 ELG fraction

We obtain the fraction of star forming ELGs, in the same way that the number de AGNs vs the total number of cluster sources, using same bins in cluster centric distance (Fig5.30). ELG emitters fraction is minimum near the cluster core, similarly to the work of Koyama et al. (2010), that found that Hα emitters avoid cluster central region and/or high density regions. On the other hand, the ELG fraction increases in the intermediate region of the cluster ($\sim$ 1 Mpc). Pintos-Castro et al. (2013) have suggested a similar result at z$\sim$ 0.8 in RXJ1257.2+47.8.

5.3.5 Star formation rate

One of the main properties of a galaxy is its star formation rate. This activity is as well a direct probe of the status and transformational processes taking place in different areas of the cluster and is directly linked to the environmental effects on the galaxy evolution. An accurate calculation of the SFR in cluster galaxies is key to understanding such evolution and the process influencing it.

There are several star formation indicators, each of them sensitive to different galaxy characteristics. The population of young stars in a galaxy emits a radiation field that peaks in the UV and that can be directly observable. However several obscurization procesess inside the galaxy may hinder those high energy photons. The dusty environment where the star formation takes place absorbs a significant ammount of such radiation, re-emitting it in different infrared ranges, from rest frame 4-8 μm by PAHs to hot–warm dust grains at 24μm and FIR emmiting cold dust.

In this work we followed three different methods of SFR estimation: From L(Hα), $L(IR)$ and $L(UV)$

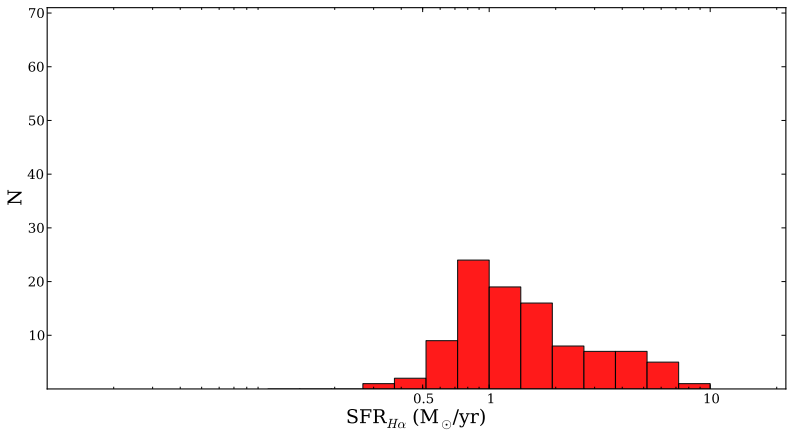

Figure 5.31: Distribution of SFR obtained from Hα.

For ELG galaxies, we have computed the star formation rate applying the standard luminosity-SFR conversion from Kennicutt (1998), and correcting to the initial mass function (IMF) from Chabrier (2003). In Sánchez-Portal et al. (2015), we have used a standard value for extinction of 1 magnitude. In this thesis, we have derived the Balmer decrement for our ELG sample using TF Hβ data (see Chapter **??**). The value of the calculated correction is of 1.41 magnitude of extinction at the line.

$L(IR)$ is not sensitive to dust extinction, it is in fact the direct effect of the extinction as an energy re-processing and re-emission mechanism. Both L_{UV} and L(Hα) do suffer from extinction, and the SFR estimated from then must be corrected from this effect.

In fact, the total SFR comes from adding the value calculated from $L(UV)$ and that derived from $L(IR)$, although the contribution from L_{UV} is frequently neglible with respect to the former. (Oteo et al. 2011; Buat et al. 2010)

Following Kennicutt (1998), and using the IMF from Chabrier (2003), the relation between the star formation rate and $L(IR)$ (integrated from 8 to 1000μm) is:

$$SFR_{IR}(M_{\odot}yr^{-1}) = 4.5 \times 10^{-44} L_{IR}(ergs^{-1}) \tag{5.3}$$

Figure 5.32 shows the distribution of L_{IR} for the SF cluster galaxies and ELGs (red). They peak at 3.7 and 2.7 $M_{\odot}yr^{-1}$. The mean values are 4.5 and 5.2 $M_{\odot}\ yr^{-1}$ for SF and ELGs respectively.

More massive stars emit the bulk of their energy in the ultraviolet and have shorter lives than the

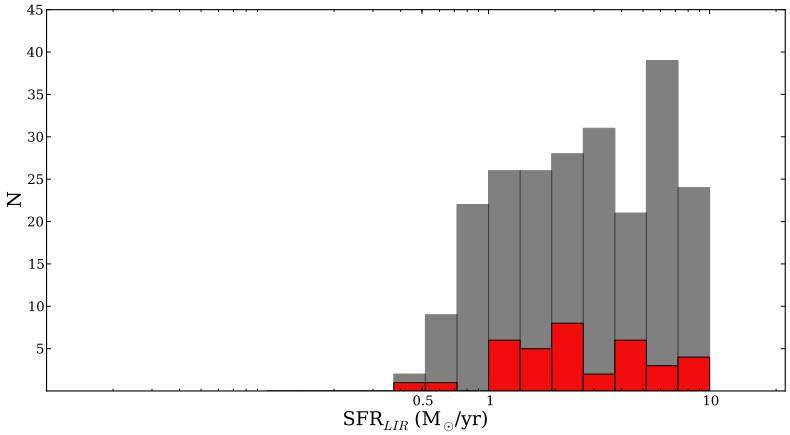

Figure 5.32: SFR obtained from L_{IR}. All SF galaxies with L_{IR} are included (grey bars). ELGs are represented in red color bars.

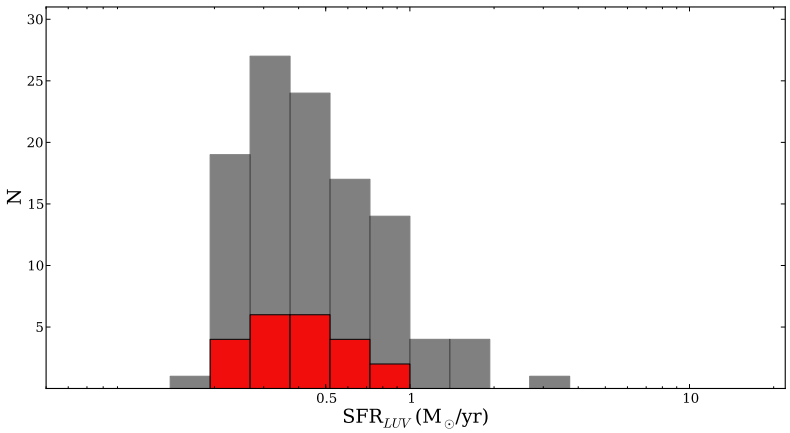

Figure 5.33: SFR obtained from L_{UV}. All SF galaxies with m_{FUV} are included (grey bars). ELGs are represented in red color bars.

typical galaxy age. The ultraviolet spectral range is dominated by young massive stars. Therefore the star formation rate is directly related to the L_{UV}. There are several empiric relations between L_{UV} and SFR. In this work we adopt the calibration described in Kennicutt (1998) with an Initial Mass Function as used in Chabrier (2003):

$$SFR_{UV}(M_{\odot}yr^{-1} = 1.4 \times 10^{-28} L_{UV}(ergs^{-1}) \tag{5.4}$$

SFR obtained from $L(UV)$ are significantly lower than those derived from $L(IR)$, peaking in 0.2-0.3 $M_\odot$ yr^{-1}, with a mean value for both samples ~0.35 $M_\odot$ yr^{-1}.

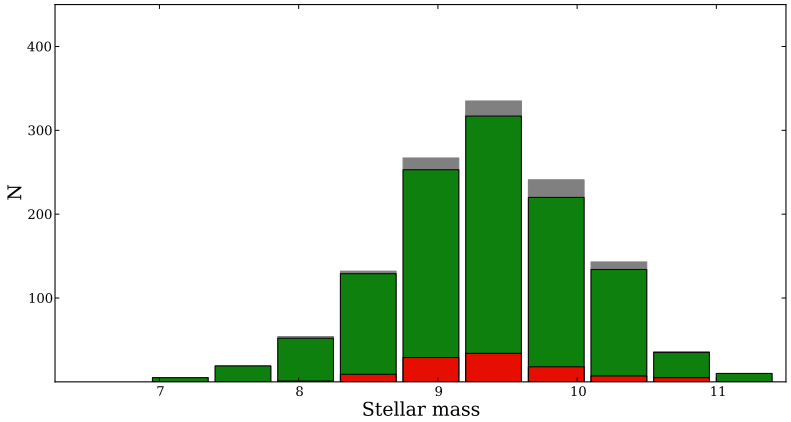

Figure 5.34: Stellar masses obtained from LePhare fitting. All SF galaxies are included (grey bars). ELGs are represented in red color bars.

5.3.6 Stellar Masses

The stellar mass, M_*, is a key element in the study of the evolution of galaxies. Some authors have reported a correlation between the SFRs and M_* in galaxies with star formation activity at local redshift (Peng et al. 2010). The so called "main sequence" has also been observed at further distances (Whitaker et al. 2012, and refereces therein) and is suggested to be independent from the environment (Peng et al. 2010). Sobral et al. (2010) have performed an Hα survey up to $z \sim 1$ finding the stellar mass as one of the main indicators of star formation activity. At the same time they propose the environment as the main responsible for star formation quenching in galaxy clusters.

We obtained the stellar masses of our star forming sample from *Le PHARE*, using BC03 templates as model for the best fit algorithm. The inferred values span from 6.55 $M_\odot$ to 11.83 $M_\odot$ for the overall SF population. The emission line galaxy subsample has stellar masses between 7.8 $M_\odot$ and 11.0 $M_\odot$. Both sets peaks in 9.45 $M_\odot$.

One method of separating star forming galaxies from quiescent objects is by locating them in either the red sequence or the blue cloud (Ilbert et al. 2013). Figure 5.35 displays both populations, with the boundary established in 1.58, and the dependence between the stellar mass and the B-R colour. Passive population are mostly massive objects with $log_{10}(M_*/M\odot) \geq 10.0$.

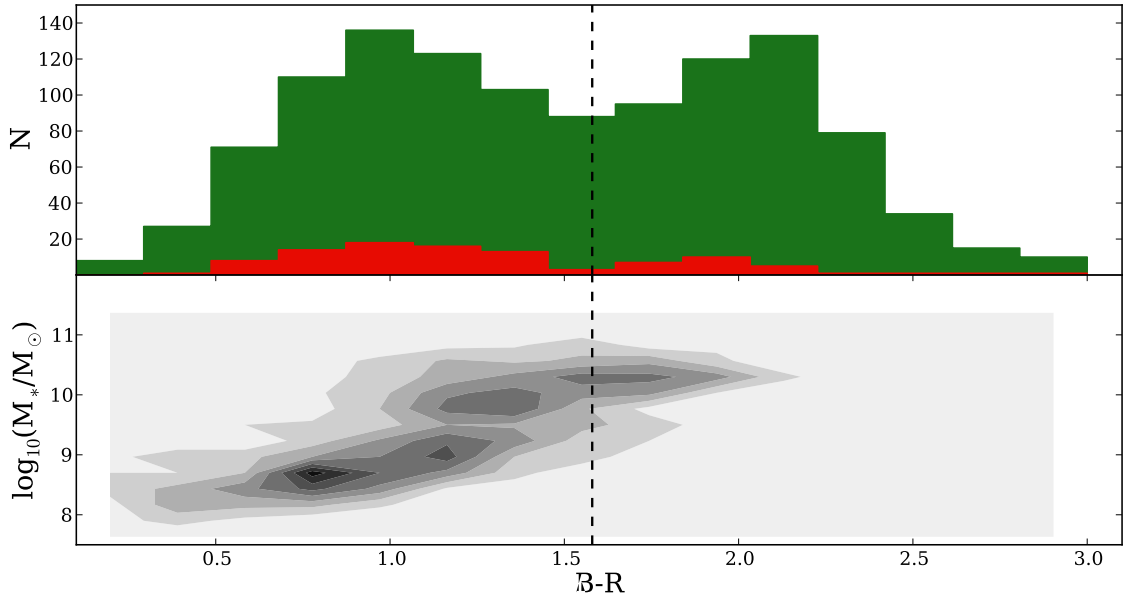

Figure 5.35: *Bottom:* B-R colour distribution of star forming galaxies. Dashed vertical line marks the red sequence and blue cloud separation. *Top:* B-R colour versus $log_{10}(M_*/M_\odot)$. Quiescent population is mostly formed by massive objects with $log_{10}(M_*/M\odot) \geq 10.0$.

6

Environmental effects

Abstract: This chapter addresses on of the main drivers of this work: where does the cluster environment alters the galaxies' characteristics. The influence of the clustercentric distance has been already explored in Chapter 5. Now we identify local density structures in the cluster from both X–ray maps and optical sources distribution. We also obtain the local surface density of each source, Σ_5, and establish a relationship between it and the distance to the centre. With these two approximations, the bulk of the transformation processes are located in the intermediate density, with clear no AGNs in the highest density regions and clear subrepresentation of the other subsample.

From early studies in clusters of galaxies it has been apparent that objects in them are different from those in the field in terms of, among others, colours, morphology and nuclear or star formation activity (Zwicky et al. 1961; Dressler 1980, and many others). As discussed in Chapter 5, the fraction of different kind of sources is also known to vary not only with the cluster redshift but within the cluster structure. Identifying the exact mechanisms for which field galaxies mutate into cluster objects is key to understand the overall galaxy evolution.

In general, we can group these processes in three broad sets: galaxy - galaxy interactions, galaxy

- intracluster medium (ICM) interaction and galaxy - cluster gravitational potential interaction. Although all of them are ubiquitous within the cluster, their dominance varies along the cluster and indeed may change its structure, including the mass distribution, internal kinematics and star formation and nuclear activity. The effect on the internal galaxy activity and its gravitational well also affects the morphologies of cluster objects. (See Chapter 1 for further details).

To disentangle these mechanisms, we need to establish the different influence areas in terms of clustercentric distance and density. The former has been addressed along Chapter 5. We will now discuss the density structure from both an overall cluster and local approach.

6.1 Cluster Substructure Maps

Substructures are the signature of the hierarchical growth of galaxy clusters. These substructures are statiscally significant inhomogeneities in the surface density with sizes larger than the typical galaxy sizes. By studying them not only can the hierarchical model be tested and better understood, but also its relation with the processes affecting the galaxy evolution under the effect of both the cluster potential well and the higher galaxy density environment. That evolution is known to be enhanced by the cluster-subcluster collision and the interaction with the intracluster medium.

There are various ways to address the analysis of cluster substructures. One option is to inspect the distribution of the projected radial velocities with respect to the distance to the cluster centre (Geller & Beers 1982) . Other is the study of the shear pattern in the background population produced by gravitational lensing. Yet another method is the analysis of the X–ray surface brightness of the intracluster gas (Ettori et al. 2013). Each of these methods is specially sensitive to one or other effect. The optical analysis of the individual sources in the cluster is relatively independent of redshift, but suffers from projection effects more than X–ray studies. On the other hand, the effect of cluster-subcluster collisions on the intracluster gas and the individual galaxies are observed at different wavelengths: Enhancement of star formation by galaxy-galaxy interactions is noticeable in optical wavelengths, while its quenching by ram-pressure striping of galaxy gas and its traces behind the substructure objects are observable in X–rays (Barrena et al. 2002). It is therefore necessary the use of both techniques.

In this work we will use two methods to analyse the density profiles in ZwCl0024+1652. First we will use X–ray maps from *XMM–Newton* to search for peaks in the cluster surface brightness. Then we will analyse the projected concentrations of objects from optical observations using different smoothing adaptative kernels.

6.1.1 X–ray substructure profiles

ZwCl0024+1652 is an X–ray cluster with a relatively faint bolometric X–ray luminosity of $2.9 \pm 0.1 \times 10^{44} h_{70}^{-2}\ erg\ s^{-1}$ as reported by Zhang et al. (2005). Thorough analysis of the X–ray emission in that work shows a complex structure in the cluster core ($r < 0.5$) and one substructure in the North-West. There are two more density peaks correspondent to galaxy groups. They find a surface brightness profile fitted by a β-model:

$$n_{gas} = n_{0,gas}\left(1 + \frac{r}{r_c}^2\right)^{-3\beta/2} \tag{6.1}$$

with $\beta \sim 0.56 \pm 0.02$ and a core radius, $r_c \sim 0.3 \pm 0.03$. The temperature profile is fitted by an isothermal sphere up to $r \sim 1.5$ arcmin and a power law of $\gamma \sim 0.98$ outside this radio.

We have obtained *XMM–Newton* images from the XMM Scientific Archive and corrected them as explained in Chapter 2. The output image is then used as a low resolution proxy of the cluster structure, provided the surface brightness and temperature profiles described above. The cluster X–ray emission is concentrated within $r \leq 3$ arcmin. The image is clearly dominated by the background beyond 5 arcmin. We constrain our study of the X–ray structure of the cluster to that area.

Figure 6.1 shows the main substructures in the cluster: the core area (A), the SE-NW structure found by Kneib et al. (2003) (B), and the galaxy group reported by Czoske et al. (2001) (C). We also mark the existence of a subdensity area (3σ detection threshold) at the East of the cluster core (D) that has been not reported before. These zones can be seen in Figure 6.1 together with the X–ray centre of the cluster at 00h 26m 36ss +17 09 46 (Soucail et al. 2000). This position differs from the BCG coordinates, taken as cluster centre along this work, by 9.1 arcsec.

In figure 6.2 we have overlaid two different cluster populations over the density distribution mapped from the X–ray contours, drawn at levels from 3σ to 9σ in 1σ steps. The first one (Figure 6.2a) depicts the ELGs from Sánchez-Portal et al. (2015) and the AGNs (see Chapter 5). We can see how both the ELG and AGN population follow the general SE-NW overdensity, although the AGNs clearly avoid the highest density region.

A similar effect can be seen in Figure 6.2b, with the FIR population showing even higher presence in the overdensity areas. In all the cases described, the different families of sources avoid the subdensity marked as "D" in the maps.

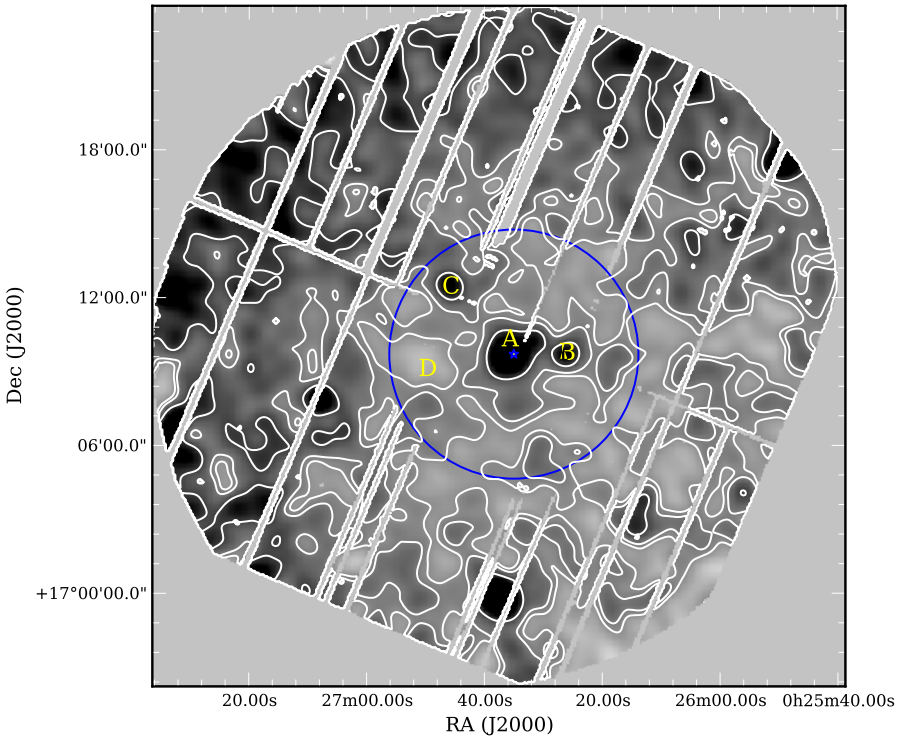

Figure 6.1: X–ray map and contours at $\sigma \sim 6$, 7 and 10. The three known substructures are marked with "A": the cluster core, "B": the NW elogation and C: the galaxy pair. We also mark a low density area (D). The cluster core is labelled with a blue star.The blue circle shows the 5 arcmin boundary beyond which the X–ray emission is noise dominated.

We can conclude that overdensity regions marked by X–ray maps do not favour the presence of active galaxies, selected either by their emission lines or $L(IR)$, although region A is not empty of these galaxies. AGNs are located in the surroundings of regions B and C, however, they avoid the highest density areas including the cluster core. Remarkably, no infra-red galaxy is found in the subdensity region D. Unfortunately, region D falls out of OSIRIS maps, so the behaviour of ELGs can not be traced.

Notably, region D is actually devoid of cluster members (see Figure **??**), suggesting a deviation from the hydrostatic equilibrium as a consequence of the interaction with the cluster core, as the bow-shock like alignment of galaxies between this area and zone A indicates. It is also noticeable its symmetry with region B with respect to the cluster centre.

Figure **??** also shows that cluster galaxies concentrate and surround region C and B, without seating inside those areas.

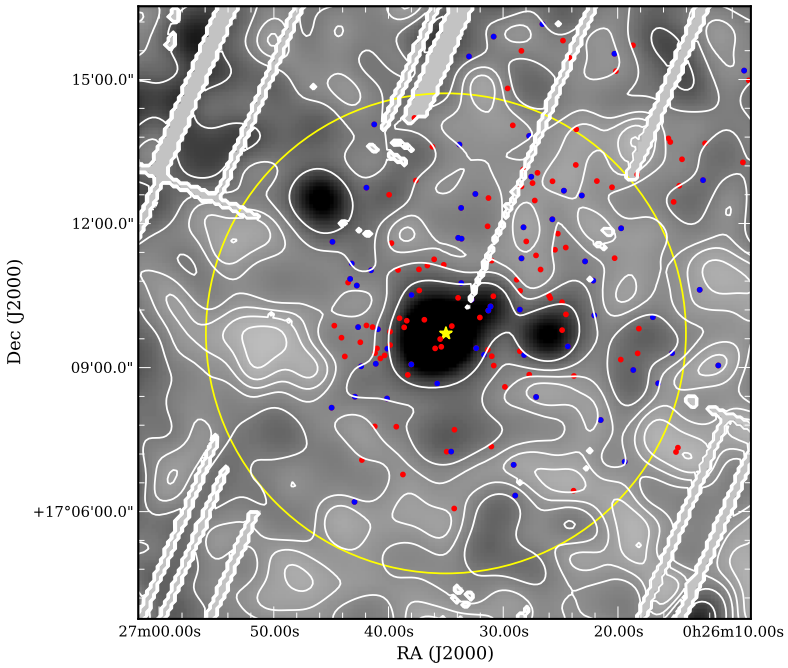

(a) ELGs (red dots) and AGNs (blue dots) galaxies over X–rays density map.

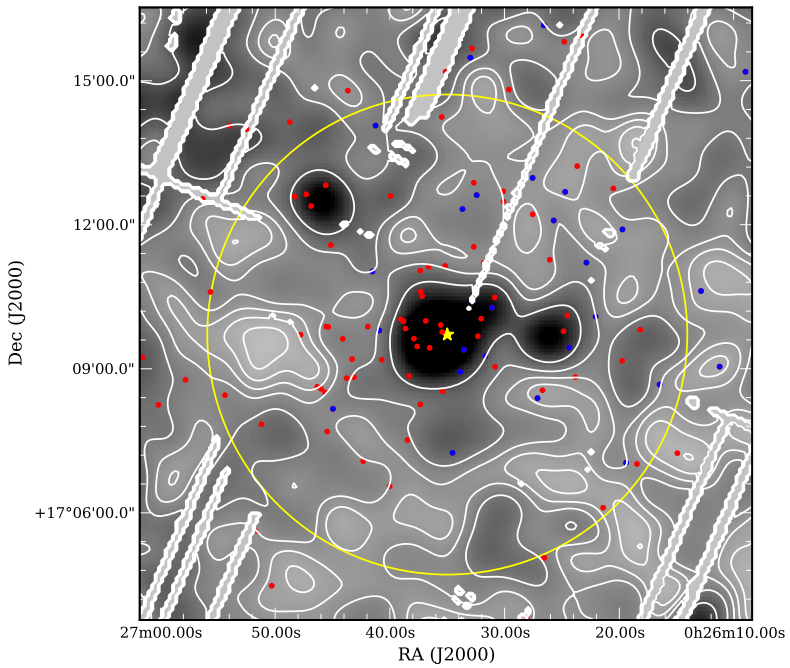

(b) Far infrared objects (red dots) over X–rays density map. The FIR AGN subsample is marked with blue dots.

Figure 6.2: X–ray maps depicting contours from 3σ to 9σ in 1σ steps. The emission line and far infrared galaxies are marked in red (*top* and *bottom* panels respectively), with their AGN fraction depicted in blue. Yellow circle shows the 5 arcmin boundary.

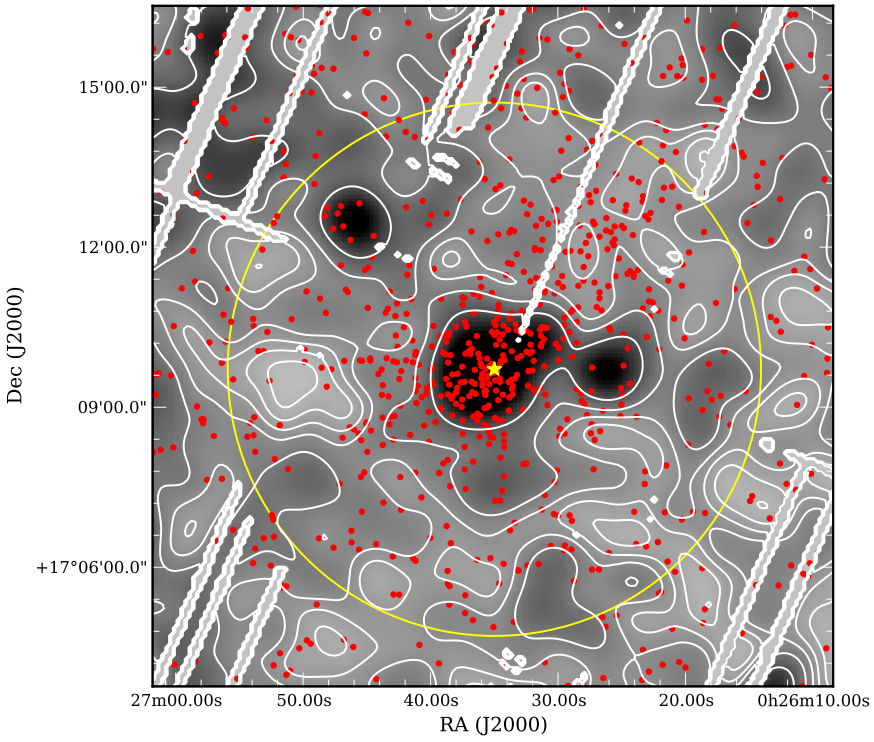

Figure 6.3: X–ray map and contours at $\sigma \sim 6$, 7 and 10. The red dots mark the cluster members. The cluster core is labelled with a yellow star. The yellow circle shows the 5 arcmin boundary beyond which the X–ray emmision is noise dominated.

6.1.2 Optical density profile

A part of the X–ray information on the cluster substructures, we also searched for density gradients by smoothing the position distribution of cluster members using an adaptative gaussian kernel (Pisani 1993, 1996). This procedure is specially fitted for our purposes since it is completely non-parametric, does not require large samples to produce reliable results and is scale invariant. As a basic outline, the software used, DEDICA, estimates the probability density function associated with our galaxies approximating a two dimensional gaussian kernel centered in the source position and with variable standard deviation. Once the best estimate of this kernel is obtained, it identifies the local maxima of the probability density function and the likelihood ratio of a source to be part of that particular substructure. We selected density peaks above 3σ with respect to the background density fluctuation.

We have obtained three different density maps tracing sources selected by redshift procedence criteria: spectroscopic redshift, photometric redshift and objects with no redshift in M05. After inspecting various combinations, we found that the density map obtained from objects with spectroscopic redshift and that from the photometric redshift sample behave similarly, tracing the same

density clumps. However, when comparing with the population with no redshift in M05, the result was obviously different. That allowed us to confirm once again the validity of the photometric redshift selection. The best map (i.e.: the map with higher statistical significance of the clumps found) was produced by running DEDICA over our sample of 1262 objects with redshifts in the cluster range. For details on the redshift selection, refer to Section 6.2.

Figure 6.4a displays the ELGs position over the optical density map of ZwCl0024+1652. Figure 6.4b shows the contours over the OSIRIS image of the cluster. As explained in Chapter 3, the catalogue was cropped to a wider area than GLACE FoV to avoid border effects in these maps.

The density distribution obtained from this method successfully traces the SE-NW elongation shown in X–rays, although other ICL overdensities like structure B and C in Figure 6.1 are missed with this technique. The main cluster structure shows higher complexity in the optical map than in the X–ray one. Figure 6.5 depicts the density profile derived from the optical sources over the X–ray map of the cluster. Both BGC and X–ray centres are flagged as a blue and yellow star respectively.

Optically derived high density areas are not overpopulated by either AGNs or infra-red galaxies nor are devoid of star forming objects. The significance of these areas over the three cluster populations discussed in Chapter 5 is negligible.

6.2 Local densities

Local density measurements

The structures described in section 6.1 reveal high density regions in the cluster at spatial scales suitable to study the overall influence of the cluster medium on the galaxies. However, they may fail to trace the effect of local over/underdensities, galaxy-galaxy interactions or small substructures in the global cluster mass profile, overlooked or smoothed by algorithms like DEDICA or others.

To measure the local densities we applied a modified version of the method first described by Dressler *et. al.* in 1980. We calculate the projected distance in Mpc, using the correspondent cosmology, to the k^{th} object in the field of view (see Chapter 1). Then we obtain the local density as:

$$\Sigma_k = \frac{k+1}{\pi R_k^2} \tag{6.2}$$

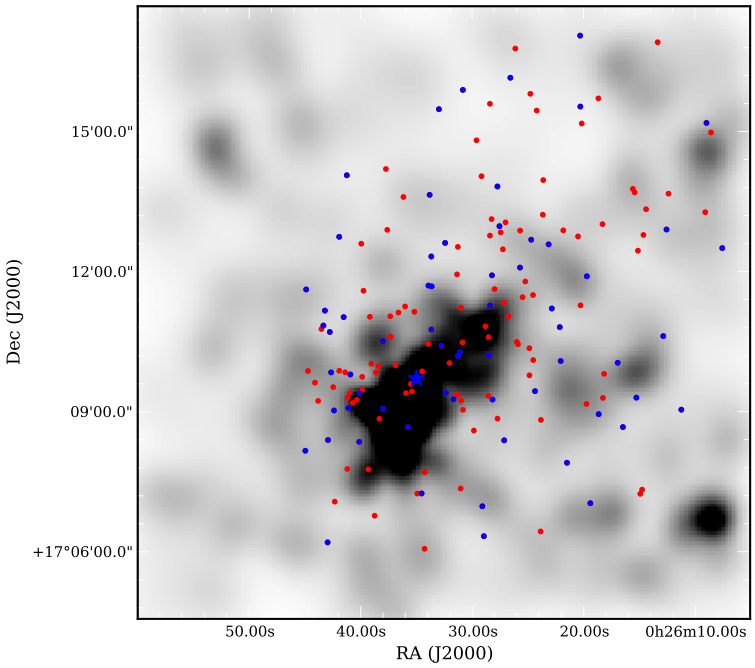

(a) ELGs (dots) over optical density maps derived from DEDICA. AGNs are marked in blue, while star forming galaxies are shown in red.

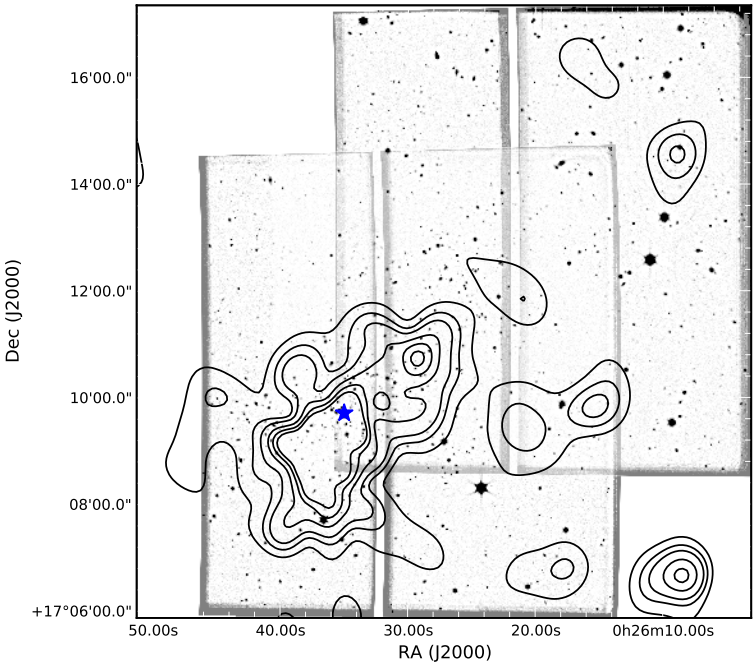

(b) Density contour maps over the mosaic OSIRIS deep observation. Contour curves are drawn at $3\sigma - 9\sigma$ in steps of 1σ.

Figure 6.4: Optical density maps showing the probability of a source in a given position pertaining to a substructure as obtained from DEDICA over the distribution of sources with redshifts (either spectroscopic or photometric) within the cluster range. Blue star marks the BGC position.

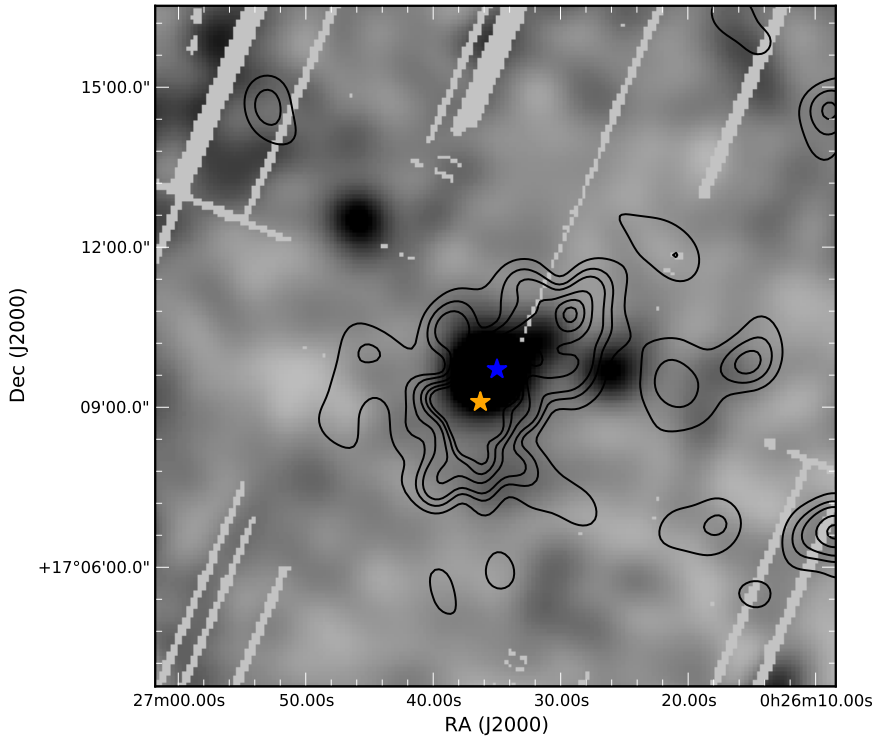

Figure 6.5: X–ray map and optical density contours at $\sigma \sim 6$, 7 and 10. The BGC, whose position has been considered as cluster centre along this work, is marked with a yellow star. X–ray derived centre corresponds to the blue star.

Where R_k is the projected distance in Mpc from the considered galaxy to the k^{th} closest object.

To benefit from the depth of the M05 catalogue, and in order to calculate the density function using only cluster members, we did not constrain the catalogue in limiting magnitude or colours, but applied the following approach: We assigned a weight between 1 and 0 to every source in the source list, similarly but not equal to Moran et al. (2005). All sources with a spectroscopy redshift within the cluster range got a value of 1. We took that redshift range as $z \geq 0.365$ and $z \leq 0.425$. This establishes a symetrical redshift interval around the nominal redshift of the cluster $z = 0.395$ (Treu et al. 2003) that includes all ELGs sources considered cluster members in Sánchez-Portal et al. (2015). We assigned a variable weight function to objects with photometric redshit. First, provided the intrinsic uncertainties of the *photo-z* values, we established the photo-z limits of our cluster as $z \geq 0.30$ and $z \leq 0.485$. Then, we assigned a weight of the form:

$$W = W_0 \pm Kd * D \tag{6.3}$$

where $W_0 = 0.85$ is the ratio of sources with z_{spec} and z_{phot} that are assigned to the cluster by both values, considering the redshift ranges for one and the other case. D is the probability of a source at the particular position of the object studied to be a cluster member. Other authors obtain this value by binning the FoV in circular or annular areas and dividing the number of known members over the total amount of sources in the bin. This approach is not advisable in fields with known complex density structures like galaxy clusters, since these crude clustercentric bins may smooth away the high/low local density spots that are the target of the study. We used the density maps provided by DEDICA (see Section 6.1.2). We produced the ratio of two density maps: that of objects with redshift values in M05 lying inside the cluster and that of objects with redshift out the cluster. Once normalised, this new map gives the probability of a source with uncertain redshift actually be a cluster member. Kd is a normalization factor chosen to make $W_{max} = 1$. Sources in the catalogue with no information on z were given $W = D$, taking then into account that they might be cluster members as well. All sources with either z_{spec} or z_{phot} out of the cluster redshifts were given a value of $W = 0$. Once all objects had a weight based on the existence/procedence of its redshift and its position over the general density map of the cluster, k^* was defined as the k-element whose cumulative weight is greater than k, and Σ_k^* as the ratio of that cumulative weight and the area encircled by the K^* element.

We tried different values of k to check the best estimate of the local density (see Figure 6.6). The rms variation between Σ_{10} and Σ_5 is of 0.02. In parallel with the rest of the GLACE publications we chose Σ_5 as the best value for the local density and that rms as its uncertainty.

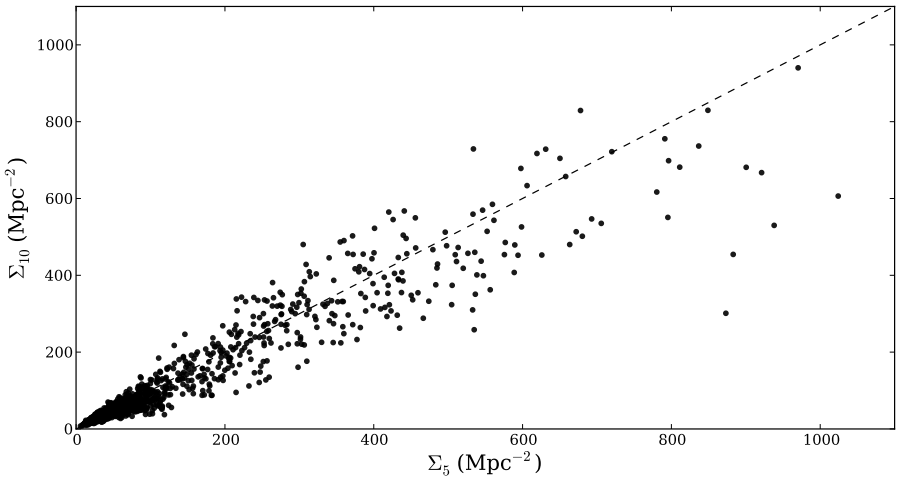

Figure 6.6: Σ_{10} versus Σ_5 calculated for all cluster members. The typicall scatter is negligible (rms $\sim$ 0.02), specially in the low density region. For higher densities, Σ_5 gives consistent higher values than Σ_{10}.

In order to analyse the effect of the local density on the various galaxy characteristics, we considered three environmental bins. These bins should map the relatively narrow regions where a significant change in colour distribution takes place. To establish the bin boundaries we followed a double approach: First we took as reference of the galaxy characteristics the B-R vs R diagram. This colour-magnitude diagram provides a good idea of the relative importance of past and recent star formation. Then we traced the first, second and third quartile of the B-R number counts along Σ_5 (green lines in Figure 6.7) searching for significant gradients in the density-colour relation. We found intial boundaries at $log(\Sigma_5) \sim 1.45$ and $log(\Sigma_5) \sim 2.05$. Then we followed a bootstrap

method to minimise the effect of this election on the final results. We performed a bootstrap analysis by randomly varying the region limits as per a gaussian distribution of standard deviation one half the width of the initial bins. The boundaries where allowed to be within one sigma from the gaussian peak. We run 1000 simulations and measured the gradient in B-R of the number counts per Σ_5, averaged along each region. The maximum of those gradients marked the optimal bin selection. We finally established the density margins at 1.5 and 2.1.

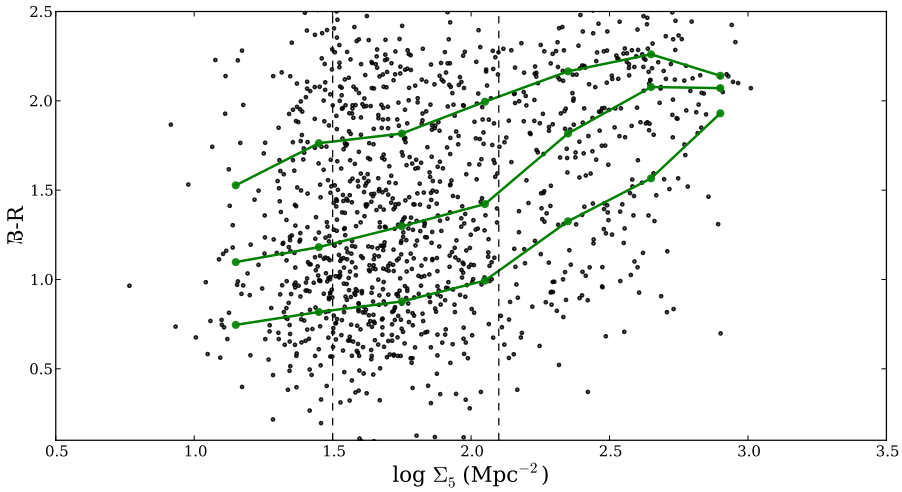

Figure 6.7: B-R colour vs Σ_5. Green lines represents first, second and third quartiles of the B-R fraction.

There is a good correspondence between local surface density and cluster estructure. The high density region relates with the cluster inner core, $r \leq 0.5\ r_{vir}$ and in whole cluster dimension as per

$$\Sigma_5 \propto e^{-2r} \tag{6.4}$$

with no major deviation or clumps outstanding from the distribution. We nevertheless notice larger scatters beyond the local radius. We compared the local density versus the clustercentric distance as tracer of the environment effect on the morphology distribution. Figure 6.8 depicts the morphological types as per both magnitudes. In general, both parameters mark the distribution along the cluster estructure equally well, though Σ_5 values characterises better the distribution of disk galaxies (E/S0 and S0), what is consistent with the expected outcome.

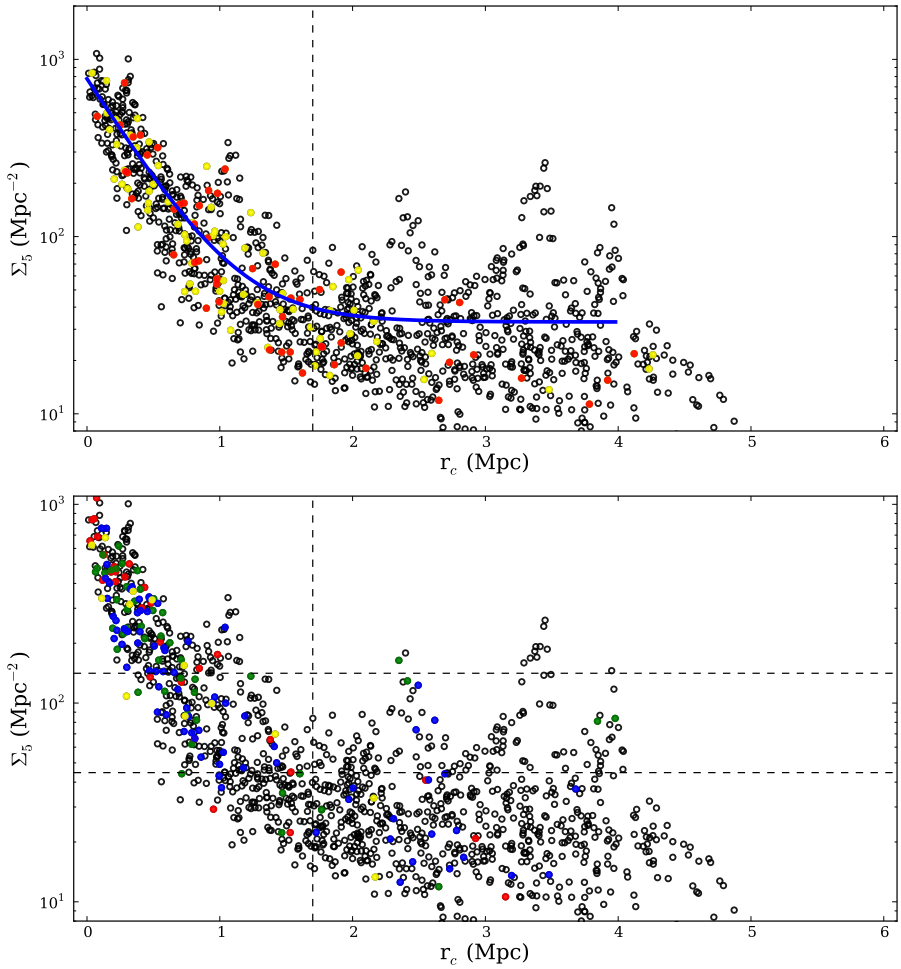

Figure 6.8: *Top:* Σ_5 vs clustercentric distance. The IR population is marked in red (LIRGs) and yellow (the rest). *Bottom:* Σ_5 versus clustercentric distance. The morphological types are marked in red (elipticals), blue (spirals), Green (disk galaxies) and yellow (irregulars). Vertical dashed line shows the r_{vir}. Horizontal dashed lines depicts the local density boundaries.

6.3 Dependence on local density

Colour relation with density

The morphology-density relation was the first quantitative observation of environment dependent galaxy features (Dressler 1980; Dressler et al. 1997). It is the variation of the fraction of Hubble morphological types with local surface density. Elliptical galaxies favour high density regions, late type galaxies are more frequent in low density areas and disk like galaxies keep the same presence in both environments (Smith et al. 2005; Postman et al. 2005).

The variation of the morphology fraction is simultaneous with the variation of the colours. High density environments harbor older stellar population with redder colours (see Pintos-Castro et al. 2013 among others) while the opposite is applicable to low density regions.

Figure 6.9 shows the colour distribution of our sample as per the three regions defined in Section 6.2, i.e.:, $\Sigma_5 < 1.5$ Mpc, Σ_5 between 1.5 and 2.1 Mpc and $\Sigma_5 > 2.1$, for low–, medium– and high–density space phase areas respectively. The black vertical lines mark the median value of the colour per the bin (1.15, 1.38 y 1.96). This colour separation is even more evident when we display the fraction of red galaxies (ratio of galaxies with B-R >1.58 over the total population) versus the local surface density. The red fraction passes from 30% to 70% across the three Σ_5 regions, increasing with larger Σ_5 (Figure 6.10a), practically the opposite of the blue cloud objects, whose fractional presence in the high density area is 30% and 70% en the lowest one. This confirms the bimodality found in the CMD relation, as discussed in Chapter 5, with bluer galaxies avoiding the denser zones. The ELGs sample, however, follows a different trend (see Figure 6.10b). The star forming subsample fraction is boosted in the intermediate density region, with similar values in the lowest and highest Σ_5 areas. The AGN subset shows a less pronounced behaviour, with a smaller presence in the highest local density areas and a similar fraction in the lowest and intermediate zones.

The stellar masses of the cluster population also reflects the bimodality found in the colour - magnitud diagram. Red galaxies are in general more massive than the blue fraction (see Figure 6.11). The former are dominant in the 9 to 10.5 bins while the presence of the latter is more significant in the 7 to 9 bins. In any case, this distribution shows a less prominent difference between one and other population than that based in the colour magnitud diagram. We therefore use this last criterion for subsequent analysis.

SFR and Local Density

To analyse the dependency between the local surface density and the star forming rate, we split the population in red and blue galaxies, as explained in previous section. Figure 6.12 shows the SFR

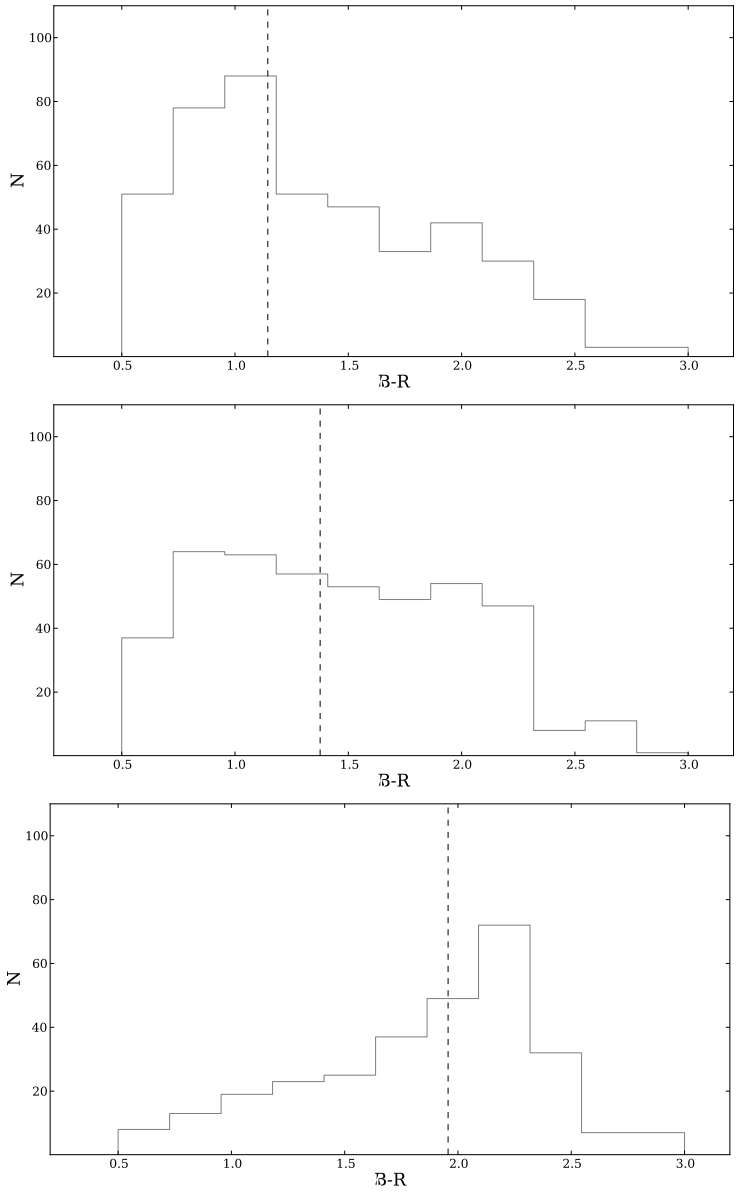

Figure 6.9: B-R colour distribution in each density region: low- (top), medium (center) and high (bottom). Dashed line in each pannel is the median value of the colour in the bin.

versus the local density (*left*) and the stellar mass (*right*). The median values of the star formation rates per bin follow a linear decrease with higher densities. We do not find a transitional area with significant changes in this trend. This can be seen in both the red and blue galaxies. On the other hand, the red sequence is clearly distinguished in the SFR/M_* relation. Their locus in the diagram are aligned with the main sequence reported by Koyama et al. (2013) in a cluster at similar redshift (solid black line), while the blue galaxies occupy the low mass / high SFR area in the same plot.

Figure 6.13 shows the specific star formation rate versus density relation (*left*) and versus the stellar mass (*right*). The sSFR decreases with higher local densities for both the red and blue galaxies, although the latter shows a less steep dependency with Σ_5. We took into account that the diagram includes a strong anticorrelation between M_* and the sSFR (Elbaz et al. 2007), since the more massive galaxies are usually redder.

6.4 Close encounters

Galaxy to galaxy interaction is one of the main mechanisms suggested to explain the various processes involved in the transformation of galaxies along its infall into the cluster core area. As Mihos (2003) shows, a typical cluster galaxy should suffer several close encounters along its lifetime. Although these interactions would take place in the whole cluster structure, they would be dominant in the galaxy outskirts and intermediate area, around 1.0 r_{vir}, where the effect of the cluster gravitational potential and the influence of the intracluster medium have not yet come into full force (Treu et al. 2003).

We can summarise the outcome of a galaxy-galaxy encounter in three different phenomena, depending on the relative velocities and mass ratios. Low velocities and similar masses involve higher mass exchanges and usually lead to mergers and an increase in the star formation rate. High velocities, however, usually strips gas out of the galaxies (*harrasment*) and enriches the intracluster medium. Depending on the fraction and rate of the gas removed either the galaxy activity is quenched or slowed (*starvation*). Morphological transformations have been also linked to high local densities and galaxy-galaxy interactions (Dressler et al. 1997).

In general, encounters in clusters are characterized by higher collision speeds that those in the field, specially in the inner cluster areas. The effect of fast interactions on the galaxies is related to its initial internal dynamics (morphology), although simulations shows that repeated high speed collisions drive to transformation into elliptical galaxies (Moore et al. 1998). Slow interactions trigger more intense responses in both star formation activity and morphological transformations, and are more efficient in heating and stripping the galaxies than fast ones. However, unlike in field mergers, the tidal field efficiently removes the loose gas clouds weakly bound to the merger, adding it to the intracluster medium. This affects the longevity and detectability of the tidal debris and prevents the resettling of the material onto the merger, shortening the star formation activity likely triggered by the process. On the other hand, the effects of the cluster gravitational field

lengthen the time scale by adding energy to the galaxy orbits. Simulations show cases where this energy input is enough to unbind galaxy pairs, opening the possibility of the two objects remaining separated after strong mass exchange (Mihos 2003). For all these reasons, identifying a galaxy as the result of a close interaction in terms of the usual signs in the field (enhanced star formation activity, disturbed morphologies or concentration index) becomes very difficult after short time intervals.

In the field, the usual distance scale for galaxy interaction varies from 200 to 250 kpc. To investigate the effect of close encounters in ZwCl0024+1652, we focused in galaxies pairs laying at a maximum projected distance of 100 kpc, (20 arcsec), to unselect interactions that are not taking place in the moment of the observations or the inmediate past or with weak effects on the galaxies. Then we applied a second filter to keep only those objects with spectroscopic redshifts and whose redshift difference was less than 0.005. This would select sources at the same radial distance and with similar peculiar velocities, that are more likely to undergo merging processes, as explained above. This involves some degeneracy since the cosmological redshift and the peculiar velocity could couple to give a false match. A third filter was applied, based on enhanced star formation activity, high IR luminosity and morphological types. We visually inspected the resulting population for direct detection of interacting galaxies.

We obtained a list of 88 galaxy pair candidates. The distribution of their position with respect the clustercentric distance can be seen in figure 6.15. Most of these galaxy pairs, 64%, concentrates in the internal and intermediate core, at $r < 1\ Mpc$. Its fraction over the full member peaks at aproximately 1 Mpc. The pairs clearly favours the main cluster structure in the distance vs radial velocity plot (Figure 6.16) with a presence of 96% . Its distribution over the local surface density shows a concentration in high Σ_5 region, peaking in $log_{10}\Sigma_5 = 2.3$, as seen in Figure 6.17.

We study the physical characteristics of the galaxy pairs by inspecting their $L(IR)$, nuclear and star forming activity and morphology. With respect to this last parameter, 26 % of the galaxies in pairs show disk-like morphology, while 29% of them are classified as spirals. Surprisingly, only 2 % galaxies are flagged as irregular in M05. A visual inspection of thumbnails from HST-WFPC2 however show candidates of distorted morphologies. A more thorough analysis would be required to fully assess this relation, but a morphological reclassification of the cluster members falls beyond the scope of this work.

With respect of the infrared luminosity, 20% of the galaxies in pairs are *Herschel* sources, with LIRs ranging from $10^{10.26}L_{\odot}$ to $10^{11.73}L_{\odot}$. Although in general the infrared fraction of this population follows the general trend of the rest of the *Herschel* sources, there is a drop in the presence in the brightest distribution end (see Figure 6.18). Only 17 galaxies (10%) are LIRGs. A similar number of AGNs is found (22), posing a 12% of the objects in pairs. 8 out of these 22 AGNs are also LIRGs.

On the other hand, when inspecting the star formation activity of the galaxies in pairs, they are found to follow the general trend of the infrared galaxies in the low to moderate SFR range (0.5 to 5 $M_{\odot}$/yr), showing much lower values in the high SFR end (5 to 10 $M_{\odot}$/yr). (See Figure 6.19).

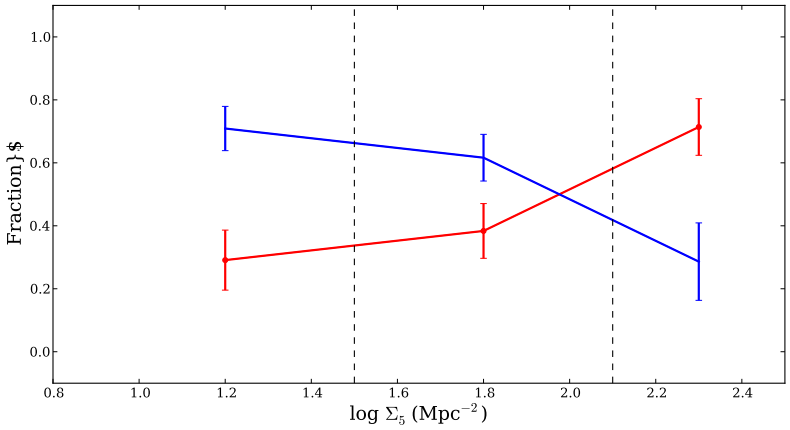

(a) Fraction of red sequence galaxies and blue cloud objects (red and blue line respectively) across the three density regions defined in section 6.2.

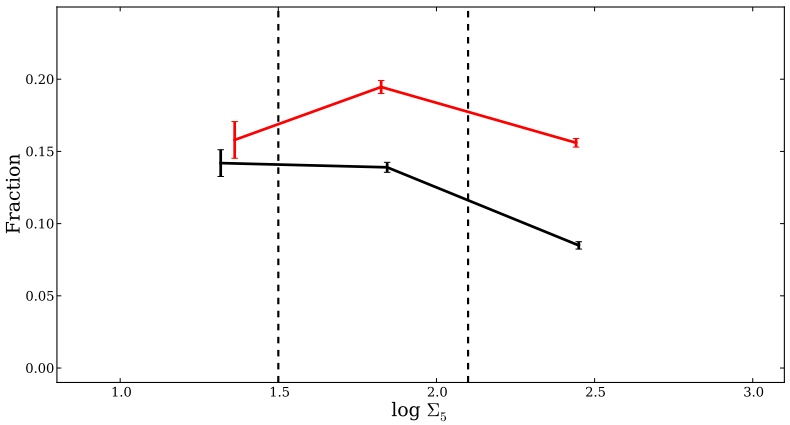

(b) Fraction of ELGs galaxies along the three density regions defined in section 6.2. Red line marks the fraction of star forming galaxies, while the black line traces the fraction of AGNs.

Figure 6.10: *Top:* Fraction of cluster population with respect to their colours. *Red line:* red sequence objects, *blue line:* blue cloud galaxies. Red sources clearly favour the high density zone, while the blue population is shifted towars lower densities. *Bottom:* Fraction of ELGs: star forming (red line) and AGNs (black line). The intermediate zone marks the transitional area where the star formation activity is boosted. AGN fraction significanctly decreases with higher Σ_5

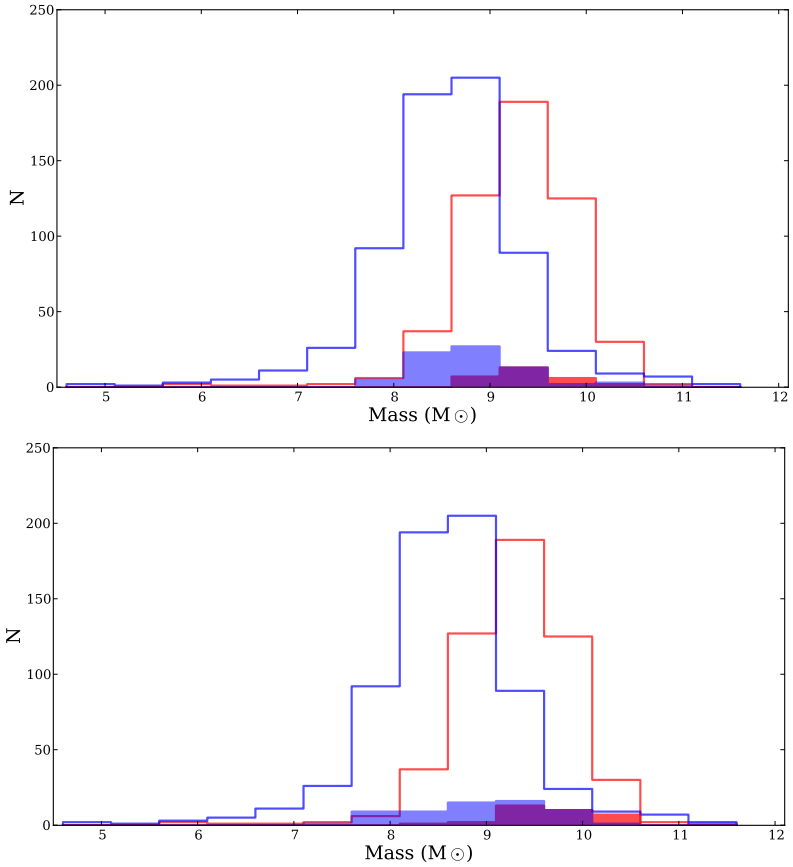

Figure 6.11: Histograms of stellar mass distributions. Red and blue colour s indicate galaxies in the red sequence or the blue cloud respectively. *Top:* Filled bars correspond to ELGs. *Bottom:* Filled bars show the red and blue population of FIR objects.

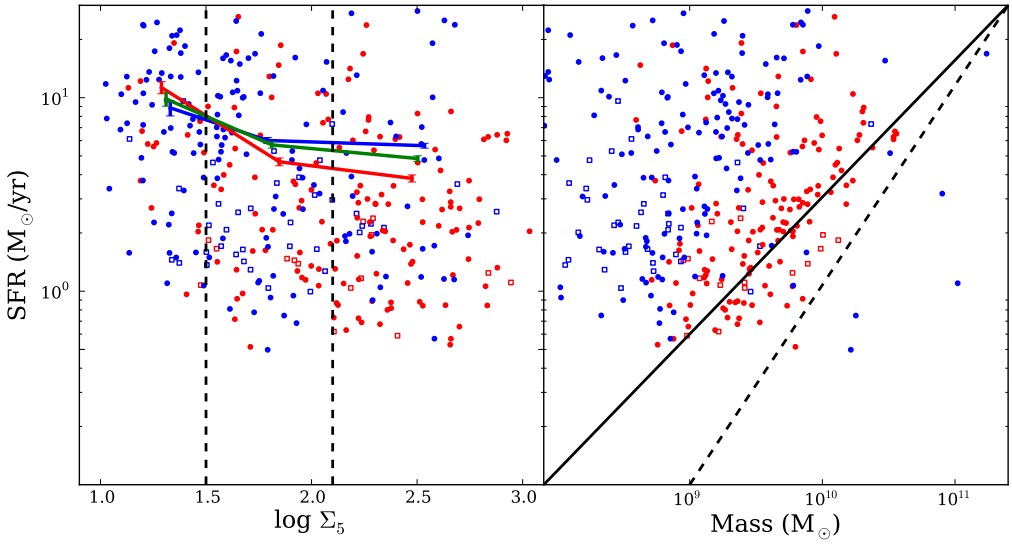

Figure 6.12: *Left:* Star formation rate versus log(Σ_5). Blue galaxies are marked in blue and red galaxies in red. SFRs calculated from Hα are depicted as squares, while SFRs derived from L_{IR} are marked as dots. The red, blue and green lines join the median values of the SFR of red and blue galaxies and the total population respectively. The error bars are computed as the standard deviation of the median values distribution. Vertical dashes lines mark the three surface density regions as discussed in Section 6.2. *Right:* Star formation rate versus stellar mass. Symbols follow the same code as before. Red galaxies follow the main sequence (solid black line) as described by Koyama et al. (2013) for $z \sim 0.4$. The dashed line depicts the main sequence found by Whitaker et al. (2012) at local redshift.

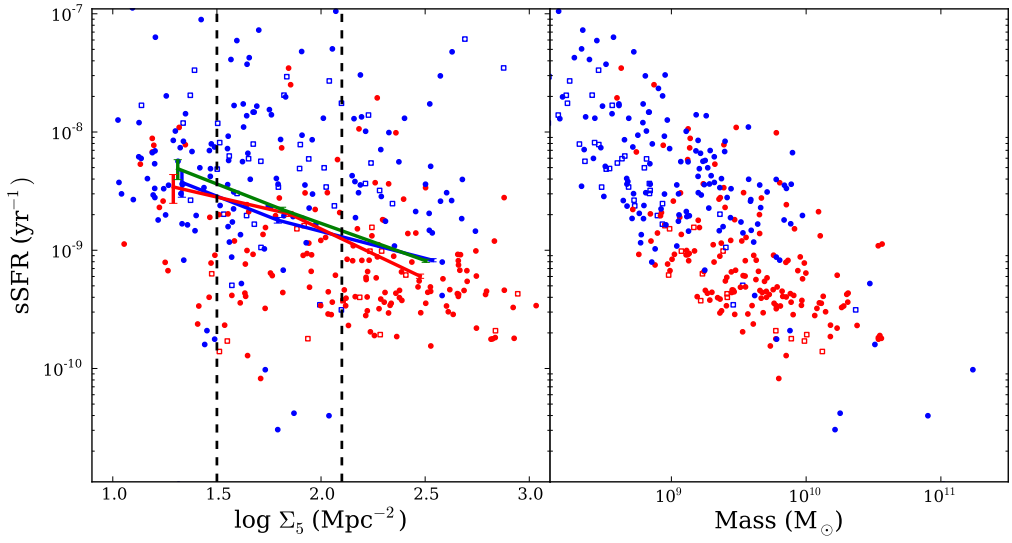

Figure 6.13: *Left:* Specific star formation rate versus log(Σ_5). Blue galaxies are marked in blue and red galaxies in red. sSFRs calculated from Hα are depicted as squares, while SFRs derived from L_{IR} are marked as dots. The red, blue and green lines join the median values of the sSFR of red and blue galaxies and the total population respectively.The error bars are computed as the standard deviation of the median values distribution. Vertical dashes lines mark the three surface density regions as discussed in Section 6.2. *Right:* Specific star formation rate versus stellar mass. Symbols follow the same code as before.

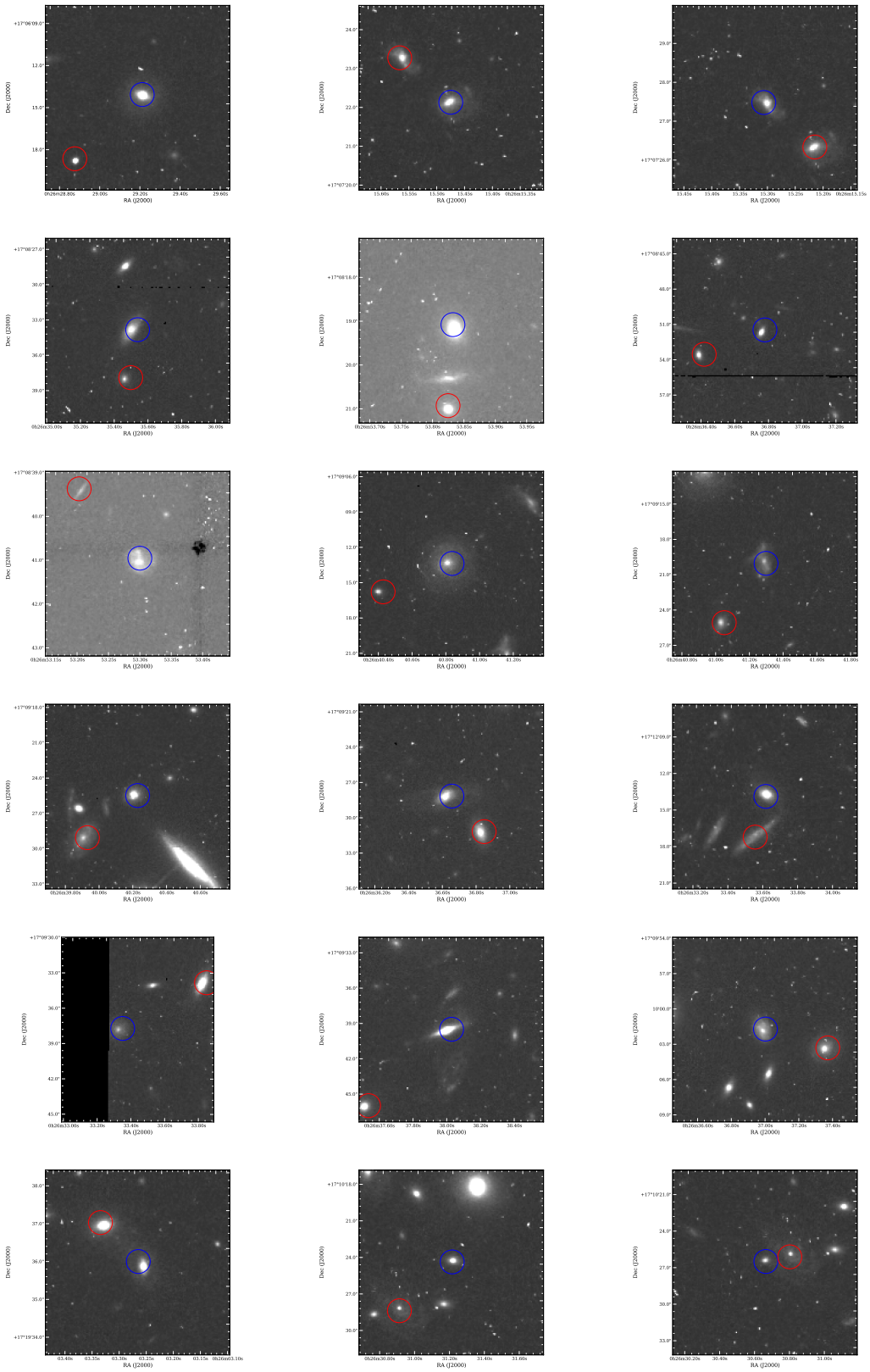

Figure 6.14: HST postcards of selected galaxy pairs.

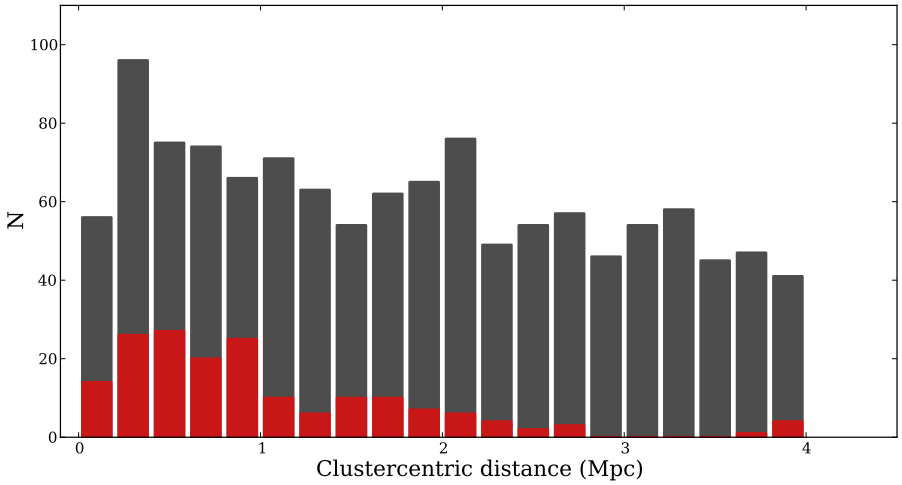

Figure 6.15: Close encounters distribution with respect to the clustercentric distance. Red bars marks the number of close encounters, grey bars are the number of cluster members. Close-encounters are mainly located in the area within 1 Mpc.

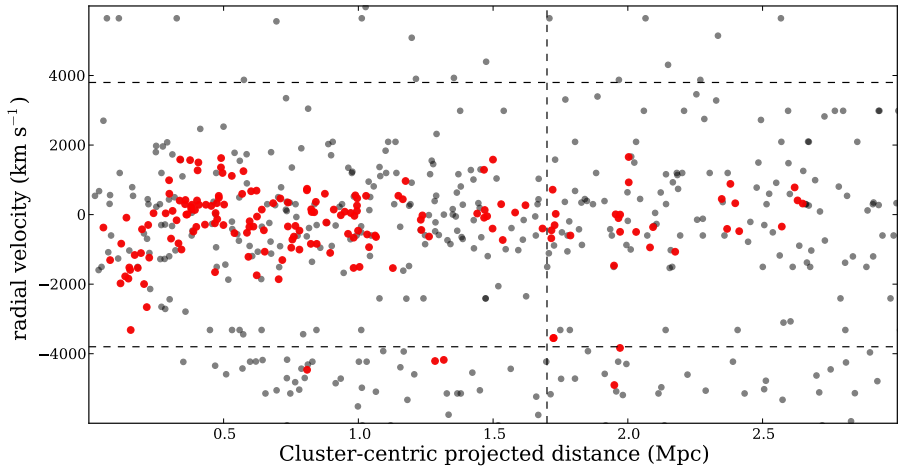

Figure 6.16: Close encounters distribution with respect to the clustercentric distance versus radial velocity. Red dots marks close encounters, grey dots are the rest of cluster members. Close-encounters are mostly located in the main cluster structure.

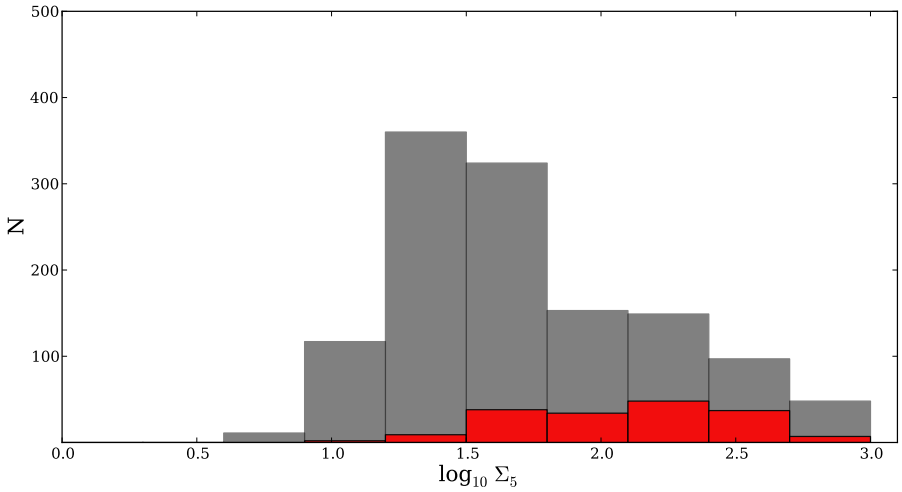

Figure 6.17: Fraction of close encounters distribution with respect to Σ_5. Red bars mark the fraction of close encounters, grey bars are the fraction of cluster members. The close encounters are more present in the high surface density end.

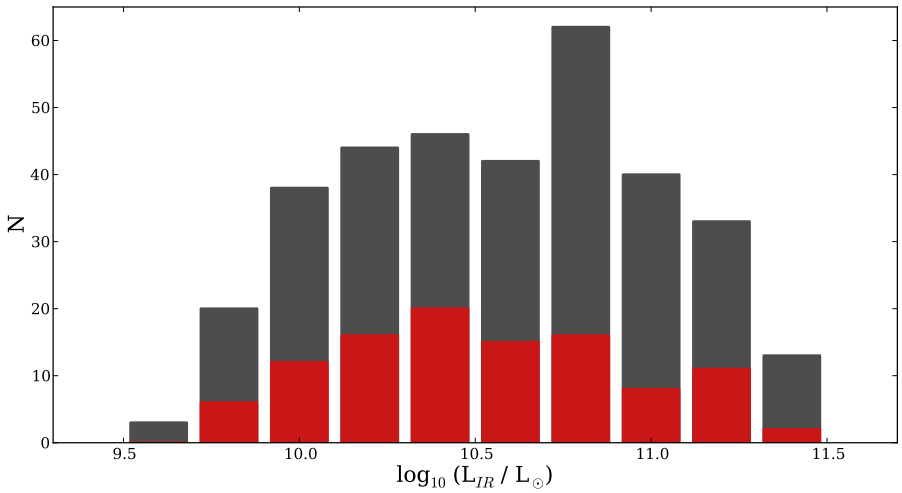

Figure 6.18: Close encounters distribution with respect to L_{IR}. Red bars mark the number of close encounters, grey bars are the number of cluster members.

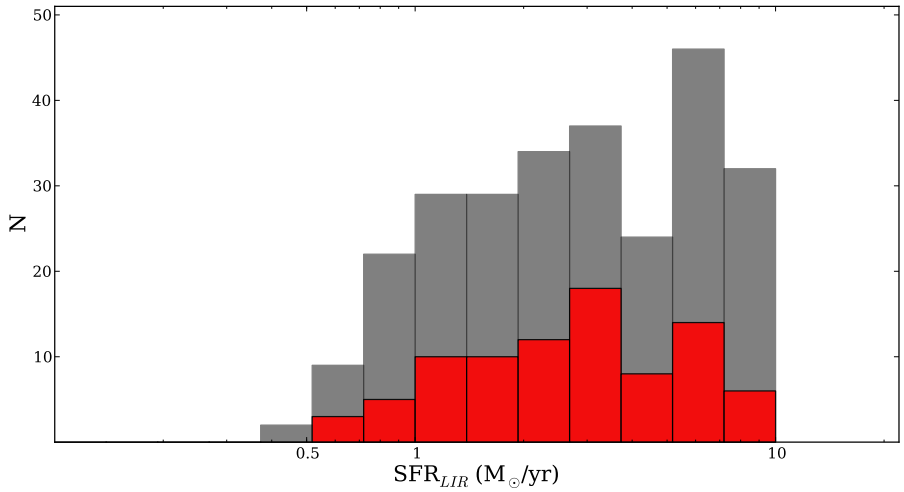

Figure 6.19: Close encounters number distribution with respect to the star formation rate derived from L(IR). Red bars mark the number of close encounters, grey bars are the number of cluster members.

7

Summary and Conclusions

Abstract: Through the present work we have addressed the construction of a robust multi-wavelength catalogue of ZwCl0024+1652 members and the derivation of magnitudes such as $L(IR)$, $L(UV)$, SFRs, stellar masses etc by different means. We have selected three different cluster populations: far-infrared objects, AGNs and star forming galaxies, and analysed these characteristics with respect each other and their location in the cluster. Then we have studied the various environmental areas of the cluster, both physical and Σ_5 phase - space and their influence in the galaxy evolution. We find that the bulk of the transformation processes take place at a distance of 0.7 r_{vir}. The galaxies going through these mutation avoid both high density areas, both local and projected.

ZwCL0024+1652 has been thoroughly studied in previous chapters by tracing the characteristics of three different populations: The far-infrared galaxies form a set of objects observed by *Herschel* has been never analysed before. The AGN population has been selected by four different criteria and represents the largest AGN sample ever studied in this cluster. The star forming galaxies have been also studied, deriving their SFRs from their Hα flux, extinction corrected via the Balmer decrement, and from $L(IR)$, revealing different star formation scenarios.

The cluster and its substructures have been analysed as well, using X–rays and optical data. The

regions found produce a clear influence on the general members characteristics, mapping the presence or absence of one or other type of galaxies. Local surface densities have been used as well in order to identify the areas where the bulk of the transformations occurs. The results and main conclusions can be found below.

7.1 Summary

Along the course of this work we have established that OSIRIS is an outstanding resource to obtain integral field low resolution spectroscopy. The capabilities and performance of the Fabry-Pérot interferometers together with the large colective area of GTC make it possible to acomplish deep emission line surveys at various redshifts.

GLACE has obtained deep Hα/[N II] and Hβ images on ZwCl0024+1652, that have provided a welth of new spectroscopic redshifts. The Hα data have made it possible to select the AGN population using $EW\alpha n$ diagnostic diagrams (Cid Fernandes et al. 2010) and by finding characteristic broad lines in the pseudospectra. The Hβ information has allowed to calculate accurate star formation rates by providing an extinction correction from the Balmer decrement.

These newly detected ELGs have been matched with catalogues from different procedences, both archival (*XMM–Newton*, *Chandra*, *GALEX*) and published (Moran et al. 2005), ranging from X–rays to far-infrared. We have also reduced archival observations from *Spitzer* and *Herschel* to obtain source lists in the mid and far infrared, as well as X–ray maps from *XMM–Newton*. We have then produced a master catalogue using robust cross matching algorithms that guarantee its overall reliability and consistency. This is crucial when dealing with such a wide spectral range and the peculiarities of the various instruments involved. This is the most comprehensive multiwavelength catalogue of ZwCl0024+1652 members currently available.

We have fitted the spectral energy distributions of our sources to template libraries using *Le PHARE* (Arnouts et al. 1999; Ilbert et al. 2006), obtaining infrared and ultraviolet luminosities as well as stellar masses. Each real source was represented by a family of 500 simulated objects produced by varying each photometric point along its error bar following a Gaussian profile. Once the best fit was selected, the whole family was made to fit to the preferred model in order to accurately estimate the errors. This double run approach is key to obtain a reliable output from *Le PHARE*.

We have calculated the star formation rate of cluster members accounting from gas and dust extinction. This can be done in two ways: by adding the SFRs derived from ultraviolet and infrared luminosities on the one hand, and calculating them from Hα fluxes on the other. In this last case we have applied the actual extinction correction by means of the Balmer decrement derived from the Hβ line. To this end, we have performed OSIRIS TF observations mapping some ±3000 km s^{-1} around the wavelength of the redshifted Hβ line. We have developed a method to estimate

the Hβ absorption strength, based on the *Le PHARE* best fit to BC03 composite stellar populations and ages. The distribution of absorption line equivalent widths (W_{abs}) presents two peaks, at ~ 2.5 Å and 5 Å.

It has been possible to determine the extinction correction for a small sample of counterparts of Hα sources that shows clear emission in Hβ (27 objects). For this sample, the distribution of $A_{H\alpha}$ is double peaked, around $A_{H\alpha} = 0$ (unabsorbed objects) and $A_{H\alpha} = 1$ mag. The former peak is very likely due to the incompleteness of the Hβ sample of counterparts of Hα emitters (24%).

A linear correlation is found between the uncorrected and extinction-corrected SFR(Hα) when limiting the sample to 12 $M_\odot$ yr^{-1}. This suggests that $A_{H\alpha} = 1.41$ mag is a sensible global value of the Hα extinction to be applied to the cluster Hα SF galaxies.

We have compared the SFR(Hα) and SFR(IR) and investigated the amount of extinction required to reconcile them. We find that, for a majority of the objects, a dust extinction ranging from 1 to 3 magnitudes at Hα can account for the observed relation. In particular, the value of 1.41 magnitude explained above seems specially good to account for it.

In general, the star forming fraction in the cluster follows a bimodal distribution when the B-R colours are studied. We have classified the morphology in four types: elliptical, disk-like, spiral and irregular. Star forming galaxies clearly favours the spiral and disklike types, specially in the internal part of the galaxy, where the disklike galaxies are dominant. Among the star forming galaxies, the distribution of the emission line subsample along the clustercentric distance peaks at 1.0 Mpc ($0.6r_{vir}$), with a minimum presence in the internal cluster core (~ 0.3 Mpc).

It is possible to notice another bimodality in the colour - stellar mass diagram. Not only do the galaxies separate by colours in blue or red fraction, the stellar mass also traces two populations, with passive galaxies depicting higher stellar masses. On the other hand, the blue cloud objects clearly dominate the secondary cluster structure (the line-of-sight infalling group reported by Czoske et al. (2001)), and the outer cluster zones. The red galaxies fraction is significantly higher in the cluster core.

The AGN fraction is distributed along the clustercentric distance with a clear underrepresentation in the internal cluster core ($r_c \leq 0.4$ Mpc) and a peak at $r_c \leq 1.2$ Mpc, i.e.: $0.7r_{vir}$. The colour - magnitude diagram locates them in the green valley, as expected. The morphologies of AGNs in the cluster are dominated by late type galaxies (0.6 fraction of the total AGN sample with morphological information). However, there is a significant increase of the disk-like galaxies around r_{vir}. All our AGN selection are infrared emitters ($log(L_{IR}) > 10$).

Among the infrared emitters, we focused in the newly studied *Herschel* population. By B-R colours, the sources selected in the far infrared concentrates in the blue cloud and, more significantly, the green valley, with a clear underrepresentation in the red sequence. We have obtained

their infrared luminosities by two methods: deriving it from the 24μm measurement as described in Chary & Elbaz (2001) or integrating it from the SED best fit. We have found that the former method systematically underestimates the output in the cases where there are available photometric data at 100μm and/or beyond. We have therefore used the $L(IR)$ derived from *Le PHARE*.

All the far infrared selected sample are are infrared emitters ($log(L_{IR}) > 10$), with a mean value $10^{11.24\pm0.02} L_{\odot}$. 52 out of the total 122 FIR sources are LIRGs, although no ULIRG has been observed.

This population covers the full range of projected distances, favouring the main structure in the cluster with respect to the line of sight infalling group. The proportion of the FIR fraction in one and other structure exceeds a factor of 2.

We have obtained mass density profiles in two ways: using the projected distribution of optical sources and analysing the extended X–ray emission. As expected, the far-infrared population traces the overdensity areas (regions A, B and C in Figure 6.1) and avoids the low density zone (region D in the same figure). Star forming galaxies follow a similar trend, while AGNs avoid the core of the highest density zone. Region D is also empty of member galaxies, further confirming the existence of a cavity in the mass distribution. This substructure has never been reported before.

To analyse the effect of the local surface density, we have calculated the Σ_5 distribution of cluster members. There is a good correspondence with the clustercentric distance, specially for $r_c \leq 0.5 r_{vir}$, with $\Sigma_5 \propto e^{-2r}$.

Relating it with B-R colours it is apparent the existence of three regions in the colour - density phase space, depicting the zone where the change in the colour distribution takes place. We have established the boundaries of these regions at $\Sigma_5 = 1.5$ and $\Sigma_5 = 2.1$. The colour distribution in each region transits from peaking in B-R ~ 1.1 in the lowest density bin to 2.3 in the highest one. Red galaxy fraction in the highest density zone is 0.7, clearly dominating the bin, while the blue faction is higher in the lower density end.

We have studied the star formation - density relation. SFRs and sSFRs uniformily decrease with higher local densities. On the other hand, when analysing the star formation dependency with stellar mass, we have found that the red sequence sample is aligned with the main sequence reported by Koyama et al. (2013), whith the blue galaxies scattered along the low mass / high SFR area in the same diagram. In general, the red galaxy fraction have higher stellar masses, with typical values between $10^{8.5}$ $M\odot$ and $10^{10.5}$ $M\odot$ and peaking at $10^{9.5}$ $M\odot$. The mass distribution of the blue fraction ranges from $10^{7.0}$ $M\odot$ to $10^{10.0}$ $M\odot$ and peaks at $10^{8.5}$ $M\odot$.

To finish with the analysis presented in this work, we have searched for recent or on going mergers. We have selected 88 galaxy pairs with a maximum projected distance of 100 kpc and low relative velocities ($\Delta z \leq 0.005$) to look for tracers of merging such as disturbed morphologies or enhanced

star formation activity. 64% of these pairs are in the intermediate and internal area of the cluster ($r < 1$ Mpc), with a significant drop beyond this point. These close encounters clearly favour the main cluster structure, where 96% of them are located.

The infrared luminosities of these close encounters are similar to the rest of the cluster population, although there is noticeable subrepresentation in the brightest end of the distribution. Only a 10% of the galaxies in these pairs are classified as LIRGs. With respect to the star formation activity, these galaxies are predominantly in the low to intermediate SFR region (0.5 - 5 $M_{\odot}$/yr) , and clearly deviates from the star formation trend of the infrared sources in the higher SFR end.

7.2 Conclusions

The work presented in the thesis is the most comprehensive view of ZwCl0024+1652 to date, including photometric information from X–rays to far-infrared images, together with deep Hα/[N II] and Hβ observations and public (and published) catalogues.

The analysis of the presence of the three populations selected as probes (far-infrared galaxies, AGNs and star forming objects) across the cluster spatial structure; the variation of their optical colours, infrared and ultraviolet luminosities, morphologies, SFRs etc and their relation with the local surface density and mass distribution sheds new light on the processes driving the influence of the cluster on its individual members.

We have identified the intermediate to outer region of the virial volume as the spatial zone where cluster members first show signs of the effects of the environment. At a clustercentric distance of 0.7-0.9 r_{vir} (1.2 Mpc to 1.5 Mpc) the fractions of AGNs, far infrared sources and ELGs are the highest with respect to other distance bins. The objects in this region are predominantly spirals and disk-like galaxies (44% and 36% respectively). All the three populations have a significant fraction of disk-like morphologies for the first time here. This is especially remarkable for the far-infrared population, where most of intermediate luminosity LIRGs ($L(IR) \sim 10^{11.3} L_{\odot}$) are disk-like objects. This suggests that this region is the scenario of moderate enhancement of the star forming activity and the start of the morphological transformation from field spirals into cluster core ellipticals.

A similar view comes from the analysis of the local surface density. When inspecting the Σ_5 phase-spaces, the area where the fractions of blue and red galaxies or the ELGs experience a change in their trend is the intermediate one ($1.5 < \log \Sigma_5 < 2.1$, Figure 6.10). Same happens with the SFR (Figure 6.12). This Σ_5 zone corresponds to 0.7-0.9 r_{vir} as per the equation 6.4, found in Section 6.2 (see Figure 6.8).

Provided that the referred area is within the virial radius, but yet far from the internal core, and

that the proximity of other galaxies is not (or just starts to be) significant, the main transformation driver is the interaction with the ICM. It first compress the gas and dust in the infalling galaxies, enhancing their nuclear and star forming activity as well as their infrared luminosity, to finally slowly quench them. The mildness of the processes triggered (no ULIRG has been found, and only few galaxies have SFRs larger than $10M_{\odot}/yr$) suggests the prime mechanism in action is moderate ram pressure stripping (starvation). This is consistent with the under-representation of AGNs, far infrared sources and ELGs in the internal cluster core ($0.3r_{vir}$, $r_c < 0.5$ Mpc), where the material fuelling the galaxy activity has been nearly exhausted. (See Figures 5.30, 5.17 and 5.6).

Another evidence supporting this conclusion is the small number of galaxy-galaxy interactions detected beyond 1 Mpc: 34% of pairs are spread from 1 Mpc to 2.5 Mpc, while 66% are concentrated in the internal 1 Mpc. This spatial separation implies this mechanism has not a significant role in the effects observed in the area of interest.

These close encounters present low or moderate SFRs (typical values below 5 $M_{\odot}/yr$), with only a 10% qualifying as LIRGs and 12% as AGNs. Since they are mainly located in the internal virial area (96% of them are in the main cluster structure), the signs of low activity suggest that the gas and dust contents of the galaxies have been already depleted when the interaction takes places. On the other hand, the increasingly significant effect of the potential well and the more intense ram pressure exercised on the pairs in this region prevent the material disturbed during the encounter from resettling on the merged system, prematurely quenching the star formation or nuclear activity eventually triggered. Both mechanisms are consistent with the scenario observed and will be probably acting simultaneously.

With respect to the specific characteristics of the three populations studied, we have found a smaller fraction of AGNs (13.5%) than reported in previous works in this cluster, 20% and 22% in Pérez-Martínez et al. 2013; Sánchez-Portal et al. 2015 respectively. Pérez-Martínez et al. (2013) considered only NLAGNs, but a shallower sample, while Sánchez-Portal et al. (2015) restrict their study to AGNs selected from ELGs extracted from a deep optical observation. The inclusion of selection criteria based in infrared, optical and X–rays makes the area considered irregular and may underestimate the fraction of AGNs. In fact, when an area correction is considered, both numbers come to a closer agreement (15.4% in this work versus 17% in Sánchez-Portal et al. (2015)).

The colour - magnitude diagram of the star forming galaxies (Figure 5.24) shows a smooth transition in the B-R colour from ELGs with no infrared emission to ELGs - infrared objects and infrared galaxies with no emission lines, with the population of the first group falling mainly in the blue cloud and shifting towards the red sequence with the increase of the infrared luminosity. This scenario suggests a gradual obscuration of the star formation activity by gas and dust, with Hα being more and more absorbed and its energy re-emitted in the far infrared until the line finally disappears completely. Taking this into account, the far infrared galaxies seating in the red sequence are not typical red objects (i.e.: with negligible star formation), but highly obscured star forming galaxies. This also explains the difference between the SFR derived from Hα with respect to that based in $L(IR)$ (the former much smaller than the latter).

The line-of-sight infalling group reported by Czoske et al. (2001) is mainly populated by galaxies in the blue cloud of the referred colour-magnitude diagram and harbours a larger fraction of infrared sources than the main structure (Figures 5.25 and 5.7). This is an indication of the enhanced star formation and nuclear activity due to the shock between both structures. It also explains the mild transition trends observed with respect to the clustercentric distance, since the projection on the cluster core of this infalling group overestimates the signs of galaxy activity and morphology fraction in the internal region.

With respect to the cluster structure, we have found a cavity in the mass distribution at 4 arcmin East from the X–Ray cluster centre. This cavity is actually empty of galaxies (see Figure 6.3) and its low X–ray luminosity points to a local deviation from the hydrostatic equilibrium, underlined by the alignment of cluster members perpendicular with respect to the clustercentric direction. The cavity is symmetrical to the overdensity reported by Kneib et al. (2003) with respect the centre of the cluster, suggesting a common origin, although we lack of evidences to make a stronger statement.

In summary, the processes driving the bulk of the transition effects in ZwCl0024+1652 take place in the intermediate-outer area of the virial volume (0.7 - 0.9 R_{vir}) by the interaction with the intracluster medium. The small gradient in the trends of the different galaxy characteristics indicates that the evolution of the galaxies in this area is dominated by starvation. On the other hand, the presence of galaxies with moderate to high activity in the line-of-sight infalling group supports the scenario of enhanced star formation and AGN presence due to the shock with the main structure. At the same time, this group alters the observation of the galaxies in the internal cluster region since its objects are projected onto the cluster core. With respect to the infrared population, extensively studied for the first time in this work, they harbour large amounts of star formation completely obscured that had remained hidden so far.

7.3 Future work

The GaLAxy Cluster Evolution program plans to extend its emission line survey to nine clusters at three redshift windows targetting for Hα/[N II], Hβ, [O II]and [O III]. So far we have completed the observations of two of the proposed clusters: ZwCl0024+1652 and RX J1257.2+4738.

The work presented here comprises the analysis of Hα/[N II] and Hβ emission lines in ZwCl0024-+1652, together with extensive data at the widest available spectral range. Now we plan to extend the study of star formation rates of cluster members incorporating the results from [O II]and comparing with those obtained from Hα and Hβ and from the infrared luminosity. The analysis of [O III] data will allow us to apply yet another AGN selection criteria via the BPT diagram.

We will also address the metallicity distribution in ZwCl0024+1652 by applying diagnostics based

in the N2 index (Denicoló et al. 2002), R23 (Pagel et al. 1979) and O2N2 (Alloin et al. 1979). The data required for this analysis is already available ([O II] and [O III]) and in the process of being reduced.

The incoming catalogs of cluster members from spectral line detections in the rest of the clusters will also open the possibility of performing in depth studies of the far infrared population, further exploiting *Spitzer* and *Herschel* data. This will expand our view of the processes taking place in highly obscured objects and their dependence with redshift.

Last, but not least, the results from other on going surveys like HiZels or OTELO will allow us to thoroughly compare our findings related to cluster members to the field population at similar redshifts and areas.

In summary, we plan to fully exploit the wealth of data that GLACE will produce in the coming years to extent our current knowledge of the evolution of galaxies across the $z \leq 1$ time scale.

A

Cl0024+1654 multiwavelength catalogue

Table A.1: Fragment of the ZwCl0024+1652 multiwavelength catalogue of cluster members

ID	RA	DEC	XMM	ErrXMM	Chandra	ErrChan	FUV	ErrFUV	B	ErrB	K	ErrK	IR1	ErrIR1	MIPS	ErrMIPS	PACS	ErrPACS	SPIRE	ErrSPIRE	z
24935	6.527	17.058	-99.00	-99.00	-99.00	-99.00	24.93	0.29	23.58	0.03	22.77	0.27	-99.00	-99.00	-99.00	-99.00	-99.00	-99.00	-99.00	-99.00	0.423
39223	6.619	17.156	-99.00	-99.00	-99.00	-99.00	24.90	0.25	23.13	0.02	23.15	0.30	21.25	0.02	-99.00	-99.00	-99.00	-99.00	-99.00	-99.00	0.390
40513	6.661	17.164	-99.00	-99.00	-99.00	-99.00	24.85	0.27	22.36	0.01	21.80	0.09	20.08	0.01	18.23	0.08	13.75	0.35	-99.00	-99.00	0.391
60917	6.681	17.304	-99.00	-99.00	-99.00	-99.00	24.84	0.35	23.26	0.02	23.57	-99.00	-99.00	-99.00	-99.00	-99.00	-99.00	-99.00	-99.00	-99.00	0.381
52479	6.682	17.247	-99.00	-99.00	-99.00	-99.00	24.83	0.41	23.87	0.04	23.05	0.31	-99.00	-99.00	18.26	0.16	13.91	0.59	-99.00	-99.00	0.393
21139	6.547	17.034	-99.00	-99.00	-99.00	-99.00	24.79	0.29	23.37	0.02	22.94	0.26	-99.00	-99.00	-99.00	-99.00	-99.00	-99.00	-99.00	-99.00	0.387
32106	6.475	17.105	-99.00	-99.00	-99.00	-99.00	24.78	0.26	22.49	0.01	21.00	0.06	-99.00	-99.00	18.46	0.13	-99.00	-99.00	-99.00	-99.00	0.444
39346	6.635	17.157	-99.00	-99.00	-99.00	-99.00	24.77	0.26	22.96	0.01	23.87	0.51	21.51	0.02	-99.00	-99.00	-99.00	-99.00	-99.00	-99.00	0.391
43747	6.567	17.187	-99.00	-99.00	-99.00	-99.00	24.73	0.27	23.67	0.03	23.56	-99.00	-99.00	-99.00	-99.00	-99.00	-99.00	-99.00	-99.00	-99.00	0.363
53155	6.657	17.251	-99.00	-99.00	-99.00	-99.00	24.73	0.28	23.18	0.03	23.32	-99.00	-99.00	-99.00	-99.00	-99.00	-99.00	-99.00	-99.00	-99.00	0.397
43840	6.595	17.187	-99.00	-99.00	-99.00	-99.00	24.73	0.25	22.46	0.01	22.23	0.16	20.43	0.02	18.78	0.14	14.00	0.43	-99.00	-99.00	0.397
47779	6.636	17.215	-99.00	-99.00	-99.00	-99.00	24.72	0.26	22.97	0.01	21.88	0.08	-99.00	-99.00	18.44	0.12	14.20	0.49	-99.00	-99.00	0.415
38129	6.724	17.147	-99.00	-99.00	-99.00	-99.00	24.71	0.30	22.36	0.01	21.08	0.06	-99.00	-99.00	-99.00	-99.00	-99.00	-99.00	-99.00	-99.00	0.395
28388	6.588	17.081	-99.00	-99.00	-99.00	-99.00	24.70	0.37	22.69	0.02	21.17	0.07	-99.00	-99.00	-99.00	-99.00	-99.00	-99.00	-99.00	-99.00	0.406
35952	6.552	17.132	-99.00	-99.00	-99.00	-99.00	24.70	0.37	23.56	0.03	23.48	-99.00	-99.00	-99.00	-99.00	-99.00	-99.00	-99.00	-99.00	-99.00	0.379
26501	6.642	17.069	-99.00	-99.00	-99.00	-99.00	24.68	0.23	23.38	0.02	23.18	0.32	21.81	0.03	-99.00	-99.00	-99.00	-99.00	-99.00	-99.00	0.391
21662	6.466	17.038	-99.00	-99.00	-99.00	-99.00	24.60	0.24	23.75	0.04	23.51	-99.00	-99.00	-99.00	-99.00	-99.00	-99.00	-99.00	-99.00	-99.00	0.394
42780	6.681	17.181	-99.00	-99.00	-99.00	-99.00	24.60	0.25	23.57	0.03	23.59	-99.00	-99.00	-99.00	-99.00	-99.00	-99.00	-99.00	-99.00	-99.00	0.396
60154	6.598	17.300	-99.00	-99.00	-99.00	-99.00	24.57	0.23	23.78	0.03	23.81	-99.00	-99.00	-99.00	-99.00	-99.00	-99.00	-99.00	-99.00	-99.00	0.373
37087	6.444	17.141	-99.00	-99.00	-99.00	-99.00	24.55	0.37	23.81	0.03	23.74	-99.00	-99.00	-99.00	-99.00	-99.00	-99.00	-99.00	-99.00	-99.00	0.379
26645	6.583	17.069	-99.00	-99.00	-99.00	-99.00	24.53	0.35	22.20	0.01	20.86	0.04	-99.00	-99.00	-99.00	-99.00	-99.00	-99.00	-99.00	-99.00	0.379
39356	6.631	17.156	-99.00	-99.00	-99.00	-99.00	24.51	0.23	23.11	0.02	22.95	0.30	21.00	0.01	-99.00	-99.00	-99.00	-99.00	-99.00	-99.00	0.387
38357	6.578	17.149	-99.00	-99.00	-99.00	-99.00	24.49	0.22	23.07	0.02	21.62	0.08	-99.00	-99.00	-99.00	-99.00	-99.00	-99.00	-99.00	-99.00	0.400
47086	6.717	17.210	-99.00	-99.00	-99.00	-99.00	24.48	0.35	22.71	0.01	21.80	0.09	-99.00	-99.00	-99.00	-99.00	-99.00	-99.00	-99.00	-99.00	0.392
53275	6.536	17.250	-99.00	-99.00	-99.00	-99.00	24.47	0.34	22.80	0.02	21.67	0.12	-99.00	-99.00	-99.00	-99.00	-99.00	-99.00	-99.00	-99.00	0.396
50868	6.719	17.233	-99.00	-99.00	-99.00	-99.00	24.46	0.32	21.74	0.01	19.56	0.01	-99.00	-99.00	16.43	0.03	12.70	0.26	12.87	0.09	0.380
61662	6.672	17.310	-99.00	-99.00	-99.00	-99.00	24.45	0.21	23.08	0.02	23.20	0.29	-99.00	-99.00	-99.00	-99.00	-99.00	-99.00	-99.00	-99.00	0.395
26774	6.585	17.070	-99.00	-99.00	-99.00	-99.00	24.45	0.21	22.26	0.01	22.50	0.19	-99.00	-99.00	-99.00	-99.00	-99.00	-99.00	-99.00	-99.00	0.417
41587	6.699	17.162	-99.00	-99.00	-99.00	-99.00	24.39	0.25	17.88	0.00	16.94	0.00	18.81	0.01	17.10	0.04	13.31	0.25	13.01	0.06	0.399
57926	6.506	17.283	-99.00	-99.00	-99.00	-99.00	24.39	0.21	22.42	0.01	21.59	0.09	-99.00	-99.00	-99.00	-99.00	-99.00	-99.00	-99.00	-99.00	0.363
45426	6.505	17.198	-99.00	-99.00	-99.00	-99.00	24.38	0.21	23.68	0.04	23.53	-99.00	-99.00	-99.00	-99.00	-99.00	-99.00	-99.00	-99.00	-99.00	0.392
35325	6.643	17.128	-99.00	-99.00	-99.00	-99.00	24.35	0.29	22.42	0.01	22.64	0.21	20.75	0.01	-99.00	-99.00	-99.00	-99.00	-99.00	-99.00	0.381
38048	6.616	17.148	-99.00	-99.00	-99.00	-99.00	24.33	0.21	23.48	0.03	23.46	-99.00	21.99	0.03	-99.00	-99.00	-99.00	-99.00	-99.00	-99.00	0.381
44872	6.442	17.195	-99.00	-99.00	-99.00	-99.00	24.32	0.23	23.85	0.04	23.46	-99.00	-99.00	-99.00	-99.00	-99.00	-99.00	-99.00	-99.00	-99.00	0.396
26115	6.527	17.067	-99.00	-99.00	-99.00	-99.00	24.30	0.30	23.30	0.02	23.44	0.39	-99.00	-99.00	-99.00	-99.00	-99.00	-99.00	-99.00	-99.00	0.402
19719	6.735	17.021	-99.00	-99.00	-99.00	-99.00	24.30	0.23	22.67	0.01	22.42	0.19	-99.00	-99.00	17.89	0.06	-99.00	-99.00	-99.00	-99.00	0.395
52772	6.481	17.248	-99.00	-99.00	-99.00	-99.00	24.30	0.22	22.94	0.02	21.92	0.13	-99.00	-99.00	-99.00	-99.00	-99.00	-99.00	-99.00	-99.00	0.397
46057	6.607	17.201	-99.00	-99.00	-99.00	-99.00	24.29	0.21	21.80	0.01	20.81	0.04	-99.00	-99.00	17.14	0.04	13.04	0.20	-99.00	-99.00	0.392
43674	6.647	17.186	-99.00	-99.00	-99.00	-99.00	24.28	0.22	21.94	0.01	21.19	0.06	19.68	0.01	17.79	0.06	13.82	0.37	-99.00	-99.00	0.394
32796	6.494	17.112	-99.00	-99.00	-99.00	-99.00	24.27	0.23	23.81	0.04	23.65	-99.00	-99.00	-99.00	-99.00	-99.00	-99.00	-99.00	-99.00	-99.00	0.393
60215	6.672	17.299	-99.00	-99.00	-99.00	-99.00	24.25	0.22	22.50	0.01	21.28	0.07	-99.00	-99.00	18.56	0.15	-99.00	-99.00	-99.00	-99.00	0.402
29122	6.577	17.087	-99.00	-99.00	-99.00	-99.00	24.24	0.20	22.92	0.02	22.78	0.22	-99.00	-99.00	-99.00	-99.00	-99.00	-99.00	-99.00	-99.00	0.351
24540	6.481	17.056	-99.00	-99.00	-99.00	-99.00	24.24	0.28	22.30	0.01	21.54	0.06	-99.00	-99.00	17.65	0.07	-99.00	-99.00	-99.00	-99.00	0.423
35039	6.660	17.125	-99.00	-99.00	-99.00	-99.00	24.21	0.30	22.04	0.01	20.43	0.03	19.16	0.00	17.75	0.06	13.99	0.42	13.88	0.10	0.392
22128	6.444	17.040	-99.00	-99.00	-99.00	-99.00	24.20	0.20	22.47	0.01	22.48	0.22	-99.00	-99.00	-99.00	-99.00	-99.00	-99.00	-99.00	-99.00	0.432
28411	6.527	17.082	-99.00	-99.00	-99.00	-99.00	24.20	0.31	23.49	0.02	22.98	0.24	-99.00	-99.00	-99.00	-99.00	-99.00	-99.00	-99.00	-99.00	0.396
23885	6.553	17.051	-99.00	-99.00	-99.00	-99.00	24.19	0.31	22.00	0.01	20.72	0.05	-99.00	-99.00	18.10	0.10	-99.00	-99.00	-99.00	-99.00	0.393
31057	6.638	17.099	-99.00	-99.00	-99.00	-99.00	24.17	0.31	22.79	0.02	23.23	-99.00	-99.00	-99.00	-99.00	-99.00	-99.00	-99.00	-99.00	-99.00	0.408
48327	6.532	17.218	-99.00	-99.00	-99.00	-99.00	24.15	0.24	23.43	0.03	23.43	-99.00	-99.00	-99.00	-99.00	-99.00	-99.00	-99.00	-99.00	-99.00	0.441
28717	6.465	17.081	-99.00	-99.00	-99.00	-99.00	24.14	0.28	22.91	0.03	22.27	0.26	-99.00	-99.00	-99.00	-99.00	-99.00	-99.00	-99.00	-99.00	0.450
60135	6.521	17.299	-99.00	-99.00	-99.00	-99.00	24.14	0.29	23.24	0.03	23.45	-99.00	-99.00	-99.00	-99.00	-99.00	-99.00	-99.00	-99.00	-99.00	0.383

Table A.2: continued

ID	RA	DEC	XMM	ErrXMM	Chandra	ErrChan	FUV	ErrFUV	B	ErrB	K	ErrK	IR1	ErrIR1	MIPS	ErrMIPS	PACS	ErrPACS	SPIRE	ErrSPIRE	z
28184	6.490	17.080	-99.00	-99.00	-99.00	-99.00	24.10	0.19	22.86	0.02	22.47	0.24	-99.00	-99.00	-99.00	-99.00	-99.00	-99.00	-99.00	-99.00	0.447
43730	6.656	17.184	-99.00	-99.00	-99.00	-99.00	24.10	0.22	22.58	0.02	21.85	0.13	20.42	0.01	18.33	0.09	13.88	0.39	-99.00	-99.00	0.396
58169	6.462	17.287	-99.00	-99.00	-99.00	-99.00	24.09	0.27	24.26	0.06	23.52	-99.00	-99.00	-99.00	-99.00	-99.00	-99.00	-99.00	-99.00	-99.00	0.471
20485	6.495	17.029	-99.00	-99.00	-99.00	-99.00	24.07	0.24	22.30	0.01	21.98	0.11	-99.00	-99.00	18.83	0.18	-99.00	-99.00	-99.00	-99.00	0.480
27600	6.670	17.076	-99.00	-99.00	-99.00	-99.00	24.05	0.30	23.25	0.03	22.03	0.19	21.80	0.02	-99.00	-99.00	-99.00	-99.00	-99.00	-99.00	0.378
26757	6.629	17.070	-99.00	-99.00	-99.00	-99.00	24.05	0.20	23.49	0.03	22.49	0.17	-99.00	-99.00	-99.00	-99.00	-99.00	-99.00	-99.00	-99.00	0.394
24253	6.615	17.054	-99.00	-99.00	-99.00	-99.00	24.03	0.21	22.32	0.01	22.10	0.15	-99.00	-99.00	-99.00	-99.00	-99.00	-99.00	-99.00	-99.00	0.390
20211	6.709	17.027	-99.00	-99.00	-99.00	-99.00	24.01	0.19	23.07	0.02	22.31	0.16	21.82	0.02	-99.00	-99.00	-99.00	-99.00	-99.00	-99.00	0.375
37698	6.665	17.145	-99.00	-99.00	-99.00	-99.00	24.01	0.18	23.25	0.02	23.45	0.34	21.73	0.03	-99.00	-99.00	-99.00	-99.00	-99.00	-99.00	0.390
42837	6.620	17.181	-99.00	-99.00	-99.00	-99.00	24.01	0.23	22.91	0.02	22.69	0.21	21.14	0.02	-99.00	-99.00	-99.00	-99.00	-99.00	-99.00	0.391
37037	6.751	17.137	-99.00	-99.00	-99.00	-99.00	23.99	0.23	21.33	0.01	19.71	0.02	-99.00	-99.00	17.49	0.08	19.06	4.28	-99.00	-99.00	0.378
40703	6.671	17.163	-99.00	-99.00	-99.00	-99.00	23.98	0.23	22.02	0.01	19.91	0.02	18.62	0.00	-99.00	-99.00	13.47	0.29	-99.00	-99.00	0.396
44574	6.602	17.192	-99.00	-99.00	-99.00	-99.00	23.98	0.19	22.54	0.01	22.75	0.28	-99.00	-99.00	-99.00	-99.00	-99.00	-99.00	-99.00	-99.00	0.390
50142	6.538	17.221	-99.00	-99.00	-99.00	-99.00	23.95	0.17	16.74	0.00	18.09	0.04	-99.00	-99.00	18.41	0.18	-99.00	-99.00	-99.00	-99.00	0.404
21983	6.711	17.039	-99.00	-99.00	-99.00	-99.00	23.94	0.30	23.00	0.02	23.25	0.42	21.41	0.02	-99.00	-99.00	-99.00	-99.00	-99.00	-99.00	0.392
39106	6.576	17.155	-99.00	-99.00	-99.00	-99.00	23.90	0.25	23.12	0.02	23.14	0.27	-99.00	-99.00	-99.00	-99.00	-99.00	-99.00	-99.00	-99.00	0.381
63049	6.644	17.320	-99.00	-99.00	-99.00	-99.00	23.86	0.24	23.97	0.05	23.53	-99.00	-99.00	-99.00	-99.00	-99.00	-99.00	-99.00	-99.00	-99.00	0.395
25001	6.465	17.059	-99.00	-99.00	-99.00	-99.00	23.86	0.23	23.11	0.02	22.99	0.25	-99.00	-99.00	-99.00	-99.00	-99.00	-99.00	-99.00	-99.00	0.477
34497	6.629	17.123	-99.00	-99.00	-99.00	-99.00	23.85	0.23	22.47	0.01	21.80	0.13	20.51	0.01	-99.00	-99.00	-99.00	-99.00	-99.00	-99.00	0.381
47973	6.614	17.214	-99.00	-99.00	-99.00	-99.00	23.84	0.17	20.28	0.00	18.90	0.01	-99.00	-99.00	-99.00	-99.00	-99.00	-99.00	-99.00	-99.00	0.380
38621	6.575	17.152	-99.00	-99.00	-99.00	-99.00	23.80	0.25	24.06	0.04	23.80	-99.00	-99.00	-99.00	-99.00	-99.00	-99.00	-99.00	-99.00	-99.00	0.381
28309	6.525	17.077	-99.00	-99.00	-99.00	-99.00	23.77	0.15	22.02	0.01	21.72	0.13	-99.00	-99.00	-99.00	-99.00	-99.00	-99.00	-99.00	-99.00	0.380
23160	6.513	17.045	-99.00	-99.00	-99.00	-99.00	23.76	0.19	21.90	0.01	20.49	0.04	-99.00	-99.00	17.82	0.06	-99.00	-99.00	-99.00	-99.00	0.360
21275	6.691	17.035	-99.00	-99.00	-99.00	-99.00	23.70	0.20	23.16	0.03	23.19	-99.00	21.99	0.02	-99.00	-99.00	-99.00	-99.00	-99.00	-99.00	0.366
54692	6.618	17.260	-99.00	-99.00	-99.00	-99.00	23.68	0.15	22.81	0.02	23.24	-99.00	-99.00	-99.00	-99.00	-99.00	-99.00	-99.00	-99.00	-99.00	0.390
43598	6.673	17.184	-99.00	-99.00	-99.00	-99.00	23.67	0.15	21.45	0.01	20.05	0.02	18.76	0.00	17.10	0.03	13.30	0.24	13.24	0.06	0.391
39399	6.564	17.155	-99.00	-99.00	-99.00	-99.00	23.66	0.23	23.07	0.03	23.17	-99.00	-99.00	-99.00	-99.00	-99.00	-99.00	-99.00	-99.00	-99.00	0.398
27596	6.453	17.074	-99.00	-99.00	-99.00	-99.00	23.66	0.15	21.38	0.01	19.62	0.02	-99.00	-99.00	-99.00	-99.00	-99.00	-99.00	12.40	0.09	0.378
62820	6.659	17.313	-99.00	-99.00	-99.00	-99.00	23.66	0.22	22.07	0.01	19.71	0.02	-99.00	-99.00	16.74	0.03	-99.00	-99.00	13.36	0.16	0.396
31033	6.612	17.099	-99.00	-99.00	-99.00	-99.00	23.61	0.22	23.14	0.02	23.51	-99.00	-99.00	-99.00	-99.00	-99.00	-99.00	-99.00	-99.00	-99.00	0.408
31327	6.643	17.101	-99.00	-99.00	-99.00	-99.00	23.57	0.18	22.33	0.01	22.10	0.13	-99.00	-99.00	-99.00	-99.00	-99.00	-99.00	-99.00	-99.00	0.382
29007	6.653	17.083	-99.00	-99.00	-99.00	-99.00	23.56	0.14	22.64	0.02	22.91	0.44	21.59	0.02	-99.00	-99.00	-99.00	-99.00	-99.00	-99.00	0.312
38520	6.628	17.151	-99.00	-99.00	-99.00	-99.00	23.54	0.14	22.72	0.01	23.98	-99.00	21.97	0.03	17.95	0.06	14.09	0.45	-99.00	-99.00	0.393
60608	6.629	17.302	-99.00	-99.00	-99.00	-99.00	23.50	0.21	22.78	0.01	23.03	0.28	-99.00	-99.00	-99.00	-99.00	-99.00	-99.00	-99.00	-99.00	0.395
54557	6.753	17.261	-99.00	-99.00	-99.00	-99.00	23.49	0.20	23.34	0.03	23.55	-99.00	-99.00	-99.00	-99.00	-99.00	-99.00	-99.00	-99.00	-99.00	0.404
64582	6.559	17.339	-99.00	-99.00	-99.00	-99.00	23.49	0.19	17.69	0.00	17.28	0.01	-99.00	-99.00	-99.00	-99.00	-99.00	-99.00	-99.00	-99.00	0.381
64083	6.591	17.324	-99.00	-99.00	-99.00	-99.00	23.48	0.18	20.86	0.00	19.70	0.02	-99.00	-99.00	16.27	0.02	-99.00	-99.00	12.62	0.09	0.381
52537	6.477	17.245	-99.00	-99.00	-99.00	-99.00	23.45	0.19	22.01	0.01	20.58	0.04	-99.00	-99.00	17.58	0.05	-99.00	-99.00	13.76	0.19	0.459
39287	6.672	17.155	-99.00	-99.00	-99.00	-99.00	23.45	0.21	22.36	0.01	23.50	-99.00	21.38	0.02	-99.00	-99.00	-99.00	-99.00	-99.00	-99.00	0.400
39753	6.602	17.157	-99.00	-99.00	-99.00	-99.00	23.44	0.24	22.22	0.01	21.13	0.08	19.95	0.02	18.77	0.18	13.79	0.36	15.09	0.25	0.394
52736	6.668	17.246	-99.00	-99.00	-99.00	-99.00	23.44	0.16	22.17	0.01	22.21	0.19	-99.00	-99.00	-99.00	-99.00	-99.00	-99.00	-99.00	-99.00	0.376
38655	6.671	17.151	-99.00	-99.00	-99.00	-99.00	23.38	0.21	22.53	0.02	23.23	-99.00	21.44	0.02	-99.00	-99.00	-99.00	-99.00	-99.00	-99.00	0.380
58199	6.585	17.284	1.145e-14	1.121e-15	7.742e-15	8.831e-16	23.37	0.12	21.82	0.01	20.05	0.02	-99.00	-99.00	17.59	0.05	-99.00	-99.00	-99.00	-99.00	0.385
29006	6.655	17.086	-99.00	-99.00	-99.00	-99.00	23.31	0.22	23.16	0.02	22.44	0.16	21.56	0.02	-99.00	-99.00	-99.00	-99.00	-99.00	-99.00	0.387
28590	6.468	17.082	-99.00	-99.00	-99.00	-99.00	23.31	0.11	22.71	0.02	23.16	-99.00	-99.00	-99.00	-99.00	-99.00	-99.00	-99.00	-99.00	-99.00	0.423
27216	6.525	17.072	-99.00	-99.00	-99.00	-99.00	23.29	0.19	21.73	0.01	20.36	0.03	-99.00	-99.00	15.80	0.01	-99.00	-99.00	12.12	0.04	0.390
41087	6.675	17.165	-99.00	-99.00	-99.00	-99.00	23.24	0.12	21.12	0.01	19.65	0.02	18.20	0.00	16.32	0.01	12.90	0.17	-99.00	-99.00	0.394
42818	6.472	17.178	-99.00	-99.00	-99.00	-99.00	23.21	0.21	22.70	0.02	21.52	0.10	-99.00	-99.00	-99.00	-99.00	-99.00	-99.00	-99.00	-99.00	0.360
53895	6.586	17.253	-99.00	-99.00	-99.00	-99.00	23.19	0.11	21.67	0.01	21.19	0.08	-99.00	-99.00	-99.00	-99.00	-99.00	-99.00	-99.00	-99.00	0.393
32400	6.517	17.105	-99.00	-99.00	-99.00	-99.00	23.17	0.15	21.43	0.01	20.30	0.07	-99.00	-99.00	17.96	0.07	-99.00	-99.00	14.25	0.28	0.400

Table A.3: continued

ID	RA	DEC	XMM	ErrXMM	Chandra	ErrChan	FUV	ErrFUV	B	ErrB	K	ErrK	IR1	ErrIR1	MIPS	ErrMIPS	PACS	ErrPACS	SPIRE	ErrSPIRE	z
39892	6.677	17.159	-99.00	-99.00	-99.00	-99.00	23.12	0.10	22.08	0.01	22.98	0.27	20.80	0.01	-99.00	-99.00	-99.00	-99.00	-99.00	-99.00	0.399
41056	6.633	17.167	-99.00	-99.00	-99.00	-99.00	22.96	0.15	21.55	0.01	21.27	0.06	19.57	0.01	16.34	0.02	12.79	0.16	-99.00	-99.00	0.402
49334	6.449	17.215	-99.00	-99.00	-99.00	-99.00	22.95	0.15	16.63	0.00	16.75	0.01	-99.00	-99.00	-99.00	-99.00	-99.00	-99.00	-99.00	-99.00	0.363
25960	6.748	17.063	-99.00	-99.00	-99.00	-99.00	22.84	0.38	21.09	0.01	20.11	0.04	-99.00	-99.00	17.56	0.05	-99.00	-99.00	-99.00	-99.00	0.396
52921	6.632	17.250	-99.00	-99.00	-99.00	-99.00	22.81	0.52	23.61	0.03	23.75	-99.00	-99.00	-99.00	-99.00	-99.00	-99.00	-99.00	-99.00	-99.00	0.391
27855	6.530	17.075	-99.00	-99.00	-99.00	-99.00	22.75	0.09	21.66	0.01	21.34	0.09	-99.00	-99.00	-99.00	-99.00	-99.00	-99.00	-99.00	-99.00	0.380
22581	6.748	17.041	-99.00	-99.00	-99.00	-99.00	22.64	0.08	21.50	0.01	22.14	0.19	19.84	0.02	-99.00	-99.00	-99.00	-99.00	-99.00	-99.00	0.387
27655	6.444	17.069	-99.00	-99.00	-99.00	-99.00	22.63	0.07	20.81	0.00	21.13	0.08	-99.00	-99.00	-99.00	-99.00	-99.00	-99.00	-99.00	-99.00	0.432
40486	6.576	17.164	1.234e-14	7.944e-16	1.248e-14	8.326e-16	22.46	0.08	18.49	0.00	18.61	0.01	-99.00	-99.00	17.30	0.08	13.34	0.25	13.32	0.06	0.394
38359	6.641	17.149	-99.00	-99.00	-99.00	-99.00	22.04	0.38	21.94	0.01	22.66	0.20	20.64	0.01	18.21	0.08	13.77	0.36	-99.00	-99.00	0.447
66643	6.602	17.347	-99.00	-99.00	-99.00	-99.00	-99.00	-99.00	26.37	-99.00	23.20	-99.00	-99.00	-99.00	-99.00	-99.00	-99.00	-99.00	-99.00	-99.00	0.327
66629	6.641	17.346	-99.00	-99.00	-99.00	-99.00	-99.00	-99.00	26.79	-99.00	23.63	-99.00	-99.00	-99.00	-99.00	-99.00	-99.00	-99.00	-99.00	-99.00	0.330
66409	6.462	17.346	-99.00	-99.00	-99.00	-99.00	-99.00	-99.00	25.55	0.21	23.42	-99.00	-99.00	-99.00	-99.00	-99.00	-99.00	-99.00	-99.00	-99.00	0.417
66328	6.553	17.347	-99.00	-99.00	-99.00	-99.00	-99.00	-99.00	22.77	0.01	20.23	0.02	-99.00	-99.00	-99.00	-99.00	-99.00	-99.00	-99.00	-99.00	0.300
66147	6.486	17.343	-99.00	-99.00	-99.00	-99.00	-99.00	-99.00	26.66	-99.00	23.49	-99.00	-99.00	-99.00	-99.00	-99.00	-99.00	-99.00	-99.00	-99.00	0.315
66114	6.499	17.344	-99.00	-99.00	-99.00	-99.00	-99.00	-99.00	26.41	-99.00	22.40	0.25	-99.00	-99.00	-99.00	-99.00	-99.00	-99.00	-99.00	-99.00	0.300
66097	6.723	17.344	-99.00	-99.00	-99.00	-99.00	-99.00	-99.00	24.62	0.08	21.61	0.10	-99.00	-99.00	-99.00	-99.00	-99.00	-99.00	-99.00	-99.00	0.357
66053	6.516	17.343	-99.00	-99.00	-99.00	-99.00	-99.00	-99.00	24.11	0.04	21.43	0.07	-99.00	-99.00	-99.00	-99.00	-99.00	-99.00	-99.00	-99.00	0.309
66036	6.572	17.344	-99.00	-99.00	-99.00	-99.00	-99.00	-99.00	24.22	0.06	21.74	0.11	-99.00	-99.00	-99.00	-99.00	-99.00	-99.00	-99.00	-99.00	0.303

Col.1: ObjID (M05), *Col.2:* RA (deg), *Col.3:* DEC (deg), *Col.4:* EPIC/XMM flux in 0.5-12keV (erg/cm^2/s),*Col.5:* EPIC/XMM error in 0.5-12keV (erg/cm^2/s), *Col.6:* Chandra flux in 0.5-7keV (erg/cm^2/s),*Col.7:* Chandra flux error in 0.5-7keV (erg/cm^2/s), *Col.8:* FUV flux (AB magnitude), *Col.9:* FUV error (AB magnitude) *Col.10:* B flux (AB magnitude), *Col.11:* B error (AB magnitude), *Col.12:* K (AB magnitude), *Col.13:* K error (AB magnitude), *Col.14:* IRAC 3.5μm flux (AB magnitude), *Col.15:* IRAC 3.5μm error (AB magnitude), *Col.16:* MIPS 24μm flux (AB magnitude), *Col.17:* MIPS 24μm error (AB magnitude), *Col.18:* PACS 100μm flux (AB magnitude), *Col.19:* PACS 100μm error (AB magnitude),*Col.20:* SPIRE 250μm flux (AB magnitude), *Col.21:* SPIRE 250μm error (AB magnitude), *Col.22:* Object redshift

B

Cl0024+1654 parameters catalogue

Table B.1: Fragment of the ZwCl0024+1652 parameters catalogue of cluster members

ID	RA	DEC	z	Type	MORPH	L_{IR}	Err($_{IR}$)	Stellar Mass	ErrStellarMass	SFR(Hα)	Σ_5	r_c
24935	6.5272	17.0579	0.423	SF_ZphotNoELG	99	-99.00	0.00	8.24	0.00	-99.00	27.60	2.95
39223	6.6190	17.1557	0.390	SF_ELG	5	10.17	0.01	8.35	0.00	1.46	193.62	0.51
40513	6.6610	17.1640	0.391	SF_ELG	5	10.83	0.00	9.27	0.00	5.63	236.55	0.28
60917	6.6806	17.3044	0.381	SF_ZspecNoELG	99	-99.00	4.49	8.85	0.90	-99.00	49.54	2.81
52479	6.6819	17.2466	0.393	SF_ZspecNoELG	99	10.81	0.03	8.22	0.16	-99.00	26.57	1.76
21139	6.5468	17.0341	0.387	SF_ZphotNoELG	99	-99.00	0.00	8.99	0.00	-99.00	17.51	3.05
32106	6.4752	17.1052	0.444	SF_ZphotNoELG	99	10.97	0.01	9.52	0.00	-99.00	15.93	3.31
39346	6.6348	17.1567	0.391	AGN_ELG	3	10.14	0.01	-99.00	0.00	-99.00	232.39	0.22
43747	6.5672	17.1870	0.363	SF_ZphotNoELG	99	-99.00	0.00	8.56	0.00	-99.00	20.42	1.52
53155	6.6571	17.2509	0.397	SF_ZspecNoELG	99	-99.00	0.00	8.84	0.00	-99.00	41.32	1.72
43840	6.5952	17.1869	0.397	AGN_ELG	5	10.59	0.00	-99.00	0.00	-99.00	99.95	1.04
47779	6.6361	17.2146	0.415	SF_ZspecNoELG	3	10.88	0.01	8.43	0.00	-99.00	56.51	1.03
38129	6.7243	17.1469	0.395	SF_ZspecNoELG	5	-99.00	0.00	9.33	0.00	-99.00	37.99	1.47
28388	6.5876	17.0808	0.406	SF_ZspecNoELG	99	-99.00	0.00	9.32	0.00	-99.00	37.09	1.89
35952	6.5524	17.1324	0.379	SF_ZspecNoELG	99	-99.00	0.00	8.44	0.05	-99.00	22.58	1.80
26501	6.6424	17.0694	0.391	SF_ZspecNoELG	99	-99.00	0.00	8.23	0.00	-99.00	19.31	1.78
21662	6.4662	17.0378	0.394	SF_ZspecNoELG	99	-99.00	0.00	8.30	0.14	-99.00	14.14	4.07
42780	6.6806	17.1808	0.396	AGN_ELG	99	-99.00	0.00	-99.00	0.00	-99.00	127.43	0.73
60154	6.5979	17.2997	0.373	SF_ZspecNoELG	3	-99.00	0.00	8.44	0.00	-99.00	25.42	2.79
37087	6.4440	17.1413	0.379	SF_ZspecNoELG	1	-99.00	0.00	8.44	0.00	-99.00	8.01	3.72

Table B.2: continued

ID	RA	DEC	z	Type	MORPH	L_{IR}	Err($_{IR}$)	Stellar Mass	ErrStellarMass	SFR(Hα)	Σ_5	r_c
26645	6.5833	17.0687	0.379	SF_ZspecNoELG	99	-99.00	0.00	9.32	0.00	-99.00	21.72	2.12
39356	6.6306	17.1562	0.387	SF_ELG	3	10.26	0.01	8.39	0.00	1.54	151.35	0.30
38357	6.5777	17.1492	0.400	AGN_ELG	7	-99.00	0.00	-99.00	0.00	-99.00	92.14	1.27
47086	6.7169	17.2097	0.392	SF_ZspecNoELG	3	-99.00	0.00	8.47	0.00	-99.00	19.13	1.59
53275	6.5357	17.2497	0.396	SF_ELG	4	-99.00	0.00	8.56	0.00	4.19	13.73	2.63
50868	6.7188	17.2332	0.380	SF_ZspecNoELG	99	11.23	0.01	10.28	0.00	-99.00	25.14	1.91
61662	6.6723	17.3103	0.395	SF_ZspecNoELG	99	-99.00	0.00	9.08	0.00	-99.00	33.90	2.89
26774	6.5854	17.0704	0.417	SF_ZphotNoELG	99	-99.00	2.57	9.33	0.01	-99.00	29.96	2.08
41587	6.6991	17.1619	0.399	SF_ZspecNoELG	99	11.19	0.00	11.30	0.00	-99.00	53.98	0.98
57926	6.5061	17.2835	0.363	SF_ZphotNoELG	99	-99.00	0.00	9.19	0.00	-99.00	17.48	3.46
45426	6.5047	17.1983	0.392	SF_ZspecNoELG	99	-99.00	4.80	8.40	0.68	-99.00	8.37	2.68
35325	6.6427	17.1285	0.381	SF_ELG	99	10.39	0.00	9.26	0.00	3.61	91.02	0.64
38048	6.6155	17.1476	0.381	SF_ELG	6	-99.00	5.59	8.24	0.03	2.03	125.35	0.62
44872	6.4420	17.1945	0.396	SF_ZphotNoELG	99	-99.00	0.00	8.42	0.00	-99.00	8.45	3.79
26115	6.5265	17.0667	0.402	SF_ZphotNoELG	99	-99.00	0.00	8.45	0.12	-99.00	55.68	2.85
19719	6.7346	17.0213	0.395	SF_ZspecNoELG	0	11.03	0.00	9.10	0.00	-99.00	10.59	3.15
52772	6.4814	17.2475	0.397	SF_ZspecNoELG	5	-99.00	0.00	8.48	0.00	-99.00	13.56	3.43
46057	6.6071	17.2015	0.392	AGN_ELG	3	11.29	0.00	-99.00	0.00	-99.00	240.54	1.04
43674	6.6466	17.1857	0.394	SF_ELG	99	10.89	0.05	9.44	0.00	7.89	141.03	0.46
32796	6.4939	17.1122	0.393	SF_ZphotNoELG	99	-99.00	0.00	8.46	0.00	-99.00	21.49	2.94

Table B.3: continued

ID	RA	DEC	z	Type	MORPH	L_{IR}	Err($_{IR}$)	Stellar Mass	ErrStellarMass	SFR(Hα)	Σ_5	r_c
60215	6.6721	17.2987	0.402	SF_ZspecNoELG	99	10.79	0.01	9.26	0.00	-99.00	29.40	2.67
29122	6.5770	17.0869	0.351	SF_ZphotNoELG	99	-99.00	0.00	8.97	0.00	-99.00	23.79	1.91
24540	6.4813	17.0560	0.423	SF_ZphotNoELG	99	11.22	0.00	9.33	0.00	-99.00	21.07	3.64
35039	6.6603	17.1253	0.392	SF_ZspecNoELG	3	10.82	0.00	10.01	0.00	-99.00	94.49	0.75
22128	6.4440	17.0402	0.432	SF_ZphotNoELG	99	-99.00	0.00	8.75	0.00	-99.00	13.09	4.38
28411	6.5274	17.0819	0.396	SF_ZphotNoELG	99	-99.00	0.00	8.46	0.00	-99.00	41.13	2.66
23885	6.5528	17.0508	0.393	SF_ZspecNoELG	3	10.94	0.01	9.42	0.00	-99.00	14.67	2.73
31057	6.6383	17.0991	0.408	SF_ZspecNoELG	99	-99.00	0.00	9.00	0.00	-99.00	79.67	1.21
48327	6.5317	17.2180	0.441	SF_ZphotNoELG	99	-99.00	5.05	8.09	0.46	-99.00	14.64	2.35
28717	6.4654	17.0813	0.450	SF_ZphotNoELG	99	-99.00	0.00	9.14	0.59	-99.00	26.24	3.65
60135	6.5212	17.2989	0.383	SF_ZspecNoELG	5	-99.00	0.00	9.12	0.00	-99.00	17.08	3.48
28184	6.4896	17.0802	0.447	SF_ZphotNoELG	3	-99.00	0.00	8.62	0.00	-99.00	12.09	3.27
43730	6.6556	17.1841	0.396	SF_ELG	99	10.55	0.00	8.99	0.00	2.98	154.46	0.46
58169	6.4616	17.2866	0.471	SF_ZphotNoELG	99	-99.00	0.00	7.92	0.00	-99.00	29.18	4.14
20485	6.4948	17.0292	0.480	SF_ZphotNoELG	99	10.92	0.01	9.52	0.00	-99.00	6.18	3.76
27600	6.6703	17.0758	0.378	SF_ZspecNoELG	99	-99.00	0.00	8.92	0.00	-99.00	14.69	1.71
26757	6.6293	17.0704	0.394	SF_ZspecNoELG	99	-99.00	0.00	8.48	0.54	-99.00	19.63	1.78
24253	6.6150	17.0535	0.390	SF_ZspecNoELG	3	-99.00	0.00	9.38	0.00	-99.00	33.94	2.16
20211	6.7086	17.0273	0.375	SF_ZspecNoELG	99	-99.00	0.00	8.66	0.00	-99.00	23.78	2.83
37698	6.6651	17.1454	0.390	SF_ZphotNoELG	99	9.98	0.01	8.53	0.00	-99.00	211.79	0.47

Table B.4: continued

ID	RA	DEC	z	Type	MORPH	L_{IR}	Err($_{IR}$)	Stellar Mass	ErrStellarMass	SFR(Hα)	Σ_5	r_c
42837	6.6201	17.1805	0.391	SF_ELG	3	-99.00	0.00	8.42	0.00	1.53	191.13	0.59
37037	6.7508	17.1375	0.378	SF_ZspecNoELG	99	10.23	0.32	10.25	0.00	-99.00	28.33	1.98
40703	6.6705	17.1633	0.396	AGN_ELG	3	11.38	0.01	-99.00	0.00	-99.00	288.80	0.45
44574	6.6022	17.1917	0.390	SF_ELG	99	10.45	0.01	8.71	0.00	3.42	156.54	0.98
50142	6.5378	17.2212	0.404	SF_ELG	5	10.86	0.01	11.46	0.00	5.87	20.70	2.28
21983	6.7106	17.0393	0.392	SF_ZspecNoELG	99	-99.00	0.00	8.67	0.00	-99.00	28.76	2.64
39106	6.5761	17.1549	0.381	SF_ELG	1	-99.00	2.54	8.49	0.00	2.48	68.49	1.28
63049	6.6442	17.3200	0.395	SF_ZspecNoELG	99	-99.00	0.00	8.44	0.02	-99.00	21.73	3.03
25001	6.4652	17.0594	0.477	SF_ZphotNoELG	99	-99.00	0.00	8.70	0.14	-99.00	22.51	3.85
34497	6.6293	17.1226	0.381	SF_ELG	5	10.39	0.00	8.64	0.00	2.70	66.34	0.81
47973	6.6143	17.2141	0.380	SF_ELG	3	-99.00	0.00	10.70	0.00	5.00	125.23	1.16
38621	6.5747	17.1524	0.381	SF_ZspecNoELG	99	-99.00	0.00	8.02	0.02	-99.00	89.49	1.32
28309	6.5246	17.0773	0.380	SF_ZspecNoELG	99	-99.00	0.00	9.43	0.00	-99.00	45.22	2.75
23160	6.5129	17.0455	0.360	SF_ZphotNoELG	99	10.92	0.00	9.44	0.00	-99.00	17.56	3.31
21275	6.6913	17.0347	0.366	SF_ZphotNoELG	99	-99.00	0.00	8.42	0.57	-99.00	32.54	2.58
54692	6.6183	17.2600	0.390	SF_ELG	99	-99.00	0.00	8.49	0.08	1.94	36.25	1.95
43598	6.6730	17.1838	0.391	AGN_ELG	99	11.14	0.00	-99.00	0.00	-99.00	78.93	0.65
39399	6.5636	17.1550	0.398	AGN_ELG	99	-99.00	0.00	-99.00	0.00	-99.00	38.43	1.51
27596	6.4526	17.0745	0.378	SF_ZphotNoELG	99	11.67	0.14	10.24	0.00	-99.00	15.49	3.92
62820	6.6590	17.3131	0.396	SF_ZspecNoELG	99	11.07	0.03	10.08	0.00	-99.00	21.51	2.91

Table B.5: continued

ID	RA	DEC	z	Type	MORPH	L_{IR}	Err($_{IR}$)	Stellar Mass	ErrStellarMass	SFR(Hα)	Σ_5	r_c
31033	6.6116	17.0993	0.408	SF_ZspecNoELG	2	-99.00	0.00	8.18	0.00	-99.00	28.35	1.35
31327	6.6428	17.1011	0.382	SF_ELG	99	-99.00	0.00	9.35	0.00	3.63	66.38	1.17
29007	6.6528	17.0835	0.312	SF_ZphotNoELG	99	-99.00	0.00	8.48	0.00	-99.00	31.01	1.51
38520	6.6284	17.1507	0.393	SF_ELG	1	11.00	0.01	8.50	0.64	11.07	113.36	0.38
60608	6.6288	17.3023	0.395	SF_ZspecNoELG	99	-99.00	0.00	8.67	0.00	-99.00	44.58	2.71
54557	6.7526	17.2610	0.404	SF_ZspecNoELG	3	-99.00	0.00	8.30	0.00	-99.00	15.29	2.73
64582	6.5588	17.3386	0.381	SF_ZspecNoELG	99	-99.00	0.00	11.07	0.00	-99.00	23.89	3.75
64083	6.5906	17.3240	0.381	SF_ZspecNoELG	99	11.34	0.01	9.98	0.00	-99.00	15.90	3.27
52537	6.4774	17.2454	0.459	SF_ZphotNoELG	5	11.00	0.05	9.71	0.00	-99.00	13.68	3.48
39287	6.6715	17.1551	0.400	SF_ELG	6	10.03	0.96	8.76	0.65	4.37	330.47	0.49
39753	6.6015	17.1574	0.394	AGN_ELG	99	10.48	0.01	-99.00	0.00	-99.00	49.13	0.82
52736	6.6682	17.2461	0.376	SF_ZspecNoELG	99	-99.00	2.99	8.82	0.01	-99.00	34.77	1.67
38655	6.6713	17.1514	0.380	AGN_ELG	5	-99.00	0.00	-99.00	0.00	-99.00	210.92	0.51
58199	6.5846	17.2843	0.385	AGN_ELG	99	10.85	0.00	-99.00	0.00	-99.00	12.44	2.60
29006	6.6554	17.0858	0.387	SF_ZphotNoELG	99	-99.00	0.00	8.75	0.00	-99.00	54.09	1.47
28590	6.4684	17.0820	0.423	SF_ZphotNoELG	99	-99.00	4.65	8.83	0.73	-99.00	19.83	3.60
27216	6.5251	17.0720	0.390	SF_ZspecNoELG	99	11.57	0.00	9.57	0.00	-99.00	42.48	2.81
41087	6.6747	17.1646	0.394	SF_ELG	3	11.41	0.01	9.89	0.00	12.45	317.46	0.53
42818	6.4719	17.1782	0.360	SF_ZphotNoELG	5	-99.00	0.00	9.18	0.00	-99.00	18.35	3.20
53895	6.5859	17.2535	0.393	SF_ZphotNoELG	99	10.60	0.00	9.63	0.00	-99.00	87.68	2.07

Table B.6: continued

ID	RA	DEC	z	Type	MORPH	L_{IR}	Err($_{IR}$)	Stellar Mass	ErrStellarMass	SFR(Hα)	Σ_5	r_c
32400	6.5174	17.1051	0.400	SF_ZspecNoELG	3	10.68	0.01	9.80	0.01	-99.00	21.92	2.60
39892	6.6769	17.1588	0.399	SF_ELG	5	10.25	0.01	9.02	0.00	7.34	144.00	0.57
41056	6.6335	17.1674	0.402	SF_ELG	99	11.37	0.00	9.11	0.00	26.56	425.96	0.25
49334	6.4488	17.2146	0.363	SF_ZphotNoELG	5	-99.00	0.00	11.39	0.00	-99.00	16.93	3.75
25960	6.7479	17.0626	0.396	SF_ZspecNoELG	99	11.16	0.00	9.87	0.00	-99.00	38.07	2.67
52921	6.6318	17.2498	0.391	SF_ZspecNoELG	99	-99.00	0.00	8.53	0.00	-99.00	63.43	1.71
27855	6.5300	17.0751	0.380	SF_ZspecNoELG	99	-99.00	0.00	9.02	0.00	-99.00	66.89	2.70
22581	6.7476	17.0413	0.387	SF_ZphotNoELG	99	-99.00	0.00	8.98	0.00	-99.00	18.96	2.97
27655	6.4436	17.0686	0.432	SF_ZphotNoELG	99	-99.00	0.00	9.81	0.00	-99.00	10.80	4.12
40486	6.5757	17.1635	0.394	SF_ELG	99	11.15	0.00	10.79	0.00	7.64	41.46	1.29
38359	6.6411	17.1489	0.447	SF_ZphotNoELG	5	10.85	0.01	9.00	0.00	-99.00	197.44	0.26
66643	6.6019	17.3473	0.327	SF_ZphotNoELG	99	-99.00	0.00	7.94	0.97	-99.00	10.54	3.65
66629	6.6412	17.3465	0.330	SF_ZphotNoELG	-1	-99.00	0.00	9.06	0.37	-99.00	10.69	3.54
66409	6.4624	17.3457	0.417	SF_ZphotNoELG	99	-99.00	0.00	9.03	0.68	-99.00	9.08	4.87
66328	6.5531	17.3473	0.300	SF_ZphotNoELG	99	-99.00	0.00	8.93	0.00	-99.00	11.20	3.94
66147	6.4862	17.3430	0.315	SF_ZphotNoELG	99	-99.00	0.00	7.87	0.71	-99.00	18.84	4.54
66114	6.4986	17.3437	0.300	SF_ZphotNoELG	99	-99.00	0.00	7.73	1.72	-99.00	16.75	4.41
66097	6.7231	17.3440	0.357	SF_ZphotNoELG	99	-99.00	0.00	9.06	0.00	-99.00	24.25	3.77
66053	6.5164	17.3432	0.309	SF_ZphotNoELG	99	-99.00	0.00	9.08	0.00	-99.00	21.21	4.21
66036	6.5719	17.3438	0.303	SF_ZphotNoELG	99	-99.00	0.00	8.60	0.00	-99.00	12.53	3.75

Col.1: ObjID (M05), *Col.2:* RA (deg), *Col.3:* DEC (deg), *Col.4:* Object redshift, *Col.5:* Object classification (SF/AGN; Zspec/Zphot; ELG/noELG), *Col.6:* Morphological classification (Treu et al. 2003), *Col.7:* Infrared luminosity (8-1000μm) (log L$\odot$),*Col.8:* Infrared luminosity error, *Col.9:* Stellar Mass ((log M$\odot$), *Col.10:* Stellar Mass error, *Col.11:* Star Formation Rate (from Hα flux) (M$\odot$/yr), *Col.12:* Local Density (Mpc^{-2}), *Col.13:* Cumulocentric distance (Mpc)

Bibliography

Abraham, R. G., van den Bergh, S., Glazebrook, K., et al. 1996, ApJS, 107, 1

Alloin, D., Collin-Souffrin, S., & Joly, M. 1979, A&AS, 37, 361

Altieri, B., Berta, S., Lutz, D., et al. 2010, A&A, 518, L17

Arnouts, S., Cristiani, S., Moscardini, L., et al. 1999, Monthly Notices of the Royal Astronomical Society, 310, 540

Arribas, S., Mediavilla, E., García-Lorenzo, B., & del Burgo, C. 1997, ApJ, 490, 227

Baldwin, J. A., Phillips, M. M., & Terlevich, R. 1981, PASP, 93, 5-19

Balogh, M. L., Morris, S. L., Yee, H. K. C., Carlberg, R. G., & Ellingson, E. 1999, ApJ, 527, 54

Barrena, R., Biviano, A., Ramella, M., Falco, E. E., & Seitz, S. 2002, A&A, 386, 816

Bauer, F. E., Alexander, D. M., Brandt, W. N., et al. 2004, AJ, 128, 2048

Bertin, E. & Arnouts, S. 1996, A&A, 117, 393

Biviano, A. & Katgert, P. 2004, A&A, 424, 779

Biviano, A., Metcalfe, L., McBreen, B., et al. 2004, A&A, 425, 33

Blanton, M. R. & Roweis, S. 2007, AJ, 133, 734

Bruzual, G. & Charlot, S. 2003, Monthly Notices of the Royal Astronomical Society, 344, 1000

Buat, V., Giovannoli, E., Burgarella, D., et al. 2010, MNRAS, 409, L1

Burton, C. S., Jarvis, M. J., Smith, D. J. B., et al. 2013, MNRAS, 433, 771

Butcher, H. & Oemler, Jr., A. 1984, ApJ, 285, 426

Cabrera-Lavers, A. 2015, in Highlights of Spanish Astrophysics VIII, ed. A. J. Cenarro, F. Figueras, C. Hernández-Monteagudo, J. Trujillo Bueno, & L. Valdivielso, 782–785

Calzetti, D., Armus, L., Bohlin, R. C., et al. 2000, ApJ, 533, 682

Cepa, J., Aguiar, M., Bland-Hawthorn, J., et al. 2003, in Revista Mexicana de Astronomia y Astrofisica Conference Series, Vol. 16, Revista Mexicana de Astronomia y Astrofisica Conference Series, ed. J. M. Rodriguez Espinoza, F. Garzon Lopez, & V. Melo Martin, 13–18

Cepa, J., Aguiar, M., Castañeda, H. O., et al. 2005, in Revista Mexicana de Astronomia y Astrofisica Conference Series, Vol. 24, Revista Mexicana de Astronomia y Astrofisica Conference Series, ed. A. M. Hidalgo-Gámez, J. J. González, J. M. Rodríguez Espinosa, & S. Torres-Peimbert, 1–6

Chabrier, G. 2003, PASP, 115, 763

Chary, R. & Elbaz, D. 2001, ApJ, 556, 562

Cid Fernandes, R. G., Stasińska, M. S., Schlickmann, A., et al. 2010, MNRAS, 403, 1036

Ciliegi, P., Zamorani, G., Hasinger, G., et al. 2003, Astronomy and Astrophysics, 398, 901

Coia, D., McBreen, B., Metcalfe, L., et al. 2005, A&A, 431, 433

Constantin, A., Hoyle, F., & Vogeley, M. S. 2008, ApJ, 673,715

Cuillandre, J.-C., Mellier, Y., Dupin, J.-P., et al. 1996, PASP, 108, 1120

Czoske, O., Kneib, J.-P., Soucail, G., et al. 2001, A&A, 372, 391

Czoske, O., Moore, B., Kneib, J.-P., & Soucail, G. 2002, A&A, 386, 31

de Graauw, T., Helmich, F. P., Phillips, T. G., et al. 2010, A&A, 518, L6

de Ruiter, H. R., Willis, A. G., & Arp, H. C. 1977, A&AS, 28, 211

den Herder, J. W., Brinkman, A. C., Kahn, S. M., et al. 2001, A&A, 365, L7

Denicoló, G., Terlevich, R., & Terlevich, E. 2002, MNRAS, 330, 69

Domínguez Sánchez, H., Bongiovanni, A., Lara-López, M. A., et al. 2014, MNRAS, 441, 2

Donley, J. L., Koekemoer, A. M., Brusa, M., et al. 2012, ApJ, 748,142

Dressler, A. 1980, ApJ, 236, 351

Dressler, A., Oemler, Jr., A., Couch, W. J., et al. 1997, ApJ, 490, 577

Eastman, J., Martini, P., Sivakoff, G., et al. 2007, ApJ, 664,L9

Elbaz, D., Daddi, E., Le Borgne, D., et al. 2007, A&A, 468, 33

Ettori, S., Donnarumma, A., Pointecouteau, E., et al. 2013, Space Sci. Rev., 177, 119

Evans, I. N., Primini, F. A., Glotfelty, K. J., et al. 2010, ApJS, 189,37

Fazio, G. G., Hora, J. L., Allen, L. E., et al. 2004, ApJS, 154, 10

Fernández Lorenzo, M., Cepa, J., Bongiovanni, A., et al. 2009, A&A, 496, 389

Filippenko, A. & Greenstein, J. L. 1984, PASP, 96, 530

Galametz, A., Stern, D., Eisenhardt, P. R. M., et al. 2009, ApJS, 694, 1309

García-Lorenzo, B., Sánchez, S. F., Mediavilla, E., González-Serrano, J. I., & Christensen, L. 2005, ApJ, 621, 146

Geach, J. E., Smail, I., Ellis, R. S., et al. 2006, ApJ, 649, 661

Geller, M. J. & Beers, T. C. 1982, PASP, 94, 421

Gilmour, R., Gray, M. E., Almaini, O., et al. 2007, MNRAS, 380,1467

González, J. J., Cepa, J., González-Serrano, J. I., & Sánchez-Portal, M. 2014, MNRAS, 443, 3289

Griffin, M. J., Abergel, A., Abreu, A., et al. 2010, A&A, 518, L3

Gruppioni, C., Pozzi, F., Rodighiero, G., et al. 2013, MNRAS, 432, 23

Haines, C. P., Pereira, M. J., Smith, G. P., et al. 2013, ApJ, 775, 126

Haines, C. P., Smith, G. P., Egami, E., et al. 2009, ApJ, 704, 126

Haines, C. P., Smith, G. P., Pereira, M. J., et al. 2010, A&A, 518, L19

Ho, L. C., Filippenko, A. V., & Sargent, W. L. W. 1997, ApJS, 112, 315

Hobson, M. P., Rocha, G., & Savage, R. S. 2010, Bayesian source extraction, 167

Hopkins, A. M., Driver, S. P., Brough, S., et al. 2013, MNRAS, 430, 2047

Houck, J. R., Roellig, T. L., van Cleve, J., et al. 2004, ApJS, 154, 18

Humason, M. & Sandage, A. 1957, Carnegie yearbook 1956, 61

Ilbert, O., Arnouts, S., McCracken, H. J., et al. 2006, Astronomy and Astrophysics, 457, 841

Ilbert, O., McCracken, H. J., Le Fèvre, O., et al. 2013, A&A, 556, A55

Jee, M. J., Ford, H. C., Illingworth, G. D., et al. 2007, ApJ, 661, 728

Jones, H. 2002, in Scientific Drivers for ESO Future VLT/VLTI Instrumentation, ed. J. Bergeron & G. Monnet, 66

Jones, H., Renzini, A., Rosati, P., & Seifert, W. 2001, The Messenger, 103, 10

Kaspi, S., Maoz, D., Netzer, H., et al. 1996, ApJ, 470, 336

Kauffmann, G., White, S. D. M., Heckman, T. M., et al. 2004, MNRAS, 353, 713

Kennicutt, Jr., R. C. 1992, ApJ, 388, 310

Kennicutt, Jr., R. C. 1998, ARA&A, 36, 189

Kewley, L. J., Dopita, M. A., Sutherland, R. S., Heisler, C. A., & Trevena, J. 2001, ApJ, 556, 121

Klesman, A. J. & Sarajedini, V. L. 2014, MNRAS, 442, 314

Kneib, J.-P., Hudelot, P., Ellis, R. S., et al. 2003, ApJ, 598, 804

Kodama, T. & Smail, I. 2001, MNRAS, 326, 637

Koyama, Y., Kodama, T., Shimasaku, K., et al. 2010, MNRAS, 403, 1611

Koyama, Y., Smail, I., Kurk, J., et al. 2013, MNRAS, 434, 423

Lara-López, M. A., Cepa, J., Castañeda, H., et al. 2010, PASP, 122, 1495

Lemaux, B. C., Lubin, L. M., Shapley, A., et al. 2010, ApJ, 716, 970

Luo, B., Brandt, W. N., Xue, Y. Q., et al. 2010, The Astrophysical Journal Supplement, 187, 560

Lutz, D., Poglitsch, A., Altieri, B., et al. 2011, A&A, 532, A90

Maccacaro, T., Gioia, I. M., Wolter, A., Zamorani, G., & Stocke, J. T. 1988, apj, 326, 680

Madau, P., Pozzetti, L., & Dickinson, M. 1998, ApJ, 498, 106

Makovoz, D. & Marleau, F. R. 2005, PASP, 117, 1113

Martin, D. C., Fanson, J., Schiminovich, D., et al. 2005, ApJ, 619, L1

Martini, P., Kelson, D. D., Mulchaey, J. S., & Trager, S. C. 2002, ApJ, 576, L109

Martini, P., Miller, E. D., Brodwin, M., et al. 2013, ApJ, 768, 1

Martini, P., Sivakoff, G. R., & Mulchaey, J. S. 2009, ApJ, 701, 66

Mason, K. O., Breeveld, A., Much, R., et al. 2001, A&A, 365, L36

Metcalfe, L., Fadda, D., & Biviano, A. 2005, Space Sci. Rev., 119, 425

Mihos, C. 2003, ArXiv Astrophysics e-prints

Miller, C. J., Nichol, R. C., Gómez, P. L., Hopkins, A. M., & Bernardi, M. 2003, ApJ, 597, 142

Monet, D. G., Levine, S. E., Canzian, B., et al. 2003, AJ, 125, 984

Moore, B., Lake, G., & Katz, N. 1998, ApJ, 495, 139

Moran, S. M., Ellis, R. S., Treu, T., et al. 2005, The Astrophysical Journal, 634, 977

Moran, S. M., Ellis, R. S., Treu, T., et al. 2007, ApJ, 671, 1503

Morrissey, P., Conrow, T., Barlow, T. A., et al. 2007, ApJS, 173, 682

Oemler, Jr., A. 1974, ApJ, 194, 1

Oke, J. B. 1974, ApJS, 27, 21

Oke, J. B. 1990, AJ, 99, 1621

Oliver, S. J., Bock, J., Altieri, B., et al. 2012, MNRAS, 424, 1614

Oliver, S. J., Wang, L., Smith, A. J., et al. 2010, A&A, 518, L21

Osterborck, D.E. & Ferland, G. 2006, Mercury, 35, 40

Oteo, I., Bongiovanni, A., Pérez García, A. M., et al. 2011, ApJ, 735, L15

Oteo, I., Magdis, G., Bongiovanni, Á., et al. 2013, MNRAS, 435,158

Ott, S., Bakker, J., Brumfitt, J., et al. 2006, in Astronomical Society of the Pacific Conference Series, Vol. 351, 516, Astronomical Data Analysis Software and Systems XV, ed. C. Gabriel, C. Arviset, D. Ponz, & S. Enrique

Pagel, B. E. J., Edmunds, M. G., Blackwell, D. E., Chun, M. S., & Smith, G. 1979, MNRAS, 189, 95

Pascual, S., Gallego, J., & Zamorano, J. 2007, PASP, 119, 30

Peng, Y.-j., Lilly, S. J., Kovač, K., et al. 2010, ApJ, 721, 193

Pérez-Martínez, R., Sánchez-Portal, M., Pintos-Castro, I., et al. 2013, Astronomische Nachrichten, 334,458

Petty, S. M., Armus, L., Charmandaris, V., et al. 2014, AJ, 148, 111

Pilbratt, G. L., Riedinger, J. R., Passvogel, T., et al. 2010, A&A, 518, L1

Pimbblet, K. A., Shabala, S. S., Haines, C. P., Fraser-McKelvie, A., & Floyd, D. J. E. 2013, MNRAS, 429, 1827

Pimbblet, K. A., Smail, I., Edge, A. C., et al. 2001, MNRAS, 327, 588

Pineau, F.-X., Motch, C., Carrera, F., et al. 2011, Astronomy and Astrophysics, 527, A126

Pintos-Castro, I., Sánchez-Portal, M., Cepa, J., et al. 2013, A&A, 558, A100

Pisani, A. 1993, MNRAS, 265, 706

Pisani, A. 1996, MNRAS, 278, 697

Poggianti, B. M., Smail, I., Dressler, A., et al. 1999, ApJ, 518, 576

Poglitsch, A., Waelkens, C., Geis, N., et al. 2010, A&A, 518, L2

Polletta, M., Tajer, M., Maraschi, L., et al. 2007, The Astrophysical Journal, 663, 81

Popesso, P., Biviano, A., Romaniello, M., & Böhringer, H. 2007, A&A, 461, 411

Postman, M., Franx, M., Cross, N. J. G., et al. 2005, ApJ, 623, 721

Rieke, G. H., Young, E. T., Engelbracht, C. W., et al. 2004, ApJS, 154, 25

Rosa-González, D., Terlevich, E., & Terlevich, R. 2002, MNRAS, 332, 283

Rosen, S., Watson, M., Pye, J., et al. 2015, in Astronomical Society of the Pacific Conference Series, Vol. 495, Astronomical Society of the Pacific Conference Series, ed. A. R. Taylor & E. Rosolowsky, 319

Ruderman, J. T. & Ebeling, H. 2005, ApJ, 623, L81

Sánchez-Portal, M., Pintos-Castro, I., Pérez-Martínez, R., et al. 2015, A&A, 578, A30

Savage, R. S. & Oliver, S. 2007, ApJ, 661, 1339

Seaton, M. J. 1979, MNRAS, 187, 73P

Skrutskie, M. F., Cutri, R. M., Stiening, R., et al. 2006, AJ, 131, 1163

Smith, G. P., Edge, A. C., Eke, V. R., et al. 2003, ApJ, 590, L79

Smith, G. P., Treu, T., Ellis, R. S., Moran, S. M., & Dressler, A. 2005, ApJ, 620,78

Sobral, D., Best, P. N., Geach, J. E., et al. 2010, MNRAS, 404, 1551

Soucail, G., Ota, N., Böhringer, H., et al. 2000, A&A, 355, 433

Stasińska, G., Cid Fernandes, R., Mateus, A., Sodré, L., & Asari, N. V. 2006, MNRAS, 371, 972

Stern, D., Eisenhardt, P., Gorjian, V., et al. 2005, ApJ, 631, 163

Strüder, L., Briel, U., Dennerl, K., et al. 2001, A&A, 365, L18

Sutherland, W. & Saunders, W. 1992, MNRAS, 259, 413-420

Szokoly, G. P., Bergeron, J., Hasinger, G., et al. 2004, ApJS, 155, 271

Taylor, M. B. 2005, in Astronomical Society of the Pacific Conference Series, Vol. 347, Astronomical Data Analysis Software and Systems XIV, ed. P. Shopbell, M. Britton, & R. Ebert, 29

Trager, S. C., Worthey, G., Faber, S. M., Burstein, D., & González, J. J. 1998, ApJS, 116, 1

Treu, T., Ellis, R. S., Kneib, J.-P., et al. 2003, ApJ, 591, 53

Turner, M. J. L., Abbey, A., Arnaud, M., et al. 2001, A&A, 365, L27

Tyson, J. A., Kochanski, G. P., & Dell'Antonio, I. P. 1998, ApJ, 498, L107

Veilleux, S. & Osterbrock, D. E. 1987, ApJS, 63, 295

Walcher, J., Groves, B., Budavári, T., & Dale, D. 2011, Astrophysics and Space Science, 331, 1

Webb, T. M. A., O'Donnell, D., Yee, H. K. C., et al. 2013, The Astronomical Journal, 146, 84

Werner, M. W., Roellig, T. L., Low, F. J., et al. 2004, ApJS, 154, 1

Whitaker, K. E., van Dokkum, P. G., Brammer, G., & Franx, M. 2012, ApJ, 754, L29

Wilkes, B. 1999, in Astronomical Society of the Pacific Conference Series, Vol. 162, Quasars and Cosmology, ed. G. Ferland & J. Baldwin, 15

Wilson, J. C., Eikenberry, S. S., Henderson, C. P., et al. 2003, in Society of Photo-Optical Instrumentation Engineers (SPIE) Conference Series, Vol. 4841, 451, Instrument Design and Performance for Optical/Infrared Ground-based Telescopes, ed. M. Iye & A. F. M. Moorwood

Zhang, Y.-Y., Böhringer, H., Mellier, Y., Soucail, G., & Forman, W. 2005, A&A, 429, 85

Zwicky, F., Herzog, E., Wild, P., Karpowicz, M., & Kowal, C. T. 1961, Catalogue of galaxies and of clusters of galaxies, Vol. I

Esta tesis doctoral ha sido compuesta en LaTeX,
originalmente desarrollado por Leslie Lamport y basado
en TeX, de Donald Knuth.

Se terminó de escribir en Madrid el 10 de Noviembre de
2015.

This thesis was typeset using the LaTeX typesetting
system originally developed by Leslie Lamport, based on
TeX created by Donald Knuth.

It was finished in Madrid, on the 10^{th} of November, 2015.